LEABHARLANN CHOLÁISTE NA TRÍONÓIDE, BAILE ÁTHA CLIATH | TRINITY COLLEGE LIBRARY DUBLIN
Ollscoil Átha Cliath | The University of Dublin

Terms and Conditions of Use of Digitised Theses from Trinity College Library Dublin

Copyright statement

All material supplied by Trinity College Library is protected by copyright (under the Copyright and Related Rights Act, 2000 as amended) and other relevant Intellectual Property Rights. By accessing and using a Digitised Thesis from Trinity College Library you acknowledge that all Intellectual Property Rights in any Works supplied are the sole and exclusive property of the copyright and/or other IPR holder. Specific copyright holders may not be explicitly identified. Use of materials from other sources within a thesis should not be construed as a claim over them.

A non-exclusive, non-transferable licence is hereby granted to those using or reproducing, in whole or in part, the material for valid purposes, providing the copyright owners are acknowledged using the normal conventions. Where specific permission to use material is required, this is identified and such permission must be sought from the copyright holder or agency cited.

Liability statement

By using a Digitised Thesis, I accept that Trinity College Dublin bears no legal responsibility for the accuracy, legality or comprehensiveness of materials contained within the thesis, and that Trinity College Dublin accepts no liability for indirect, consequential, or incidental, damages or losses arising from use of the thesis for whatever reason. Information located in a thesis may be subject to specific use constraints, details of which may not be explicitly described. It is the responsibility of potential and actual users to be aware of such constraints and to abide by them. By making use of material from a digitised thesis, you accept these copyright and disclaimer provisions. Where it is brought to the attention of Trinity College Library that there may be a breach of copyright or other restraint, it is the policy to withdraw or take down access to a thesis while the issue is being resolved.

Access Agreement

By using a Digitised Thesis from Trinity College Library you are bound by the following Terms & Conditions. Please read them carefully.

I have read and I understand the following statement: All material supplied via a Digitised Thesis from Trinity College Library is protected by copyright and other intellectual property rights, and duplication or sale of all or part of any of a thesis is not permitted, except that material may be duplicated by you for your research use or for educational purposes in electronic or print form providing the copyright owners are acknowledged using the normal conventions. You must obtain permission for any other use. Electronic or print copies may not be offered, whether for sale or otherwise to anyone. This copy has been supplied on the understanding that it is copyright material and that no quotation from the thesis may be published without proper acknowledgement.

Galaxy Clusters, Voids and Elliptical galaxies using the ROSAT PSPC.

by

Michael Carr

M.Sc.

A Thesis submitted to

The University of Dublin

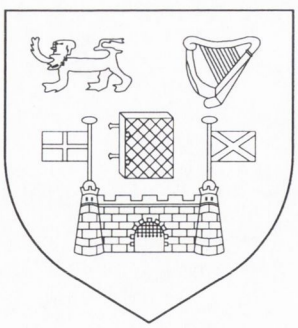
for the degree of

Doctor in Philosophy

Department of Physics

University of Dublin

Trinity College



October, 2002

TRINITY COLLEGE
21 MAY 2003
LIBRARY DUBLIN
THESIS
7888
7248

Abstract

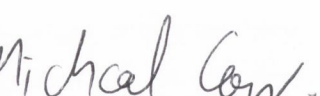
The ROSAT data archive contains of the order of 100,000 sources observed by the ROSAT PSPC (Position Sensitive Proportional Counter). For many sources detected with the ROSAT PSPC there is not a sufficient number of photons ($\sim$ 1,000) to make reliable spectra. As an alternative to spectra, Hardness Ratios (HR's)(ratios of photons in selected bands of the spectra) are calculated. It is not possible to determine spectral parameters directly from HR's.

In this thesis as a tool for calculating spectral parameters from HR plots, spectra are simulated for an Absorbed Power law model (with a range of values of absorbing N_H and photon index Γ) and a Raymond-Smith model (with a range of values of absorbing N_H and temperaure, T and redshift, z.). HR's are calculated from the simulations giving a well defined grid of points in a diagram of HR1 v HR2. Observed HR's may then be compared with the grid of HR's to set limits on spectral parameters. These simulated grids are then applied to three levels of structure in the Universe, namely Voids in the Large Scale Structure (we find evidence of processed gas), Galaxy clusters and Elliptical galaxies (values of temperature and N_H are derived for 22 clusters and 86 ellipticals respectively).

Declaration

This thesis has not been submitted as an exercise for a degree at any other University. Except the following listed articles and where otherwise stated, the work described herein has been carried out by the author alone. This thesis may be borrowed or copied upon request with the permission of the Librarian, University of Dublin, Trinity College. The copyright belongs jointly to the University of Dublin, Dunsink Observatory and Michael Carr.

X-ray Spectral charactreistics and brightness profiles of EMSS clusters, derived from ROSAT PSPC observations
M. J. Carr, L. Norci and E. J. A. Meurs, In prep., *ROSAT Hardness Ratio analysis for Early Type Galaxies*
M. J. Carr, and E. J. A. Meurs, In prep., *Processed material in Voids in the Large Scale Structure using ROSAT PSPC observations*
M. J. Carr, and E. J. A. Meurs, In prep., *X-raying the Voids in the Large Scale Structure*
M. J. Carr, and E. J. A. Meurs, 2001, ssx.proc..345C

Signature of Author 
Michael Carr
October, 2002

Summary

The ROSAT data archive contains of the order of 100,000 sources observed by the ROSAT PSPC (Position Sensitive Proportional Counter). For many sources detected with the ROSAT PSPC there is not a sufficient number of photons ($\sim$ 1,000) to make reliable spectra. As an alternative to spectra, Hardness Ratios (HR's)(ratios of photons in selected bands of the spectra) are calculated. It is not possible to determine spectral parameters directly from HR's.

In this thesis as a tool for calculating spectral parameters from HR plots, spectra are simulated for an Absorbed Power law model (with a range of values of absorbing N_H and photon index Γ) and a Raymond-Smith model (with a range of values of absorbing N_H and temperaure, T and redshift, z.). HR's are calculated from the simulations giving a well defined grid of points in a diagram of HR1 vs. HR2. Observed HR's may then be compared with the grid of HR's to set limits on spectral parameters. These simulated grids are then applied to three levels of structure in the Universe. First the grid using the Absorbed Power law model is used to search for processed gas in Voids in the Large Scale Structure. Voids may be checked for the presence of absorbing material by examining spectra of galaxies at the front and back of the void and comparing for intergalactic absorption. It is only possible to check for absorbing material if processed material is involved, as the X-ray absorption is largely determined by the heavier elements. Three voids are selected from the combined CFA-SSRS redshift surveys (de Lapparent et al. 1986), (da Costa et al. 1988), (da Costa et al. 1994) and their positions were cross correlated against the WGA Rosat point source catalogue (White et al. 1994). For most of the galaxies retrieved, there are not enough photons for reliable spectra (i.e. $\sim$ 1000). Alternatively we calculate Hardness

Ratios(HR). Calculating values of N_H from these HR's we find evidence of the presence of processed gas in two of the three voids. In the third void we observe excess absorption. But this is probably caused by the position of the galaxies on the front of the void within a local wall which may contain a lot of gas. In the second part of this thesis we use the Raymond-Smith grid to estimate the temperature and N_H of 22 EMSS clusters. These determinations are then used to calculate fluxes and luminosities for the clusters. In the third and final part, our simulated Raymond-Smith grid is applied to a sample of 86 Ellipticals galaxies determining reliable temperatures for 69 of these. In all three cases we test the reliability of our grid against spectral temperatures and overall we find good agreement .i.e for all our observations the grid temperatures agree with the spectral temperatures to an accuracy of 2 σ. This means that our grid approach works and we are able to extract spectral information from sources with less than 1000 photons, provided they are described by an Absorbed Power law or Raymond-Smith model. It is now also possible to extend this work to other models (e.g. Black-Body) or to observations from other satellites. Finally our grids may be used to discriminate between types of objectse.g. is an object described by a Raymond-Smith model or an Absorbed Power law model telling us if the galaxy in question is active or not.

Acknowledgements

Firstly, I would like to thank my supervisor, Professor Evert Meurs, for all his help and advice during these years. I am very grateful to him for proof-reading this thesis as it was being written and providing me with invaluable comments on it. Secondly I would like to thank Dr. Laura Norci, with whom I collaborated with for the EMSS clusters work, for all her help with with the Data Analysis techniques. Dr. Sara McMurry, my internal supervisor in the Physics Department of TCD. I would especially like to thank John Cunniffe without whose endless help with software and physics problems I don't think I would ever have finished this thesis and for all the cups of tea with fig rolls on the wall. To my mother Annie and my two sisters Maryrose and Caitriona. To Mickey O and Pio for all the free drinks when i was a poor student. To Mickey and Susan for all their help during my many years in college. To all my friends and neighbours in Donegal. To Dan and Ceciila for all the free dinners. Thanks to Jim and Brian in DIT, Bolton St. To Dan Curran and everyone in TCD boxing club. To my Physics teacher Assumpta Harvey for encouraging my interest in Physics. I would also like to thank my two flatmates, Treasa and Rory, during these last five years. And finally a special big hug to Eabhnat for all her presents and patience and for not being high maintenance.

To my father, Charlie.
Love Michael.

Abbreviations

AGN	Active Galactic Nuclei
ASCA	Advanced Satellite for Cosmology and Astrophysics
AXAF	Advanced X-ray Astronomy Facility
CDS	Strasbourg astronomical Data Centre
EXSAS	Extended Scientific Analysis System
FOV	Field of View
HR	Hardness Ratio
HRI	High Resolution Imager
HST	Hubble Space Telescope
IPC	Imaging Proportional Counter
ML	Maximum Likelihood
MPC	Monitor Proportional Counter
MPE	Max Planck Institute for Extraterrestrial Physics
NED	NASA/IPAC Extragalactic Database
PET	Photon Event Table
PSF	Point Spread Function
PSPC	Position Sensitive Proportional Counter
ROSAT	Röntgen Satellite
SASS	Standard Analysis Software System
SIMBAD	Set of Identifications, Measurements and Bibliography for Astronomical Data
XMM	X-ray Multi-Mirror
XRT	X-ray Telescope

Contents

Abstract i

Declaration ii

Summary iii

Acknowledgements v

Abbreviations vii

1 Standard Cosmology 1

1.1 Introduction 1

1.2 Friedman-Robertson-Walker metric (FRW) 2

1.2.1 The Hubble Expansion Law 4

1.3 Redshift Surveys 4

1.4 Large-scale Structure 6

1.5 Cosmological Models 6

1.5.1 Voronoi Models 7

1.6 Voids 9

1.6.1 Lyα- only absorption systems 10

1.7 Galaxy Clusters 10

1.8 Ellipticals 12

2 X-ray Astronomy 13

2.1 Einstein 13

2.1.1 Mission Characteristics 14

2.1.2 Science Highlights: 15

2.2 ROSAT 15
2.2.1 Mission Characteristics 17
2.2.2 Science Highlights: 17
2.3 Position Sensitive Proportional Counter 18
2.3.1 Quantum Efficiency of the PSPCs 18
2.4 X-ray Spectra 18
2.4.1 Supernova Remnants (SNRs) 20
2.4.2 High-Mass X-ray Binaries (Orbs) 21
2.4.3 Low-Mass X-ray Binaries (LMXBs) 21
2.4.4 X-ray Emission from Normal Galaxies 21
2.4.5 Ellipticals 21
2.4.6 Clusters of Galaxies 22
2.4.7 Active Galactic Nuclei (AGNs) 22
2.4.8 Seyfert Galaxies 22
2.4.9 Seyfert 1 Galaxies 23
2.4.10 Seyfert 2 Galaxies 24
2.4.11 Quasars (Quasi Stellar Radio Sources) 24
2.4.12 QSOs(Quasi Stellar Objects) 24
2.4.13 Radio Galaxies 24
2.4.14 BL Lac objects 24
2.4.15 Unified Theory of AGNs 25
2.5 Galactic Neutral Hydrogen 25

3 Simulation of Power law grid **27**
3.1 Introduction 27
3.2 Spectral Modeling 28
3.3 Grid 37
3.4 Relation of N_H and Γ to HR1,HR2 40

4 Application of Simulated grid **44**
4.1 **Data reduction** 44
4.2 **Selection of voids** 45
4.2.1 Weighted Averages and Statistical test 45
4.2.2 Void A 47
4.2.3 Void A: Results 49

4.2.4 Void B: 55
4.2.5 Void C: 59
4.3 Comparison of simulations with observations 62
4.3.1 NGC3786 69
4.3.2 NGC4253 73
4.3.3 NGC4151 76
4.3.4 NGC4051 79
4.4 Discussion 81

5 Clusters of Galaxies **89**
5.1 Introduction 89
5.2 The Sample 91
5.2.1 A Summary of X-ray Observations of the Sample. . . . 91
5.3 X-ray Data Reduction 94
5.3.1 Preparation of Images 94
5.3.2 Spectral Analysis and Flux Calculation 95
5.3.3 X-ray Brightness Profiles 98
5.3.4 Simulation of Hardness Ratios 99
5.3.5 Application of the Simulated Grid 105
5.3.6 Difference between a zero redshift absorber and a redshifted absorber 114
5.3.7 Comparison of β and r_c Values with Results from the Literature 114
5.3.8 Correlation between r_c and β. 114
5.4 Comparison with Nichol and WARPS fluxes 115
5.5 ROSAT temperatures versus ASCA temperatures 119
5.6 Discussion 123
5.6.1 Appendices 124

6 Contour plots for the EMSS Galaxy Clusters **125**

7 Isothermal β Model Fits **137**

8 Furhter Isothermal β Model Profiles. **149**

9 ROSAT Hardness Ratio Analysis for Early Type Galaxies 152
9.1 Selection of Galaxies and X-ray Data Analysis 153
9.1.1 Data Analysis 153
9.2 Determination of the Extent of the Early Type Galaxies . . . 154
9.3 Hardness Ratio Spectral Grids 156
9.4 Reliability of the Simulated Grid 157
9.4.1 NGC1399 161
9.4.2 NGC1404 161
9.4.3 NGC4472 162
9.4.4 NGC5322 162
9.5 kT-σ Correlation 181
9.6 The L_x:T_x relation 182
9.7 Using Grids to search for activity 184
9.8 Results 185
9.9 Conclusion 186
9.10 Notes 187
9.10.1 NGC221 187
9.10.2 NGC1052 188
9.10.3 NGC 4486 188
9.10.4 IC 1459 189

10 Conclusions and Future Work 192
10.1 Conclusions 192
10.2 Future Work 193

A Spectral fits for the EMSS clusters 201

B Further Spectral Fits of EMSS Clusters 205

C 2 Dimensional χ^2 for the EMSS Galaxy Clusters 210

D 1 dimensional χ^2 for the EMSS Galaxy Clusters 222
D.1 Notes on Individual Clusters discussed in chapter 5 234
D.1.1 MS 0015.9 +1609 (Cl0016+16) 234
D.1.2 MS 0353.6-3542 (S400) 234
D.1.3 MS 0418.3-3844 234

D.1.4 MS 0451.5+0250(A520) 234
D.1.5 MS 0451.6-0305 235
D.1.6 MS 0735.6 +7421(z1370) 235
D.1.7 MS0811.6+6301 235
D.1.8 MS 1020.7+6820(A981) 236
D.1.9 MS1111.8-3754 236
D.1.10 MS1201.5 +2824(A1455) 236
D.1.11 MS 1208.7+3928 236
D.1.12 MS 1308.8+3244 236
D.1.13 MS 1335.2-2928 236
D.1.14 MS 1358.4+6245(ZW6429) 236
D.1.15 MS1426.4+0158 237
D.1.16 MS1512.4+3647 237
D.1.17 MS 1546.1+1132 237
D.1.18 MS1617.1+3237 237
D.1.19 MS2137.3-2353 237
D.1.20 MS2255.7+2039(A2092) 237
D.1.21 MS2311.2-4259 (Abell S1101) 238
D.1.22 MS2354.4-3502 (Abell 4059) 238
D.2 Comparison of β values obtained with published values with other work 238

List of Figures

1.1 The CfA redshift survey,DEC 15-20 deg and recessional velocity 0-15,000 km/s. 7
1.2 The CfA redshift survey,DEC 20-25 deg and recessional velocity 0-15,000 km/s. 8

2.1 The Einstein satellite 14
2.2 The ROSAT satellite 16
2.3 The quantum efficiency of the ROSAT PSPC as a function of energy. Included are the window transmission, the average transmission of the window support mesh, and the gas stopping efficiency. 19
2.4 AGN 23

3.1 Spectral simulation 30
3.2 Spectral simulation 31
3.3 Simulation for 20 counts 32
3.4 Simulation for 20 counts 32
3.5 Simulation for 50 counts 33
3.6 Simulation for 50 counts 33
3.7 Simulation for 1000 counts 34
3.8 Simulation for 1000 counts 34
3.9 Standard deviation of HR1 v counts 36
3.10 Standard deviation of HR2 v counts 36
3.11 A simulation of mean HR1 v HR2 38
3.12 HR grid for 50 counts 38
3.13 HR grid for 50 counts 39
3.14 HR grid for 100000 counts 39

3.15 HR grid for 100000 counts 40
3.16 N_H versus mean simulated HR1 41
3.17 N_H versus mean simulated HR2 41
3.18 Γ (photon index) versus mean simulated HR1 43
3.19 Γ versus mean simulated HR2 43

4.1 Void A: Slice A 48
4.2 Void A: Slice B 50
4.3 Void A: Slice C 51
4.4 Void A: HR1 v HR2 52
4.5 Void A: HR1 v recessional velocity 53
4.6 Void A: HR2 versus recessional velocity 54
4.7 Void B: Slice A 60
4.8 Void B:Slice B 60
4.9 Void B: HR1 v HR2 62
4.10 Void B: HR1 vs recessional velocity 64
4.11 Void B: HR2 vs recessional velocity 65
4.12 Void C:Slice A 66
4.13 Void C:Slice B 66
4.14 Void C:Slice C 67
4.15 Void C: Slice D 67
4.16 Void C:Slice E 68
4.17 Void C: HR1 vs HR2 68
4.18 Void C: HR1 vs z 69
4.19 Void C: HR1 vs z, ... 72
4.20 Power Law fit to the galaxy NGC3786 73
4.21 Contour plot of χ^2, for the galaxy NGC3786 74
4.22 Contour plot of χ^2, for the galaxy NGC3786 75
4.23 Power Law fit to the galaxy NGC4253 76
4.24 Contour plot of χ^2, for the galaxy NGC4253 77
4.25 Contour plot of χ^2, for the galaxy NGC4253 78
4.26 Power Law fit to the galaxy NGC4151 80
4.27 Power Law and black body fit to the galaxy NGC4151 81

4.28 Contour plot of χ^2, for the galaxy NGC4151 as a function of the column density N_H (in units of $10^{21} cm^{-2}$) for two confidence levels of 68.3 % and 94.5 %. 82
4.29 Contour plot of χ^2, for the galaxy NGC4151 83
4.30 Power Law fit to the galaxy NGC4051 84
4.31 Contour plot of χ^2, for the galaxy NGC4051 85
4.32 Contour plot of χ^2, for the galaxy NGC4051 86

5.1 Frequency distribution of redshifts for the cluster sample . . . 94
5.2 Histogram of the background-subtracted 0.1-2.4keV counts for each cluster 94
5.3 Contour plot for the cluster MS0015.9+ 1609 96
5.4 Contour plot of χ^2, for the cluster MS0015.9+1609 as a function of the temperature (in keV) and the column density N_H (in $10^{21} cm^{-2}$) for two confidence levels of 68.3 % and 94.5 % . 97
5.5 Contour plot of χ^2, for the cluster MS0015.9+1609 97
5.6 Isothermal β model fitted to the radial profile of the cluster MS0015.9+ 1609 99
5.7 We plot the effect of q_0 on the value of the luminosity 104
5.8 Spectral simulation of 100,000 cts, ... 105
5.9 Spectral simulation of 100,000 cts, ... 108
5.10 Spectral simulation of 100,000 cts 109
5.11 Grid at z=0.4 109
5.12 Grid at z=0.4 110
5.13 Observed values of HR1 and HR2 110
5.14 β versus the core radius 116
5.15 Plot of N97 flux (0.1-2.4 keV) versus our flux (0.1-2.4 keV). . 119
5.16 Plot of WARP's flux (0.5-2keV) (using the MEKAL model) versus our flux(0.5-2 keV). 121
5.17 X-ray K-corrections for the 0.5-2 keV band 122
5.18 A histogram of the ROSAT PSPC temperatures for the EMSS clusters. 122
5.19 Plot of ROSAT temperature(this paper) versus ASCA temperature 123

6.1 Contour plot for the galaxy cluster MS0015.9+1609. 125
6.2 Contour plot for the galaxy cluster MS0353.6-3642 126
6.3 Contour plot for the galaxy cluster MS0418.3-3844. 126
6.4 Contour plot for the galaxy cluster MS0451.5+0250. 127
6.5 Contour plot for the galaxy cluster MS0451.6-0305 127
6.6 Contour plot for the galaxy cluster MS0735.6+7421 128
6.7 Contour plot for the galaxy cluster MS0811.6+6301 129
6.8 Contour plot for the galaxy cluster MS1020.7+6820 129
6.9 Contour plot for the galaxy cluster MS1111.8-3754 130
6.10 Contour plot for the galaxy cluster MS1201.5+2824 130
6.11 Contour plot for the galaxy cluster MS1208.7+3928 131
6.12 Contour plot for the galaxy cluster MS1308.8+3244 131
6.13 Contour plot for the galaxy cluster MS1335.2-2928 132
6.14 Contour plot for the galaxy cluster MS1335.2-2928 132
6.15 Contour plot for the galaxy cluster MS1426.4+0158 133
6.16 Contour plot for the galaxy cluster MS1512.4+3647 133
6.17 Contour plot for the galaxy cluster MS1546.1+1132 134
6.18 Contour plot for the galaxy cluster MS1617.1+3237 134
6.19 Contour plot for the galaxy cluster MS2137.3-2353 135
6.20 Contour plot for the galaxy cluster MS2255.7+2039 135
6.21 Contour plot for the galaxy cluster MS2311.2-4259 136
6.22 Contour plot for the galaxy cluster MS2354.4-3502 136

7.1 Fit of the Isothermal β model to the radial profile of MS0015.9+1609.137
7.2 Fit of the Isothermal β model to the radial profile of MS0353.6-3642. 141
7.3 Fit of the Isothermal β model to the radial profile of MS0418.3-3844. 141
7.4 Fit of the Isothermal β model to the radial profile of MS0451.5+0250 142
7.5 Fit of the Isothermal β model to the radial profile of MS0451.6-0305. 142
7.6 Fit of the Isothermal β model to the radial profile of MS0735.6+7421. 143

7.7 Fit of the Isothermal β model to the radial profile of MS0811.6+6301. 143
7.8 Fit of the Isothermal β model to the radial profile of MS1020.7+6820.144
7.9 Fit of the Isothermal β model to the radial profile of MS1111.8-3754 144
7.10 Fit of the Isothermal β model to the radial profile of MS1201.5+2824.145
7.11 Fit of the Isothermal β model to the radial profile of MS1208.7+3928.145
7.12 Fit of the Isothermal β model to the radial profile of MS1308.8+3244. 146
7.13 Fit of the Isothermal β model to the radial profile of MS1335.2-2928 146
7.14 Fit of the Isothermal β model to the radial profile of MS1335.2-2928. 147
7.15 Fit of the Isothermal β model to the radial profile of MS1426.4+0158.147
7.16 Fit of the Isothermal β model to the radial profile of MS1512.4+3647.148
7.17 Fit of the Isothermal β model to the radial profile of MS1546.1+1132.148

8.1 it of the Isothermal β model to the radial profile of MS1617.1+3237.149
8.2 Fit of the Isothermal β model to the radial profile of MS2137.3-2353. 150
8.3 Fit of the Isothermal β model to the radial profile of MS2255.7+2039.150
8.4 Fit of the Isothermal β model to the radial profile of MS2311.2-4259. 151
8.5 Fit of the Isothermal β model to the radial profile of MS2354.4-3502. 151

9.1 Contour plot for the early type galaxy NGC2329 155
9.2 Contour plot for the early type galaxy NGC708 156
9.3 Contour plot for the early type galaxy NGC1316 157
9.4 Radial profile of the early type galaxy IC 310 158
9.5 Radial profile of the early type galaxy IC 1860 159
9.6 Grid at z=0, for T $\geq$ 2 KeV 159
9.7 Grid at z=0, for T $\leq$ 2 keV in steps of 0.2 160
9.8 Spectrum of NGC1399. 162
9.9 2 dimensional χ^2 plot for the elliptical galaxy NGC1399 . . . 163

9.10 1 dimensional χ^2 plot for the elliptical galaxy NGC1399 163
9.11 Spectrum of NGC1404 164
9.12 2 dimensional χ^2 plot for the elliptical galaxy NGC1404 164
9.13 1 dimensional χ^2 plot for the elliptical galaxy NGC1404 . . . 165
9.14 Spectrum of NGC4472 165
9.15 2 dimensional χ^2 plot for the elliptical galaxy NGC4472 . . . 166
9.16 1 dimensional χ^2 plot for the elliptical galaxy NGC4472 166
9.17 Spectrum of NGC5322. 167
9.18 2 dimensional χ^2 plot for the elliptical galaxy NGC5322 168
9.19 1 dimensional χ^2 plot for the elliptical galaxy NGC5322 . . . 169
9.20 Observed values of HR1 and HR2. 170
9.21 Observed values of HR1 and HR2 170
9.22 Comparison of Temperatures with those of DW 171
9.23 Comparison of Temperatures with those of DW 171
9.24 The log of kT versus the log of the velocity dispersion 182
9.25 The log of kT versus the log of the velocity dispersion, for the sample B 183
9.26 Luminosity versus Temperature 184
9.27 Galaxies outside the Raymond-Smith grid 185
9.28 Outlying galaxies plotted against the Power Law grid 186
9.29 Histogram of temperatures 187
9.30 Plots of HR 1 against recessional velocity for 86 elliptical galaxies 188
9.31 Plots of HR 2 against recessional velocity 189
9.32 Histogram of counts 190
9.33 HR1 v L 190
9.34 HR2 v L 191

A.1 Spectral fit of the Raymond-Smith model to the galaxy cluster MS0015.9+1609 with a reduced χ^2=1.01. 201
A.2 Spectral fit of the Raymond-Smith model to the galaxy cluster MS0353.6-3642 with a reduced χ^2= 0.98. 202
A.3 Spectral fit of the Raymond-Smith model to the galaxy cluster MS0418.3-3844with a reduced χ^2=1.57. 202
A.4 Spectral fit of the Raymond-Smith model to the galaxy cluster MS0451.5+0250with a reduced χ^2=0.84. 202

A.5 Spectral fit of the Raymond-Smith model to the galaxy cluster MS0451.6-0305 with a reduced χ^2=1.55. 203
A.6 Spectral fit of the Raymond-Smith model to the galaxy cluster MS0735.6+7421 with a reduced χ^2=0.70. 203
A.7 Spectral fit of the Raymond-Smith model to the galaxy cluster MS0811.6+6301 with a reduced χ^2=1.40. 203
A.8 Spectral fit of the Raymond-Smith model to the galaxy cluster MS1020.7+6820 with a reduced χ^2=1.26. 204
A.9 Spectral fit of the Raymond-Smith model to the galaxy cluster MS1111.8-3754 with a reduced χ^2=1.32. 204
A.10 Spectral fit of the Raymond-Smith model to the galaxy cluster MS1201.5+2824 with a reduced χ^2=0.64. 204

B.1 Spectral fit of the Raymond-Smith model to the galaxy cluster MS1208.7+3928 with a reduced χ^2=1.22. 205
B.2 Spectral fit of the Raymond-Smith model to the galaxy cluster MS1308.8+3244 with a reduced χ^2=1.16 206
B.3 Spectral fit of the Raymond-Smith model to the galaxy cluster MS1335.2-2928 with a reduced χ^2=1.60. 206
B.4 Spectral fit of the Raymond-Smith model to the galaxy cluster MS1335.2-2928 with a reduced χ^2=0.77. 206
B.5 Spectral fit of the Raymond-Smith model to the galaxy cluster MS1426.4+0158 with a reduced χ^2=0.58. 207
B.6 Spectral fit of the Raymond-Smith model to the galaxy cluster MS1512.4+3647 with a reduced χ^2=0.59. 207
B.7 Spectral fit of the Raymond-Smith model to the galaxy cluster MS1546.1+1132 with a reduced χ^2=1.35. 207
B.8 Spectral fit of the Raymond-Smith model to the galaxy cluster MS1617.1+3237 with a reduced χ^2=0.20. 208
B.9 Spectral fit of the Raymond-Smith model to the galaxy cluster MS2137.3-2353 with a reduced χ^2=0.07. 208
B.10 Spectral fit of the Raymond-Smith model to the galaxy cluster MS2255.7+2039 with a reduced χ^2=0.64. 208
B.11 Spectral fit of the Raymond-Smith model to the galaxy cluster MS2311.2-4259 with a reduced χ^2=1.22. 209

B.12 Spectral fit of the Raymond-Smith model to the galaxy cluster MS2354.4-3502 with a reduced χ^2=1.96. 209

C.1 2 dimensional χ^2 plot for the galaxy cluster MS0015.9+1609. 210
C.2 2 dimensional χ^2 plot for the galaxy cluster MS0353.6-3642 . 211
C.3 2 dimensional χ^2 plot for the galaxy cluster MS0418.3-3844 . 211
C.4 2 dimensional χ^2 plot for the galaxy cluster MS0451.5+0250. . 212
C.5 2 dimensional χ^2 plot for the galaxy cluster MS0451.6-0305. . 212
C.6 2 dimensional χ^2 plot for the galaxy cluster MS0735.6+7421. 213
C.7 2 dimensional χ^2 plot for the galaxy cluster MS0811.6+6301. 213
C.8 2 dimensional χ^2 plot for the galaxy cluster MS1020.7+6820. 214
C.9 2 dimensional χ^2 plot for the galaxy cluster MS1111.8-3754 . 214
C.10 2 dimensional χ^2 plot for the galaxy cluster MS1201.5+2824. 215
C.11 2 dimensional χ^2 plot for the galaxy cluster MS1208.7+3928. 215
C.12 2 dimensional χ^2 plot for the galaxy cluster MS1308.8+3244. 216
C.13 2 dimensional χ^2 plot for the galaxy cluster MS1335.2-2928 . 216
C.14 2 dimensional χ^2 plot for the galaxy cluster MS1358.4+6245. 217
C.15 2 dimensional χ^2 plot for the galaxy cluster MS1426.4+0158. 217
C.16 2 dimensional χ^2 plot for the galaxy cluster MS1512.4+3647. 218
C.17 2 dimensional χ^2 plot for the galaxy cluster MS1546.1+1132. 218
C.18 2 dimensional χ^2 plot for the galaxy cluster MS1617.1+3237. 219
C.19 2 dimensional χ^2 plot for the galaxy cluster MS2137.3-2353. . 219
C.20 2 dimensional χ^2 plot for the galaxy cluster MS2255.7+2039. 220
C.21 2 dimensional χ^2 plot for the galaxy cluster MS2311.2-4259. . 220
C.22 2 dimensional χ^2 plot for the galaxy cluster MS2354.4-3502. . 221

D.1 1 dimensional χ^2 plot for the galaxy cluster MS0015.9+1609, for N_H fixed at 0.6 $\times 10^{21} cm^{-2}$. 222
D.2 1 dimensional χ^2 plot for the galaxy cluster MS0353.6-3642 , for N_H fixed at 0.1 $\times 10^{21} cm^{-2}$. 223
D.3 1 dimensional χ^2 plot for the galaxy cluster MS0418.3-3844, for N_H fixed at 0.207 $\times 10^{21} cm^{-2}$. 223
D.4 1 dimensional χ^2 plot for the galaxy cluster MS0451.5+0250, for N_H fixed at 0.78 $\times 10^{21} cm^{-2}$. 224

D.5 1 dimensional χ^2 plot for the galaxy cluster MS0451.6-0305,for N_H fixed at galactic value, 0.437 $\times 10^{21} cm^{-2}$. 224
D.6 1 dimensional χ^2 plot for the galaxy cluster MS0735.6+7421,for N_H fixed at galactic value ,0.348 $\times 10^{21} cm^{-2}$. 225
D.7 1 dimensional χ^2 plot for the galaxy cluster MS0811.6+6301,for N_H fixed at galactic value, 0.428 $\times 10^{21} cm^{-2}$. 225
D.8 1 dimensional χ^2 plot for the galaxy cluster MS1020.7+6820, for N_H fixed at 0.6 $\times 10^{21} cm^{-2}$. 226
D.9 1 dimensional χ^2 plot for the galaxy cluster MS1111.8-3754,for N_H fixed at 1 $\times 10^{21} cm^{-2}$. 226
D.10 1 dimensional χ^2 plot for the galaxy cluster MS1201.5+2824,for N_H fixed at galactic value, 0.244 $\times 10^{21} cm^{-2}$. 227
D.11 1 dimensional χ^2 plot for the galaxy cluster MS1208.7+3928, for N_H fixed at $10^{21} cm^{-2}$. 227
D.12 1 dimensional χ^2 plot for the galaxy cluster MS1308.8+3244, for N_H fixed at galactic value, 0.296 $\times 10^{21} cm^{-2}$. 228
D.13 1 dimensional χ^2 plot for the galaxy cluster MS1335.2-2928, for N_H fixed at galactic value, 0.373 $\times 10^{21} cm^{-2}$. 228
D.14 1 dimensional χ^2 plot for the galaxy cluster MS1358.4+6245,for N_H fixed at 0.244 $\times 10^{21} cm^{-2}$. 229
D.15 1 dimensional χ^2 plot for the galaxy cluster MS1426.4+0158,for N_H fixed at 0.3 $\times 10^{21} cm^{-2}$. 229
D.16 1 dimensional χ^2 plot for the galaxy cluster MS1512.4+3647, for N_H fixed at 0.3 $\times 10^{21} cm^{-2}$. 230
D.17 1 dimensional χ^2 plot for the galaxy cluster MS1546.1+1132, for N_H fixed at galactic value, 0.361 $\times 10^{21} cm^{-2}$. 230
D.18 1 dimensional χ^2 plot for the galaxy cluster MS1617.1+3237,for N_H fixed at 0.2 $\times 10^{21} cm^{-2}$. 231
D.19 1 dimensional χ^2 plot for the galaxy cluster MS2137.3-2353,for N_H fixed at 0.4 $\times 10^{21} cm^{-2}$. 231
D.20 1 dimensional χ^2 plot for the galaxy cluster MS2255.7+2039, for N_H fixed at 1.1 $\times 10^{21} cm^{-2}$. 232
D.21 1 dimensional χ^2 plot for the galaxy cluster MS2311.2-4259, for N_H fixed at galactic value 0.176 $\times 10^{21} cm^{-2}$. 232

D.22 1 dimensional χ^2 plot for the galaxy cluster MS2354.4-3502,for N_H fixed at 0.12 $\times 10^{21} cm^{-2}$. 233

List of Tables

4.1 The coordinate ranges for the three voids, A,B and C. 48
4.2 Void A 49
4.3 Void A results 50
4.4 Void A: Calculation of the N_H at the front and back of Void A 51
4.5 Void B:The List of Galaxies selected from around Void B . . . 56
4.6 Calculated HR's for the galaxies surrounding Void B 57
4.7 Void B results 58
4.8 Void C 61
4.9 The list of galaxies selected from Void C 63
4.10 Void C results 64
4.11 Reliability of grid determinations 70
4.12 Reliability of grid determinations 71

5.1 X-ray observations for our sample other than ROSAT PSPC and Einstein 93
5.2 Table of temperature, flux and luminosity for the 22 galaxy clusters in our sample 103
5.3 Table of N_H derived from 2-D χ^2 plots 106
5.4 Table of T derived from 1-D χ^2 plots 107
5.5 Table of measured β and core radius for all the clusters in our sample. 113
5.6 Table of ROSAT and ASCA temperatures 120

7.1 Table of measured β and core radius for all the clusters in our sample.Col (3) the core radius in arcseconds, Col (4) the net number of counts available for each cluster,Col(5) is the reduced χ^2 of the fit to the isothermal β model, Col(6) is the core radius in Kpc, Col(7) is β as measured in the literature and (8) is the Core radius as measured from the literature in Kpc (except MS1201.5+2824 which is given in arcseconds), an $*$ indicates that r_c was calculated assuming β =2/3. References for r_c are given in Appendix B Col(9) is the cut radius in arcseconds to get the best fit (those marked with a $\star$ are known cooling flows c.f Appendix A for the references and Col (10) notes on individual clusters (see Appendix A). 140

9.1 Elliptical galaxies 180

Chapter 1

Standard Cosmology

1.1 Introduction

Our current understanding of the evolution of the universe is based upon the Friedman-Robertson-Walker (FRW) cosmological model, more popularly known as the Hot Big Bang model. This model has become so successful that is known as the Standard Cosmology. Its development may be traced back to 1917, when Einstein argued that a closed homogeneous world model would fit very well into general relativity theory. In 1926 Hubble demonstrated that the large scale distribution of galaxies is homogeneous and isotropic with no indication of an edge or a boundary[1]. In 1927 Lemaître showed that the uniform distribution of galaxies corresponds with the pattern of galaxy redshifts. The homogeneous model, when generalized to allow for evolution, yields a linear redshift-distance relation consistent with what Hubble found from his estimates of galaxy distances (Hubble 1929). All of this led to the assumption of the cosmological principle, and thus the birth of our standard cosmology. This model successfully describes the evolution of the universe from about $10^{-2}s$ after the initial explosion until the present day. It requires the assumption of the Cosmological Principle, which states that the universe is the same in every direction from every point in space, i.e. it is both isotropic and homogeneous. The Cosmological Principle simplifies the analysis and is confirmed by observations, e.g. the observed isotropy of the

[1]By today's standards this was not an actual proof, but at the time it was accepted as quite strong evidence.

cosmic microwave background radiation (Smoot et al 1992).

1.2 Friedman-Robertson-Walker metric (FRW)

We describe the universe using the FRW -metric

$$ds^2 = (cdt)^2 - R(t)^2 \left(\frac{dr^2}{1-kr^2} + r^2(d\theta^2 + \sin^2\theta d\phi^2) \right), \tag{1.1}$$

where t is the physical time, $R(t)$ is the scale factor, k is the constant of curvature and (r, θ, ϕ) are spherical coordinates. The homogeneity of the matter content of the universe implies that fluid flows are along constant (r, θ, ϕ) trajectories and so these are described as co moving coordinates. It is possible to rescale r and $R(t)$ so that k assumes one of the three discrete values $-1, 0, 1$ depending on the spatial topology and geometry of the universe.

A variety of kinematic effects follow immediately from the FRW metric. Consider two co moving particles separated by a distance d, which will grow proportionally with $R(t)$. There will be a corresponding recessional velocity given by

$$v = Hd, \tag{1.2}$$

where the Hubble parameter H is

$$H = \frac{\dot{R}(t)}{R(t)}, \tag{1.3}$$

with dots denoting derivatives with respect to the cosmic time t. Relation(1.2) is known empirically as Hubble's law, i.e. distant galaxies are receding from our own galaxy with velocity proportional to their distance. The value of H today is

$$H_0 \approx 100h \; kms^{-1}Mpc^{-1}, \tag{1.4}$$

where $0.5 \leq h \leq 1.0$. Another implication of the metric (1.1) is that light with a frequency ν from a source moving away from us will be redshifted. Consider a photon emitted from a source at a coordinate $r = r_i$ at the time t_i, and arriving at a detector coordinate r_0, at time t_0. Photons are bound to travel along null geodesics ($ds^2 = 0$), implying

$$\int_{t_i}^{t_0} \frac{cdt}{R(t)} = \int_0^{r_i} \frac{dr}{\sqrt{1-kr^2}}. \tag{1.5}$$

A photon emitted at $t_i + \delta t_i$ arrives at the detector at time $t_0 + \delta t_0$ with

$$\int_{t_i}^{t_0} \frac{dt}{R(t)} = \int_{t_i+\delta t_i}^{t_0+\delta t_0} \frac{dt}{R(t)}, \tag{1.6}$$

Assuming that $\delta t \ll t$, this implies that $\delta t_i/R(t_i) = \delta t_0/R(t_0)$. If the number of photons emitted by the source per unit time is n_γ^e, then the number of photons received per unit of time by the detector at $r = 0$ is

$$n_\gamma^r = n_\gamma^e \times \frac{R(t_i)}{R(t_0)}. \tag{1.7}$$

Also if δt_i is taken to be the wavelength λ_γ^e of the light emitted by the source at the time t_i we see that the wavelength of the light as measured by the detector at the time t_0 satisfies

$$1 + z \equiv \frac{\lambda_\gamma^r}{\lambda_\gamma^e} = \frac{R(t_0)}{R(t_i)}, \tag{1.8}$$

where z is the redshift of the source. This implies that the energy of an individual photon evolves as $E_\gamma \propto R(t)^{-1}$. Observations of galaxy spectra show that for all galaxies, except those nearby, the spectrum is redshifted, which is very strong evidence of expansion.

We now introduce the idea of a luminosity distance d_L to a source of radiation with luminosity $\mathcal{L}$,

$$d_L^2 = \frac{\mathcal{L}}{4\pi\mathcal{F}}, \tag{1.9}$$

where $\mathcal{F}$ is the energy measured per unit area per unit time. The luminosity distance may only be determined if the absolute luminosity is already known. To solve this problem standard candles are used, e.g. Cepheid variables, whose properties are calibrated locally. If the source at a co-moving coordinate $r = r_i$ emits light at the time t_i and the detector at $r = 0$ receives the light at time t_0 then conservation of energy implies that

$$d_L^2 = R^2(t_0) r_i^2 (1 + z)^2. \tag{1.10}$$

One factor of $(1+z)$ is just the ratio between the number of photons emitted by the source and the number of photons crossing the sphere centred on

the source and containing the detector per unit time. The other is due to the redshift of photons as they travel from the source to the detector. The Hubble law now takes the form

$$H_0 d_L = z + \frac{1}{2}(1 - q_0)z^2 + O(z^3), \tag{1.11}$$

where $H_0 = (\dot{R}/R)_{t_0}$ and $q_0 = -(\ddot{R}R/\dot{R}^2)_{t_0}$ are respectively the Hubble parameter and deceleration parameter at the present time (Coles & Lucchin 1995), (Kolb & Turner 1989). This equation may be used to calculate q_0, using standard candles at very large distances. Recently q_0 has been constrained in the range $q_0 = 0.3 \pm 0.3$ (Perlmuter et al. 1997).

1.2.1 The Hubble Expansion Law

Hubble's discovery that distant galaxies are receding from our own with a recessional velocity proportional to their distance was the first observational evidence for the Hot Big Bang model. The Hubble parameter is defined by $H = \dot{R}(t)/R(t)$ and its value today, H_0, is expressed as

$$H_0 = 100h \; kms^{-1}Mpc^{-1}. \tag{1.12}$$

Recent estimates give $h = 0.69 \pm 0.08$ (Tanvir et al. 1995), $h = 0.85 \pm 0.05$ (Willick & Butra 2001) and $h = 0.65 \pm 0.05$ (Koopmans et al 2001). Methods of determining the Hubble constant range from using Cepheid variables, to gravitational lensing to the Sunyaev- Zel'dovich effect.

1.3 Redshift Surveys

The first consideration in any redshift survey is the choice of a galaxy catalogue to be used as a basis for the survey. To study Large Scale Structure, redshift surveys are required that cover large areas of the sky to a much greater depth than was possible when the older catalogues were made. The geometry of the survey also has to be decided upon, as this affects the type of structures which may be detected. There exist three main types of survey: The first is the pencil beam survey. This is an almost one dimensional survey which measures redshifts along a line of sight. Such surveys can be very deep

but cover only a small angular area of the sky. As a compromise between the depth of pencil beam surveys and the relative shallowness of filled three-dimensional surveys (see below), two-dimensional surveys offer an efficient means of testing the geometry of the galaxy distribution. The third possibility, the three-dimensional survey, covers a large area of the sky and allows the examination of the three dimensional distribution of galaxies. These are the best for topological studies of the three-dimensional structure but they are very expensive in terms of observing time (Giovanelli & Haynes 1991).

Once the catalogue has been obtained and the geometry of the catalogue decided upon it is possible to start taking spectra. This can be quite a slow procedure. Up until 1980, approximately 8,250 radial velocities had been determined but advances in both detector and spectrometer technology meant that by 1990, the redshift of more than 30,000 galaxies were known (Giovanelli & Haynes 1991). In recent years three of the most important redshift surveys have been the Las Campanas Redshift Survey (LCRS) (Shectmann & Landy 1996), Southern Sky Redshift Survey (SSRS) (da Costa et al. 1988) and the Center for Astrophysics (CfA) redshift survey, (de Lapparent et al. 1986). This vast increase in numbers of redshift determined has been due to the development of multiple object spectrography in their various forms which are capable of taking up to 400 spectra at the same time (Maddox et al. 1998). These surveys are dwarfed by the 2df Galaxy redshift survey which had already observed 100,000 redshifts by June 2001 (Colless et al. 2001) and will eventually contain 250,000 redshifts.

1.4 Large-scale Structure

The CfA redshift survey, SSRS and LCRS provide striking evidence for the existence of structure in the large scale distribution of galaxies. Figures 1.1 & 1.2 show two neighbouring redshift 'slices of the universe' from the CfA redshift survey. These figures show that the galaxies are not distributed randomly in redshift space but are clustered together to form elongated filamentary structures. Clusters appear in the plots as dark lines or fingers. Clusters and filaments appear to surround large low density regions (voids). If we compare Figure 1.1 and Figure 1.2, we see a remarkable similarity in the structures visible in both slices. In fact, the correlation between structures in different slices in the CfA survey have been found to be very high (de Lapparent et al 1988). One theory of LSS which accounts for the observation of such filaments is that the galaxies lie on sheets which form a foam-like structure in space. Large voids, 'almost empty of galaxies', are surrounded by thin sheets in which the density of galaxies is very high. As we move up through the slices (i.e. increase the declination) the size of the void decreases, eventually disappearing. This is what we would expect to observe if we were looking at cross-sections of a bubble like structure (Icke 1984).

1.5 Cosmological Models

Cosmological models are required which predict the observed large-scale distribution of galaxies, i.e. very inhomogeneous, containing voids and superclusters. These models must reconcile the existence of small-scale structures, galaxies, groups and clusters with the overall homogeneity of the universe on scales larger than Large Scale Structure (LSS). Most of these models, such as the 'hot dark matter' and 'cold dark matter' models, require large N-body simulations in order to produce more detailed predictions (Navarro et al. 1995). These N-body simulations are very expensive in computer time and generally require the use of supercomputers. Simpler macroscopic models have been proposed which reproduce, albeit in a less detailed way, the general properties of LSS. We shall consider one such model, the Voroni model developed by Icke & Van de Weygaert 1989 .

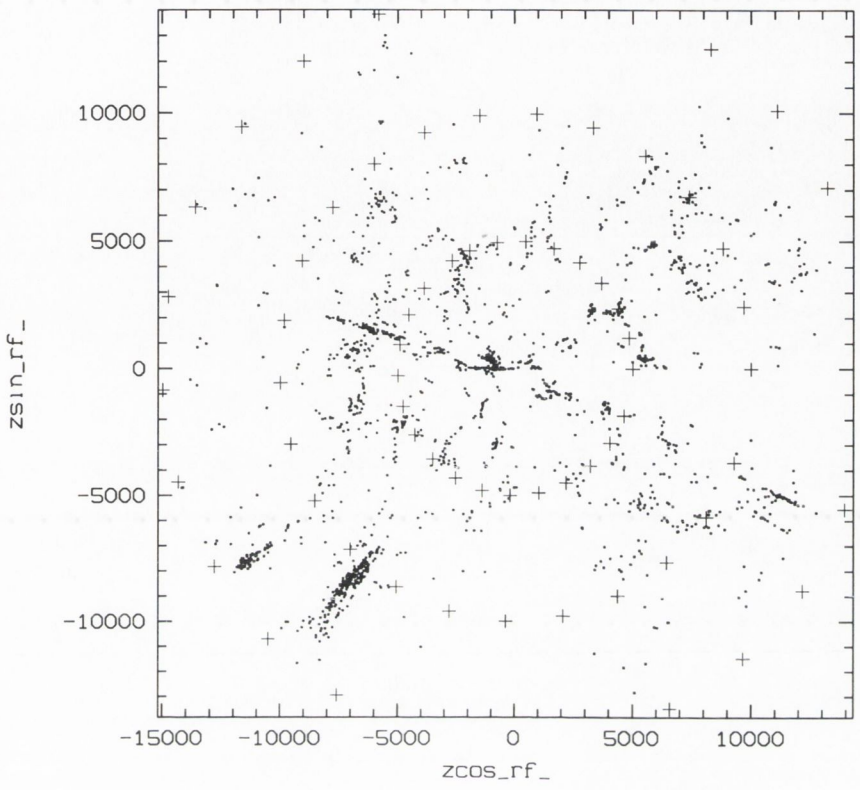


Figure 1.1: The CfA redshift survey in the range R.A 0-24h, DEC 15-20 deg and recessional velocity 0-15,000 km/s. We are projecting a slice of declination 20 deg onto a flat surface so it appears as if a bit is missing i.e we are projecting a cone on to a plane surface. This is done so that we may read the real angular size of a void from our plots. The grid of + signs represent recessional velocities of 5,000, 10,000 and 15,000 km/s respectively and we observe from the point (0,0).

1.5.1 Voronoi Models

We begin with a homogeneous distribution of matter with some small underdensities. The Voronoi model examines the outcome of having a large number of scattered expansion centres. Icke (1984), extending an argument by Lynden-Bell (1969), showed that all large scale density excesses are systematically magnified by the expansion of the universe and produce large filamentary structures. But when the positive density parts undergo collapse, the

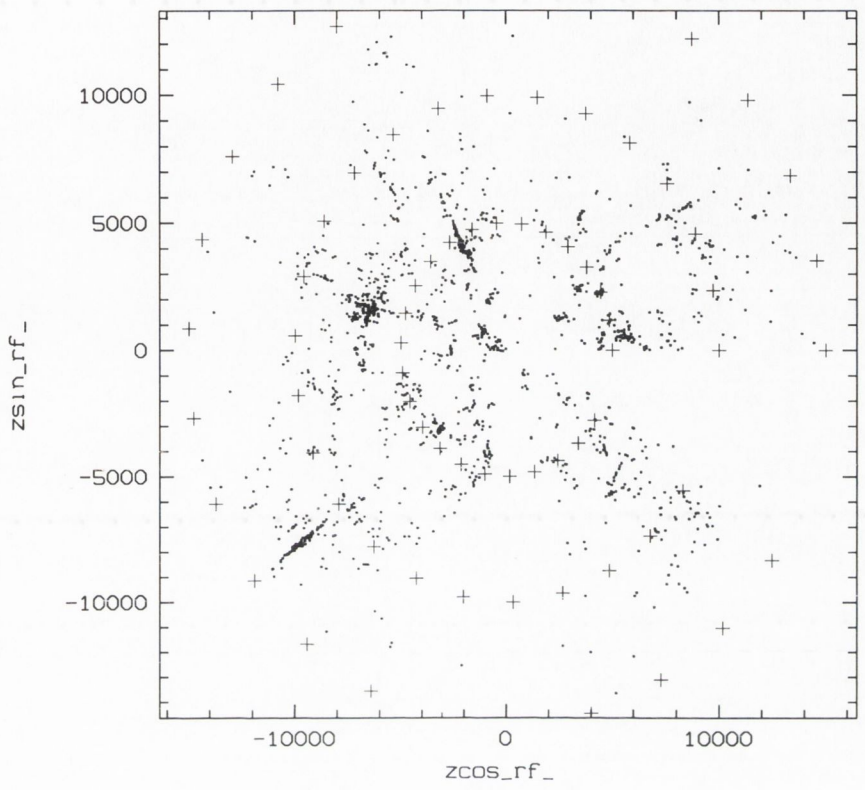


Figure 1.2: The CfA redshift survey in the range R.A 0-24h, DEC 20-25 deg and recessional velocity 0-15,000 km/s. We are projecting a slice of declination 25 deg onto a flat surface so it appears as if a bit is missing.This is done so that we may read the real angular size of a void from our plots.The grid of + signs represent recessional velocities of 5,000, 10,000 and 15,000 km/s respectively and we observe from the point (0,0).

voids expand with matter flowing away from them, and as the void expands its asphericities gradually disappear and it becomes more spherical in shape. After a certain length of time, matter from neighbouring voids will come into contact and walls of matter are formed. Three types of feature are formed. Firstly 2-d surfaces or pancakes. At the intersection of the pancakes we find filaments and finally at the intersection of the filaments nodes form. Matter flows along the cell walls to form filaments and then along the filaments into the nodes. The nodes accrete matter from all directions and become

the densest regions of the distribution. The fact that not all the structures are growing at the same rate causes the distribution of galaxies to have a more sponge like topology in agreement with Gott (Gott et al. 1986). This scenario may be also be viewed inversely, i.e. the matter flows away from the void centres toward the nodes. The era at which galaxy formation begins is still unresolved. The matter which flows toward the nodes may be in the form of gas, resulting in the formation of ill-defined structures. Alternatively formation of (Porto-)galaxies may take place much earlier in the development of the structure and when the voids come into contact, the material involved is mostly in the form of whole galaxies. Galaxies are known to be very sticky when they collide, thus producing very sharp structures.

1.6 Voids

Early redshifts surveys detected huge empty regions in space- Voids. The first indication for the existence of voids came from two early redshift surveys, namely the Coma/A1367 survey (Gregory & Thompson 1978) and the Hercules/A2199 survey (Chincarini et al. 1981) both detecting voids on the scale of $\sim 20h^{-1}Mpc$. This was followed by the discovery of a void with diameter $\sim 60h^{-1}Mpc$ in Bootes (Kirshner et al. 1987). The CfA redshift survey (de Lapparent et al. 1986) and the SSRS and SSRS2 (da Costa et al. 1988; da Costa et al. 1994) have shown that large voids are ubiquitous. Theories on formation and evolution of galaxies had predicted that voids should contain so called "failed galaxies" (Grogin & Geller 2000). Possibilities as to what may constitute these failed galaxies include diffuse dwarfs and Malin 1-type giants (Dekal & Silk 1986; Hoffman et al. 1992), or galaxies with a similar mix as higher density regions outside clusters (Balland,Silk & Schaeffer 1998). Alternatively Lacey et al. (1993) predict that due to the absence of tidal interactions to trigger star formation there may be no luminous galaxies at all. It has been shown that dwarf galaxies follow the distribution of the more luminous galaxies (Kuhn et al. 1997; Popescu et al. 1997 and Bingelli 1989). Low surface-brightness giants are not found in voids and are relatively rare (Szomuru et al. 1996), (Bothun et al. 1993), (Weinberg et al. 1991) and (Henning & Kerr 1989) . About 60 galaxies have

been observed in the Bootes void. These galaxies formed as normal galaxies in local dense pockets (Szomuru et al. 1996).

There have been HI observations of Blue Compact Galaxies (Pustilnik et al. 2002) and intergalactic hydrogen clouds (Manning 2002), (McLin et al. 2002) in voids.

1.6.1 Lyα- only absorption systems

Foreground absorption systems (including Lyα- only absorption systems) have been discovered in quasi-stellar object (QSO) spectra. Competing theories exist as to the nature and origin of Lyα- only absorption systems. Arons (Arons 1972) suggested they might consist of primordial material, whilst alternatively Bahcall & Spitzer (Bahcall & Spitzer 1969) proposed that they may arise in the diffuse gas of extended galaxy halos. These Lyα clouds have been detected in voids (McLin et al. 2002). Recent simulations of structure formation indicate that these absorbers are not directly related to galaxies but are gas associated with an intergalactic medium that varies in density (Dave et al. 1999; Escude 1996) . As the X-ray absorption is largely determined by the heavier elements, it is possible to search for the presence of processed absorbing material by examining X-ray spectra for intergalactic material

1.7 Galaxy Clusters

Clusters, conglomerations of galaxies a few mega-parsecs across, typically contain 50-100 luminous galaxies in the central mega-parsec. Clusters are filled with hot intergalactic gas bound to the cluster by gravity. Large clusters may contain thousands of galaxies e.g. Virgo, Fornax. The luminous matter in galaxy clusters is primarily hot gas radiating at X-ray energies as opposed to stars or gas within galaxies. The mass of cluster gas is so big, that it could not all have been blown out of galaxies. The material remaining after galaxy formation may have dropped into the cluster and have been heated to the observed temperatures by shock waves. Supernova explosions may have carried material with high metal content (formed in stars) out from the galaxies to mix with clusters gas. Alternatively many stars may have formed

in smaller clumps, and the metal-enriched gas may have been shaken out as the clumps fell together to form galaxies (Sparke & Gallagher 2000) .

Clusters of galaxies, as the largest virialised objects in the Universe, with X-ray emission originating from hot ($T \geq 10^7 K$) intra-cluster gas, offer a means of probing the formation of structure and constraining the fundamental cosmological parameters governing its evolution. Therefore it is of interest to determine their basic physical properties, such as temperature of the intra-cluster gas, size, mass, etc. Because of the high gas temperature, observations at X-rays are especially appropriate. Constraints on structure formation models may be obtained from physical cluster parameters using scaling relations such as the X-ray luminosity-temperature relationship.

Temperatures of the gas pervading clusters of galaxies are known to be high, of the order of several keV, and a metallicity of about 1/3 of the solar abundance. In particular, recent work with the ASCA X-ray satellite has suggested that temperatures of 6-10 keV are ubiquitous (Markevitch et al. 1998). The luminosity-temperature relation may be used to estimate the temperature once the luminosity has been derived on the basis of a first guess for the temperature. This relation has been calibrated by, amongst others, the WARPS consortium (Wide Angle ROSAT Pointed Survey) (Fairley et al. 2000). It is particularly valuable, however, to determine the gas temperatures directly, by means of spectral modeling of X-ray data. The gas emits a large X-ray flux due to bremsstrahlung radiation. Assuming hydrostatic equilibrium, the gas luminosity profile can be modeled by an Isothermal-β model (c.f. Section 5.3). Since the gas density at the cluster centre is high, cooling is very efficient and the temperature difference with the outer cluster parts creates a pressure gradient causing hot gas to flow toward the centre and accumulates there. These cooling flows are observed in many clusters, for which the surface brightness is strongly peaked at the very centre. X-ray observations confirm this where significantly lower temperatures are observed at the cluster centre (Fabian 1994).

1.8 Ellipticals

Ellipticals are galaxies that appear ellipsoidal, have no disks, spiral arms, bars or dust lanes (properties associated with ongoing star formation), indicating that nearly all the stars in ellipticals are old. Despite forming less than 15% of galaxies in the general field, the majority of bright galaxies in large clusters are ellipticals. Classical ellipticals (E galaxies) have M_V (absolute visual magnitude) in the range -23 down to -16 mag. cD galaxies are found at the centre of clusters, and are among the most luminous galaxies in the Universe. The degree of elongation of an elliptical is given by Hubble's classification subclass 10(1-b/a) where a and b refer to the major and minor axes of the galaxy respectively e.g. E0 is round (a=b) and E7 is elongated (b/a=0.3). Unlike spherical galaxies, the angular momentum is not dominant in E galaxies and the 3-dimensional shape is maintained mainly by the dispersion of stellar velocities within it. X-ray emission from Ellipticals is discussed in the next chapter.

Chapter 2

X-ray Astronomy

The study of X-ray astronomy commenced circa 1948 largely due to the advancements made in rocket technology. During this year the first solar X-ray emissions were observed. However, it was not until 1962 that extra-solar X-ray emissions were detected, originating from Sco X-1 in the Scorpious constellation. Subsequent rocket flights detected approximately thirty other extra-solar sources, but no proper surveys were conducted until the launch of the Uhuru satellite in 1970 which provided a catalogue of 161 sources. Uhuru was succeeded by various missions, including the Ariel 5 and Ariel 6 projects. 1978 saw the launch of the Einstein observatory, carrying the first X-ray imaging telescope yielding unparalleled accuracy and sensitivity. Einstein was only capable of doing pointed observations of preselected objects which did not yield new samples or classes of objects. With ROSAT a solution to this problem was provided by conducting an all sky survey during the first 6 months of its operation. After the all-sky survey, ROSAT became a pointed mission, concentrating on objects selected from the initial survey.

2.1 Einstein

The second of NASA's three High Energy Astrophysical Observatories, HEAO-2, renamed Einstein after launch, was the first fully imaging X-ray telescope to be put into space. With a few arc-second angular resolution, a field-of-view of tens of arc-minutes, and a sensitivity several hundred

times greater than any previous mission provided, for the first time, the

capability to image extended objects, diffuse emission, and to detect faint sources. Overall, it was a key mission in X-ray astronomy and its scientific outcome completely changed the view of the X-ray sky[1].

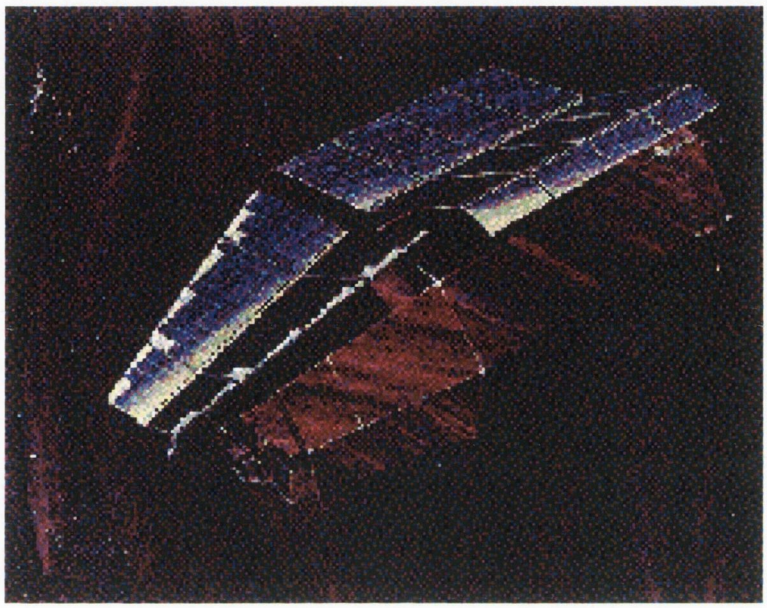


Figure 2.1: The Einstein satellite

2.1.1 Mission Characteristics

Lifetime : 12 November 1978 - April 1981
Energy Range : 0.2 - 20 keV
Special Features : First imaging X-ray telescope in space
Payload : A Wolter Type I grazing incidence telescope. Four instruments could be rotated, one at a time, into the focal plane:

1. Imaging Proportional Counter (IPC; 0.4-4.0 keV) effective. area 100 cm^2, FOV 75 arc-min, $\sim$1 arc-min spatial resolution.

2. High Resolution Imager (HRI; 0.15-3.0 keV) effective. area 5 - 20 cm^2, FOV 25 arc-min , $\sim$2 arc-sec spatial resolution.

[1]c.f http://heasarc/gsfc.nasa.gov/docs/einstein/heao.html

3. Solid State Spectrometer (SSS; 0.5-4.5 keV) effective. area 200 cm^2, FOV 6 arc-min, $\frac{E}{\Delta E}$ of 3-25

4. Focal Plane Crystal Spectrometer (FPCS; 0.42-2.6 keV) effective. area 0.1 - 1.0 cm^2, FOV 6 arc-min, 1×20, 2×20, 3×30, $\frac{E}{\Delta E}$ of 50-100 for E < 0.4 keV, $\frac{E}{\Delta E}$ of 100-1000 for E > 0.4 keV

5. Monitor Proportional Counter (MPC; 1.5-20 keV) effective. area 667 cm^2, FOV 1.5 arc min, energy resolution ~20 % at 6 keV. Co-aligned with the X-ray telescope.

6. Objective Grating Spectrometer (OGS) : 500 mm^{-1} & 1000 mm^{-1}, energy resolution $\frac{E}{\Delta E} \sim 50$. Used in conjunction with HRI.

2.1.2 Science Highlights:

1. First medium and deep X-ray surveys.

2. First high resolution spectroscopy and morphological studies of supernova remnants.

3. Recognized that coronal emissions in normal stars are stronger than expected.

4. First study of the X-ray emitting gas in galaxies and clusters of galaxies revealing cooling inflow and cluster evolution.

5. Detected X-ray jets from M87 and Cen A aligned with radio jets.

6. Thousands of "serendipitous" sources discovered.

7. Resolved X-ray sources in the Magellanic Clouds and Andromeda (M31).

2.2 ROSAT

The Röntgen Satellite, ROSAT, a Germany/US/UK collaboration, was launched on June 1, 1990 and operated for almost 9 years. The first 6 months of the mission were dedicated to the all-sky survey (using the Position Sensitive

Proportional Counter detector), followed by the pointed phase. The survey obtained by ROSAT was the first X-ray and EUV all-sky survey using an imaging telescope with an X-ray sensitivity of about a factor of a thousand better than that of UHURU. During the pointed phase ROSAT made deep observations of a wide variety of objects.[2]

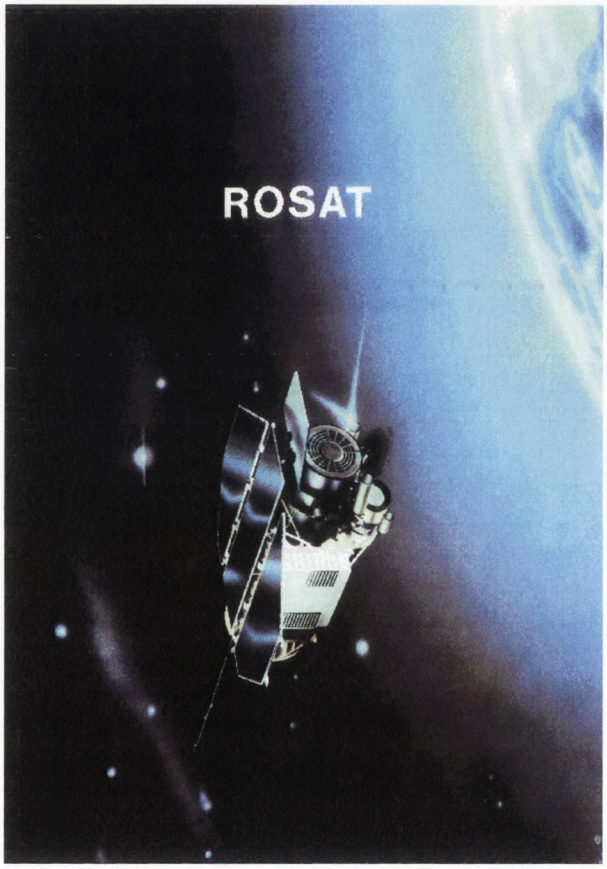


Figure 2.2: The ROSAT satellite

[2]http://heasarc.gsfc.nasa.gov/docs/rosat/rosat.html

2.2.1 Mission Characteristics

Lifetime : 1 June 1990 - 12 February 1999
Energy Range : X-ray 0.1 - 2.5 keV , EUV 62-206 eV
Special Feature : All sky-survey in the soft X-ray band
Payload : A Wolter Type II grazing incidence telescope.

An X-ray telescope used in conjunction with one of the following instruments (0.1-2.5 keV)

1. Position Sensitive Proportional Counter (PSPC) 2 units : detector B, used for the pointed phase, & detector C, used for the survey; FOV 2° diameter effective area of 240 cm^2 at 1 keV; energy resolution of $\Delta E/\mathrm{E}=0.43\ (E/0.93)^{-0.5}$. Spatial resolution of 15 arcseconds.

2. High Resolution Imager (HRI) FOV 38 arcminute square ; effective area 80 cm^2 at 1 keV; 4-6 arc-sec spatial resolution (FWHM)

3. A Wide Field Camera with its own mirror system (62-206 eV); $FOV5°$ diameter.

2.2.2 Science Highlights:

1. X-ray all-sky survey catalogue, containing more than 150,000 objects.

2. XUV all-sky survey catalogue containing 479 objects

3. Of the order of 100000 serendipitous sources contained in the source catalogs from the pointed phase (PSPC and HRI).

4. Detailed morphology of supernova remnants and clusters of galaxies.

5. Detection of shadowing of diffuse X-ray emission by molecular clouds.

6. X-ray emission from comets discovered.

7. Isolated neutron stars detected.

8. X-ray emission from the collision of Comet Shoemaker-Levy with Jupiter observed.

9. Pulsations from Geminga detected.

2.3 Position Sensitive Proportional Counter

The PSPCs are multi wire proportional counters developed by MPE. Each consists of two separate counters: one the position sensing, X-ray sensitive counter and the other an anti coincidence counter for background rejection. Each electrode is a wire grid, with the wires bonded onto a ceramic support frame. The anode grids have gold-plated tungsten wires, 10 μm in diameter and a spacing of 1.5 mm and 2 mm for the position sensing and anti coincidence counters respectively. At the edges of the anode grids are guard wires with increasing diameters to lower the electric field. The cathode grids are made of platinum iridium wires, 50 μm in diameter and with 0.5 mm spacing. The cathodes are grouped by seven or eight for signal processing.

2.3.1 Quantum Efficiency of the PSPCs

The quantum efficiency of PSPC-B (the curve for PSPC-C would be nearly identical) as a function of energy is shown below. The curve includes the window transmission, average transmission of the window support mesh (79gas. The window becomes almost completely transparent by 2 keV, where the counter gas becomes no longer optically thick. The X-ray absorption of the counter gas is close to 100X-ray mirrors also cuts off . We see the quantum efficiency drops to zero between energies 0.41-0.52 keV. These channels are omitted when calculating HRs.

2.4 X-ray Spectra

The observed spectrum is a signature of the mechanism via which the energy is radiated (Kaastra 1997; Osterbrock 1989). The production of X-rays requires extreme conditions in the source regions. The sources often have strong gravitational/magnetic fields, usually related to explosive phenomena. Theoretically there are four basic processes for producing X-rays:

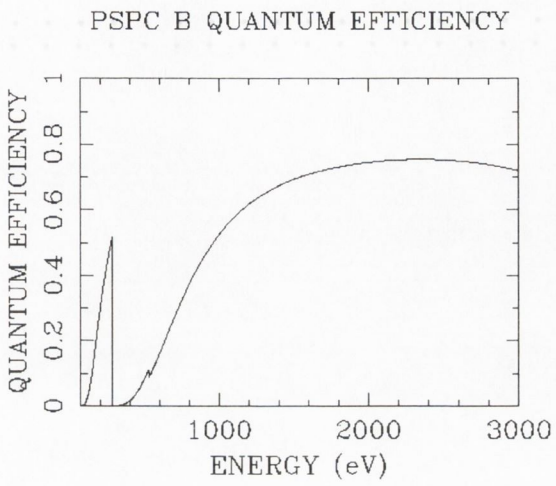


Figure 2.3: The quantum efficiency of the ROSAT PSPC as a function of energy. Included are the window transmission, the average transmission of the window support mesh, and the gas stopping efficiency.

1. Synchrotron Radiation:
   A charged particle crossing a region containing a magnetic field experiences an acceleration and therefore radiates electromagnetic waves. If the particle is highly relativistic, X-rays and γ-rays are produced.

2. Inverse Compton Scattering:
   This process involves scattering low energy photons to higher energies by ultra-relativistic electrons causing the electrons to lose energy.

3. Bremsstrahlung (Free-Free Emission):
   This is produced when an electron is accelerated in the Coulomb field of a nucleus. This "thermal emission" is observed in X-rays for optically thin plasmas having temperatures $\sim 10^6 - 10^9$ K.

4. Line Emission:
   In a hot plasma, emission lines are produced by downward radiative transitions following the population of an excited level, either by inelastic collisions or by recombination. If the transition involves the inner shells of an ion or atom with nuclear charge $Z \geq 8$, the line photon will have energy in the keV range.

For every emitting process, there is a corresponding inverse process associated with absorption e.g. synchrotron self absorption, Compton scattering, free-free absorption, photoelectric absorption.

The observed spectrum may be described by three main types:

1. Thermal emission from a hot diffuse plasma with possible emission lines e.g. Raymond-Smith, Mekal.

2. A power-law spectrum resulting from synchrotron emission.

3. A black-body spectrum resulting from an optically thick medium.

Often the spectrum of an object is best fitted by more than one of these classes across the whole X-ray spectrum or by a combination of these for the same energy range (Pierre 1996; Mewe 1997).

2.4.1 Supernova Remnants (SNRs)

SNRs, the remnants of exploded stars, may be divided into thermal and non-thermal SNRs. Non-thermal SNRs show two components: the pulsar and a synchrotron nebula. Generally these objects give a featureless power law spectrum with a typical photon index of 2. Thermal SNRs may usually be described by a power law with photon index typically 2-3 and a thermal component. SNRs may be split into several classes.

1. Type Ia supernovae : Initial mass $\sim$ 4-6$M_{\odot}$ These are due to low mass, old population stars. Accretion of matter onto a white dwarf in a binary system leads to a thermonuclear instability causing a massive explosion. No stellar remnant remains, and the ejecta consist largely of iron.

2. Type Ib supernovae : Initial mass $\geq$ 20 $M_{\odot}$. These are due to pre-main sequence stars with initial masses of at least 20$M_{\odot}$. Probably Wolf-Rayet stars and the helium cores of massive stars are the likely progenitors. The remnant (after the explosion) is a black hole or a neutron star. The ejecta contain mostly oxygen.

3. Type II supernovae : Initial mass $\geq 6M_{\odot}$. These are due to young massive stars. After it has burned all its fuel the core of a red (or blue) supergiant collapses, producing a neutron star and ejecting material into the interstellar medium (ISM). SNRs of this type may be of the non-thermal type i.e. they contain a pulsar and a synchrotron nebula.

2.4.2 High-Mass X-ray Binaries (Orbs)

These are the product of close-binary evolution. A neutron star or a black hole accretes material from a massive companion star. The spectra are rather hard (i.e. the spectra are dominated by high energy X-rays) and may be described by a power-law.

2.4.3 Low-Mass X-ray Binaries (LMXBs)

These consist of a late-type star in a close orbit around a neutron star. The spectra of LMXBs can be described by the combination of several absorbed blackbody and power-law components.

2.4.4 X-ray Emission from Normal Galaxies

X-ray spectra from normal galaxies exhibit emission from many mechanisms. Sometimes there is evidence for a diffuse hot interstellar medium. Then there is emission from discrete sources such as SNRs and XRBs. Finally in many cases there may exist a weak active nucleus or starburst activity.

2.4.5 Ellipticals

Huge quantities of hot ionized gas are prevalent in the average elliptical galaxy. This is caused by stars losing mass as they age. For a population older than $\sim 10^9$ (1 Gyr) years material shed from stellar envelopes during the red giant phase and Assymptotic Giant Branch (AGB) amounts to 1-$2M_{\odot}$ of gas per year for each $10^{10}L_{\odot}$ of luminosity. Over several gigayears, this outgassing results in the build up of a substantial amount of gas. At temperatures of 1-3 $\times 10^7$K, this gas radiates mainly in the X-ray. More

luminous galaxies with high velocity dispersions have hotter gas (Sparke & Gallagher 2000).

2.4.6 Clusters of Galaxies

The most massive objects in the universe, clusters of galaxies are known to emit X-rays from hot thermal plasmas. These are discussed in more detail in the previous chapter.

2.4.7 Active Galactic Nuclei (AGNs)

This is a collective name for several different types of extragalactic objects, such as Quasars, QSOs, Seyfert galaxies and radio galaxies. These are galaxies of whose nuclei exhibit abnormally high luminosities and non-thermal spectra. The cores of active galaxies show all or most of the following characteristics:

1. High luminosities, greater than 10^{42} erg/s at X-rays.
2. Non-thermal emission (synchrotron), leading to excessive UV, IR and X-ray flux.
3. Rapid variability, sometimes less than one day, implying that the emission originates from a small area less than one light day across (an object's luminosity cannot vary quicker than the light travel time across it).
4. High contrast of brightness between the nucleus and large-scale structures.
5. Explosive appearance or jet-like protuberances.
6. Broad emission lines, indicating strong gas motions.

2.4.8 Seyfert Galaxies

Seyfert galaxies appear as bright point like nuclei in spiral galaxies. Seyferts whilst very rare in comparison with normal galaxies are the most common type of active galaxies. They may be split into type 1 and type 2.

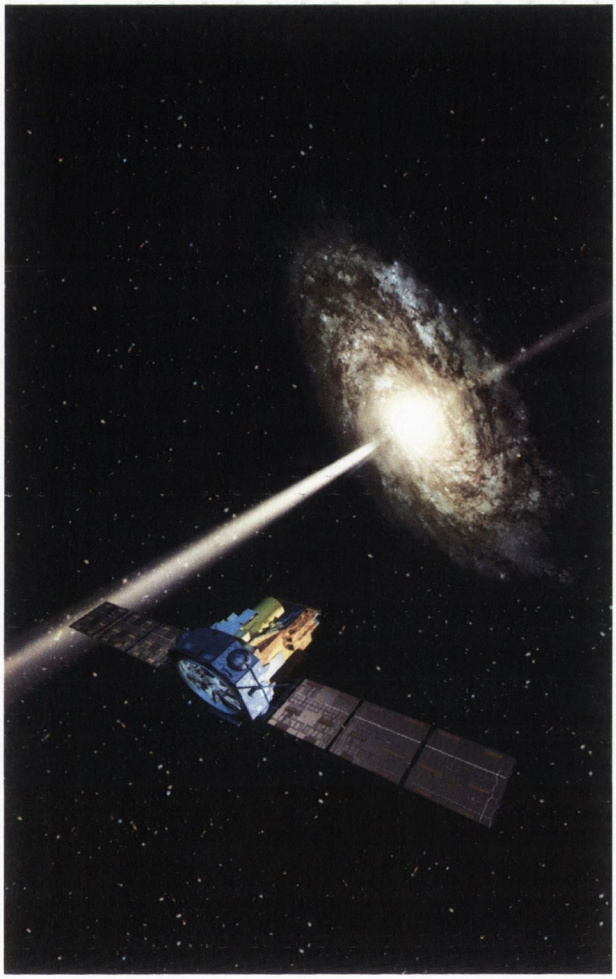


Figure 2.4: Artists impression of an AGN(http://astro.estec.esa.nl/SA-general/Projects/Integral).

2.4.9 Seyfert 1 Galaxies

Seyfert 1 galaxies have very broad HI and HeII emission lines with full widths at half maximums (FWHMs) of order 1000 to 5000 km/s while the forbidden lines like [O III], [N II] and [S II], typically have FWHMs of order 500 km/s The power is probably provided by accretion onto a massive black hole ($10^6 - 10^{10} M_\odot$). They often have a strong UV component and a soft X-ray excess above the power law component which dominates the X-ray luminosity. The soft excess is thought to be either hard X-ray emission reprocessed from the accretion disc or direct emission from the warm disc. Inverse comp-

ton emission originating in a hot corona surrounding the inner parts of the accretion disc black hole system is thought to produce the hard X-rays.

2.4.10 . Seyfert 2 Galaxies

Seyfert 2 galaxies also have a narrow emission line component ($\sim$ 500 km/s), but no broad emission lines. The X-ray emission is heavily absorbed. In Seyfert 2 galaxies the broad-line region and most of the other nuclear emission may lie hidden behind a dust torus or other absorbing structure.

2.4.11 Quasars (Quasi Stellar Radio Sources)

These look like stars with substantial redshifts. They are AGNs so luminous and so far away that in the beginning the galaxies in which they are situated could not be detected. Quasars are located mainly in elliptical galaxies and their spectra are dominated by a power-law component that often has a rather hard spectrum (i.e. the spectrum is dominated by high energy photons).

2.4.12 QSOs(Quasi Stellar Objects)

In essence they are radio-quiet Quasars.

2.4.13 Radio Galaxies

Generally these consist of two radio lobes on either side of a parent galaxy, usually a giant elliptical, which sits midway between the radio lobes. The spectrum and polarization of the radiation bears all the characteristics of synchrotron radiation, suggesting that radio galaxies have relativistic particles in a magnetic field. It is presumed that these particles reach the radio lobes via, jets emanating from the nucleus.

2.4.14 BL Lac objects

These are active nuclei that show strong beaming into our line-of-sight. Their X-ray spectra are mostly power-laws with some objects showing a break.

2.4.15 Unified Theory of AGNs

AGNs are essentially super-massive black holes surrounded by an accretion disc viewed from different angles. The supermassive black hole ($10^6 - 10^9 M_\odot$) at the centre of a normal galaxy is surrounded by a huge rotating disc. The main difference between Seyfert 1 and Seyfert 2 is often thought to be that Seyfert 2 galaxies are AGNs seen edge-on, with emission from the innermost regions being obscured by outer material, whereas we see Seyfert 1 galaxies head-on. Kepler's third law states that the inside of the disc rotates faster than the outside, causing friction between layers, heating up the gases as they spiral toward the hole. Matter is ejected relativistically perpendicular to the disk.

2.5 Galactic Neutral Hydrogen

When observing extra-galactic objects we must account for galactic absorption. This is usually done my measuring the strength of the 21 cm line of neutral hydrogen and estimating the amount of absorbing material by taking a suitable abundance model. Radio emission at 21cm was studied intensely in the 1950's by astronomers in Holland and Australia. The ubiquity of atomic hydrogen in the Galaxy, the low energy of the 21-cm transition, its long lifetime and its relatively high temperature (compared with the radio continuum temperature in most directions) make it easily detectable in emission in every direction despite its low opacity. It is the strongest thermal line in radio astronomy. For the purposes of this thesis we had three main catalogues of galactic N_H from which to choose.

1. Dickey & Lockmann 1990
   Attention is given to observations of interstellar atomic hydrogen from Lyman-alpha and the 21-cm line through indirect tracers such as dust and gamma rays; to what can be learned from such observations; to what the H I sky looks like; and to the state of knowledge in this area and the future prospects. Consideration is also given to results from recent H I investigations that bear on two important areas: the spatial organization of interstellar H I and its vertical distribution in the Galaxy.

2. Stark et al. 1992
   Results of observations of the sky north of delta = -40 deg in the 21-cm line of atomic hydrogen are reported. The survey covers a velocity range of 654 km/s centered on the Galactic standard of rest, with 5.3-km/s wide filters. Calibration and reduction of the observations are described. The survey is presented as a series of images of the sky, each covering a 10-km/s wide velocity range. This survey is distinguished by its sensitivity to low surface brightness features (TA is approximately equal to 50 mK) and relative freedom from side lobe contamination. High-velocity clouds are extracted and cataloged automatically. At the resolution of the survey, the lowest H I column density in the sky is $5.7 \times 10^{19} cm^{-2}$. This work was extended to the southern hemisphere in 1998 by Ingalls et al.(1998).

3. Murphy et al. 1996
   Murphy et al. have determined accurate values of the Galactic neutral hydrogen column density, N_H toward 220 quasars and active galactic nuclei from 21 cm H I measurements made on the NRAO Green Bank 140 Foot Telescope (42.7 m). Accurate values of N_H have now been obtained for the whole PG bright quasar sample and most quasars that have been observed by ROSAT and the Hubble Space Telescope through mid-1993. The spectra were corrected for stray 21 cm radiation yielding values of NH with a typical uncertainty of $1 \times 10^{19} cm^{-2}$ for high Galactic latitude directions. The H I column densities will be useful for correcting for interstellar opacity at UV and soft X-ray wavelengths, and for estimating the reddening and extinction toward these objects. This only covers 220 quasars and AGN's so isn't suitable for the amount of objects observed in this thesis.

To be consistent with other major work in the area such as the WARPS consortium it was decided to use the values of N_H from Dickey & Lockmann 1990.

Chapter 3

Simulation of Power law grid

3.1 Introduction

The CfA redshift survey (de Lapparent et al. 1986) and the SSRS (Southern Sky Redshift Survey) and SSRS2 (da Costa et al. 1988;da Costa et al. 1994) have shown that large Voids in the Large Scale Structure are ubiquitous. Both normal galaxies and Lyα clouds have been found in voids (McLin et al. 2002). Voids may be checked for the presence of absorbing material by examining spectra at the front and back of the void and comparing for intergalactic absorption. It is only possible to check for absorbing material if processed material is involved, as the X-ray absorption is largely determined by the heavier elements.

For analysis of this type ROSAT is the best option for two reasons. Firstly it has the spectral resolution and energy range (0.1-2.4 keV) suitable for searching for processed material. Secondly the ROSAT data archive contains over 100,000 sources and is the only mission with enough sources to achieve good statistics when selecting galaxies from the front and back of a particular void. ROSAT carried two main instruments, the High Resolution Imager (HRI) for spatial analysis, and the Position Sensitive Proportional Counter (PSPC) for spectral analysis. The PSPC is a gas-filled proportional counter sensitive in the 0.1-2.4 keV energy range. For many sources detected with the ROSAT PSPC there is not a sufficient number of photons ($\sim$ 1000) to make reliable spectra. As an alternative to spectra, Hardness Ratios (HR's) (ratios of photons in selected bands of the spectra) are calculated. It is not

possible to determine directly from Hardness Ratios the amount of line-of-sight absorbing material (N_H). As a tool for calculating the quantity of N_H (throughout this thesis we will assume solar abundances along the line of sight) from Hardness Ratio (HR) plots, spectra are simulated for absorbed power law models with a range of values of absorbing N_H and photon index Γ (the slope of the power law). Many galaxies (especially the brighter ones) contain an AGN in their centre. The synchrotron radiation emanating from these AGN may be modeled by an absorbed power law. In general these AGN are extremely bright in comparison with their host galaxy that it is a reasonable assumption to model these galaxies with an absorbed power law. HR's are calculated from the simulations giving a well defined grid of points (1920 points) in a diagram of HR1 vs. HR2. Observed HR's may then be compared with the grid of hardness ratios (and with galactic N_H) to set limits on the amount of N_H present.

3.2 Spectral Modeling

When observations are made in the X-ray it is possible to produce spectra of these objects. X-ray spectra of these observations may be modeled and fitted to observations for objects with enough spectral counts ($\geq$ 1000 photons). From these spectra we can derive information about astronomical objects i.e., temperature, amount of neutral hydrogen present, abundances etc. We can also use Hardness Ratios (the X-ray equivalent of optical colours) to derive information about objects, that compare the photon counts in selected bands of the spectra. These are especially important for observations with low counts ($\leq$ 1000) photons. ROSAT Hardness Ratio 1 (HR1) and Hardness Ratio 2 (HR2) are defined as (Zimmermann et al. 1992)

$$HR1 = \frac{(52-201)-(11-41)}{(11-41)+(52-201)} \tag{3.1}$$

$$HR2 = \frac{(91-201)-(52-90)}{(52-90)+(91-201)} \tag{3.2}$$

where the channel numbers 11-41 correspond to the number of photons contained in the energy interval 0.11-0.41 keV. These give us ratios of the soft

and hard part of the spectrum. The channels 42-51 are omitted as ROSAT is not very sensitive in this energy range. HRs are especially useful for maximising the extraction of information from the ROSAT data archive and for work on less luminous objects.

The modeling was done using the EXSAS (Zimmermann et al. 1992) software analysis system. For the purpose of our simulations we use an absorbed power law (a Power law model multiplied by an absorption model) (Morrison & McCammon 1983). These simulations use the default detector response matrix and the effective area table for the PSPCb camera on ROSAT. There are three variables that are adjusted:

1. Photon Index Γ (-0.25 through to -4 in steps of 0.25).
2. The amount of absorbing material N_H (0.01-1.2 in steps of 0.01 $\times 10^{21}\mathrm{cm}^{-2}$)
3. The number of counts

To illustrate the relation between Hardness Ratios and N_H we show two simulated spectra (for $\Gamma = -2.0$, 1000 counts) with N_H= 0.01 $\times 10^{21}\mathrm{cm}^{-2}$ and 1 $\times 10^{21}\mathrm{cm}^{-2}$ respectively (Figure 3.1 and Figure 3.2). As N_H is increased from 0.01 to $1\times 10^{21}\mathrm{cm}^{-2}$ the soft part of the spectrum from 0.1-0.5 keV becomes highly absorbed thus changing the spectral distribution of the photons, and the Hardness Ratios (HR1=-0.44, HR2=0.25 changes to HR1=0.91, HR2=0.46).

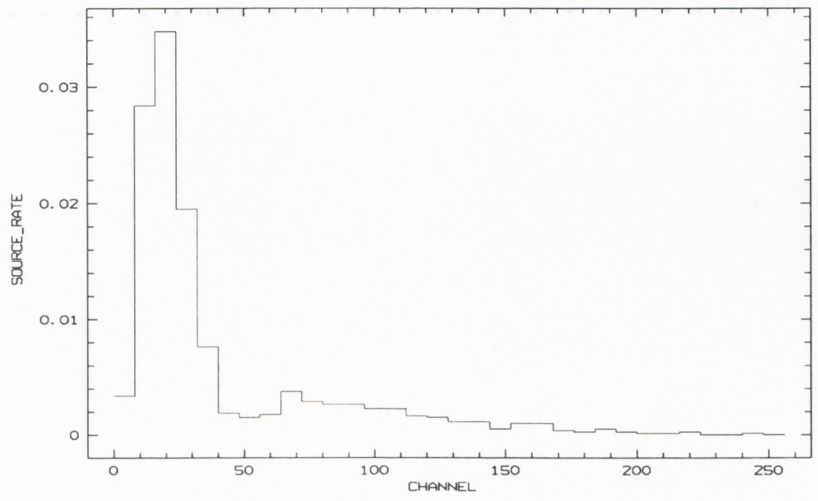


Figure 3.1: Spectral simulation of 1000 counts over 1000 seconds with parameters $N_H = 0.01 \times 10^{21} cm^{-2}$ and $\Gamma = -2.0$. The energy channels 0-250 correspond to energies of 0-2.5keV. (HR1=-0.44 HR2=0.25); only the channels 11-235 are used. The source rate corresponds to counts per second observed from the source.

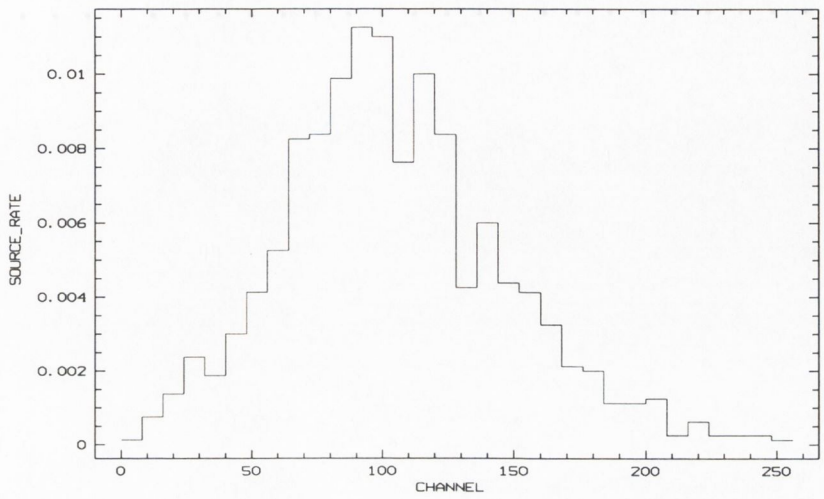


Figure 3.2: Spectral simulation of 1000 counts with $N_H = 1 \times 10^{21} cm^{-2}$ $\Gamma = -2.0$. The energy channels 0-250 correspond to energies of 0-2.5keV (HR1=0.91, HR2=0.46). The source rate corresponds to counts per second observed from the source. Note the y-axis only goes to one third the height of the y-axis in Figure 3.1.

To simulate spectra EXSAS uses a random number generator, which requires a seed. For low counts different values of HR1 and HR2 (Δ HR ~ 0.3) are produced for different seeds (due to the statistical distribution of the small number of counts). To overcome this problem a large number of iterations are run and the mean spectrum is calculated i.e for each value of Γ and N_H we calculate values of HR1 and HR2 for a large number of seeds. We generate spectra until the mean of the HR1, HR2 values stabilizes. Plots of standard deviation of the hardness ratio against the number of iterations, for total counts of 20, 50 and 1000 counts and for numbers of iterations between 10 and 10^5 (increasing logarithmically) are produced. From these plots we discern how many iterations are required to give a reliable mean simulated hardness ratio for each (N_H,Γ) combination. As an example Figure 3.3 and Figure 3.4 show, for 20 counts, the number of iterations against the standard deviation of HR1 (hr1sd) and HR2 (hr2sd). After 10000 iterations the standard deviation stabilizes. For 100,000 counts only 100 iterations are required for the standard deviation to stabilize.

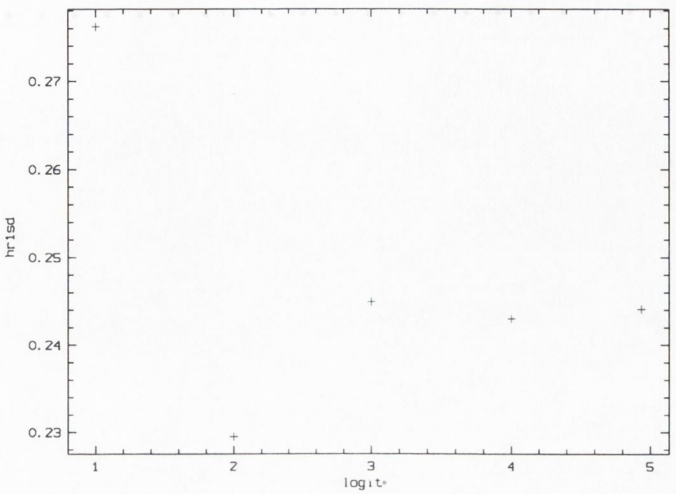


Figure 3.3: Simulation for 20 counts with $N_H = 0.1 \times 10^{21} cm^{-2}$ and $\Gamma = -1.5$. We plot standard deviation of HR1 (hr1sd) against log(no. of iterations)

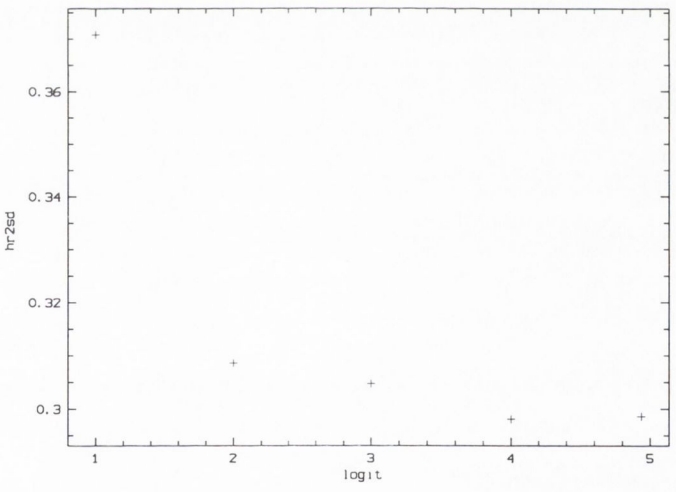


Figure 3.4: Simulation for 20 counts with $N_H = 0.1 \times 10^{21} cm^{-2}$ and $\Gamma = -1.5$. We plot standard deviation of HR2 (hr2sd) against log(no. of iterations)

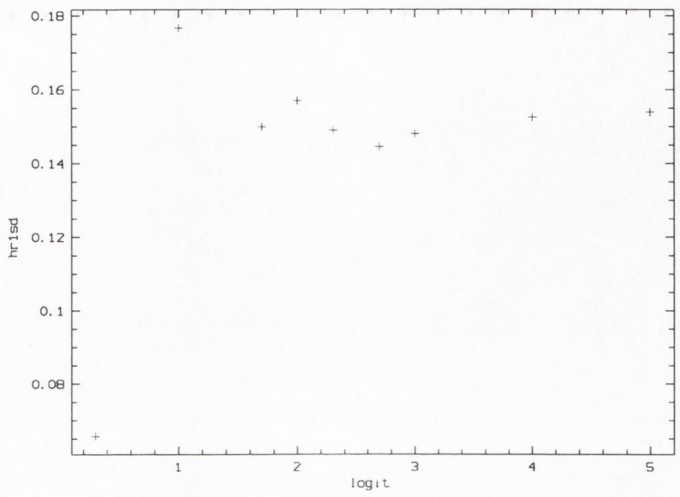


Figure 3.5: Simulation of 50 counts with $N_H = 0.1 \times 10^{21} cm^{-2}$ and $\Gamma = -1.5$. We plot standard deviation of HR1 (hr1sd) against log(no. of iterations)

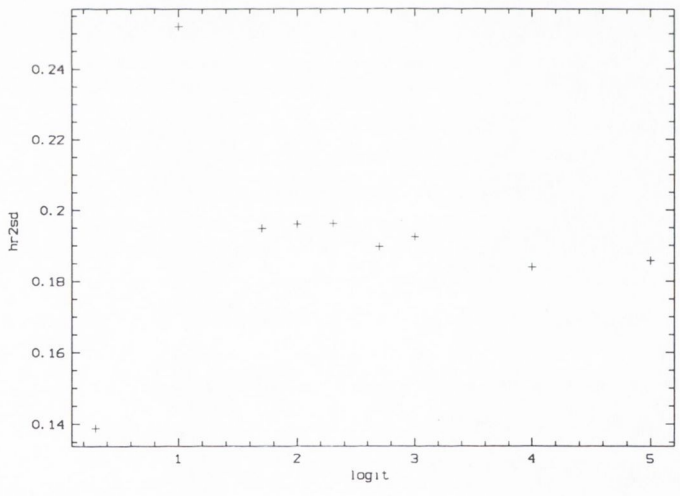


Figure 3.6: Simulation for 50 counts with $N_H = 0.1 \times 10^{21} cm^{-2}$ and $\Gamma = -1.5$. We plot the standard deviation of HR2 (hr2sd) against log(no. of iterations)

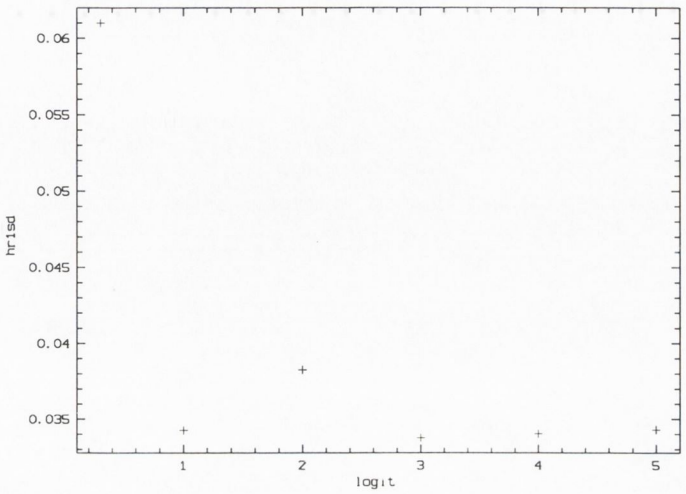


Figure 3.7: Simulation for 1000 counts with $N_H = 0.1 \times 10^{21} cm^{-2}$ and $\Gamma = -1.5$. We plot the standard deviation of HR1 (hr1sd) against log(no. of iterations)

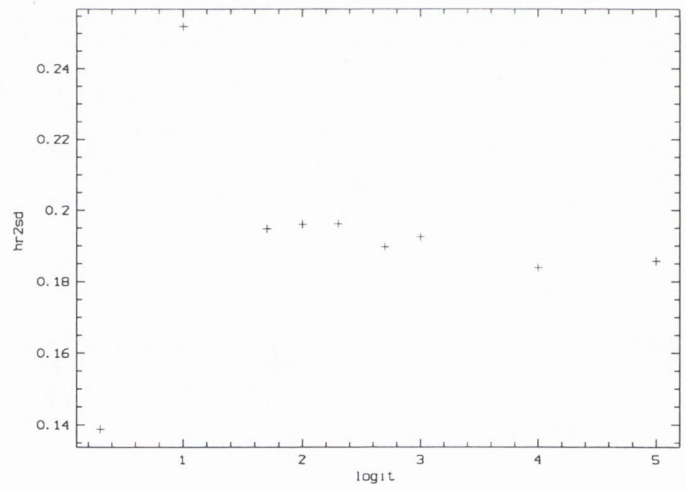


Figure 3.8: Simulation for 1000 counts with $N_H = 0.1 \times 10^{21} cm^{-2}$ and $\Gamma = -1.5$. We plot the standard deviation of HR2 (hr2sd) against log(no. of iterations)

In Figures 3.3 to Figure 3.6 we plot the standard deviation of HR1 and HR2 for 20 and 50 counts against the number of iterations. These plots establish that, for 20 and 50 counts 1000 iterations are required to produce a stable value for the standard deviation. For 1000 counts (see Figures 3.7 and Figure 3.8) the difference in the standard deviation between 100 iterations and 10^5 is very small. We decide to use 100 iterations and keep varying the number of counts. Large errors are involved when using hardness ratios from sources with very low counts. In Figure 3.9 & Figure 3.10 the standard deviation is plotted against the log_{10} of the number of counts . Predictably we find that the standard deviation reduces considerably with number of counts, decreasing almost to 0 with 100,000 counts. Our simulations are compatible with the error estimates from Poisson statistics.

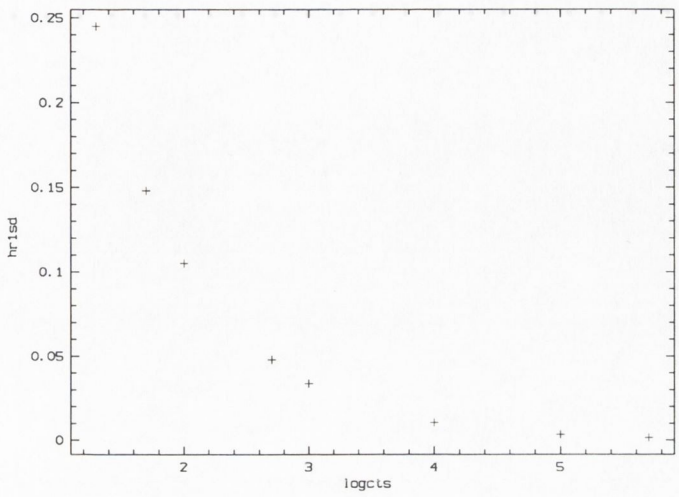


Figure 3.9: Standard deviation in HR1 (hr1sd) versus log_{10} of the counts (logcts) for $N_H = 0.1 \times 10^{21}\text{cm}^{-2}$ and $\Gamma = -1.5$ and 1000 iterations. The standard deviation decreases rapidly with increasing counts.

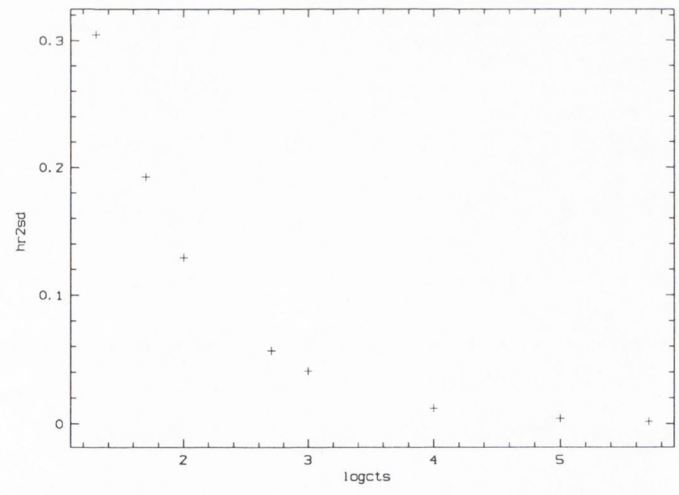


Figure 3.10: Standard deviation in HR2 (hr2sd) versus log_{10} of the counts (logcts) for $N_H = 0.01 \times 10^{21}\text{cm}^{-2}$ and $\Gamma = -1.5$ and 1000 iterations. The standard deviation decreases rapidly with increasing counts.

3.3 Grid

For illustrative purposes we simulate 4 grids for 20, 50, 1000 and 100,000 counts, respectively. Using the Absorbed Power Law model we allow Γ to take values in the interval (-0.25 tp-4 in steps of 0.25), N_H ranging from $1 \times 10^{19}\text{cm}^{-2}$ to $10 \times 10^{21}\text{cm}^{-2}$ (in steps of $1 \times 10^{19}\text{cm}^{-2}$). This range of values cover the extremes of what we would expect to observe. The grids are shown for 20, 50, 1000 and 100,000 counts in Figures 3.11, 3.12, 3.13 and 3.14. The error bars result from the standard deviation in HR1 and HR2 from the multiple simulations. From Figure 3.14 we see that our grid does not give adequate coverage of the HR1 versus HR2 plot, in particular because of the steps in Γ being too big. We decided to generate a grid, for observations with 100000 counts, with Γ in the interval (-1,-4 in steps of 0.25) and N_H in the interval $1 \times 10^{19}\text{cm}^{-2}$ to $10 \times 10^{21}\text{cm}^{-2}$ (in steps of $1 \times 10^{19}\text{cm}^{-2}$)(Figure 3.15). We do not do this for the plots of 20, 50 or 1000 counts since they would become too crowded due to the large errors.

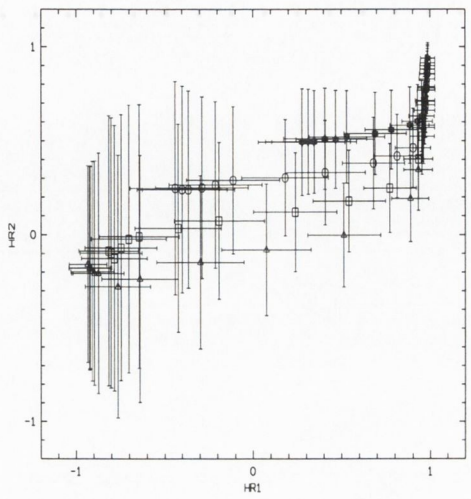


Figure 3.11: A simulation of mean HR1 v HR2 values for observations of galaxies with $\Gamma = 1(\star), \Gamma = 2(\circ), \Gamma = 3(\square)$ and $\Gamma = 4(\triangle)$. All of the points are calculated for observations with 20 photons. N_H increases from bottom left to top right.

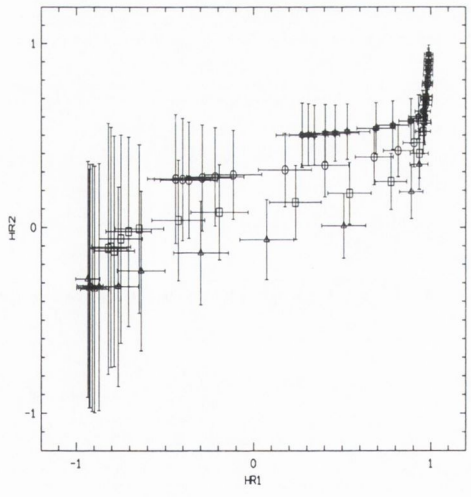


Figure 3.12: A simulation of mean HR1 v HR2 values for observations of galaxies with $\Gamma = 1(\star), \Gamma = 2(\circ), Gamma = 3(\square)$ and $\Gamma = 4(\triangle)$. All of the points are calculated for observations with 50 photons. N_H increases from bottom left to top right.

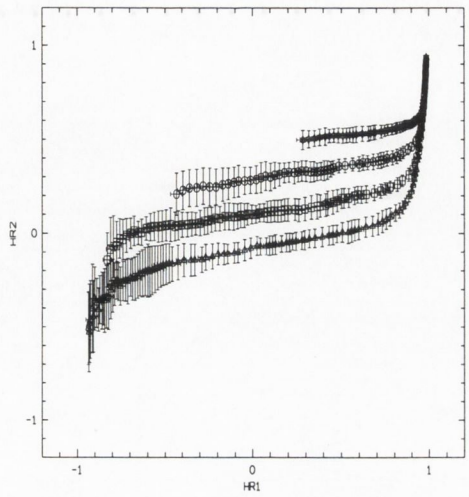


Figure 3.13: A simulation of mean HR1 v HR2 plot for observations of galaxies with $\Gamma = 1(\star), \Gamma = 2(\circ), \Gamma = 3(\square)$ and $\Gamma = 4(\triangle)$. All of the points are calculated for an observation with 1000 photons. N_H increases from bottom left to top right.

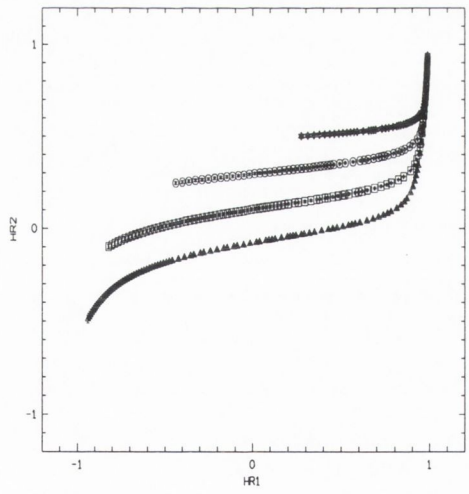


Figure 3.14: Spectral simulation of grid for 100,000 counts for 100 iterations for Γ=-1($\star$),-2($\circ$),-3($\square$),-4($\triangle$). Γ is allowed to vary from -1 to -4 and N_H varies in the range $1 \times 10^{19}\mathrm{cm}^{-2}$ to $1.9 \times 10^{21} cm^{-2}$ (in steps of $1 \times 10^{19}\mathrm{cm}^{-2}$) increases from bottom left to top right.

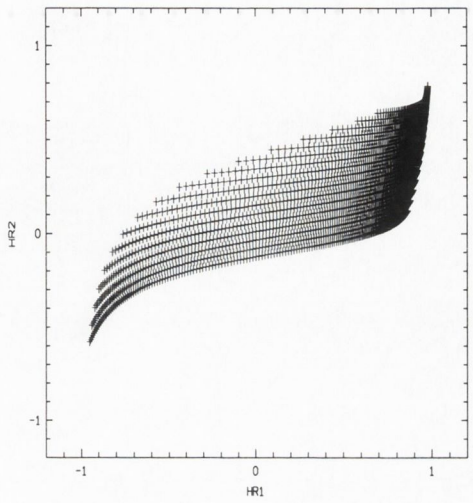


Figure 3.15: Spectral simulation of grid for 100,000 counts for 100 iterations for Γ=-0.25..-4 (in steps of 0.25) and N_H in the range $1 \times 10^{19}\mathrm{cm}^{-2}$ to $1.9 \times 10^{21} cm^{-2}$ (in steps of $1 \times 10^{19}\mathrm{cm}^{-2}$)increasing from bottom left to top right.

3.4 Relation of N_H and Γ to HR1,HR2

In Figure 3.16 and Figure 3.17 N_H is plotted against the mean simulated values of HR1 and HR2 respectively. We note that N_H has a large effect on HR1, HR1 increasing with increasing N_H, but only a very small effect on HR2 (for a given Γ), thus HR1 may be used as diagnostic of N_H. Plotting Γ against the mean simulated values of HR1 and HR2 in Figure 3.18 and Figure 3.19, we note that both HR1 and HR2 increase with increasing Γ, and both together may be used as a diagnostic of Γ.

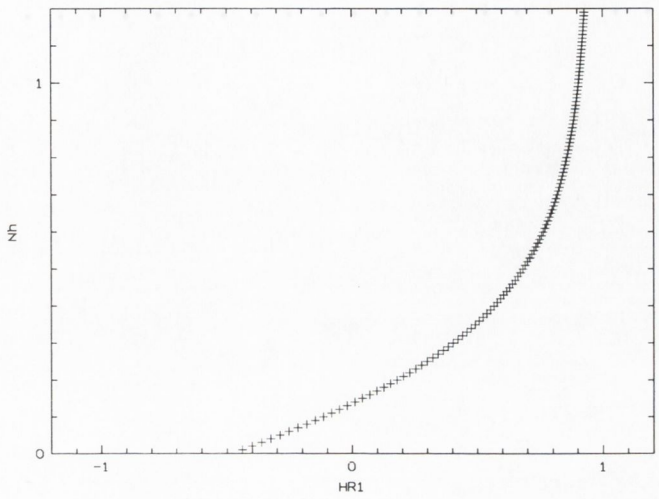


Figure 3.16: N_H versus mean simulated HR1 for Γ=-2 and N_H in the range $1 \times 10^{19} cm^{-2}$ to $1.9 \times 10^{21} cm^{-2}$ (in steps of $1 \times 10^{19} cm^{-2}$). We note the N_H increases vertically. Similar behavior is observed for all values of Γ.

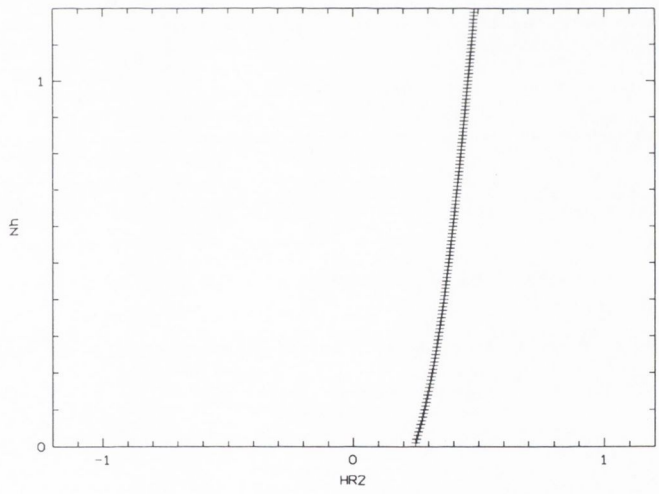


Figure 3.17: N_H versus mean simulated HR2 for Γ=-2 and N_H in the range $1 \times 10^{19} cm^{-2}$ to $1.9 \times 10^{21} cm^{-2}$ (in steps of $1 \times 10^{19} cm^{-2}$).We note the N_H increases vertically . Similar behavior is observed for all values of Γ.

With a grid of 3248 points we are able to compare values for HR1 and HR2 and read off the value of N_H and Γ. We have written a program with four input parameters, namely

1. The value of HR1
2. The error in the value of HR1(EHR1)
3. The value of HR2
4. The error in the value of HR2 (EHR2)

The program compares these values against the grid and then, extrapolating between grid points outputs a value for $(N_H)^{+x}_{-y}$ and Γ^{+x}_{-y}.

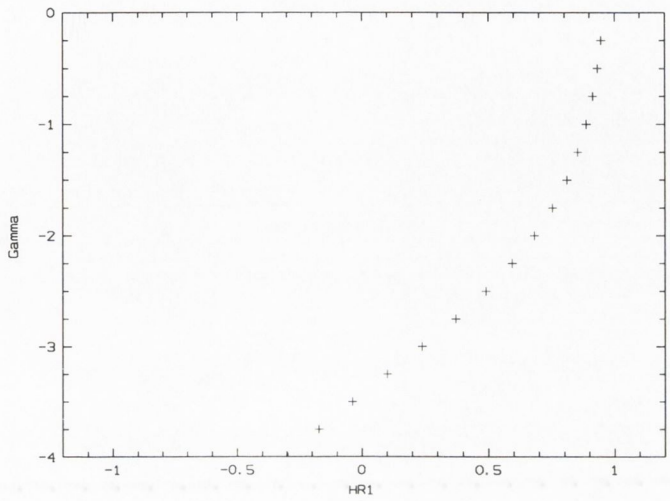


Figure 3.18: Γ versus mean simulated HR1 for $N_H = 0.5 \times 10^{21} cm^{-2}$. HR1 increases with increases Γ allowing us to use HR1 as a diagnostic of Γ. Similar behavior is observed for different values of N_H.

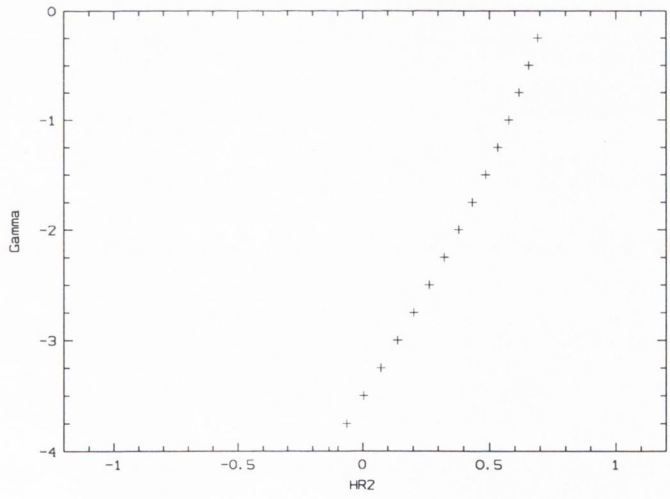


Figure 3.19: Γ versus mean simulated HR2 for $N_H = 0.5 \times 10^{21} cm^{-2}$. HR2 increases with increases Γ allowing us to use HR2 as a diagnostic of Γ. Similar behavior is observed for different values of N_H.

Chapter 4

Application of Simulated grid

Examining spectra at the front and back of the void and comparing for intergalactic absorption it is possible to check for the presence of absorbing material. However it is not feasible to check for X-ray absorption if mainly primordial material is involved, as the X-ray absorption is largely determined by the heavier elements. The three voids selected from the combined CFA-SSRS redshift surveys (de Lapparent et al. 1986; da Costa et al. 1988,1994) and their positions were cross correlated against the WGA (White, Giommi and Angelini) ROSAT point source catalogue (White et al. 1994). For most of the galaxies retrieved (38/42), there are not enough photons for reliable spectra (i.e. $\sim$ 1000). We can on the other hand calculate Hardness Ratios(HR).

4.1 Data reduction

For all of the data sets received a source detection was carried out using the Extended Scientific Analysis Software (EXSAS) (Zimmermann et al. 1992). These source detections were then matched against the list of optical galaxies retrieved from Vizier[1] and offsets were calculated. For offsets of more than 2 arc minutes the observations were rejected (Boller et al. 1992). For the remaining galaxies HR's are calculated. For the source spectrum photons are extracted (from the events table) within a radius of 160 sky pixels (2 sky

[1]http://z13.mtk.nao.ac.jp/viz-bin/VizieR maintained by the CDS(Centre de Données astronimiques de Strasbourg *http://cdsweb.u-strasbg.fr*)

pixels = 1 arcminute) from the centre. We then check an annulus between 200 and 500 sky pixels around the target source for other sources. If this area is source free, photons are then extracted from this annulus and used to calculate the background. Otherwise we take a nearby area free of sources and extract a ring of 500 pixels as the background. A spectrum is made from these data and HR's are calculated. We plot HR1 vs HR2, HR1 vs recessional velocity and HR2 vs recessional velocity for each of the voids ,A through C, used in our work. These three voids will be detailed below. HR1 and HR2 are the ratios of the number of photons received in different bands of the X-ray spectrum (c.f Chapter 3).

4.2 Selection of voids

We produced, using the Vizier service, slice projections of the combined CFA-SSRS (Center for Astrophysics -Southern Sky Redshift Survey de Lapparent et al. 1986, da Costa et al. 1988, da Costa et al. 1994) redshift surveys in the range Right Ascension (RA):0-24h, Declination $0° - 90°$ and recessional velocity from 0-15000 km/s. Each slice has a range of 5° in declination. To produce the slice projections we must first correct for the declination of the slice, by calculating rf, where $rf = RA \times cos(Declination)$. Next we plot $zsin(rf)$ against $zcos(rf)$, giving us a projection of 3 dimensional space onto a 2 dimensional surface. In the plots the grid of +'s represent recessional velocities of 5,000 km/s and 10,000 km/s respectively. We observe from the origin (0,0). We attempted to use observations out to 30,000 km/s selected from the LCRS (Las Campanas Redshift Survey) (Shectmann & Landy 1996) but there were not sufficient correlations with the ROSAT data archive. From these slices three of the most clearly defined large voids were selected. Large well-defined voids were chosen as this both simplifies the data analysis and increases the chances of matches with the ROSAT data archive.

4.2.1 Weighted Averages and Statistical test

For each void we calculate the weighted average of HR1 and HR2 for the front and back of each void (each data point is given a weighting depending on the error on each point.having calculated the weighted average we next

calculate the standard error on the mean for each set of points (e.g all the values of HR1 from the front of void A). These standard errors on the mean are shown in each plot as the error on the weighted average and they are also given in each table. Where the weighted average of the HR's of points from the front and back of a void are different and their stantard errors do not overlap we can say that these points are drawn from a different sample.

4.2.2 Void A

Galaxies are selected in the range Right Ascension:$11^h - 21^h$, Declination:$+18° - +28°$ and recessional velocity 1,000 -12,000 km/s. We retrieve 8 galaxies from the ROSAT data archive, 3 at the front and 5 at the back of the void. Slice projections for Void A are shown in Figures 4.1 to 4.3 and details of the galaxies are given in Table 4.2 and Table 4.3.

Void	RA(2000)	Dec(2000)	Velocity(km/s)
A	$11^h - 21^h$	$+18° - +28°$	1,000-12,000 km/s
B	$13^h30^m - 14^h30^m$	$+10° - +35°$	7,500-12,000 km/s
C	$8^h - 14^h$	$+5° - +45°$	0-10000 km/s

Table 4.1: The coordinate ranges for the three voids, A,B and C.

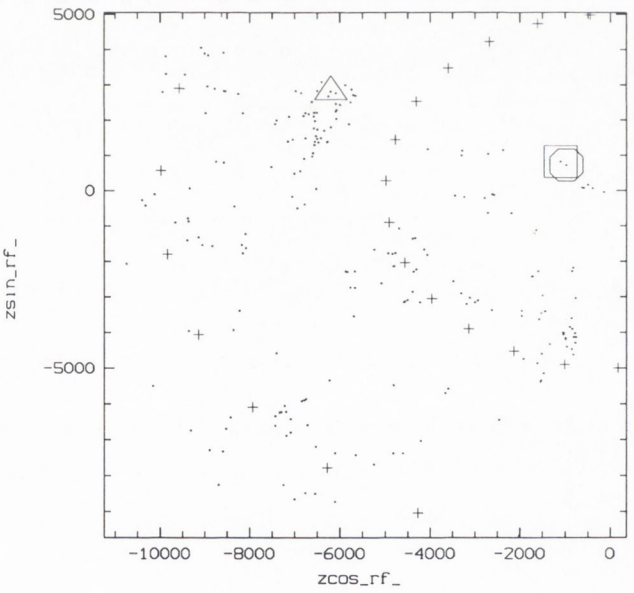


Figure 4.1: Void A:Slice A, for declination $21° - 24°$ NGC 3189 = ○, NGC 3193 = □, NGC 3618 = △. The grid of + signs represent recessional velocities of 5,000 and 10,000 km/s respectively. We observe from the point (0,0).

Name	RA(2000)	DEC(2000)	Vel.	ROSAT Seq no.	Off.	F/B	Type	SNR
(1)	(2)	(3)	(4)	(5)	(6)	(7)	(8)	(9)
NGC 3189	154.524292	21.832167	1271	800125	0.2	f	Liner	N
NGC 3193	154.603667	21.894056	1399	800125	0.3	f	E2	N
NGC 3618	169.635833	23.468889	6807	700051	0.3	b	SAB	N
NGC 4725	192.610861	25.501616	1206	900212	0.1	f	SAB Sy2	Y
NGC 5559	214.803333	24.798889	5166	701271	0.7	b	SBb	AO
I4314	204.604479	26.742405	8592	701064	0.1	b	Ell.	N
IC4423	216.574167	26.246111	9067	701369	0.2	b	S?	AO
CGCG1533.1 +2730	233.811441	27.324918	9631	201563	0.4	b	S?	N

Table 4.2: VoidA: The List of Galaxies selected from Void A. Col(1) The galaxy names
Col(2) & Col(3) give the coordinates in RA, DEC for their optical positions,
Col(4) the heliocentric recessional velocity (km/s),
Col(5) the ROSAT sequence number of the observation used,
Col(6) offset of the X-ray from the optical position (in arc minutes),
Col(7) if the object is situated at the front or back of the void,
Col(8)type of galaxy and
Col(9) if there is a Supernova remnant present, Y:yes, N:no, AO: yes but after this observation was made.

4.2.3 Void A: Results

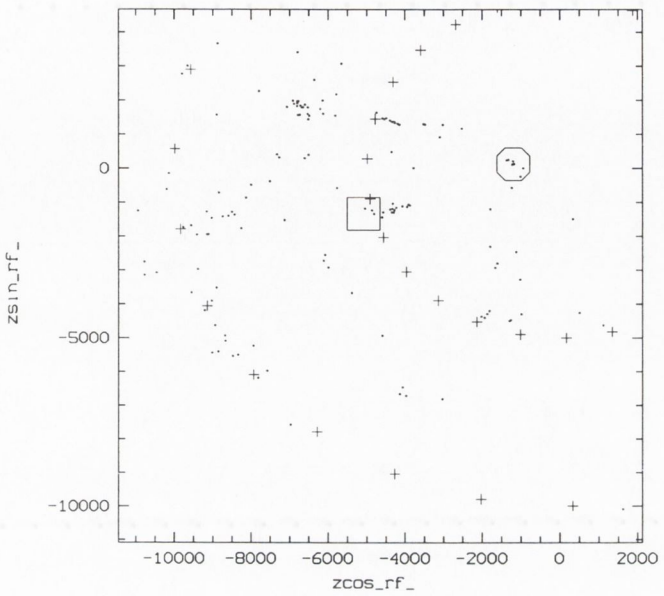


Figure 4.2: Void A :Slice B, for declination $25° - 26°$ NGC 4725 = ∘ and NGC 5559 = □. The grid of + signs represent recessional velocities of 5,000, 10,000 and 15,000 km/s respectively. We observe from the point (0,0).

Name	HR1	EHR1	HR2	EHR2	Counts	Front/Back
NGC 3189	0.16	0.18	0.02	0.07	54	f
NGC 3193	0.46	0.20	-0.04	0.10	48	f
NGC 3618	-0.15	0.16	0.03	0.05	108	b
NGC 4725	-0.46	0.04	-0.12	0.07	649	f
NGC 5559	-0.59	0.17	-0.81	0.02	66	b
I4314	0.34	0.26	-.43	0.09	56	b
IC4423	0.19	0.15	0.06	0.06	87	b
CGCG 1533.1 +2730	0.18	0.15	-0.11	0.06	263	b
Average front	-0.40	0.25	-0.12	0.04		
Average back	-0.11	0.15	-0.57	0.15		
Average	-0.316		-0.179			

Table 4.3: Void A: Calculated HR's for the galaxies surrounding Void A. EHR1,2 is the error on HR1 and HR2 respectively. Front/Back indicates if the galaxy is on the front or back of the void.

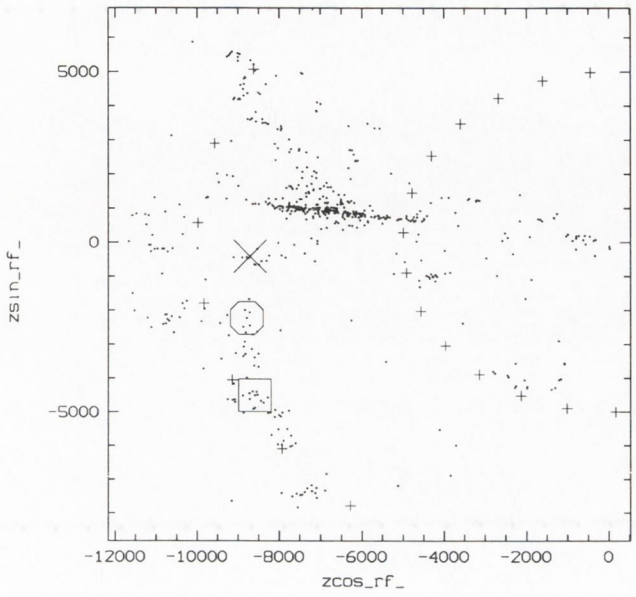


Figure 4.3: Void A: Slice C, for declination 26° – 28° I4314 = ×,IC4423 = ∘ and CGCG 1533.1+2730 = □. The grid of + signs represent recessional velocities of 5,000, 10,000 and 15,000 km/s respectively. We observe from the point (0,0).

Weighted Average	HR1	HR2	N_H
Front	-0.40	-0.12	$3.89 \times 10^{20} cm^{-2}$
Back	-0.08	-0.61	$6.2 \times 10^{20} cm^{-2}$
Combined	-0.316	-0.179	$5.70 \times 10^{20} cm^{-2}$

Table 4.4: Void A: Calculation of the N_H at the front and back of Void A. Note:To calculate the N_H at the back of the void the point (HR1=−0.08,HR2=−0.61) lies outside the limits of our grid. This is due to the large effect of NGC5559 which has a very low value of HR2 with a small error. NGC5559 (see Figure 4.1) is part of a group of galaxies and the photons may be absorbed by the intra group gas. When we take the weighted average this point dominates, giving us a value of HR1,HR2 which is outside the limits of our simulated grid. To compensate for this we estimate N_H, using the value of HR1 only.

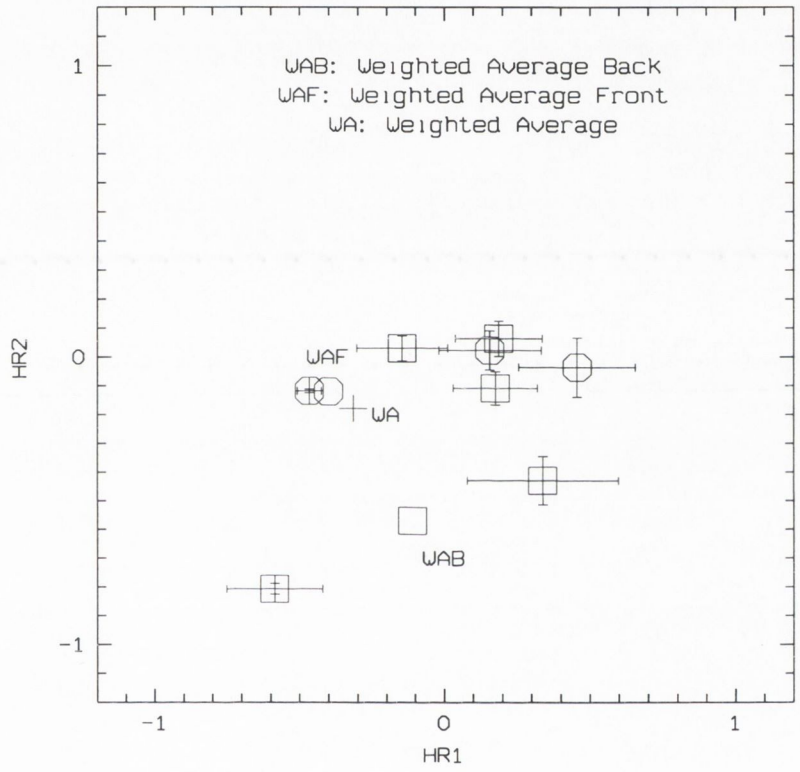


Figure 4.4: Void A: HR1 v HR2 Galaxies from the back of the void are marked by boxes and galaxies from the front of the void are marked by circles. The empty box (WAB), circle (WAF)are the weighted averages for the back and front of the void respectively and the + (WA) represents the average for the whole void

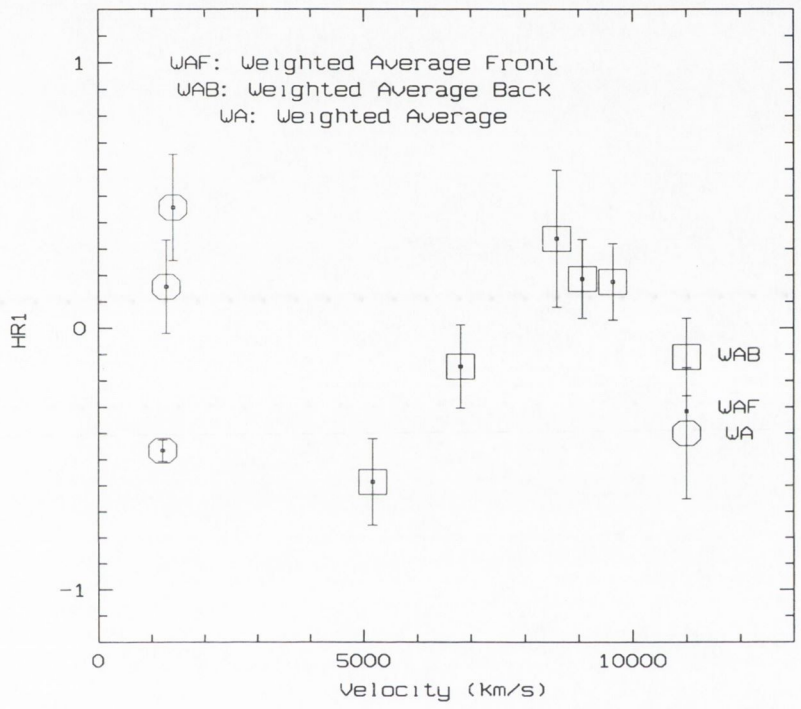


Figure 4.5: Void A: HR1 v recessional velocity (km/s). Galaxies from the back of the void are marked by boxes and galaxies from the front of the void are marked by circles. The empty box (WAB), circle (WAF) are the weighted averages for the back and front of the void respectively and the small dot (WA) represents the average for the whole void. The errors shown for the weighted averages are the standard errors on the mean. These weighted averages are set at a recessional velocity of 11,000 km/s solely for illustrative purposes.

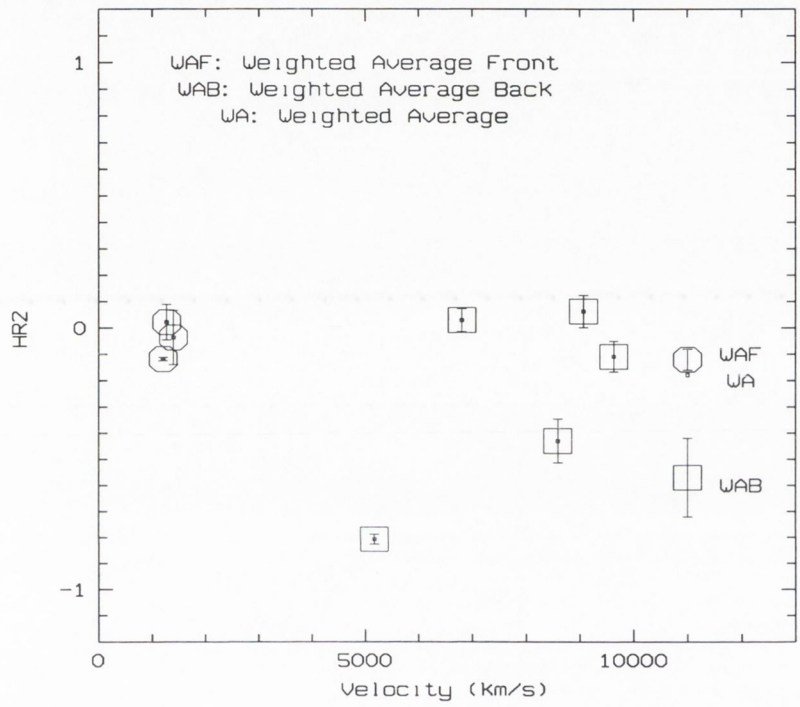


Figure 4.6: Void A: HR2 v recessional velocity (km/s). Galaxies from the back of the void are marked by boxes and galaxies from the front of the void are marked by circles. The empty box (WAB), circle (WAF) are the weighted averages for the back and front of the void respectively and the small dot (WA) represents the average for the whole void. The errors shown for the weighted averages are the standard errors on the mean. These weighted averages are set at a recessional velocity of 11,000 km/s solely for illustrative purposes.

4.2.4 Void B:

Galaxies are selected in the range Right Ascension:$13^h30m-14^h30^m$, Declination:$10°-35°$ and recessional velocity 7,500 -12,000 km/s. We retrieve 12 galaxies from the ROSAT data archive, 9 at the front and 3 at the back of the void. Slice projections for Void B are shown in Figure 4.7 and Figure 4.8 and details of the galaxies are given in Table 4.5 and 4.6.

Name	RA (2000)	DEC (2000)	Vela. (km/s)	ROSAT Seq. no.	Off.	F/B	Type	SNR
(1)	(2)	(3)	(4)	(5)	(6)	(7)	(8)	(9)
NGC3786	174.9272	31.9092	2678	700811	0.2	f	SAB Sy1.8	Ao
NGC4193	183.4732	13.1728	2480	800421	0.4	f	SAB	N
NGC4253	184.6104	29.8128	3876	700970	0.1	b	SB Sy1.5	N
NGC4450	187.1222	17.0851	1957	600160	0.1	f	SA LNR	N
NGC4459	187.2497	13.9792	1210	700346	0.4	f	SA(r)0+	N
NGC4473	187.4536	13.4293	2244	700346	0.4	f	E5	N
NGC4477	187.5100	13.6363	1353	700346	0.5	f	SB Sy2	N
NGC4565	189.0866	25.9876	1227	600415	0.2	f	SA Sy3 Sy1.9	N
NGC4614	190.3812	26.0430	4833	800475	0.1	b	SB0/a	N
NGC4615	190.4058	26.0727	4716	800475	0.5	b	Scd	N
NGC4725	192.6108	25.5016	1206	900212	0.1	f	SAB Sy2	Y
NGC5089	199.9137	30.2564	2141	600225	0.2	f	Sb	N

Table 4.5: Void B:The List of Galaxies selected from around Void B.
Col (1) the galaxy name,
Col (2) & (3) the optical position in RA,DEC
Col(4) the recessional velocity (km/s)
Col(5) the ROSAT sequence number of the observation used,
Col(6) offset of the X-ray from the optical position (in arc minutes),
Col(7) if the object is situated at the front or back of the void,
Col(8) type of galaxy and
Col(9) if there is a Supernova remnant present, Y:yes, N:no, AO: yes but after this observation was made.

Name	HR1	EHR1	HR2	EHR2	Counts	Front/Back
NGC3786	0.93	0.01	0.46	0.027	1003	f
NGC4193	0.82	0.13	0.48	0.08	139	f
NGC4253	-0.05	0.004	0.09	0.001	65223	b
NGC4450	0.31	0.04	0.26	0.03	580	f
NGC4459	0.46	0.22	-0.10	0.12	61	f
NGC4473	0.65	0.21	0.46	0.12	84	f
NGC4477	0.28	0.07	-0.15	0.04	283	f
NGC4565	0.80	0.04	0.38	0.04	497	f
NGC4614	0.49	0.27	-0.31	0.11	42	b
NGC4615	0.20	0.29	-0.09	0.10	33	b
NGC4725	-0.47	0.04	-0.12	0.01	604	f
NGC5089	0.50	0.50	-0.45	0.16	24	f
Average front	0.74	0.14	-0.05	0.11		
Average back	-0.05	0.15	0.08	0.10		
Average	0.03		0.08			

Table 4.6: Void B:Calculated HR's for the galaxies surrounding Void B. Where EHR1 and EHR2 are the errors on HR1 and HR2 respectively.

Weighted Average	HR1	HR2	N_H
Front	0.74	-0.05	$13.5 \times 10^{20} cm^{-2}$
Back	-0.05	0.08	$3.8 \times 10^{20} cm^{-2}$
Combined	0.03	0.08	$4.4 \times 10^{20} cm^{-2}$

Table 4.7: Void B: Note: To calculate the N_H at the front of the void the point (-0.74,-0.05) lies slightly outside the limits of our grid (see discussion). To compensate for this we extrapolate to the nearest point.

4.2.5 Void C:

Galaxies are selected in the range Right Ascension: $8^h - 14^h$, Declination:$5° - 45°$ and recessional velocity 0 -10,000 km/s. We retrieve 23 galaxies from the ROSAT data archive, 16 at the front and 7 at the back of the void. Slice projections for Void C are shown in Figure 4.12 through to Figure 4.16 and details of the galaxies are given in Table 4.8 and 4.9.

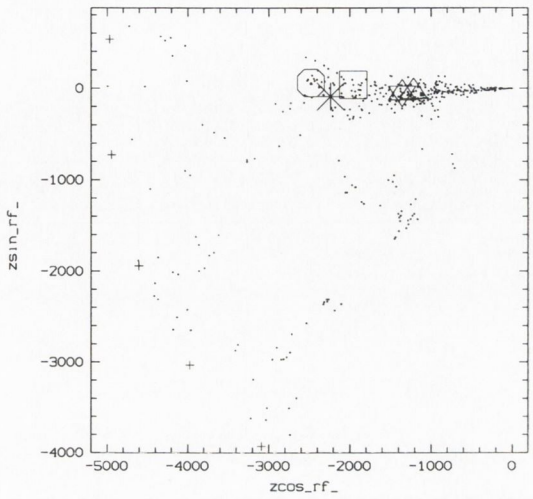


Figure 4.7: Void B: Slice A, for declination $10° - 20°$ NGC 4193=○,NGC 4450=□,NGC 4459=△, NGC 4473= $*$, NGC 4477 = $\star$. The grid of + signs represent recessional velocities of 5,000 and 10,000 km/s respectively. We observe from the point (0,0).

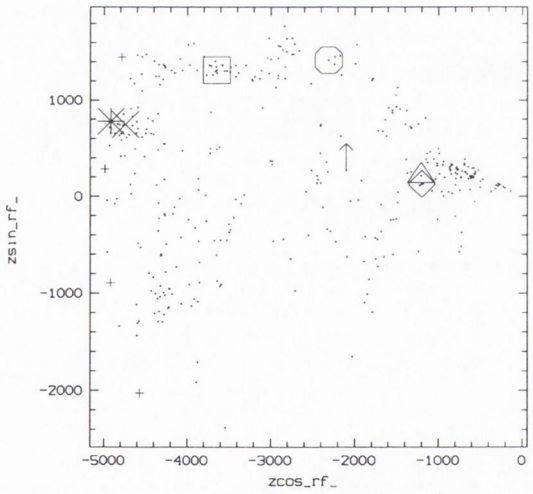


Figure 4.8: Void B: Slice B .for declination $25° - 35°$ NGC 3786=○,NGC 4253=□,NGC 4565=△, NGC 4614 = $*$, NGC 4615= $\times$, NGC 4725= $\Diamond$, NGC 5089=↑. The grid of + signs represent recessional velocities of 5,000 and 10,000 km/s. We observe from the point (0,0).

Name (1)	RA (2000) (2)	DEC (2000) (3)	Vel. (km/s) (4)	ROSAT Seq.no. (5)	Off. (6)	F/B (7)	Type (8)	SNR (9)
NGC3623	169.7329	13.0936	807	600537	0.3	f	SAB LNR	N
NGC3628	170.0706	13.5889	843	700010	0.4	f	SAb LNR	N
NGC3817	175.4700	10.3059	5998	600420	0.1	b	G	N
NGC3822	175.5466	10.2777	6138	600420	0.1	b	Sb Sy2	N
NGC3825	175.5988	10.2640	6503	600420	0.1	b	SBa	N
NGC3615	169.5276	23.3974	6684	700051	1.8	b	E	N
NGC4253	184.6104	29.8128	3876	700970	0.2	f	SB Sy1.5	N
NGC4314	185.6332	29.8953	963	701056	0.1	f	SB LNR	N
NGC5089	199.9137	30.2564	2141	600225	0.2	f	Sb	N
NGC3067	149.5896	32.3694	1476	700468	0.1	f	SAB	N
UGC05393	150.4245	33.1368	1448	800492	1.7	f	SB(r)dm:	N
NGC4203	183.7707	33.1968	1086	600130	0.0	f	SAB LNR	N
CGCG213 -027	166.3412	38.2338	8465	700925	0.0	b	G	N
UGC05048	142.1568	38.5385	3641	700850	1.6	f	Im:	N
UGC07208	183.1159	39.1103	7078	600625	0.1	b	S?	N
NGC4151	182.6357	39.4057	995	700277	0.1	f	SAB Sy1.5	N
NGC4156	182.7067	39.4727	6750	700277	0.2	b	SB LNR	Y
NGC5358	208.5018	40.2772	2401	800485	0.4	f	S0/a	N
NGC5353	208.3612	40.2830	2310	800485	0.1	f	S0 AGN	N
NGC5355	208.4397	40.3385	2408	800485	0.4	f	E3	N
NGC5350	208.3399	40.3640	2321	800485	0.1	f	SB Sbrst	N
NGC4485	187.6302	41.6994	493	900137	0.3	f	IB pec HII	N
NGC4051	180.7900	44.5313	725	700557	0.1	f	SAB Sy1.5	N

Table 4.8: Void C:The list of galaxies around Void C. Col (1) The galaxy names,
Col(2) & Col(3) the optical positions of the galaxies in RA,DEC
Col(4) the recessional velocity (km/s),
Col(5) the ROSAT sequence number,
Col(6) offset of the X-ray from the optical position (in arc minutes),
Col(7) if the object is situated at the front or back of the void,
Col(8) type of galaxy and
Col(9) if there is a Supernova remnant present, Y:yes, N:no, AO: yes but after this observation was made.

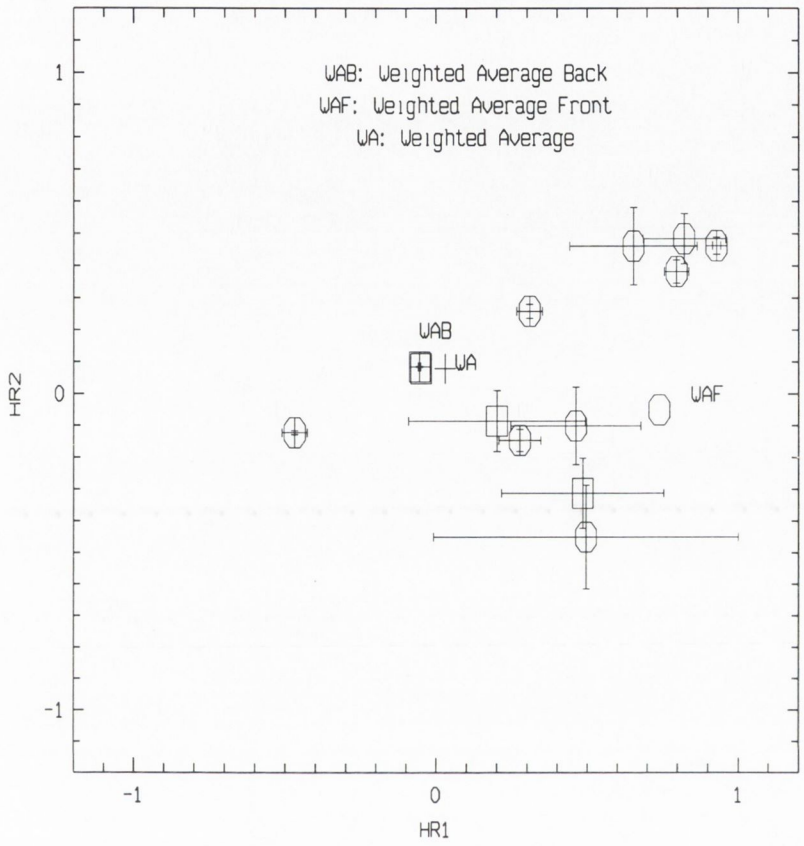


Figure 4.9: Void B: HR1 vs HR2. Galaxies from the back of the void are marked by boxes and galaxies from the front of the void are marked by circles. The empty box, circle are the weighted averages for the back(WAB) and front(WAF) of the void respectively and the small + represents the average for the whole void (WA). The empty box is (WAB) (the weighted average HR1, HR2 for the back of the void is superimposed by another point)

4.3 Comparison of simulations with observations

To measure how accurately our simulated grid predicts N_H and Γ using HR's we select the 4 galaxies in our study with more than 1000 photons, namely NGC 3786, NGC 4253, NGC 4151 and NGC 4051 (all of these are Seyfert galaxies). For these four galaxies we perform spectral fits and compare fitted

Name	HR1	EHR1	HR2	EHR2	Counts	Front/Back
NGC 3623	0.24	0.06	0.09	0.03	323	f
NGC 3628	0.91	0.03	0.66	0.03	687	f
NGC 3817	1.22	0.35	0.04	0.19	59	b
NGC 3822	0.67	0.09	0.24	0.05	222	b
NGC 3825	0.79	0.49	0.01	0.19	36	b
NGC 3615	-0.15	0.16	0.03	0.04	108	b
NGC 4253	-0.005	0.004	0.086	0.001	65223	f
NGC 4314	-0.02	0.12	-0.15	0.04	135	f
NGC 5089	0.48	0.49	-0.43	0.16	24	f
NGC 3067	0.68	0.39	-0.22	0.16	32	f
UGC 05393	0.09	0.32	-0.34	0.09	38	f
NGC 4203	0.00	0.01	0.21	0.005	500	f
CGCG 213-027	0.70	0.60	0.68	0.26	29	b
UGC 05048	-0.65	0.19	0.66	0.02	51	f
UGC 07208	0.45	0.04	0.13	0.02	727	b
NGC 4151	0.07	0.007	0.06	0.003	19226	f
NGC 4156	0.86	0.39	-0.02	0.13	109	b
NGC 5353	0.23	0.04	-0.05	0.02	681	f
NGC 5358	0.44	0.24	-0.01	0.09	73	f
NGC 5355	-0.25	0.13	-0.05	0.03	100	f
NGC 5350	0.01	0.12	0.05	0.03	140	f
NGC 4485	1.04	0.40	0.31	0.16	136	f
NGC 4051	-0.42	0.005	-0.05	0.001	40551	f
Average	-0.16		-0.002			
Av. Front	-0.16	0.11	-0.002	0.07		
Av. Back	0.46	0.15	0.12	0.08		

Table 4.9: The list of galaxies selected from Void C, along with HR1, HR2 the errors on both of these and the total number of counts. EHR1 and EHR2 are the errors om HR1 and HR2 respectively. Front/Back indicates if the galaxy is located on the front or back of the void. We give the mean value for HR1, HR2 at the front and back of the void along with the Standard error on the mean.

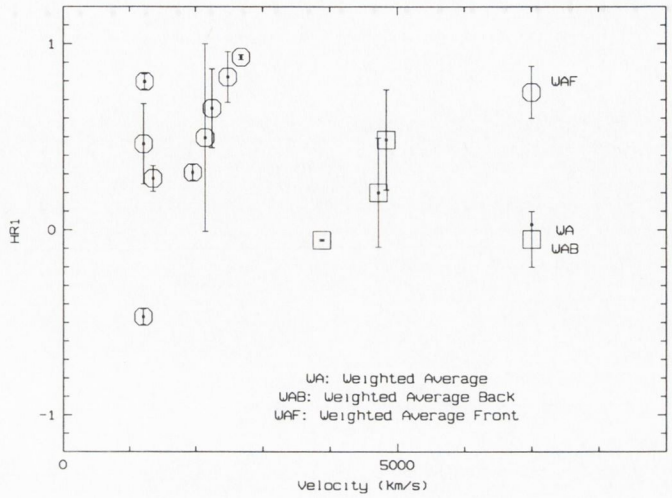


Figure 4.10: Void B: HR1 vs recessional velocity. Galaxies from the back of the void are marked by boxes and galaxies from the front of the void are marked by circles. The empty box (WAB), circle (WAF) are the weighted averages for the back and front of the void respectively and the small dot represents the average for the whole void. These three averages are displayed at a recessional velocity of 7,000 km/s purely for illustrative reasons. NGC 4725 has a value of HR1 =-0.47, this may be due to the presence of a SNR in NGC 4725. When the weighted average is calculated this value has little effect.

values of N_H and Γ with those derived from their HR's. For NGC 3786 and NGC 4051 their spectrum is well fitted by a power-law model with reduced χ^2 of 0.99 and 1.53 respectively. We find for both these galaxies that the values of N_H derived from the simulated grid are in good agreement with the values obtained by spectral fitting (i.e. the values of N_H from the grid agree

Weighted Average	HR1	HR2	N_H
Front	-0.16	-0.002	$4.8 \times 10^{20} cm^{-2}$
Back	0.46	0.12	$7.2 \times 10^{20} cm^{-2}$
Combined	-0.16	-0.002	$4.8 \times 10^{20} cm^{-2}$

Table 4.10: Void C: Excess N_H at the back of the void which may imply the presence of processed gas.

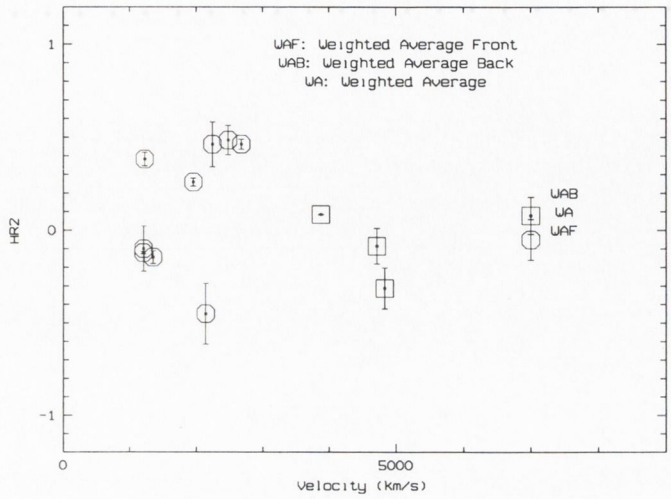


Figure 4.11: Void B: HR2 vs recessional velocity. Galaxies from the back of the void are marked by boxes and galaxies from the front of the void are marked by circles. The empty box (WAB), circle (WAF) are the weighted averages for the back and front of the void respectively and the small dot represents the average for the whole void. These three averages are displayed at at a recessional velocity of 7,000 km/s purely for illustrative reasons.

with the 1-σ errors on N_H from the 2-dimensional χ^2 plots (Contour plots of χ^2 as a function of column density N_H against the photon index Γ) see Table 4.11.

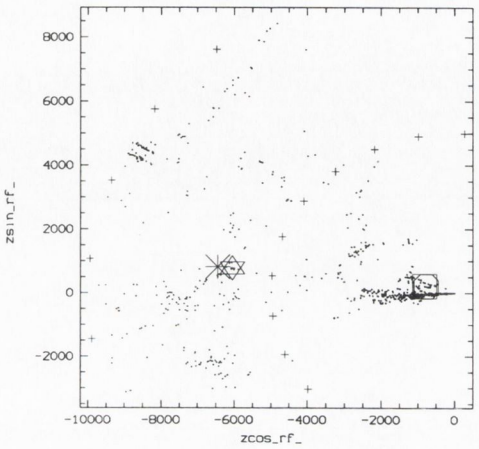


Figure 4.12: Void C:Slice A for declination $10° - 15°$ 1. $\circ$= NGC 3623 2. $\square$ = NGC 3628 3. $\triangle$ = NGC 3817 4. $\star$ = NGC 3822 5. $*$ = NGC 3825. NB. The $\star$ symbol is superimposed on the $\triangle$ symbol. The grid of + signs represent recessional velocities of 5,000 and 10,000 km/s respectively. We observe from the point (0,0).

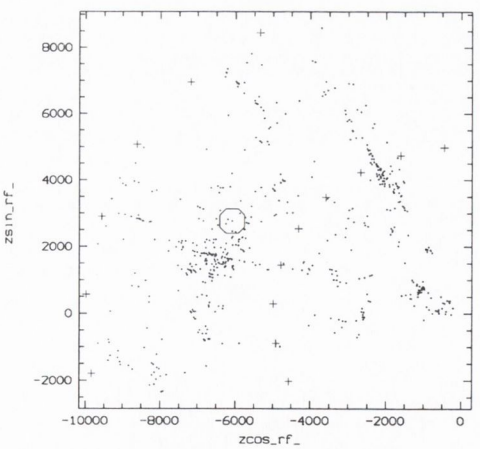


Figure 4.13: Void C:Slice B for declination $20° - 25°$. The grid of + signs represent recessional velocities of 5,000 and 10,000 km/s respectively. We observe from the point (0,0). 1. $\circ$= NGC 3615

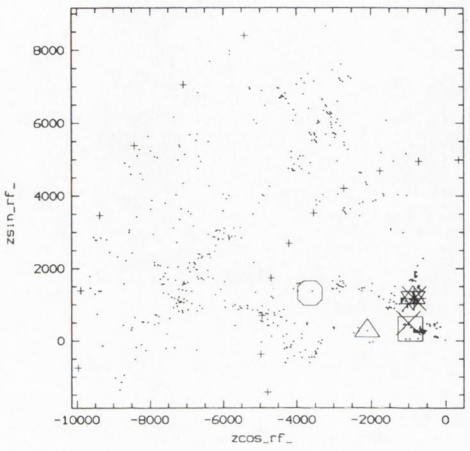


Figure 4.14: Void C:Slice C for declination $30° - 35°$ 1. $\circ$= NGC 4253 2. $\square$ = NGC 4314 3. $\triangle$ = NGC 5089 4. $\star$ = NGC 3067 5. $*$ = 09588+3322 6. [x] = NGC 4203. The grid of + signs represent recessional velocities of 5,000 and 10,000 km/s respectively. We observe from the point (0,0).

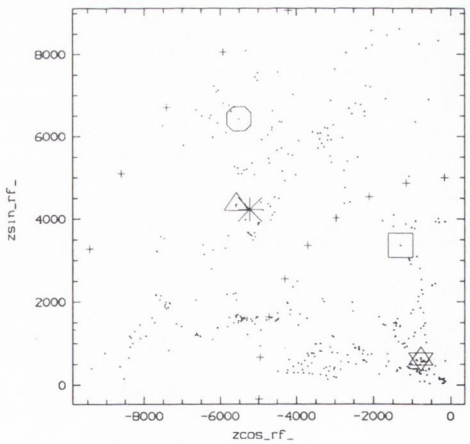


Figure 4.15: Void C: Slice D for declination $35° - 40°$ 1. $\circ$= 11025+3830 2. $\square$ = 09225+3845 3. $\triangle$ = 12099+ 3923 4. $\star$ = NGC 4151 5. $*$ = NGC 4156. The grid of + signs represent recessional velocities of 5,000 and 10,000 km/s respectively. We observe from the point (0,0).

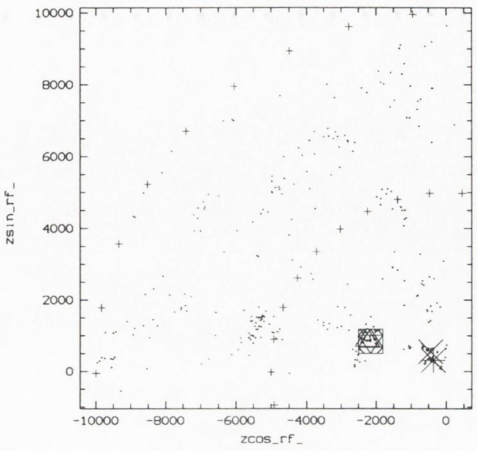


Figure 4.16: Void C: Slice E for declination $40° - 45°$ 1. o= NGC 5358 2. □ = NGC 5353 3. △ = NGC 5355 4. $\star$ = NGC 5350 5. $*$ = 4485 6.X = NGC 4051. The grid of + signs represent recessional velocities of 5,000 and 10,000 km/s respectively. We observe from the point (0,0).

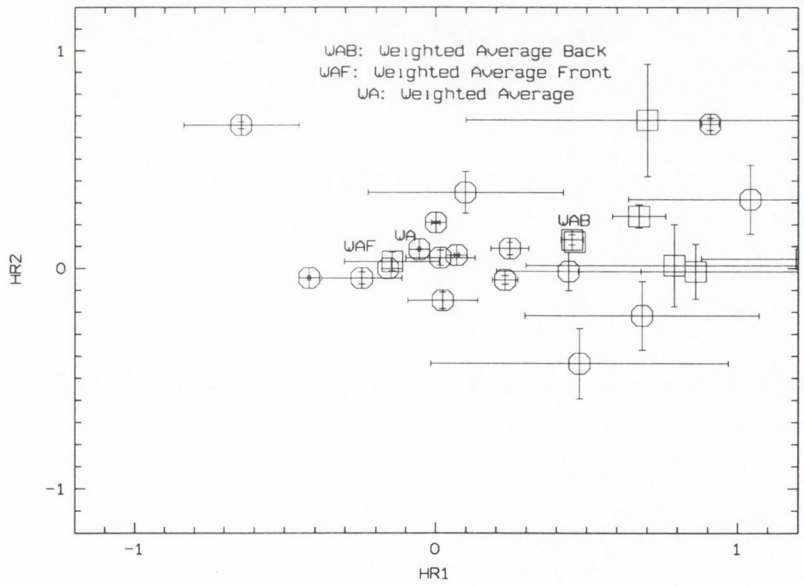


Figure 4.17: Void C: HR1 vs HR2 A plot of HR1 versus HR2 for void C. Galaxies from the back of the void are marked by boxes and galaxies from the front of the void are marked by circles. The empty box (WAB), circle (WAF) are the weighted averages for the back and front of the void respectively and the small dot (WA) represents the average for the whole void.

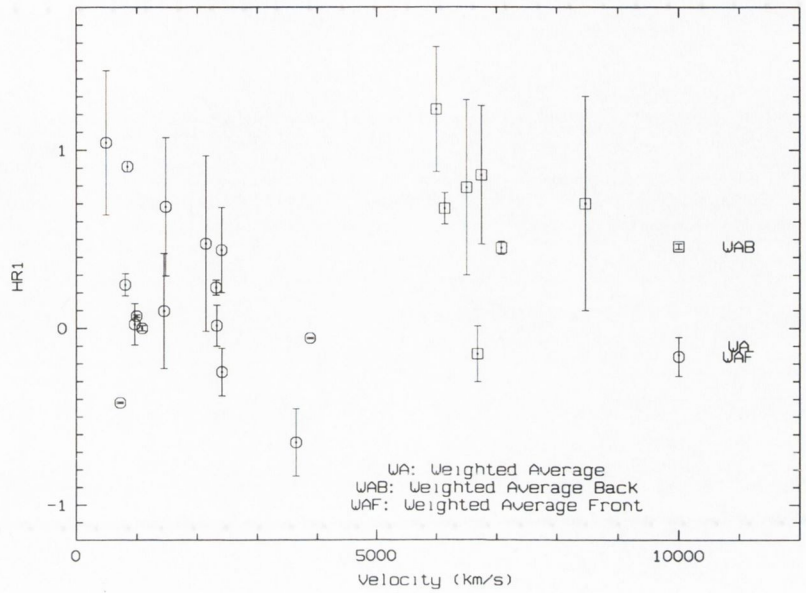


Figure 4.18: Void C: HR1 vs recessional velocity. Galaxies from the back of the void are marked by boxes and galaxies from the front of the void are marked by circles. The empty box (WAB), circle (WAF) are the weighted averages for the back and front of the void respectively and the small dot (WA) represents the average for the whole void.

4.3.1 NGC3786

We fit an absorbed power-law model to NGC3786 (MKN 744) (see Figure 4.20) with a resultant reduced χ^2=0.99. Examining the residuals we find only a small offset from the model. The value of N_H derived from our grid agrees within the 1-σ error with the value derived from the 2-D χ^2 plot, but is slightly outside the 1-σ error derived from the 1-D χ^2 plot. This is to be expected as with the grid we are simultaneously reading off the values of N_H and Γ. Komossa & Fink (1996b) analyze NGC 3786. They find an acceptable fit (reduced χ^2= 1.0) for a single power law with a cold absorption column as a free parameter, although some systematic residuals remain around 0.6-1.0 keV. The deduced power law is unusually flat, with $\Gamma \approx -1$. They find an absorbing column of $N_H \approx 8 \times 10^{20} cm^{-2}$ consistent with the value from our grid. Applying a power law with an additional absorption edge gives an excellent fit (reduced χ^2 =0.7). They find an edge energy of $E \approx 0.8keV$ and Γ

Name (1)	2D N_H (2)	1D N_H (3)	Grid N_H (4)	Gal N_H (5)	Cts (6)	Red. χ^2 (7)	V (8)
NGC3786	$0.72^{+0.73}_{-0.20}$	$0.72^{+0.16}_{-0.06}$	1.09	0.199	1003	0.99	B
NGC4253	$0.25^{+0.012}_{-0.012}$	$0.25^{+0.005}_{-0.005}$	$0.368^{+0.02}_{-0.07}$	0.171	65223	11.5	C,B
NGC4151	$0.28^{+0.03}_{-0.03}$	$0.285^{+0.005}_{-0.005}$	$0.49^{+0.01}_{-0.05}$	0.198	19226	24.3	C
NGC4051	$0.258^{+0.012}_{-0.012}$	$0.258^{+0.002}_{-0.002}$	$0.282^{+0.067}_{-0.002}$	0.132	40551	1.53	C

Table 4.11: Table of N_H derived from 2-D (with photon index Γ and 1-D χ^2 plots compared with values of N_H derived from our simulated grid. All values of N_H are given in units of $10^{21} cm^{-2}$

Col(1) the name of the galaxy

Col(2) the interval of N_H derived from the 2-D plot of Γ v N_H

Col (3) the best fit value of N_H derived from the 1D χ^2 plot of N_H

Col (4) the limits on N_H as derived from the simulated grid

Col(5) is the galactic N_H cf. Dickey & Lockmann 1990

Col (6) the number of counts and

Col(7) the reduced χ^2 of the spectral fit.

Col(8) which void contains these galaxies.

Name (1)	2D N_H (2)	1D N_H (3)	Grid N_H (4)	Gal N_H (5)	Lit (6)	Ref (7)
NGC3786	$0.72^{+0.73}_{-0.20}$	$0.72^{+0.16}_{-0.06}$	1.09	0.199	0.8	kfb
NGC4253	$0.25^{+0.012}_{-0.012}$	$0.25^{+0.005}_{-0.005}$	$0.368^{+0.02}_{-0.07}$	0.171	0.165-0.36	M
NGC4151	$0.28^{+0.03}_{-0.03}$	$0.285^{+0.005}_{-0.005}$	$0.49^{+0.01}_{-0.05}$	0.198	0.76	W
NGC4051	$0.258^{+0.012}_{-0.012}$	$0.258^{+0.002}_{-0.002}$	$0.282^{+0.067}_{-0.002}$	0.132	0.17	kfa

Table 4.12: Table of N_H derived from 2-D (with photon index Γ and 1-D χ^2 plots compared with values of N_H derived from our simulated grid. All values of N_H are given in units of $10^{21} cm^{-2}$

Col(1) the name of the galaxy

Col(2) the interval of N_H derived from the 2-D plot of Γ v N_H

Col (3) the best fit value of N_H derived from the 1D χ^2 plot of N_H

Col (4) the limits on N_H as derived from the simulated grid

Col(5) is the galactic N_H cf. Dickey & Lockmann 1990

Col (6) the number of counts and

Col(7) the literature reference for comparison kfa: Komossa & Fink 1997a, kfb:Komossa & Fink 1997b,W: Warwick et al.(1995) and M: Molendi et al. (1994)

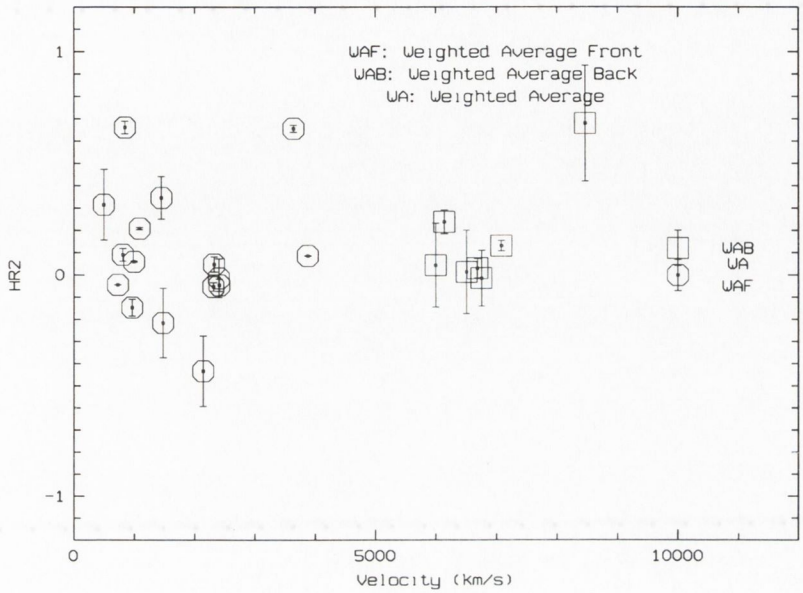


Figure 4.19: Void C: HR1 vs recessional velocity for void C. Galaxies from the back of the void are marked by boxes and galaxies from the front of the void are marked by circles. The empty box (WAB), circle (WAF) are the weighted averages for the back and front of the void respectively and the small dot (WA) represents the average for the whole void.

$= -1.9 \pm 0.3$. An even higher value of $N_H = (1.7 \pm 0.3) \times 10^{21} cm^{-2}$. The edge energy is near that expected for OVII (E=0.74 keV) and OVIII (E=0.87 keV V). This is suggestive of the presence of a warm absorber. Rush et al. (Rush et al. 1996) using RASS (ROSAT All Sky Survey data), observe NGC3786 but do not observe enough photons to fit a spectral model.

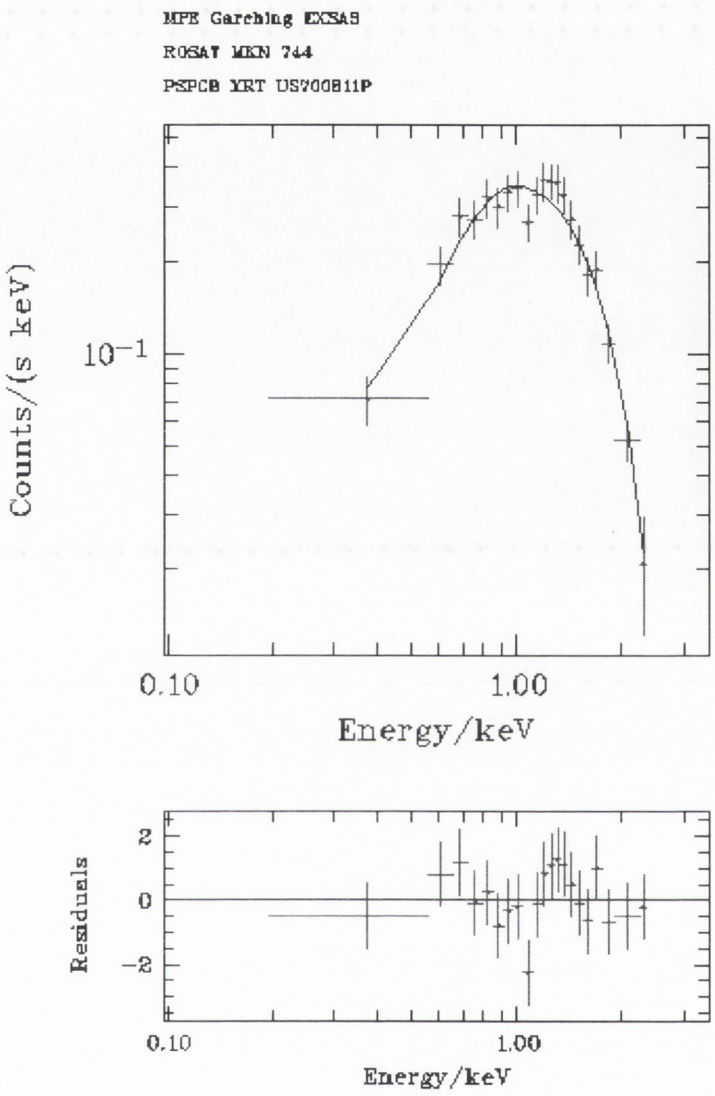


Figure 4.20: Power Law fit to the galaxy NGC3786 with a reduced $\chi^2 = 0.99$

4.3.2 NGC4253

We attempt to fit a power law model to NGC4253(MKN766) (see Figure 4.23) with a resultant reduced χ^2=11.5. Examining the residuals we find a systematic offset from the model. Subsequently attempting to fit a Raymond-Smith, Thermal bremsstrahlung and black-body model (and combinations of these) we fail to improve on the power law fit. Page et al. (Page et al. 2001) analyze

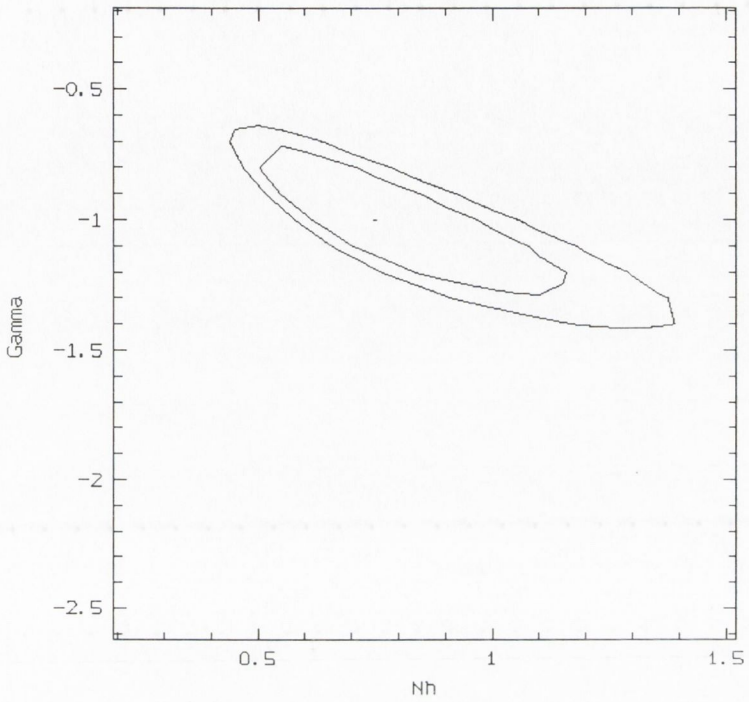


Figure 4.21: Contour plot of χ^2, for the galaxy NGC3786 as a function of the photon index Γ and the column density N_H (in units of $10^{21} cm^{-2}$) for two confidence levels of 68.3 % and 94.5 % .

the XMM spectrum of MKN 766 (NGC4253), finding that the 2-10 keV spectrum can be adequately represented by a power law and broad Fe K alpha emission. Between 0.7 and 2 keV the spectrum is harder and exhibits a flux deficit with respect to the extrapolated medium energy slope. Below 0.7 keV, however, there is a strong excess of emission. Overall we may conclude that NGC4253 isn't described by a simple power law model. The PSPC spectrum has been fitted by Molendi et al. (1994). They conclude NGC4253 cannot be represented by a single power-law component and more complicated models are required. A two component model consisting of a thermal component dominating the soft part of the spectrum plus a power-law emerging above $\approx$ 1 keV yields significantly better results than a single power-law model. They find strong evidence for the presence of a soft excess in NGC4253. When Molendi et al. fit a power law the get a value of N_H varying from 1.65 -3.60

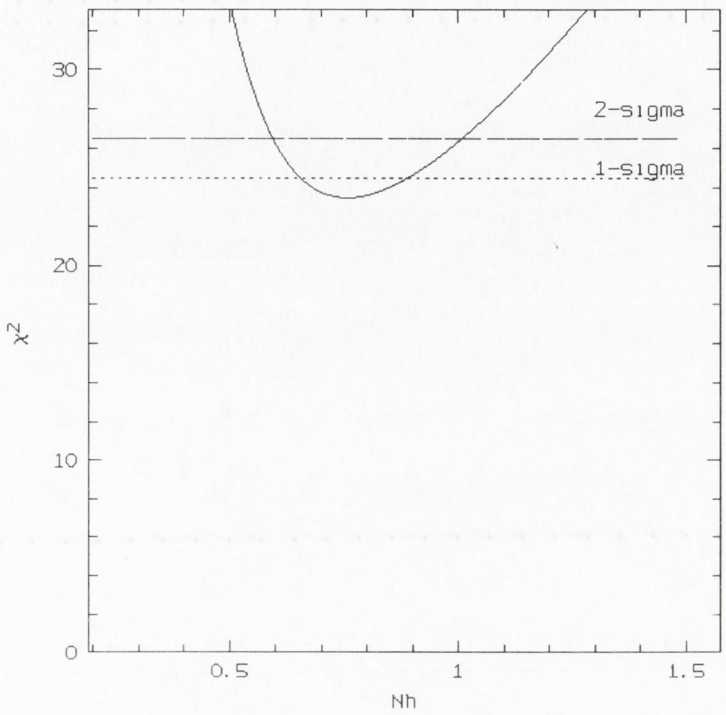


Figure 4.22: Contour plot of χ^2, for the galaxy NGC3786 as a function of the column density N_H (in units of $10^{21} cm^{-2}$) for two confidence levels of 68.3 % and 94.5 %.

$\times 10^{20} cm^{-2}$ (depending on the count rate) consistent with our grid.

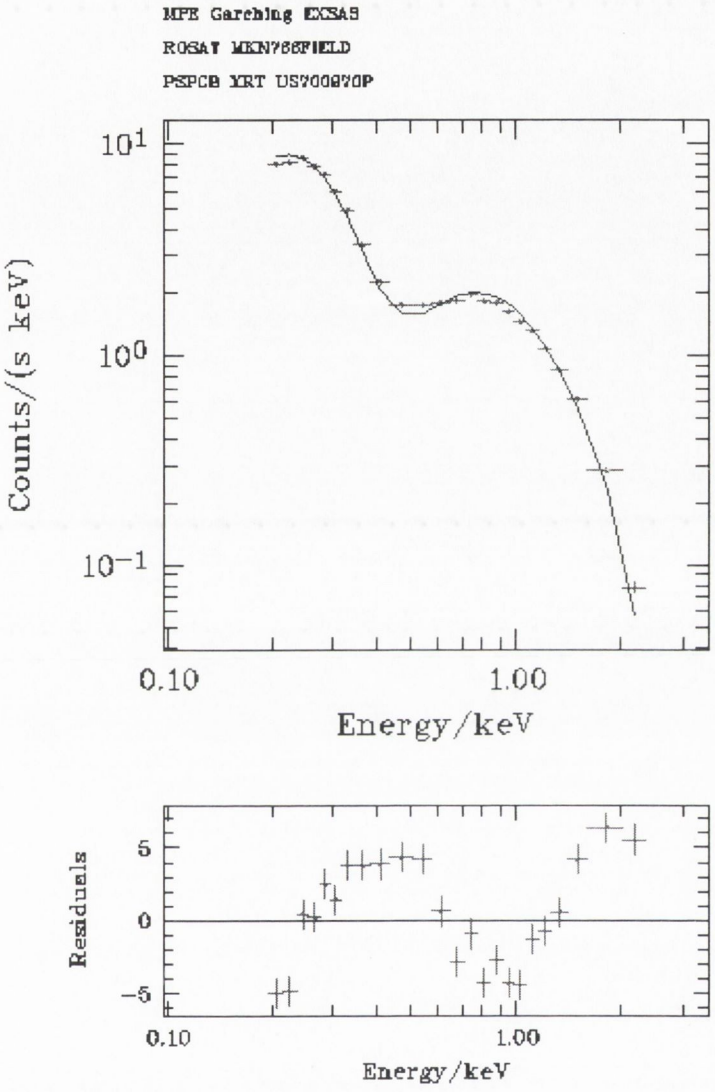


Figure 4.23: Power Law fit to the galaxy NGC4253 with a reduced $\chi^2 = 11.5$

4.3.3 NGC4151

We attempt to fit a power law model to NGC4151 (see Figure 4.26) with a resultant reduced χ^2=24.3. Examining the residuals we find a systematic offset from the model and conclude that a power law model doesn't describe the spectrum of NGC4151. Subsequently attempting to fit a Raymond-Smith, Thermal bremsstrahlung and black-body model (and combinations of these)

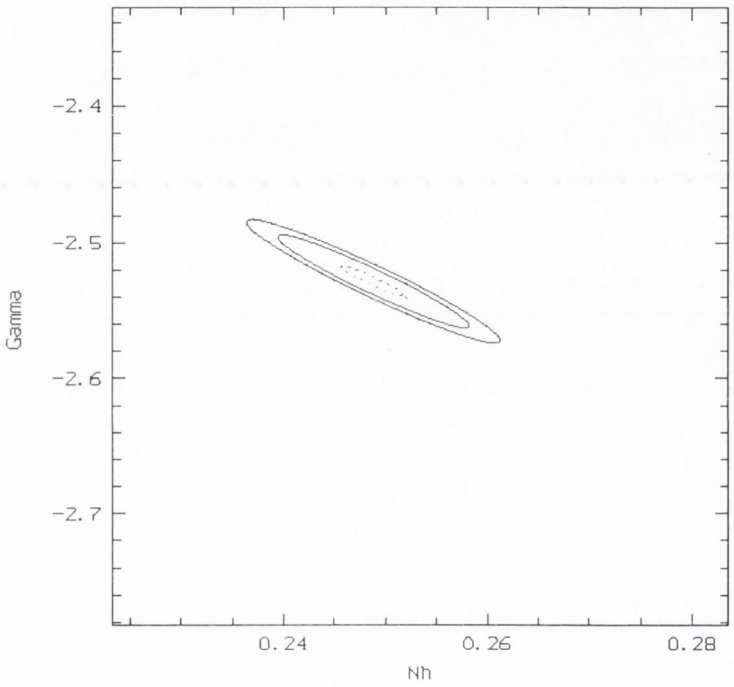


Figure 4.24: Contour plot of χ^2, for the galaxy NGC4253 as a function of the photon index Γ and the column density N_H (in units of $10^{21} cm^{-2}$) for two confidence levels of 68.3 % and 94.5 %.

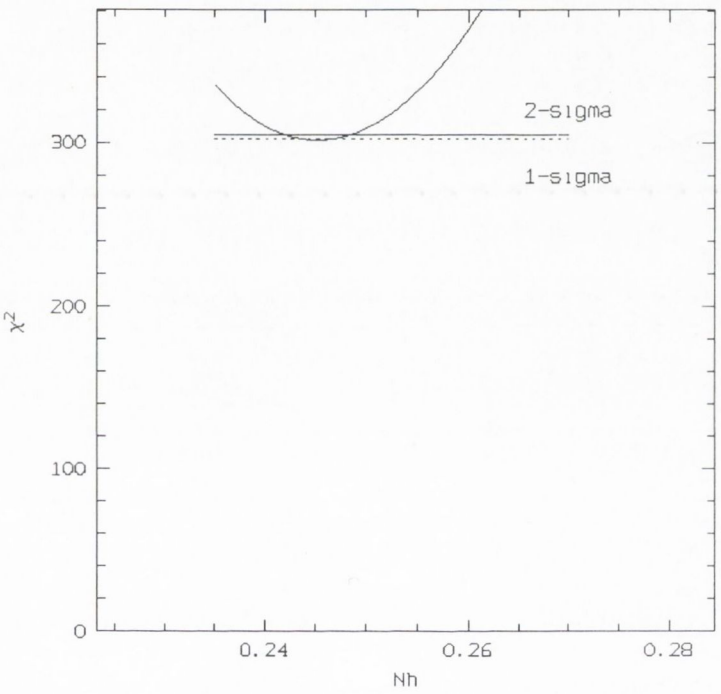


Figure 4.25: Contour plot of χ^2, for the galaxy NGC4253 as a function of the column density N_H (in units of $10^{21} cm^{-2}$) for two confidence levels of 68.3 % and 94.5 %.

we fit a combination of a power-law with a black-body with a resultant reduced χ^2= 1.29. We find that a heavily absorbed power law fits the hard part of the spectrum, while a black-body model with only slight absorption, and a temperature of $\sim$ 0.14 keV models the soft part of the spectrum which we are interested in. Yang et al. (Yang et al. 2001) observe NGC4151 with Chandra. They show that the hard X-ray component (greater than 2 keV) is spatially unresolved. The spectrum of the unresolved nuclear source may be described by a heavily absorbed hard power-law plus soft emission from either a power-law or a thermal component (consistent with our analysis). A warm absorber model may be required to fit the spectrum of NGC4151. Warwick et al. (1995) fit a simple power-law with a reduced χ^2=7 and obtain a value of N_H= 7.6 $\times 10^{20} cm^{-2}$. They conclude that the low spectral resolution of ROSAT severely limits the ability to distinguish between competing models. Rush et al. (Rush et al. 1996) do fit a power law to RASS data with Γ=2. They do not comment on the goodness of fit.

4.3.4 NGC4051

We fit a power law model to NGC4051 (see Figure 4.32) with a resultant reduced χ^2=1.53. Examining the residuals we find a systematic offset from the model, yet the power law model describes the spectrum sufficiently well that our value of N_H derived from our simulated grid is in good agreement with the fitted value. The ROSAT X-ray spectrum has also been analyzed by Komossa & Fink (Komossa & Fink 1997) finding a power law modified by absorption edges and an additional soft excess during the high-state in source flux (this soft excess may be seen in Figure 30 around 0.2 keV), this may be responsible for the residuals we observe when fitting a simple power law, whereas a power law with a warm absorber is required. Examining the X-ray spectra of NGC4051 using Chandra Collinge et al. (2001) find a soft X-ray excess. A power-law is unable to fit the Chandra data but a blackbody produces a nearly acceptable fit.

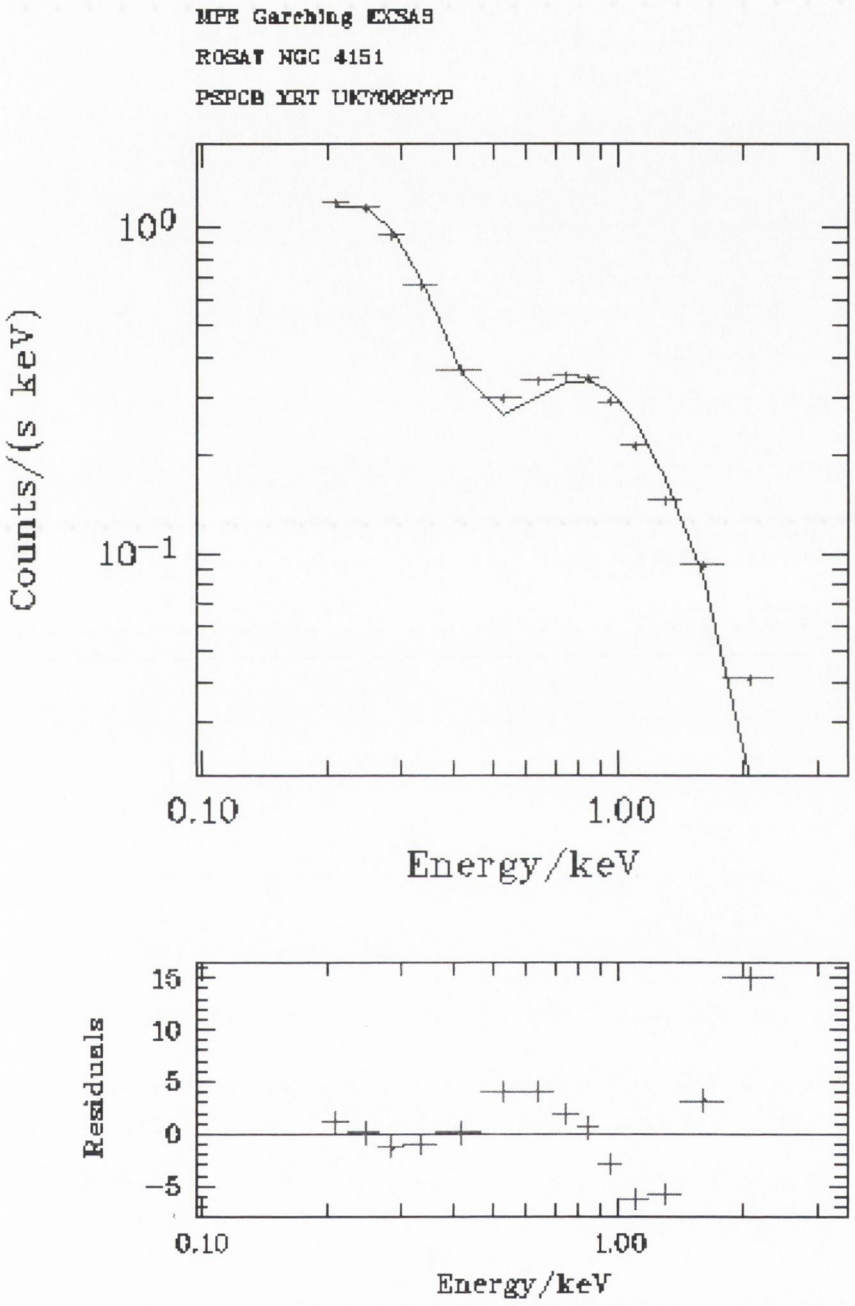


Figure 4.26: Power Law fit to the galaxy NGC4151 with a reduced $\chi^2 = 24.3$

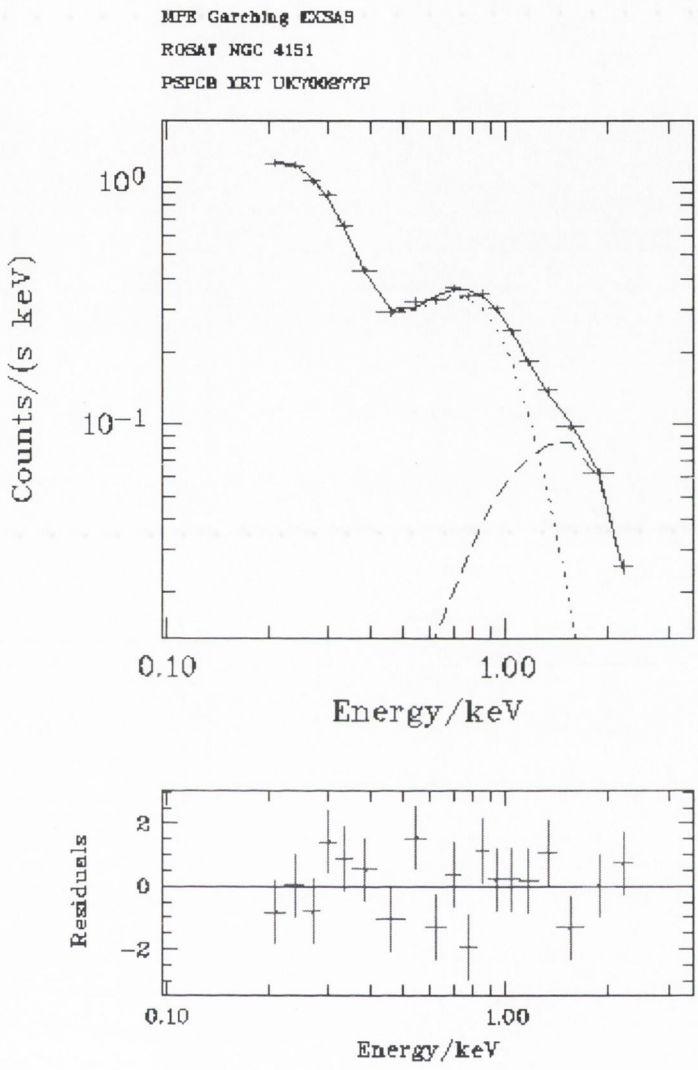


Figure 4.27: Power Law and black body fit to the galaxy NGC4151 with a reduced $\chi^2 = 1.29$

4.4 Discussion

We have simulated spectra for simple power-law models, varying Γ, the photon index and N_H, the amount of neutral free hydrogen. These simulated spectra are then used to calculate HR's producing a grid of hardness ratios with 3248 points with values of N_H in the range $1 \times 10^{19} cm^{-2}$ to 1.9 $1.9 \times 10^{21} cm^{-2}$ and for $\Gamma = -0.25.. - 4$ (in steps of 0.25).This enables us

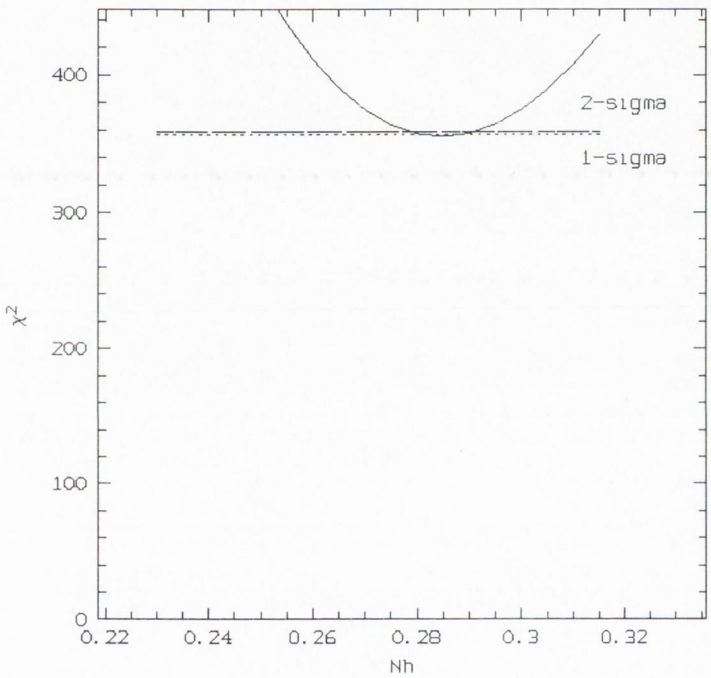


Figure 4.28: Contour plot of χ^2, for the galaxy NGC4151 as a function of the column density N_H (in units of $10^{21} cm^{-2}$) for two confidence levels of 68.3 % and 94.5 %.

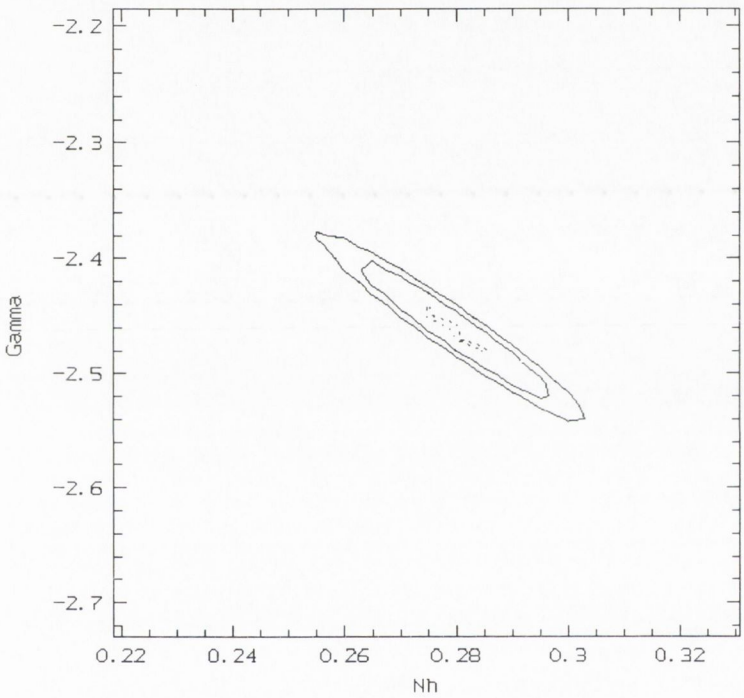


Figure 4.29: Contour plot of χ^2, for the galaxy NGC4151 as a function of the photon index Γ and the column density N_H (in units of $10^{21} cm^{-2}$) for two confidence levels of 68.3 % and 94.5 %.

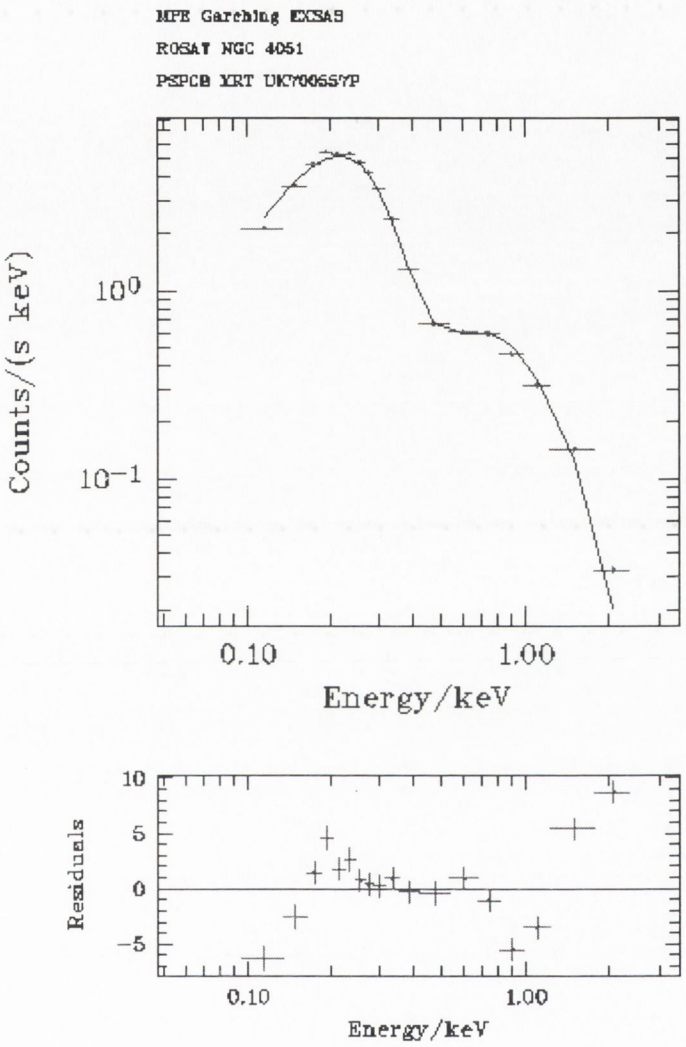


Figure 4.30: Power Law fit to the galaxy NGC4051 with a reduced $\chi^2 = 1.53$, showing a soft excess at 0.2 keV. Examining the residuals we see that a power-law is not a perfect fit.

to relate an observed HR to a value of Γ and a value of N_H. We then use this grid to search for processed gas in voids in the LSS. Galaxies from three large voids (A,B and C) in the CfA redshift survey are selected from the ROSAT data archive . Central to our work is the assumption that galaxies observed serendipitously by the ROSAT PSPC are brighter than average. This brightness may be attributed to the presence of an active core which

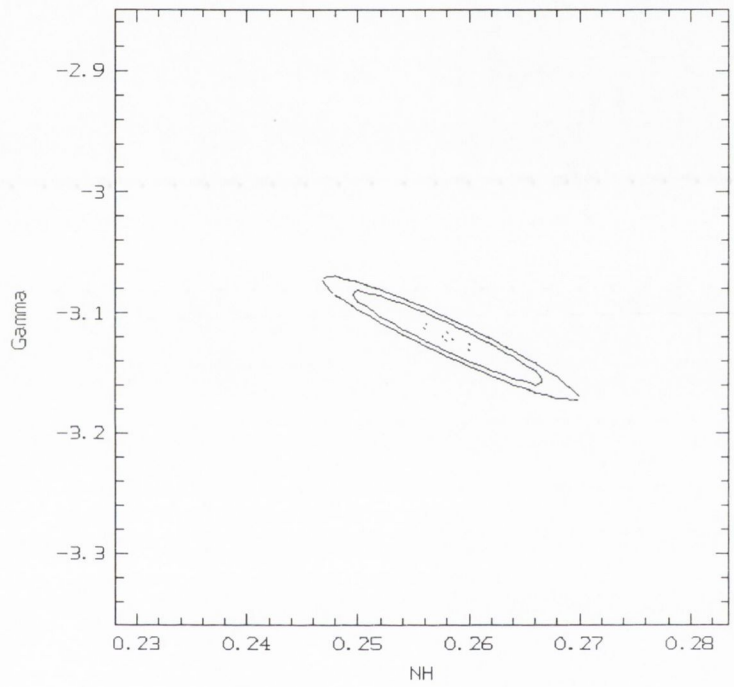


Figure 4.31: Contour plot of χ^2, for the galaxy NGC4051 as a function of the photon index Γ and the column density N_H for two confidence levels of 68.3 % and 94.5 %.

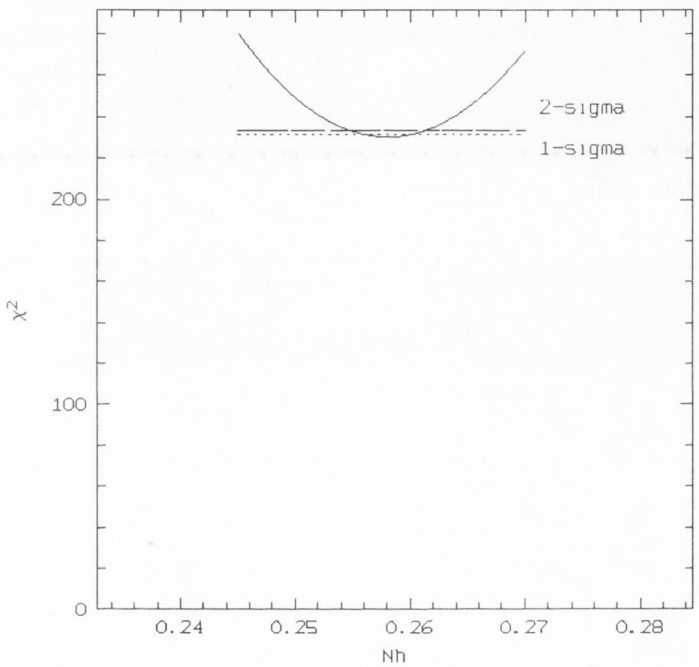


Figure 4.32: Contour plot of χ^2, for the galaxy NGC4051 as a function of the column density N_H for confidence levels of 68.3 % and 94.5 %.

dominates the emission from the galaxy. An active core may be modeled by a power-law model, thus HR's from these galaxies may be used to place limits on Γ and N_H by using our power-law grid. Voids A and C both show strong evidence of a difference in observed N_H at the front and back, and by extension evidence of processed gas present in these two voids. The case for Void B is more complicated, where more absorption is observed at the front of the void. There are several problems with void B. Firstly the sample consists of 12 galaxies, with only 3 at the back of the void. Secondly five of the galaxies at the front of the void (see Figure 4.7) form part of a high density wall. Photons from these galaxies must pass along the wall before reaching us and may be absorbed by dense material in the wall. Additional material is detected along this sight line than with the line of sight to the back of the void. On analyzing the values of HR1 we find that HR1 increases with distance from us along this line of sight. This is consistent with the theories of Icke & Van de Weygaert (1989), i.e that material collects and flows along the cell walls. This is the reason we observe more absorption in the galaxies at the front of the void. The case for Voids A and C is much simpler. Most of the galaxies located on the near/far side of these voids are observed through a clear line of sight i.e. we do not have to look along walls to observe them. This of course is a major problem when using observations from the archives, the observers has no control over the postions of the objects but must use what is available.

Comparing the values produced from our grid with the 4 observations with sufficient counts for fitting spectra we find that two (NGC 4051 and NGC 3786) spectral fits are in excellent agreement with the values derived from our simulated grid. The other two observations (NGC 4151 and NGC 4253) are not well fitted by simple power law models and require more complex models (such as a warm absorber model), thus the values of N_H derived from our grid may not be particularly accurate (nevertheless our value of N_H for NGC4253 is in good agreement with the value of N_H derived by Molendi 1994. Both of these galaxies are bright Seyfert galaxies (chosen for spectral analysis because of their large number of counts) and are not representative of the sample as a whole. Still the problem remains that many galaxies in our sample are not perfectly described by a simple power law model. Our method despite

several assumptions works well as a first order approximation and we do find strong evidence of processed gas in two of the three voids examined. This simple power-law approximation is necessary if we are to use a grid approach. We conclude that by using an approximation of a simple power-law model we are able to glean spectral information from objects in the ROSAT PSPC archive.

Finally the extraction radius of 160 sky pixels, the soft photons are only complete to 88 % (Brinkmann 1994). This may effect our values of HR1.

Chapter 5

Clusters of Galaxies

5.1 Introduction

Clusters of galaxies, as the largest virialised objects in the Universe with X-ray emission originating from hot ($T \geq 10^7$K) intra cluster gas, offer a means of probing the formation of structure and constraining the fundamental cosmological parameters governing its evolution. Therefore it is of interest to determine their basic physical properties, such as temperature of the intra cluster gas, size, mass, etc. Because of the high gas temperature, observations at X-rays are especially appropriate. Constraints on structure formation models may be obtained from physical cluster parameters using scaling relations such as the X-ray luminosity-temperature relation.

Temperatures of the gas pervading clusters of galaxies are known to be high, of the order of several keV. In particular recent work with the ASCA X-ray satellite has suggested that temperatures of 6-10 keV are ubiquitous (Markevitch et al. 1998). The luminosity-temperature relation may be used to estimate the temperature once the luminosity has been derived on the basis of a first guess for the temperature. This relation has been calibrated by, amongst others, the WARPS consortium (Wide Angle ROSAT Pointed Survey ,Fairley et al. 2000). It is particularly valuable, however, to determine the gas temperatures directly, by means of spectral modeling of X-ray data.

The galaxy clusters of the Einstein Observatory Extended Medium Sensitivity Survey (EMSS) have been selected from a flux limited and homogeneous sample of 835 serendipitous sources detected in 1435 Einstein IPC

pointed observations with centres directed away from the galactic plane ($|b|$ $\geq$ 20°). The EMSS sample is the product of an automatic detection procedure on the Einstein IPC broad band data (0.3 - 3.5 keV), using a detection cell of $2.4' \times 2.4'$. More information on this X-ray survey may be found in (Gioia et al. 1990). The cluster subsample is limited to clusters with declinations $\geq -40°$ and fluxes in the detection cell $\geq 1.33 \times 10^{-13} erg\ s^{-1} cm^{-2}$. The EMSS cluster sample is the most established catalogue of X-ray clusters out to $z \approx 0.5$ and contains 97 objects. This sample has been examined in detail in the optical and many of its sources are now considered secure identifications (Gioia et al. 1990; Stocke et al. 1991)

In this chapter we study the set of 22 EMSS clusters for which ROSAT PSPC observations are available, with the aim of extracting spectral information and in particular intra-cluster gas temperatures. The z > 0.14 part of this EMSS cluster subsample has also been studied by Nichol et al. (1997) (hereafter N97), and about half of them by Ellis & Jones (Ellis & Jones 2001). The PSPC spectral information however was not fully exploited in these papers. N97 make no attempt to measure the temperatures of the clusters but adopt a temperature of 6keV for all of the galaxy clusters. They also assume for every cluster a King profile with slope parameter $\beta = \frac{2}{3}$ and core radius r_c=250 kpc. They exclude MS1208.7+3928 which has since been found to be a cluster (Stocke et al. 1999), while two clusters (MS1333.3+1725 and MS1610.4+6616) which they include have since been found not to be clusters (Ellis & Jones 2001). They also do not include the three z < 0.14 clusters that are among the set of 22. Ellis & Jones use measured ASCA temperatures for all but one of their sample of 11 EMSS clusters. They derive values for the core radius assuming β=$\frac{2}{3}$. In order to investigate the spectral information offered by the ROSAT PSPC observations, we analyze the complete subset of 22 clusters and determine temperatures, fluxes and luminosities, as well as brightness profiles.

In Section 2 we discuss the sample used in this work. In Section 3 we describe the data analysis. In Section 4 we simulate a grid of Hardness Ratio values, which is used to extract values of N_H and temperature for all of the galaxy clusters in our sample and compare with the results from spectral fits for some well observed clusters. In Section 5 we fit our data to an

isothermal β model and compare our values for β and r_c with those available in the literature; we also examine the correlation between the values of β and core radius for the 23 clusters in our sample. In Section 6 we compare our work with other ROSAT work on the sample. In Section 7 we compare ROSAT temperatures against ASCA temperatures for clusters which have been observed with both satellites. The ASCA results have been determined in a wider and harder energy window (2-10 keV) than was the case for ROSAT (0.1-2.4 keV). In Section 8 we summarize our results and draw some general conclusions.

5.2 The Sample

In Table 5.1 the 22 clusters from the EMSS for which ROSAT PSPC observations are available. Besides the three clusters noted above and three clusters with $z \leq 0.14$, there are three further differences with the list in N97 (their Table 1). For MS1231.3+1542 we don't detect anything (N97 only detect 15 counts), and MS 1209.0+3917 has since been designated a BL-Lac (Rector et al. 1998) as has MS1219.9+7542 (Rector et al. 2000).

Figure 5.1 shows the distribution of redshifts in our sample. The clusters have redshifts in the range 0.046-0.55, and the distribution is peaked around z=0.35. Figure 5.2 shows the distribution of ROSAT PSPC counts for our sample (see Section 3). We detect counts in the range 58-22251, where 10 of our sample have less than 600 counts (so the results from a spectral fit may be unreliable); the other 12 clusters have more than 800 counts allowing us to produce spectral fits.

5.2.1 A Summary of X-ray Observations of the Sample.

As indicated in Table 5.1, 6 of our clusters have also been observed with the ROSAT HRI, 10 with ASCA,1 with Chandra and 1 by XMM. The ASCA temperatures are discussed in Section 5.5 and the other observations are noted in Appendix A.

Name (1)	HRI (2)	ASCA (3)	Chandra (4)	XMM (5)
MS0015.9+1609	x	x	o	o
MS0353.6-3642	o	x	o	o
MS0418.3-3844	o	o	o	o
MS0451.5+0250	x	x	o	o
MS0451.6-0305	x	x	o	o
MS0735.6+7421	x	o	o	o
MS0811.6+6301	o	x	o	o
MS1020.7+6820	o	o	o	o
MS1111.8-3754	o	o	o	o
MS1201.5+2824	o	o	o	o
MS1208.7+3928	o	o	o	o
MS1308.8+3244	o	o	o	o

Name (1)	HRI (2)	ASCA (3)	Chandra (4)	XMM (5)
MS1335.2-2928	o	o	o	o
MS1358.4+6245	x	x	x	o
MS1426.4+0158	o	x	o	o
MS1512.4+3647	x	x	o	o
MS1546.1+1132	o	o	o	o
MS1617.1+3237	o	o	o	o
MS2137.3-2353	o	x	o	o
MS2255.7+2039	o	o	o	o
MS2311.2-4259	o	o	o	x
MS2354.4-3502	o	x	o	o

Table 5.1: X-ray observations for our sample other than ROSAT PSPC and Einstein. An x indicates that the cluster has been observed by the instrument listed, and an o indicates if not. EMSS name (1), ROSAT HRI (2), ASCA (3), Chandra (4) and XMM(5).

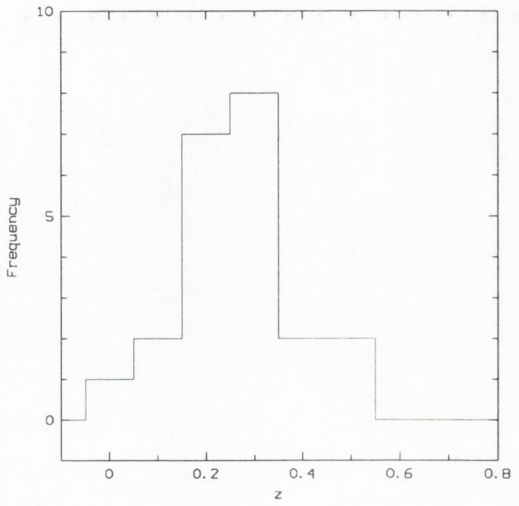


Figure 5.1: Frequency distribution of redshifts for the cluster sample in this paper (with bin size =0.1).

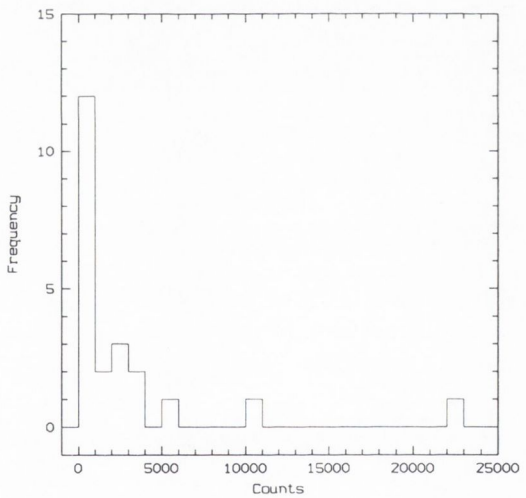


Figure 5.2: Histogram of the net 0.1-2.4keV counts for each cluster in our sample (with bin size=1000 counts.)

5.3 X-ray Data Reduction

5.3.1 Preparation of Images

The ROSAT PSPC data were analyzed using the EXSAS/MIDAS data reduction package (Zimmermann et al. 1992), with corrections for bad times

and vignetting. Images are created in the 0.2-2.35 keV energy range, binned in 15" pixels. A source detection is carried out on the PSPC images which produces a list of sources with a maximum likelihood of ≥ 10. Their coordinates are compared with the target list of EMSS clusters and only those detections with an offset less than 2' are accepted. (The mean and standard deviation of the background are calculated by selecting a large source free circular region, as near as possible to the cluster extraction circle. The net counts remaining after background subtraction are listed in Table 5.2.) Contour plots are produced for each cluster from images smoothed with a Gaussian filter. We maximize the cluster extraction area by including all the photons within a contour drawn at 2-σ above the background. Any detected sources that fall within the 2-σ extraction radius are checked against the NED and SIMBAD databases. Those which have an identification with a redshift different from that of the galaxy cluster are removed. The remaining photons in the cleaned events table are then used and the total number of cluster counts can be determined.

5.3.2 Spectral Analysis and Flux Calculation

To estimate temperatures and fluxes we perform spectral fits for all the galaxy clusters in our sample with more than 800 counts. As it is accepted that X-ray emission from galaxy clusters originates from a hot optically thin plasma, we fit the data with a Raymond-Smith model (Raymond & Smith 1977). The column density N_H is either fixed to the galactic value (Dickey & Lockman 1990) or a value greater than galactic, and a metallicity of 0.3 $Z_\odot$ is assumed throughout. The error ranges for the derived values of N_H and T are determined from plots of the χ^2 distribution for these two parameters by fitting N_H and T together . Fixing N_H subsequently to either the galactic value or a higher than galactic value (as may have been concluded from the χ^2 distributions), next only the temperature is fitted (which normally leads to higher accuracy for T than when fitting temperature and N_H concurrently) and a 1 dimensional χ^2 plot is produced for the error range relevant to this temperature value. As an illustration of this procedure, Figures 5.3-5.5 show a contour plot, a 2-D χ^2 plot and a 1-D χ^2 plot for the

cluster MS0015.9+1609. The flux is calculated with W3 Pimms [1], using temperatures from our 1-D χ^2 plots, the N_H as adopted from the 2-D χ^2 plots, and a metallicity of 0.3 $Z_\odot$. PIMMS does not allow a metallicity 0.3 $Z_\odot$ so we calculate fluxes for 0.2 $Z_\odot$ and 0.4 $Z_\odot$ and interpolate. The fluxes are then k-corrected and the luminosities are calculated assuming distances to the clusters derived from their redshifts;

$$d = \frac{c}{H_0}[z + \frac{1}{2}(1 - q_0)z^2] \tag{5.1}$$

(Coles & Lucchin 1995), where we take H_0= 50 km $s^{-1}Mpc^{-1}$ and q_0= 0.5 (to be consistent with N97 and previous work) and redshifts from the NED.

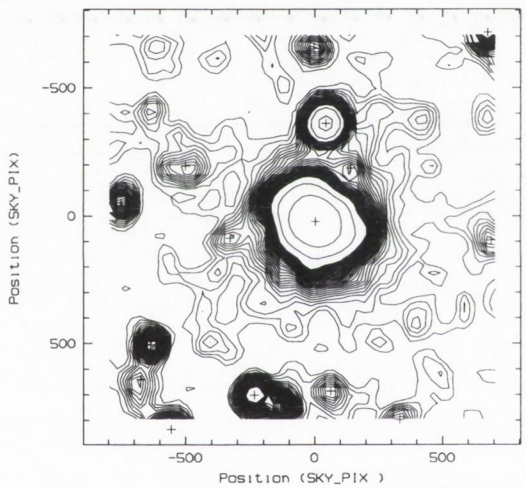


Figure 5.3: Contour plot for the cluster MS0015.9+ 1609 . The PSPC image has 5″ × 5″ pixels and is smoothed with a 3-pixel size Gaussian. Detected sources are indicated with + signs.

In Table 5.2 we list the derived count rate, N_H, temperature, flux and luminosity for the 22 clusters in our sample We have compared the values

[1] http://heasarc.gsfc.nasa.gov/Tools/w3pimms.html

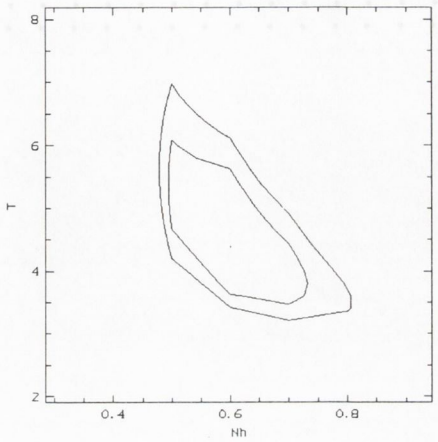


Figure 5.4: Contour plot of χ^2, for the cluster MS0015.9+1609 as a function of the temperature (in keV) and the column density N_H (in $10^{21} cm^{-2}$) for two confidence levels of 68.3 % and 94.5 % .

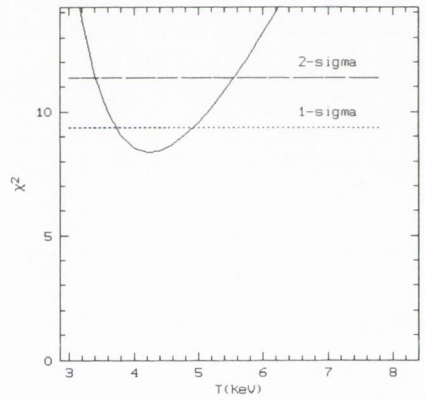


Figure 5.5: Contour plot of χ^2, for the cluster MS0015.9+1609 as a function of temperature in keV, keeping N_H fixed 0.6 $\times 10^{21} cm^{-2}$, for two confidence levels of 68.3 % and 94.5 %.

reported in Table 2 with temperature determinations obtained with other instruments; this will be commented upon in Section 5.5.

5.3.3 X-ray Brightness Profiles

We have also analyzed the spatial distribution of the X-ray emission from the EMSS galaxy clusters. To obtain an approximate description of the X-

ray surface brightness distribution we have fitted to this distribution the Isothermal β-model (Jones & Forman 1984); (Neumann & Boehringer 1997) which gives the surface brightness $S(r)$ of a galaxy cluster assuming spherical symmetry

$$S(r) = S_0[1 + (\frac{r^2}{r_c^2})]^{-3\beta+1/2} + B \tag{5.2}$$

In this expression $S(r)$ is the brightness as a function of the radius,r. S_0 is the central intensity at $r = 0$, r_c represents the core radius, B is the background intensity and β a slope parameter of the radial brightness distribution. We fit this model to the brightness distribution into the background level. In some cases the galaxy cluster may contain an additional source (usually point like) in the centre significantly reducing the quality of the fit. For each cluster we fit therefore our model with the centre intact cq. removed and select the best fit. In Figure 5.6 we show our isothermal β model fit to the radial brightness distribution of the galaxy cluster MS0015.9+1609. We measure β=$0.82^{+0.03}_{-0.03}$ and a r_c of $52''^{+1'}_{-4'}$, in excellent agreement with the values obtained by Neumann & Böhringer (1997)(β=$0.80^{+0.09}_{-0.07}$,r_c = $50''^{+8.4'}_{-7.1'}$) for this cluster with the same data. Of the 7 clusters for which we remove the centre, all show a central excess which may be evidence of a cooling flow. For these 7 clusters we extrapolate the cluster emission (using the values of β and r_c derived) to the centre and subtract it from the total emission. We get an excess emission which varies between 0.4 % and 21 %. The fit results for all 22 of the EMSS clusters considered are presented in Table 5.2. In the "column cut radius" we estimate the size of the inner part of the cluster affected by the cooling flow. For MS0735.6+7421 we estimate a cut radius of 20 " in good agreement with a value of 15 " derived by Donahue & Stocke (1995). We derive cut radii of 10 and 50 " for clusters MS1358.4+6245 and MS1512.4+3647 respectively, these values differ for the values derived by Lewis et al. (1999) (30 and 10 arcseconds respectively N.B fixing β =2/3).

5.3.4 Simulation of Hardness Ratios

For the clusters with less than 600 photons spectral fits are not very reliable(we have no clusters with 600-850 counts giving a natural break between observations with low and high counts). As an alternative to spectra we

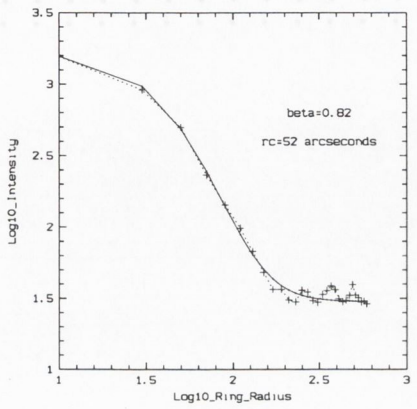


Figure 5.6: Isothermal β model fitted to the radial profile of the cluster MS0015.9+ 1609 .

have calculated hardness ratios, that compare the photon counts in selected bands of the spectra. HR1 and HR2 are defined as above.

Figure 5.13 (Section 4.1) shows a plot of hardness ratios for our selection of clusters. All of the clusters occupy a small area of the plot, namely $0 \leq HR1 \leq 1$ and $0 \leq HR2 \leq 0.5$, which is consistent with ROSAT All Sky Survey bright source Abell clusters (Voges et al. 1999). The hardness ratios of clusters with poor statistics may be used to set limits on spectral parameters.

For clusters with less than 600 photons we need to use hardness ratios to determine the spectral parameters N_H and T. To achieve this, spectra are simulated for Raymond-Smith models with a range of values of absorbing N_H (0.05 - $1.25\times10^{20}cm^{-2}$, in steps of $0.05\times10^{20}cm^{-2}$), T (0.2 - 2keV in steps of 0.2 keV and 2-15 keV in steps of 1keV) and redshift (0.0 - 0.8 in steps of 0.2). Hardness ratios are then calculated using these simulated spectra to give a grid of 3125 (N_H,T, z) points in a HR1 versus HR2 diagram. The modeling was performed employing EXSAS. To establish an average HR1, HR2 for each combination of (N_H,T,z) our simulations are run 100 times for 100,000 counts, each time using a different seed in the random number generator. To illustrate the relation between hardness ratio and N_H we show a plot of N_H against the average simulated HR1. From Figure 5.8 we can see that the value of N_H has a large effect on the value of HR1.

EMSS Name (1)	Right . Asc (2)	Dec. (3)	z (4)	Net Cts (5)	Net CR (6)	Ext Rad (7)	N_H Gal (8)	N_H Fit (9)	Red χ^2 (10)	T (keV) (11)	F_x (12)	L_x (13)	Notes (14)
MS0015.9+1609	04.62	16.43	0.547	3989	0.095	600	0.407	$0.6^{+0.13}_{-0.11}$	1.01	$4.5^{+0.75}_{-0.5}$	$22.47^{+0.36}_{-0.35}$	$47.78^{+0.38}_{-0.76}$	1
MS0353.6-3642	58.86	-36.57	0.320	173	0.09	350	0.121	0.121	0.98	$1.6^{+0.3}_{-0.2}$	$14.68^{+1.12}_{-1.12}$	$9.59^{+0.46}_{-0.73}$	2
MS0418.3-3844	65.0139	-38.62	0.35	230	0.021	350	0.207	0.207	1.57	$0.91^{+0.34}_{-0.03}$	$3.31^{+0.21}_{-0.22}$	$3.03^{+0.10}_{-0.20}$	3
MS0451.5+0250	73.53	2.91	0.201	1585	0.335	0.78	0.78	0.78	0.84	$4.6^{+1.4}_{-1.1}$	$79.13^{+1.99}_{-1.99}$	$16.72^{+0.21}_{-0.42}$	4
MS0451.6-0305	73.53	-3.00	0.539	1586	0.102	420	0.437	0.437	1.55	$3.75^{+0.5}_{-0.25}$	$22.21^{+0.56}_{-0.56}$	$46.17^{+0.58}_{-1.21}$	5
MS0735.6+7421	115.44	74.23	0.216	2586	0.304	700	0.348	0.348	0.70	$2.85^{+0.4}_{-0.3}$	$56.64^{+1.12}_{-1.12}$	$14.35^{+0.13}_{-0.28}$	6
MS0811.6+6301	123.95	62.86	0.312	124	0.02	400	0.428	0.428	1.40	$1.16^{+0.33}_{-0.03}$	$3.73^{+0.33}_{-0.33}$	$2.41^{+0.11}_{-0.22}$	7
MS1020.7+6820	156.10	68.08	0.203	595	0.046	550	0.244	0.244	1.26	$1.22^{+2.74}_{-0.1}$	$11.11^{+0.45}_{-0.46}$	$2.60^{+0.06}_{-0.11}$	8
MS1111.8-3754	168.57	-38.18	0.129	5771	0.312	700	0.915	0.915	1.32	$6^{+1}_{-0.5}$	$75.01^{+0.99}_{-0.99}$	$60.37^{+0.40}_{-0.80}$	9

EMSS Name (1)	Right . Asc (2)	Dec. (3)	z (4)	Net Cts (5)	Net CR (6)	Ext Rad (7)	N_H Gal (8)	N_H Fit (9)	Red χ^2 (10)	T (keV) (11)	F_x (12)	L_x (13)	Notes (14)
MS1201.5+2824	181.01	28.12	0.167	3875	0.155	800	0.168	$0.24^{+0.1}_{-0.06}$	0.64	$1.8^{+0.4}_{-0.2}$	$25.11^{+0.41}_{-0.40}$	$3.68^{+0.03}_{-0.06}$	10
MS1208.7+3928	182.81	39.19	0.34	988	0.028	430	0.193	0.193	1.22	$1^{+0.1}_{-0.1}$	$4.33^{+0.14}_{-0.14}$	$3.70^{+0.06}_{-0.12}$	11
MS1308.8+3244	197.79	32.46	0.245	438	0.054	280	0.111	0.111	1.16	$1.41^{+1.1}_{-1.0}$	$7.52^{+0.36}_{-0.36}$	$2.69^{+0.07}_{-0.13}$	12
MS1335.2-2928	204.51	-29.72	0.189	858	0.038	650	0.373	0.373	1.60	$3.6^{+10.0}_{-1.2}$	$7.22^{+0.25}_{-0.25}$	$1.34^{+0.03}_{-0.04}$	13
MS1358.4+6245	209.97	62.51	0.327	2486	0.112	450	0.193	$0.22^{+0.03}_{-0.03}$	0.77	$3^{+0.5}_{-0.3}$	$19.04^{+0.37}_{-0.37}$	$12.25^{+0.12}_{-0.25}$	14
MS1426.4+0158	217.25	1.74	0.320	235	0.038	400	0.275	0.275	0.58	$2.11^{+2.33}_{-0.53}$	$6.77^{+0.43}_{-0.43}$	$4.26^{+0.13}_{-0.27}$	15
MS1512.4+3647	228.59	36.60	0.373	239	0.047	500	0.138	$0.26^{+0.13}_{-0.08}$	0.59	$1.29^{+0.17}_{-0.09}$	$7.97^{+0.52}_{-0.52}$	$7.71^{+0.25}_{-0.50}$	16
MS1546.1+1132	237.31	11.39	0.226	58	0.014	200	0.361	0.361	1.35	$1.22^{+0.37}_{-0.4}$	$2.45^{+0.32}_{-0.33}$	$0.75^{+0.06}_{-0.09}$	17
MS1617.1+3237	244.76	32.50	0.274	196	0.02	250	0.192	0.192	0.20	$1.43^{+0.35}_{-0.08}$	$3.09^{+0.22}_{-0.22}$	$1.43^{+0.06}_{-0.10}$	18
MS2137.3-2353	325.04	-23.66	.313	2140	0.215	450	0.355	0.355	0.07	$2^{+0.2}_{-0.2}$	$40.57^{+0.86}_{-0.88}$	$24.43^{+0.26}_{-0.53}$	19
MS2255.7+2039	344.53	20.92	0.288	409	0.034	330	0.53	0.53	0.64	$1.42^{+0.13}_{-0.16}$	$6.91^{+0.33}_{-0.34}$	$3.61^{+0.09}_{-0.18}$	20
MS2311.2-4259	348.50	-42.73	0.058	22551	1.755	900	0.176	0.176	1.22	$2.5^{+0.1}_{-0.1}$	$259.70^{+1.70}_{-1.70}$	$4.01^{+0.01}_{-0.03}$	21

EMSS Name (1)	Right . Asc (2)	Dec. (3)	z (4)	Net Cts (5)	Net CR (6)	Ext Rad (7)	N_H Gal (8)	N_H Fit (9)	Red χ^2 (10)	T (keV) (11)	F_x (12)	L_x (13)	Notes (14)
MS2255.7+2039	344.53	20.92	0.288	409	0.034	330	0.53	0.53	0.64	$1.42^{+0.13}_{-0.16}$	$6.91^{+0.33}_{-0.34}$	$3.61^{+0.09}_{-0.18}$	20
MS2311.2-4259	348.50	-42.73	0.058	22551	1.755	900	0.176	0.176	1.22	$2.5^{+0.1}_{-0.1}$	$259.70^{+1.70}_{-1.70}$	$4.01^{+0.01}_{-0.03}$	21
MS2354.4-3502	359.25	34.76	0.046	10394	1.91	1100	0.11	0.12	1.96	$3.7^{+0.5}_{-0.4}$	$264.75^{+2.60}_{-2.60}$	$2.29^{+0.01}_{-0.03}$	22

Table 5.2: Table of temperature, flux and luminosity for the 22 galaxy clusters in our sample. In column (1) the EMSS cluster name, (2)the Right Ascension in degrees,(3) the Declination in degrees (both from the EMSS catalogue) (4)the redshift, (5) the total number of counts after correcting for the background, (6) the net count rate, (7) the extraction radius in arcseconds, (8) the galactic value of N_H in units of 10^{21} cm^{-2} ,(9) the value of N_H determined from the spectral fit (or from the simulated hardness ratio grid for clusters with less than 600 counts) and used to estimate the temperature, flux and luminosity. If the N_H returned is less than or agrees within errors with the galactic value then we take the galactic value. (10) the reduced χ^2 of the Raymond-Smith model fitted to the observed spectrum, (11) the temperature in keV as determined from the 1 dimensional χ^2 plot after fixing N_H to the value determined from the 2 dimensional χ^2 fit(simulated HR grid for less than 600 cts) or the galactic value if the fitted N_H is less than galactic(the temperature in keV as derived from the simulated hardness ratio grid for clusters with less than 600 counts) (12) the flux in units of 10^{-13} ergs $s^{-1}cm^{-2}$ in the range 0.1-2.4 keV, (13) the luminosity (k-corrected) in units of 10^{44} ergs s^{-1} in the range 0.1-2.4 KeV (for q_0 =0.5) (14) notes on individual clusters (previous observations etc; for details see Appendix A & B.)Note: 12 of the 22 galaxy clusters have 800 counts enabling us to perform spectral fits. NB. The galaxy clusters MS1020.7+6820 and MS2255.7+2039 the upper limit on N_H is unconstrained.

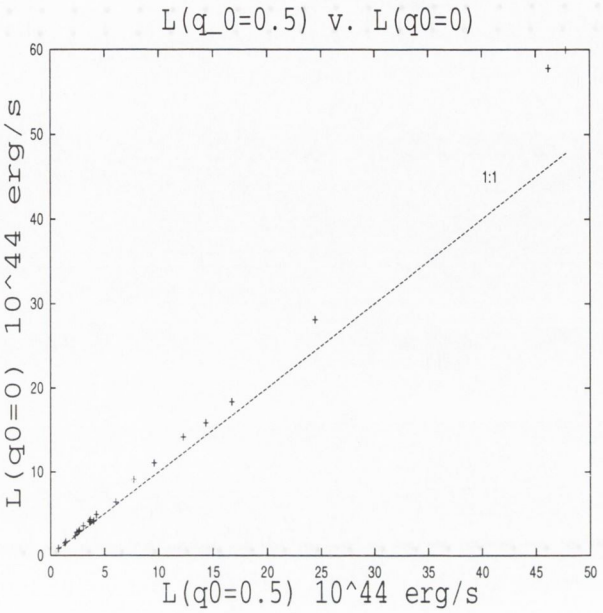


Figure 5.7: We plot the effect of q_0 on the value of the luminosity. With q_0=0 we record luminosities $\approx$ 25% higher.

Thus HR1 may be used as a diagnostic for determining N_H. From a similar plot we find that N_H has only a small effect on the value of HR2.

To illustrate the relation between hardness ratio and temperature we show plots of temperature against average simulated HR1 and HR2 in Figures 5.9 and 5.10. Temperature has very little effect on HR1 except for $T \leq 0.5$ keV, but decreasing the temperature below 2 keV has a large effect on HR2. In Figure 5.9 on going below 2 keV there is some wrapping in the values of HR1 for a given value of N_H, this is only a small effect and doesn't affect our derivation of temperatures.Thus particularly HR2 may be used to identify low temperature (T $\lesssim$ 2 keV) clusters. We also find from our simulations that redshift has very little effect on the values of HR1 and HR2. The resulting grid (including all of the redshift values z=0, 0.2, 0.4, 0.6 and 0.8) can now be used to convert hardness ratio grid points into (N_H,T) values for T in the range 0.2-15 keV and N_H=0.05-1.25 $\times 10^{21} cm^{-2}$ (the cluster redshifts are known). The portion of the grid corresponding to T $\geq$ 2 keV and z = 0.4 is shown in Figure 5.11. Values of the grid wrap around each other on going from T > 2 keV to T$\leq$ 2 keV so for illustrative purposes we show the grid in two separate portions in Figures 5.11 and 12.

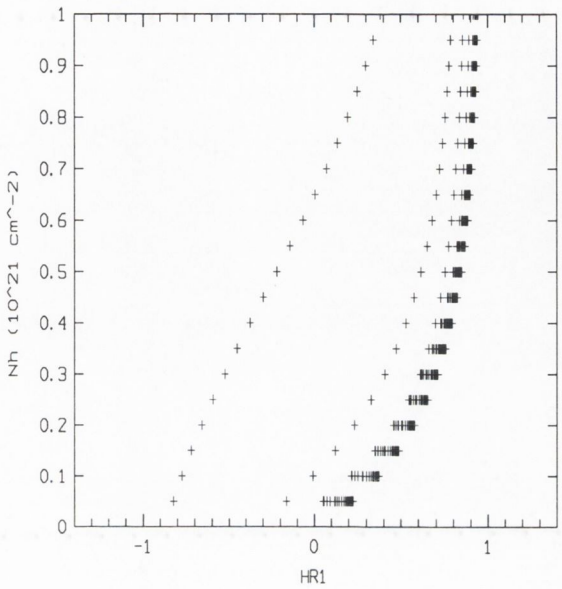


Figure 5.8: Spectral simulation of 100,000 cts, for T=0.2-1.8keV in steps of 0.2keV, T=2-15keV in steps of 1 keV, N_H=0.05-1.25 $\times 10^{21} cm^{-2}$ and z=0.4. We plot the average simulated value of HR1 against N_H derived from 100 simulations. The standard deviation of these values is smaller than the crosses. Temperature increases on going from left to right.

5.3.5 Application of the Simulated Grid

To test the reliability of our grid, we use it to calculate N_H and T from the observed hardness ratios for galaxy clusters with good statistics (more than 800 counts) and compare with the N_H and T derived from the spectral fits (see Section 3.2). For an observed pair of hardness ratios (HR1,HR2) at redshift z we interpolate values of N_H and T from the (N_H,T, z) grid. The values thus read off from the grid are in excellent agreement with the values obtained with the spectral fits; the results are in Tables 5.3.5 and 5.3.5. For clusters with less than 600 counts we use these grids to determine N_H and T, taking the errors on HR1 and HR2 into account by reading off (N_H,T) values also for their $\pm 1\sigma$ deviations. The results for these clusters are in Table 5.2.

EMSS Name	2D N_H Interval	2D N_H B. fit	Grid N_H	Grid B. fit	Gal N_H	T (fit)	Cts	No.
(1)	(2)	(3)	(4)	(5)	(6)	(7)	(8)	(9)
MS0015.9+1609	0.45-0.6	0.5	0.5-0.69	0.56	0.407	$4.5^{+0.75}_{-0.5}$	3989	1
MS0451.5+0250	0.3-0.45	0.4	0.25-0.51	0.3	0.78	$4.6^{+1.4}_{-1.1}$	1585	4
MS0451.6-0305	0.19-0.32	0.2	0.29-0.38	0.38	0.437	$3.75^{+0.5}_{-0.25}$	1586	5
MS0735.6+7421	0.19-0.25	0.22	0.18-0.40	0.19	0.348	$4.1^{+0.7}_{-0.5}$	2586	6
MS1111.8-3753	0.85-1.35	1.1	0.6-0.8	0.68	0.915	7^{+1}_{-1}	18490	8
MS1201.5+2824	0.08-0.15	0.1	0.08-0.13	0.09	0.168	$2.5^{+0.5}_{-0.4}$	3875	10
MS1208.7+3928	0.3-2	0.6	0.45-0.86	0.63	0.193	$3.4^{+1.2}_{-0.9}$	988	11
MS1335.2-2928	0.3-3	0.7	0.17-0.51	0.32	0.3	$3.6^{+4.0}_{-1.2}$	858	13
MS1358.4+6245	0.19-0.25	0.22	0.14-0.49	0.17	0.193	$2.7^{+0.3}_{-0.3}$	2486	14
MS2137.3-2353	0.3-0.41	0.4	0.25-0.41	0.32	0.355	$1.9^{+0.15}_{-0.15}$	2140	19
MS2311.2 -4259	0.09-0.1	0.9	0.05-1.2	0.06	0.176	$2.5^{+0.1}_{-0.1}$	22551	21
MS2354.4 -3502	0.08-0.095	0.09	0.1-0.14	0.14	0.11	$2.9^{+0.1}_{-0.1}$	10394	22

Table 5.3: Table of N_H derived from 2-D χ^2 plots compared with values of N_H derived from our simulated grid. Col(2) the 1 σ interval of N_H derived from the 2-D χ^2 plot of Temperature v N_H Col (3), the best fit value of N_H derived from the 2-D χ^2 plot of Temperature v N_H, Col (4) the limits on N_H as derived from the simulated grid. Col(5) the best fit value of N_H as derived from the simulated grid. Col(6) is the galactic N_H and Col (7) the Temperature extracted from 1-D χ^2 plots. Col(8) the number of counts and Col (9) notes on the galaxy cluster.

EMSS Name (1)	1D T Int. (2)	1D T (3)	2D T B. fit (4)	2D T Interval (5)	Grid B. fit (6)	Grid Int. (7)	Cts (8)	No. (9)
MS0015.9+1609	4.5	4-5.25	4.5	3.5-6	1.96	1.6-3.7	3989	1
MS0451.5+0250	4.6	3.5-6.0	8	4.7-20	1.48	1.2-4.4	1585	4
MS0451.6-0305	3.75	3.5-4.25	7.5	3.8-20	2.2	1.6-4.9	1586	5
MS0735.6+7421	4.1	3.6-4.8	2.2	1.8-3.6	1.2	1.16-1.6	2586	6
MS1111.8-3753	7	6-8	7	4-10	1.4	0.9-1.6	18490	8
MS1201.5+2824	2.5	2.1-3.0	1.8	1.55-2.53	1.08	0.5-1.25	3875	10
MS1208.7+3928	3.4	2.5-3.6	1	0.7-1.8	1.77	1.22-2.1	988	11
MS1335.2-2928	3.6	2.2-7.6	7	1-20	2.2	1-16	858	13
MS1358.4+6245	2.7	2.4-3.0	3	2.5-3.95	2.2	1.02-4.5	2486	14
MS2137.3-2353	1.9	1.75-2.05	1.95	1.75-2.3	1.26	1.1-1.5	2140	19
MS2311.2 -4259	2.5	2.4-2.6	3.4	3.2-3.65	8.5	1.5-13	22551	21
MS2354.4 -3502	2.9	2.8-3.0	3.6	2.92-4.5	0.9	0.3-1.6	10394	22

Table 5.4: Table of T derived from 1-D χ^2 plots compared with values of T derived from our simulated grid. Col(2) the Temperature extracted from 1-D χ^2 plots Col(3) the 1 σ limits on T as derived from the 1-D χ^2 plot of Temperature.Col(4)the Temperature extracted from 2-D χ^2 plots Col(5)the 1 σlimits on T as derived from the 2-D χ^2 plot of Temperature Col(6) The best fit value of T from the simulated grid Col(7) the 1 σ errors on T as derived from the simulated grid Col(8) the number of counts and Col (9) Notes on the individual clusters, see Appendix A & B.

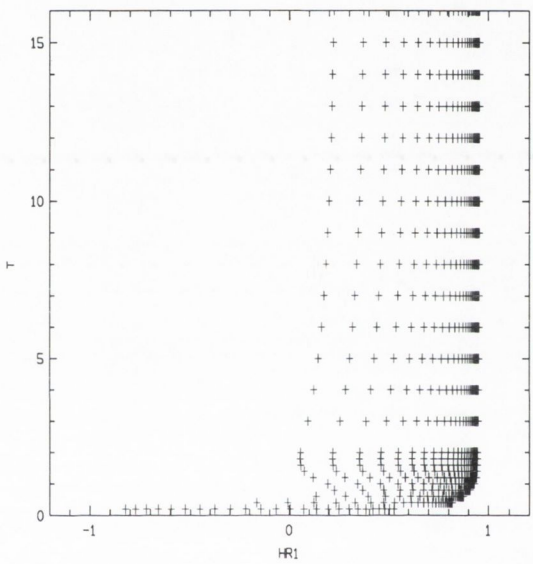


Figure 5.9: Spectral simulation of 100,000 cts, for T=0.2–2 keV in steps of 0.2 keV, T=2–15 keV in steps of 1keV, N_H=0.05 –1.25 $\times 10^{21} cm^{-2}$ in steps of 0.05 and z=0.4 . The mean simulated value of HR1 from 100 simulations is plotted against T . N_H increases from left to right.

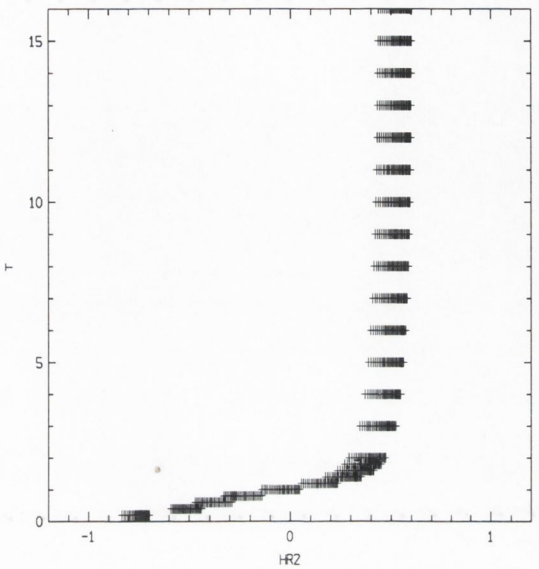


Figure 5.10: Spectral simulation of 100,000 cts, T=0.2-15KeV , N_H=0.05-1.25 $\times 10^{21} cm^{-2}$ and z=0.4. The mean simulated value of HR2, from 100 simulations, is plotted against T. N_H increases from left to right.

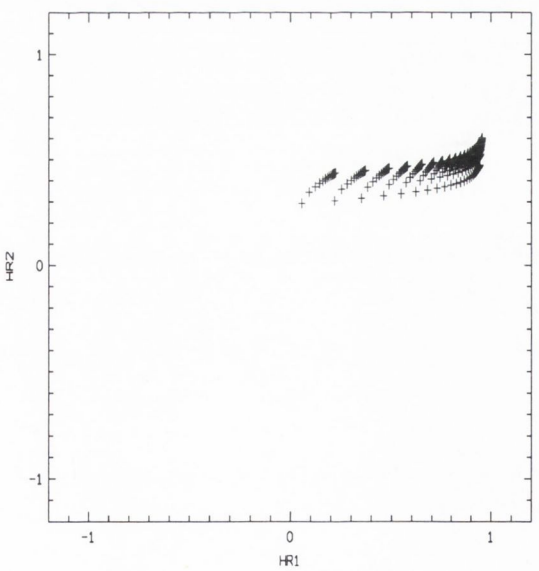


Figure 5.11: Grid at z=0.4, for T $\geq$ 2 keV in steps of 1 keV and N_H=0.05-1.2 $\times 10^{21} cm^{-2}$. T increases bottom to top and N_H increases left to right.

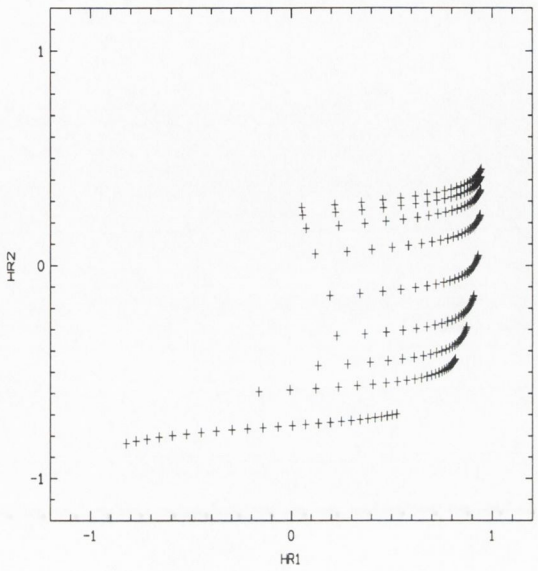


Figure 5.12: Grid at z=0.4, for T $\leq$ 2 keV in steps of 0.2 keV and N_H=0.05-1.2 $\times 10^{21} cm^{-2}$. T increases from bottom to top and N_H increases left to right.

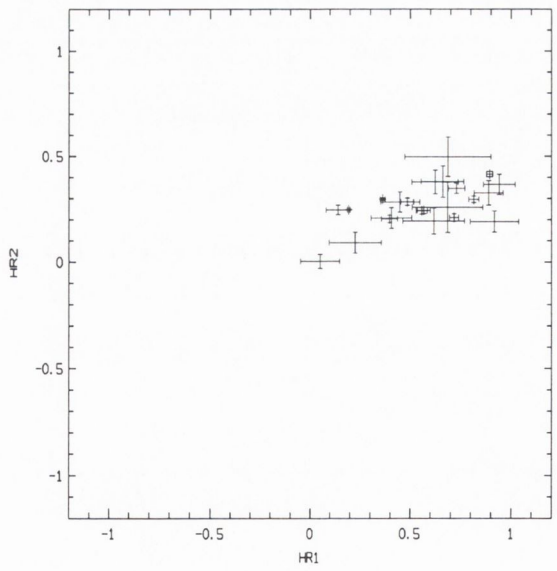


Figure 5.13: Observed values of HR1 and HR2, for the 23 EMSS clusters in our sample.

EMSS Name	β	R_c (")	Net Cts	Red χ^2	r_c (Kpc)	β lit	$R_c$lit	Cut rad	No.
(1)	(2)	(3)	(4)	(5)	(6)	(7)	(8)	(9)	10
MS0015.9+1609	$0.82^{+0.03}_{-0.03}$	52^{+1}_{-4}	3989	1.67	401^{+8}_{-32}	$0.81^{+0.09}_{-0.07}$	372^{+52}_{-62}	0	1
MS0353.6-3642	$0.78^{+0.06}_{-0.15}$	75.8^{+5}_{-25}	173	0.79	352^{+24}_{-116}		225^{+37}_{-31}*	10	2
MS0418.3-3844	$0.56^{+0.02}_{-0.02}$	127^{+48}_{-49}	230	0.77	646^{+244}_{-247}		474^{+92}_{-75}*	0	3
MS0451.5+0250	$0.61^{+0.03}_{-0.01}$	86^{+3}_{-7}	1585	1.3	251^{+9}_{-21}	$0.49^{+0.08}_{-0.08}$	100^{+50}_{-50}	0	4
MS0451.6-0305	$1.04^{+0.03}_{-0.16}$	58^{+2}_{-12}	1586	1.25	450^{+16}_{-94}	$0.92^{+0.11}_{-0.11}$	360^{+80}_{-80}	0	5
MS0735.6+7421	$0.80^{+0.03}_{-0.09}$	57^{+5}_{-16}	2586	0.98	179^{+16}_{-50}		234^{+40}_{-40}	20⋆	6
MS0811.6+6301	$0.67^{+0.05}_{-0.22}$	98^{+10}_{-50}	124	0.61	445^{+45}_{-182}		274^{+92}_{-75}*	0	7
MS1020.7+6820	$0.73^{+0.01}_{-0.27}$	50^{+1}_{-13}	595	1.24	147^{+3}_{-38}			0	8
MS1111.8-3753	$0.67^{+0.01}_{-0.06}$	83^{+5}_{-20}	5771	1.36	156^{+9}_{-38}			0⋆	9

EMSS Name	β	R_c (")	Net Cts	Red χ^2	r_c (Kpc)	β lit	$R_c$lit	Cut rad	No.
(1)	(2)	(3)	(4)	(5)	(6)	(7)	(8)	(9)	10
MS1201.5+2824	$0.51^{+0.02}_{-0.11}$	37^{+1}_{-19}	3875	1.59	89^{+3}_{-46}		14^{+4}_{-4}	0	10
MS1208.7+3928	$0.66^{+0.02}_{-0.36}$	53^{+1}_{-45}	988	1.11	262^{+5}_{-223}			15	11
MS1308.8+3244	$0.58^{+0.02}_{-0.08}$	32^{+2}_{-10}	440	0.91	114^{+7}_{-36}			0	12
MS1335.2-2928	$0.41^{+0.01}_{-0.1}$	131^{+10}_{-90}	1000	1.41	360^{+27}_{-250}			60	13
MS1358.4+6245	$0.87^{+0.07}_{-0.01}$	42^{+8}_{-1}	2678	1.99	199^{+39}_{-4}	$0.84^{+0.06}_{-0.06}$	133^{+21}_{-20} *	10⋆	14
MS1426.4+0158	$0.88^{+0.10}_{-0.33}$	129^{+5}_{-69}	235	0.61	600^{+23}_{-320}		302^{+43}_{-38}*	0	15
MS1512.4+3647	$0.55^{+0.04}_{-0.01}$	39^{+2}_{-10}	237	2.58	211^{+11}_{-54}	$0.55^{+0.04}_{-0.04}$	114^{+14}_{-14} *	50⋆	16
MS1546.1+1132	$0.76^{+0.55}_{-0.05}$	123^{+5}_{-100}	58	0.74	404^{+16}_{-330}			0	17

EMSS Name	β	R_c (")	Net Cts	Red χ^2	r_c (Kpc)	β lit	$R_c$lit	Cut rad	No.
(1)	(2)	(3)	(4)	(5)	(6)	(7)	(8)	(9)	10
MS1617.1+3237	$1.21^{+0.01}_{-0.25}$	84^{+1}_{-29}	196	0.62	334^{+4}_{-115}			0	18
MS2137.3-2353	$0.87^{+0.14}_{-0.01}$	25^{+14}_{-1}	2140	1.42	113^{+64}_{-4}		49^{+2}_{-3}	0	19
MS2255.7+2039	$0.66^{+0.1}_{-0.01}$	39^{+11}_{-1}	409	0.7	163^{+209}_{-4}			0	20
MS2311.2-4259	$0.63^{+0.06}_{-0.01}$	41^{+15}_{-1}	22551	2.21	35^{+12}_{-2}	$0.57^{+0.01}_{-0.01}$	37^{+3}_{-2}	0	21
MS2354.4-3502	$0.6^{+0.05}_{-0.02}$	86^{+2}_{-15}	10394	1.89	57^{+2}_{-10}	$0.58^{+0.02}_{-0.01}$	90^{+9}_{-8}	50	22

Table 5.5: Table of measured β and core radius for all the clusters in our sample.Col (3) the core radius in arcseconds, Col (4) the net number of counts available for each cluster,Col(5) is the reduced χ^2 of the fit to the isothermal β model, Col(6) is the core radius in Kpc, Col(7) is β as measured in the literature and (8) is the Core radius as measured from the literature in Kpc (except MS1201.5+2824 which is given in arcseconds), an $*$ indicates that r_c was calculated assuming β =2/3. References for r_c are given in Appendix B Col(9) is the cut radius in arcseconds to get the best fit (those marked with a $\star$ are known cooling flows c.f Appendix A for the references and Col (10) notes on individual clusters (see Appendix A). .

5.3.6 Difference between a zero redshift absorber and a redshifted absorber

In the analysis above we model the total absorption as being at z=0. To check if this affects our results we model a series of points with the absortion split between a zero redshift absorber (the galactic contribution) and a redshifted absorber (intrinsic absorption). For several values of HR1,HR2 we check if this effects the values of N_H we retrieve, for absorption at z=0.2,0.4, 0.6. To the level of accuracy of our grid we find no discernible difference.

5.3.7 Comparison of β and r_c Values with Results from the Literature

Fits to the brightness profiles of the clusters were derived in Section 5.3. In Appendix B we compare β and r_c with results from the literature where available, especially Lewis et al.(1999) and Ellis & Jones (2001) as these two papers contain analysis of many objects in our sample. The comparison for β and r_c is possible for 7 and 12 clusters respectively. As can be seen from Table 5.5 and the discussion in Appendix B our measured values for β and r_c are in good agreement with values obtained from the literature, lending weight to our determinations of these parameters for the galaxy clusters that previously had no published values . Our values of r_c are in good agreement with those values in the literature which do not make any assumptions about β. On the other hand values of r_c calculated assuming $\beta = 2/3$ (marked with an $*$ in Table 7) do not agree with our values. This demonstrates the inaccuracy in assuming β and only fitting r_c.

5.3.8 Correlation between r_c and β.

The β values in Table 5.5 span a wide range, 0.32–1.21, and the values of r_c vary from 37 kpc to 646 kpc. Neumann & Arnaud (1999) investigated if there is a relation between β and r_c. They plot these quantities against each other for a sample consisting of 26 mostly Abell clusters in the redshift range $0.04 \leq z \leq 0.06$ and find that the slope parameter increases with core

radius, although the correlation is not very tight, especially at low core radius values. Two parametric functions (neither of which has a physical basis) are considered for fits to their data:

$$\beta = \beta_0^l[1 + (r_c/r_s^l)] \tag{5.3}$$

$$\beta = \beta_0[1 + (r_c/r_s)^2] \tag{5.4}$$

They determine β_0^l=0.49 and r_s^l =870 kpc with a reduced χ^2=3.36 for the linear function and β_0=0.55 and r_s =885 kpc with a reduced χ^2=1.68 for the parabolic function. In both cases four clusters have been excluded to improve the fit (for the reason that their high count rates lead to small errors that greatly increase χ^2 determinations) and they only use the errors for β. In an attempt to compensate for using only the errors in β they use 2 σ errors. They conclude that a parabolic relation is a better fit than a linear fit.

We plot β against r_c for our sample of 22 galaxy cluster but are unable to fit either of these models to our data. To be consistent with Neumann & Arnaud (Neumann & Arnaud 1999) we only use the 2-σ errors in β . Examining the errors on β and r_c all clusters which have errors more than 3 σ from the mean of the distribution are subsequently excluded. Fitting only the remaining 13 data points we are still unable to fit either the linear or parabolic models. The data are shown in Figure 5.14 where the dashed line represents the parabolic fit of Neumann & Arnaud to their data. Although Neumann & Arnaud select specifically Abell clusters, the 22 EMSS clusters also contain several Abell clusters. We conclude that the EMSS clusters do not support the reality of a β-r_c relation and that the relation suggested by these authors may have been a chance result.

5.4 Comparison with Nichol and WARPS fluxes

Nicol et al.(1997) use in their study of evolution in the X-ray cluster luminosity function the same ROSAT PSPC data for 18 EMSS clusters. In order to derive fluxes and luminosities, they assume a temperature of 6 keV without attempting to measure individual temperatures. They further adopt a King profile with β=$\frac{2}{3}$ for all of the clusters, whilst we fit isothermal β models

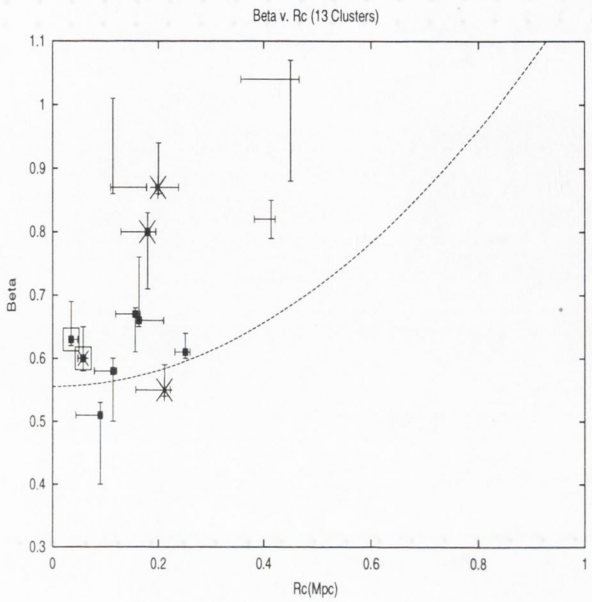


Figure 5.14: β versus the core radius for the 13 clusters in our sample, where the dashed line represents the fit of Neumann & Arnaud to their data, and the asterisks represents cooling flow clusters. In the diagram the open boxes denote the two clusters which overlap with the study of Neumann & Arnaud (1999), the filled boxes clusters with z <0.3, the large X represents clusters which have been classified as cooling flow clusters, and the small x a candidate cooling flow cluster from our analysis, i.e. we removed the centre of this cluster to get a proper fit to the Isothermal β model.

for each of the clusters. This sample has also been studied by Ellis & Jones (2001) and by the WARPS consortium in their calculations of the luminosity function (Jones et al. 1998) and analysis of the luminosity-temperature relation (Fairley et al. 2000). In this Section we compare our results with those of N97 and of WARPS, but not with those of Ellis & Jones (Ellis & Jones 2001) as they deal with only 9 out of 22 clusters.

Our flux measurements are consistently higher than those measured by N97. In a plot of N97 against our flux (Figure 5.15) we get a slope of 0.45, i.e N97 flux = 0.45 $\times$ flux in Table 2. This is caused by several factors:

1. The different method of determining the extraction radius. N97 select

a fixed metric aperture; a King profile is then assumed with $r_c = 0.25$ Mpc and $\beta = \frac{2}{3}$. Subsequently they compute the angular size of an aperture that would encompass 85% of the total cluster X-ray emission and derive a correction factor. In contrast we extract the data on the basis of the observed extent. We do not make any assumptions about r_c or β and derive these values from the data.

2. N97 use galactic N_H from Stark et al. (1992). We allow our values of N_H to vary with a lower limit set at the galactic values measured by Dickey and Lockman (1990).

3. N97 use a temperature of 6 keV to calculate the flux (with a Raymond-Smith model) whereas we use the individual temperatures determined from our spectral fits of the data. However, the temperatures used do not have a large influence on the estimate of the flux (as we will discuss in Section 8).

4. Whilst the temperatures do not have a large effect on the flux calculation they can have a large effect on the k-corrections. In Figure 5.17 we see X-ray K-corrections taken from Jones et al.(1998). At a redshift z=0.5 ,assuming a temperature of 6 keV, an incorrect temperature can affect the k-correction by up to 50%, thus affecting the total flux by 50 %.

5. N97, using the luminosity-temperature relation of Wang & Stocke (1993), estimated individual temperatures for the clusters. They found their count rate-to-flux conversion only varied by $\leq$ 10 % over a reasonable range of metallicities.

6. N97 concentrate on the hard ROSAT band, 0.4-2.0 keV. This reduces the inaccuracies caused by their use of Galactic N_H rather than a fitted value (The 0.4–2.0 keV part of the spectrum is insensitive to N_H).

The fluxes calculated by the WARPS group are in excellent agreement with our calculations of flux. In a plot of WARPS flux (MEKAL model) against our flux we get a slope of 1.15, i.e. we measure 115 % of the flux that they do (Figure 5.16). If we exclude the highest flux point, (where we measure a flux of 48 $\times 10^{-13}$ erg $s^{-1}cm^{-2}$ MS0451.5+0250) we get a slope of 0.94.

Overall this is quite good agreement despite several differences in our respective methods. The WARPS program (Fairley et al. 2000) uses the Voronoi Tessellation and Percolation method of Ebeling & Wiedenmann (1993). A Voronoi tessellation on a finite plane surface yields individual densities, or fluxes, for every single event (photons in the detector), the distribution of which allows the determination of the source contribution in the presence of a random Poissonian background field (noise). The procedure leads to a source list which is free of any assumptions about the source geometry. High-density fluctuations from the random background field will still be included in this tentative source list but can be easily eliminated, in most cases, by setting a lower threshold to the required number of events per source. Since no finite-size detection windows have been used, this analysis yields automatically straightforward fluxes for every source finally accepted. The Voronoi Tessellation and Percolation is known to give similar extraction radii as our method. They combine the photons for five clusters of similar redshift and fit a spectrum thus these temperatures do not really pertain to individual clusters. The spectral models they fitted to the data are the Raymond-Smith (Raymond & Smith 1977) and MEKAL (Mewe et al. 1995; Kaastra 1992) codes for an optically thin plasma. To calculate fluxes a constant conversion factor was used. Converting from absorbed to unabsorbed flux they take the median N_H for their sample ($3.5 \times 10^{20} cm^{-2}$). For MS0451.5+0250 we measure a value of N_H =$7.8 \times 10^{20} cm^{-2}$ much higher than the median value used by WARPS, and this is the reason why this point is the most deviant from the 1:1 line. Thus we are confident in our measurements of the fluxes. Our measurements are in much better agreement with those of the WARPS consortium than with those of N97.

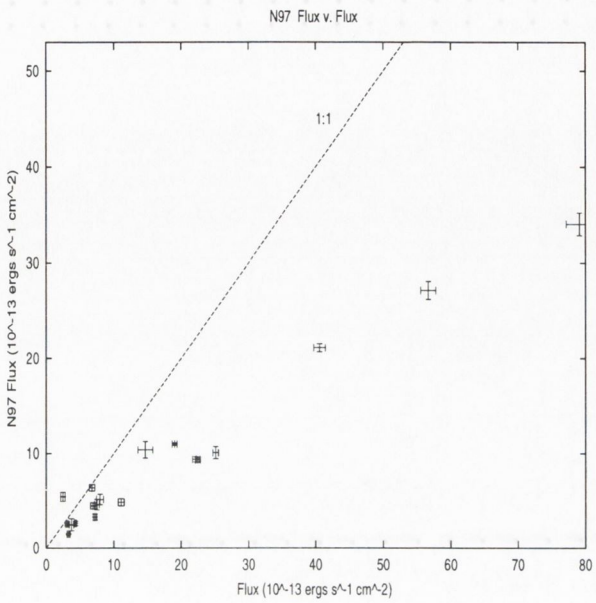


Figure 5.15: Plot of N97 flux (0.1-2.4 keV) versus our flux (0.1-2.4 keV).

5.5 ROSAT temperatures versus ASCA temperatures

Figure 5.18 shows the distribution of ROSAT temperatures for our sample, as quoted in Table 5.2. Temperatures range from 1-7 keV with a peak centred at 2 keV and a shoulder at the high temperature side out to 4 keV. Ten of the EMSS clusters have published ASCA temperatures and these are extracted from the literature and compared with the ROSAT temperatures. ROSAT temperatures are plotted against ASCA temperature for these 10 galaxy clusters in Figure 5.19 below.

In Figure 5.19 it is evident that ASCA consistently measures higher temperatures than ROSAT. This effect has already been noticed in the literature (Markevitch & Vikhlinin 1997). In Table 5.6 we quote 2 separate ASCA published temperatures whenever they are available (the first ASCA Temperature column only is used for Figure 5.19). For the 6 clusters with 2 ASCA temperatures their values are consistent. There are several reasons for the systematic discrepancy between the ROSAT and ASCA measurements.

1. For the hottest objects most of the photons emitted fall outside the

EMSS Name	ROSAT T(keV)	ASCA T(keV)	ASCA T^* (keV)	Ref. No.
MS0015.9 +1609	$4.5^{+0.75}_{-0.5}$	8^{+1}_{-1}		2
M0353.6-3642	$1.6^{+0.3}_{-0.2}$	$6.2^{+1.0}_{-0.8}$	$8.13^{+2.57}_{-1.73}$	1,2
MS0451.5+0250	$4.6^{+1.4}_{-1.1}$	$8.3^{+0.76}_{-0.75}$	$8.59^{+0.93}_{-0.9}$	2,3
MS0451.6-0305	$3.75^{+0.5}_{-0.25}$	$10.4^{+1.2}_{-1.2}$	$10.17^{+1.55}_{-1.26}$	1,2
MS0811.6+6301	$1.16^{+0.33}_{-0.03}$	$4.6^{+0.9}_{-0.6}$		1
MS1358.4+6245	$3^{+0.5}_{-0.3}$	$6.6^{+0.5}_{-0.5}$	$6.5^{+0.68}_{-0.64}$	1,2
MS1426.4+0158	$2.11^{+2.33}_{-0.53}$	$5.5^{+1.1}_{-0.7}$		1
MS1512.4+3647	$1.29^{+0.17}_{-0.09}$	$3.8^{+0.4}_{-0.3}$	$3.57^{+1.33}_{-1.74}$	1,2
MS2137.3-2353	$2^{+0.2}_{-0.2}$	$4.7^{+0.3}_{-0.2}$	$4.37^{+0.42}_{-0.34}$	1,2
MS2354.4-3502	$3.7^{+0.5}_{-0.4}$	$3.94^{+0.15}_{-0.15}$		4

Table 5.6: The first reference refers to T, and the second reference refers to T^* where 1 = Henry 1997; 2 = Mushotzky & Scharf 1997; 3 = Allen & Fabian 1998 ;and 4 = Ikebe 2002 . For clusters where less than 600 photons are detected with the ROSAT PSPC we quote temperatures derived from their hardness ratios.

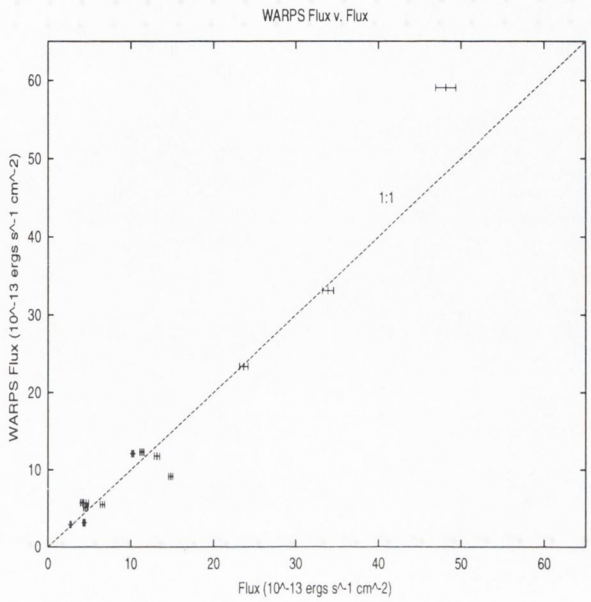


Figure 5.16: Plot of WARP's flux (0.5-2keV) (using the MEKAL model) versus our flux(0.5-2 keV). They use combine the photons from five clusters and fit a combined spectrum or where there were enough counts spectral temperatures.

spectral range of ROSAT, thus we observe relatively few photons in the ROSAT band. Given that ASCA's spectral range extends to higher temperatures it is more suited than ROSAT to measuring such high cluster temperatures than ROSAT.

2. The WARPS consortium simulate 100 clusters at 5 keV and determine the distribution of PSPC temperatures that would be derived when there are less than 190 counts. They get a distribution of temperatures from 0-17 keV with three distinct populations: at low temperatures, $\approx$ 5 keV and 17 keV (Fairley et al. 2000). Some evidence of this effect may be observed from our plot of the ASCA temperatures against ROSAT temperatures Figure 5.19, where several clusters with ASCA temperatures around 5 keV end up with lower ROSAT temperatures. In addition the overall distribution of ROSAT temperatures in Figure 5.18 shows a qualitative correspondence to the distribution of temperatures

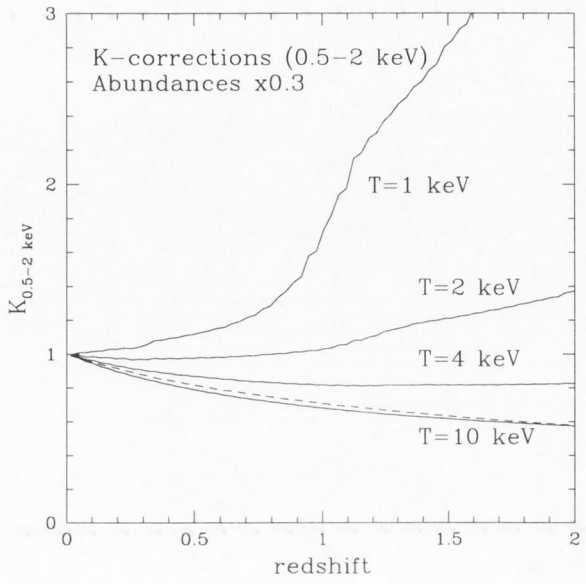


Figure 5.17: X-ray K-corrections for the 0.5-2 keV band as a function of cluster temperature. Taken from Jones et al. 1998

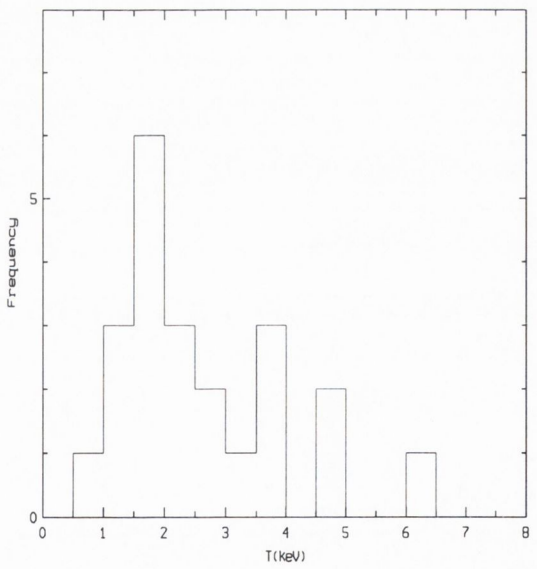


Figure 5.18: A histogram of the ROSAT PSPC temperatures for the EMSS clusters.

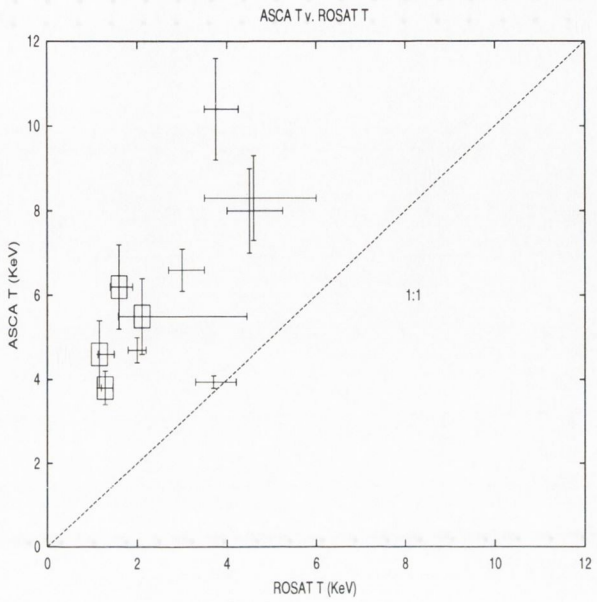


Figure 5.19: Plot of ROSAT temperature(this paper) versus ASCA temperature for 10 clusters. Points marked with a □ represent ROSAT temperatures derived using out HR grid.

recovered by Fairley et al.(2000) in their simulations.

5.6 Discussion

In this work we have devised a reliable method of directly extracting spectral information (N_H, Temperature) from observations in the ROSAT data archive with less than 600 observed photons. This method has been tested using observations of 12 galaxy clusters (with more than 800 counts) from the EMSS cluster sample. Satisfied with the validity of our approach we then proceed to use our simulated grid (with a Raymond-Smith model) to extract spectral information from the remaining-clusters with less than 600 counts observed in the ROSAT PSPC- 10 EMSS clusters in the ROSAT data archive. The spectral information retrieved is then utilized to calculate fluxes and luminosities for the 22 clusters.

Does this information greatly improve our estimates of flux and luminos-

ity as opposed to the method of N97 where a temperature of 6 keV is assumed throughout? In Section 7, on comparing ROSAT temperatures with ASCA temperatures we concluded that ROSAT may underestimate the temperatures of many clusters of galaxies. Secondly, if our temperatures are correct they do not have a large effect on the calculation of the flux. To illustrate this we take 4 temperature estimates for the galaxy cluster MS0451.6-0305(2 keV, 4 keV = ROSAT, 6 keV = N97 and 10.4 = ASCA). These give fluxes (in units of 10^{-13} erg $s^{-1}cm^{-2}$) of 21.38, 22.22, 22.65 and 23.07 respectively, an error of $\pm$ 4 % (the order of error when we take into account the error in count rate). This error is small but when K-corrections are applied(see Figure 5.17) for redshifts out to z=0.5, an error in the temperature of 3 keV may result in up to 50% change in the flux. Examining the X-ray temperature function (Ikebe et al. 2002), temperatures of 2 keV are at least 10 times more common than temperatures of 6 keV. Thus the initial guess of N97 is not very accurate and the temperatures that we derive from our grid are significantly better. We conclude that we have devised and applied a method for extracting spectral information from X-ray observations of Galaxy clusters which have less than 1000 observed photons. This spectral information has then been used to get more reliable estimates of flux and luminosity for galaxy clusters.

An isothermal β model is fitted to the radial profiles of our clusters. Values of β, the slope parameter and r_c, the core radius are compared with and found to be in good agreement with published values (see appendix) and we derive values of β (18) and r_c (13) for galaxy clusters which have no published values.

5.6.1 Appendices

Spectra, contour plots, 1 and 2 D χ^2 plots and notes on all the clusters in this chapter ar ein appendices A,B,C,D and E respectively.

Chapter 6

Contour plots for the EMSS Galaxy Clusters

Contour plots are shown for the 22 EMSS clusters in our sample.

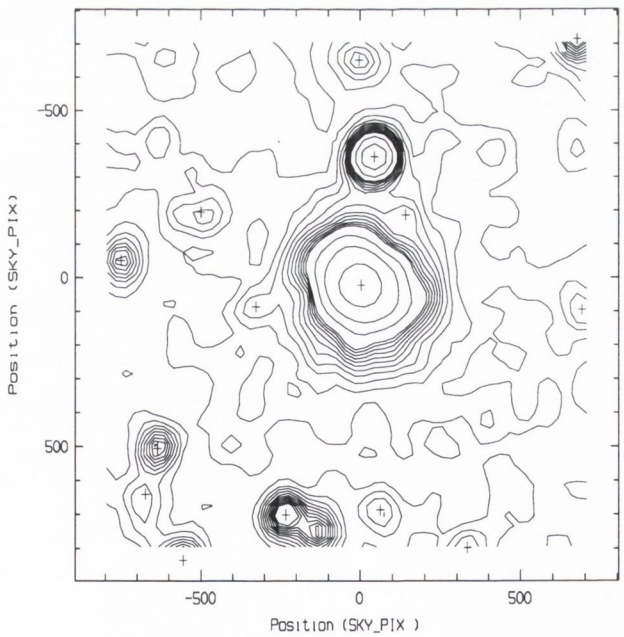


Figure 6.1: Contour plot for the galaxy cluster MS0015.9+1609.

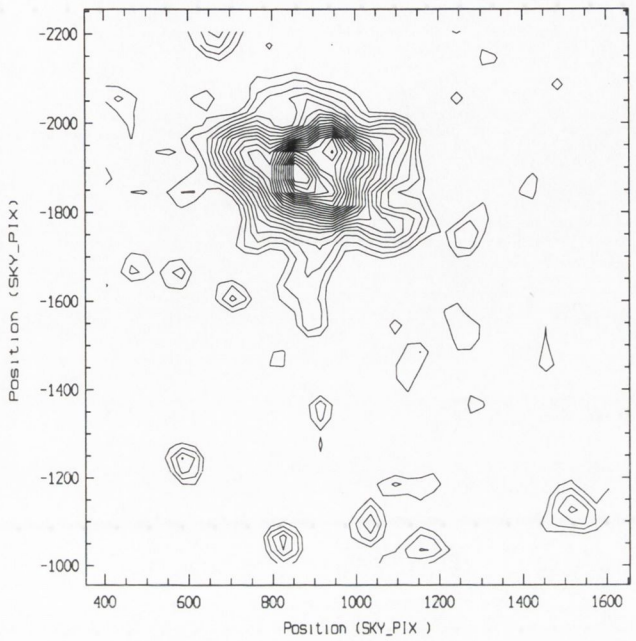


Figure 6.2: Contour plot for the galaxy cluster MS0353.6-3642 .

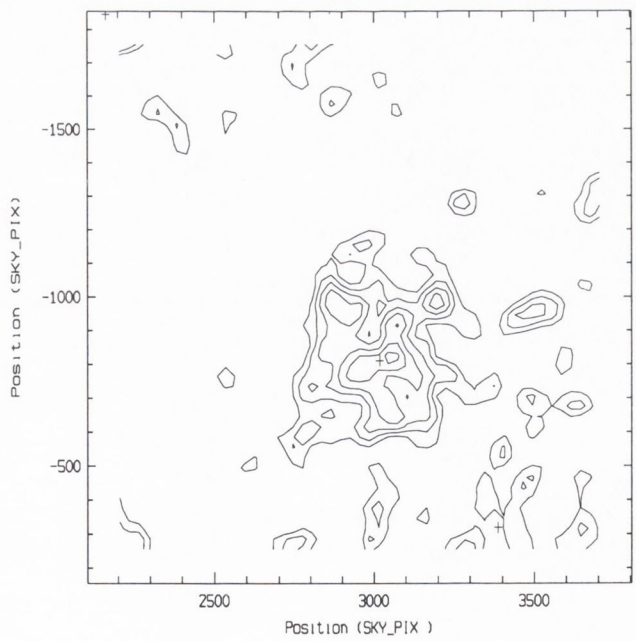


Figure 6.3: Contour plot for the galaxy cluster MS0418.3-3844.

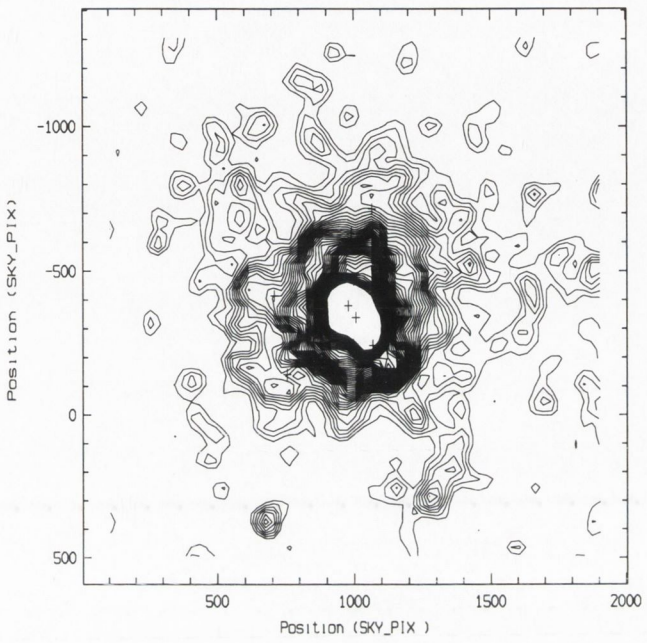


Figure 6.4: Contour plot for the galaxy cluster MS0451.5+0250.

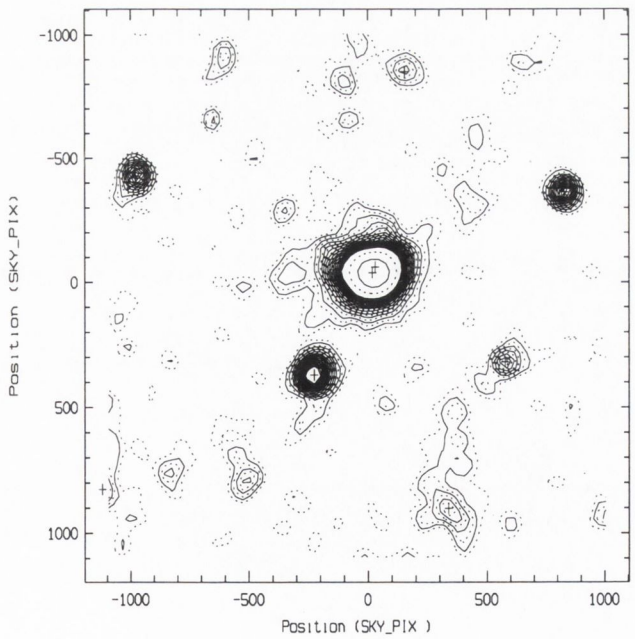


Figure 6.5: Contour plot for the galaxy cluster MS0451.6-0305

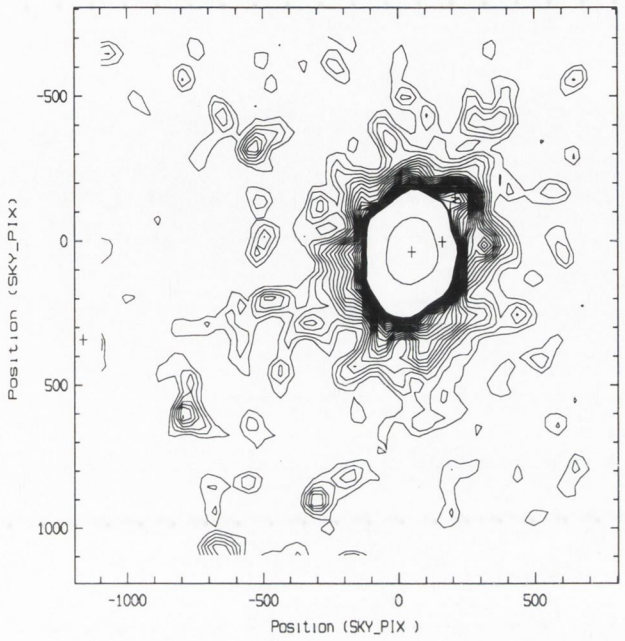


Figure 6.6: Contour plot for the galaxy cluster MS0735.6+7421

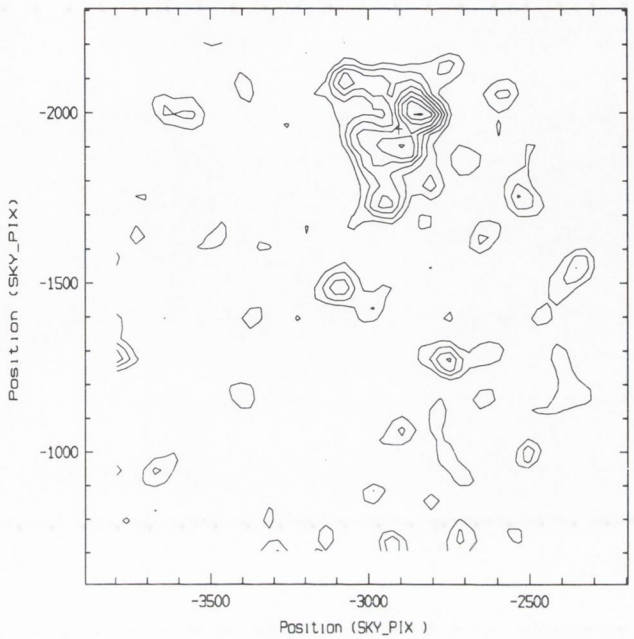


Figure 6.7: Contour plot for the galaxy cluster MS0811.6+6301

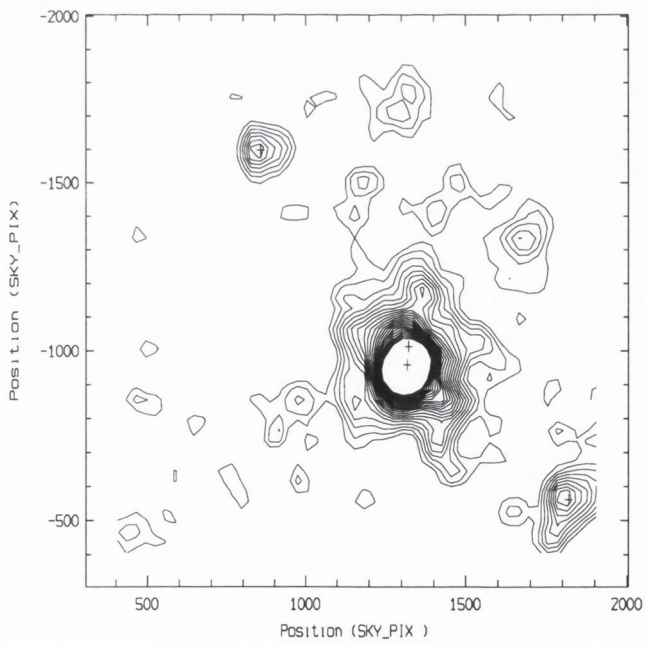


Figure 6.8: Contour plot for the galaxy cluster MS1020.7+6820

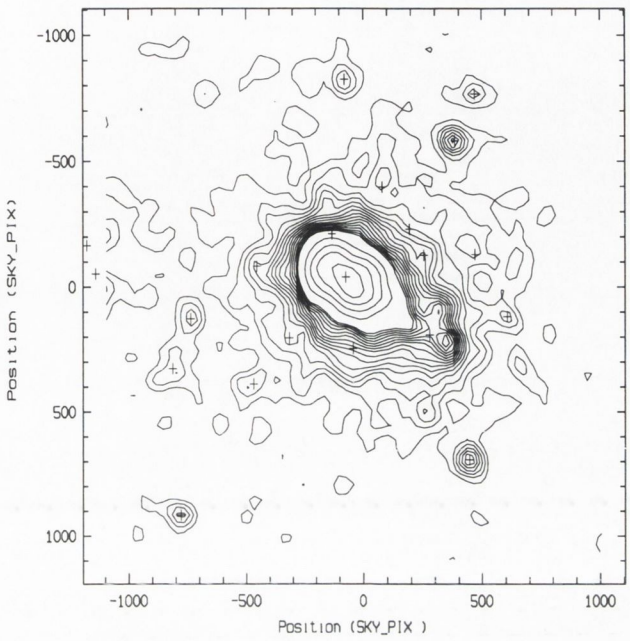


Figure 6.9: Contour plot for the galaxy cluster MS1111.8-3754

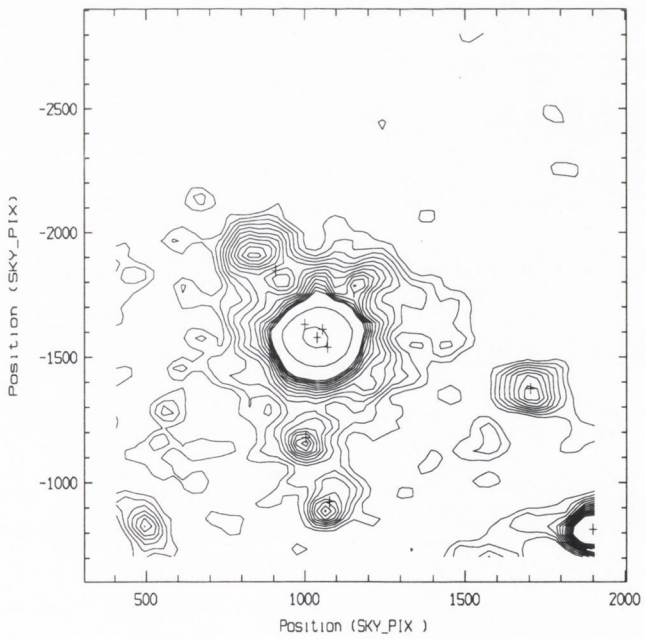


Figure 6.10: Contour plot for the galaxy cluster MS1201.5+2824

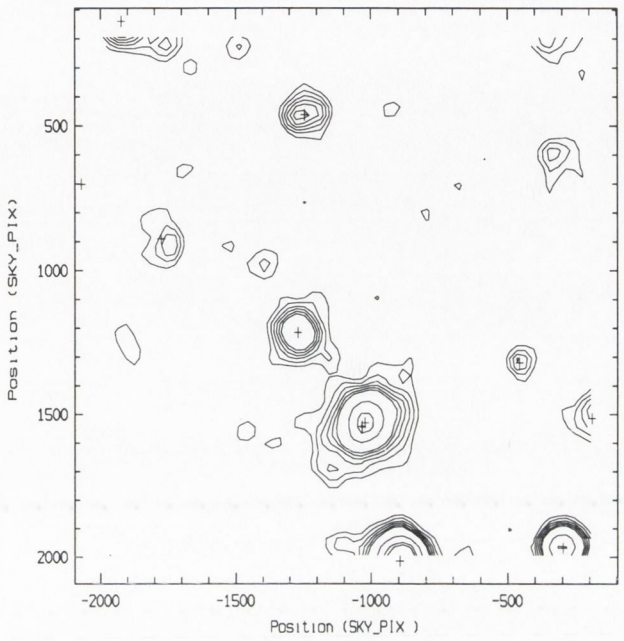


Figure 6.11: Contour plot for the galaxy cluster MS1208.7+3928

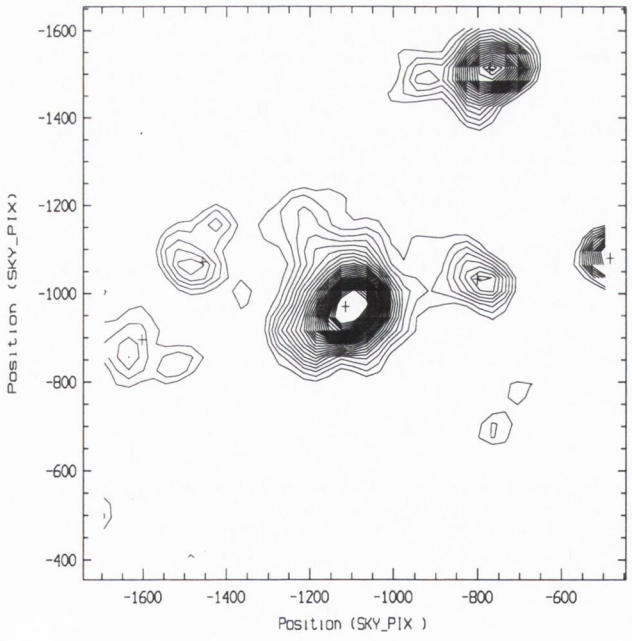


Figure 6.12: Contour plot for the galaxy cluster MS1308.8+3244

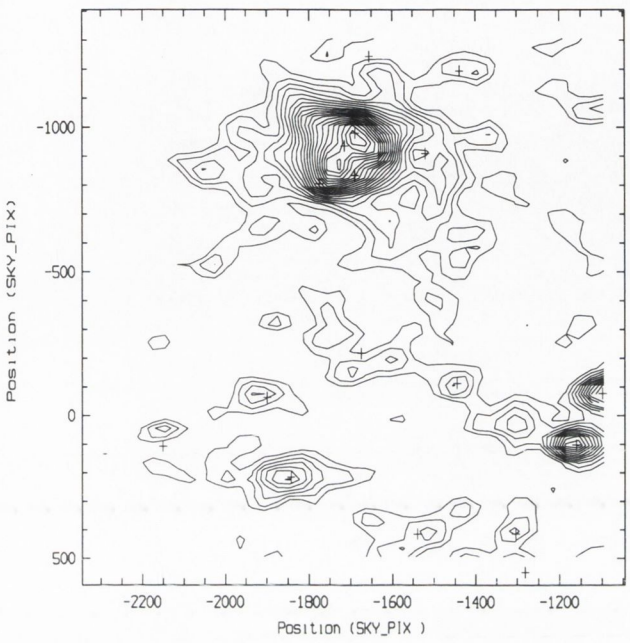


Figure 6.13: Contour plot for the galaxy cluster MS1335.2-2928

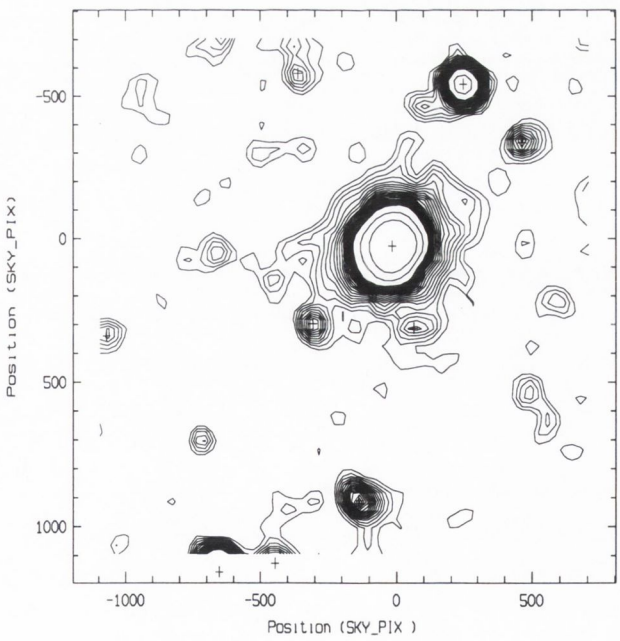


Figure 6.14: Contour plot for the galaxy cluster MS1335.2-2928

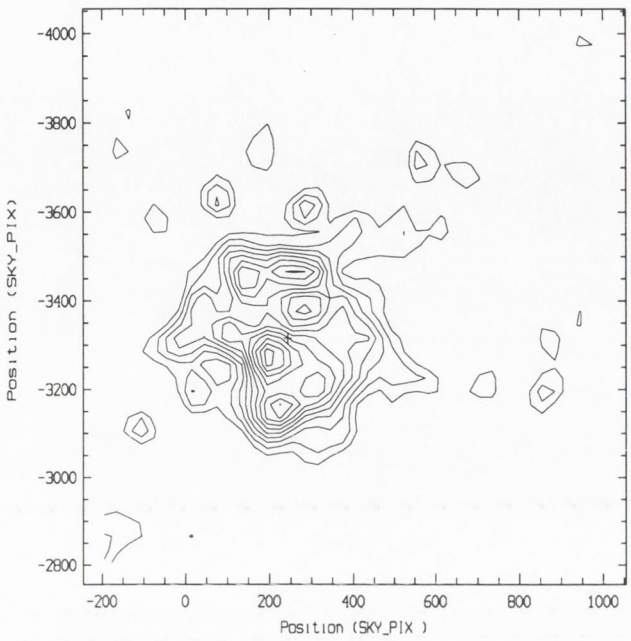


Figure 6.15: Contour plot for the galaxy cluster MS1426.4+0158

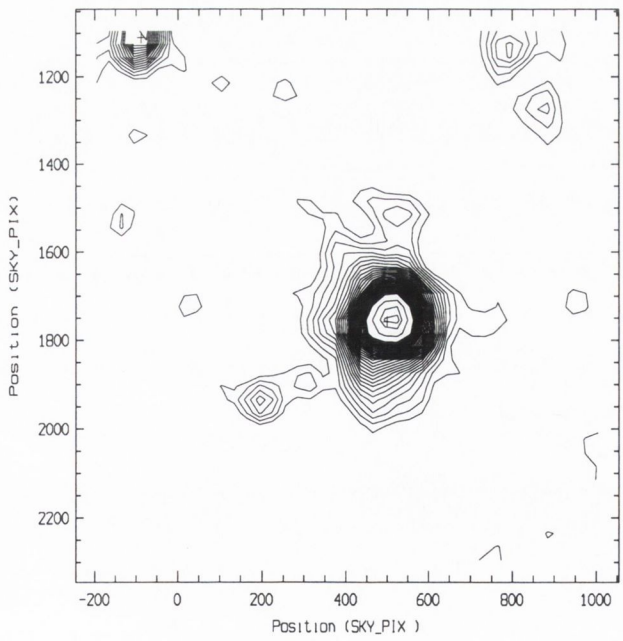


Figure 6.16: Contour plot for the galaxy cluster MS1512.4+3647

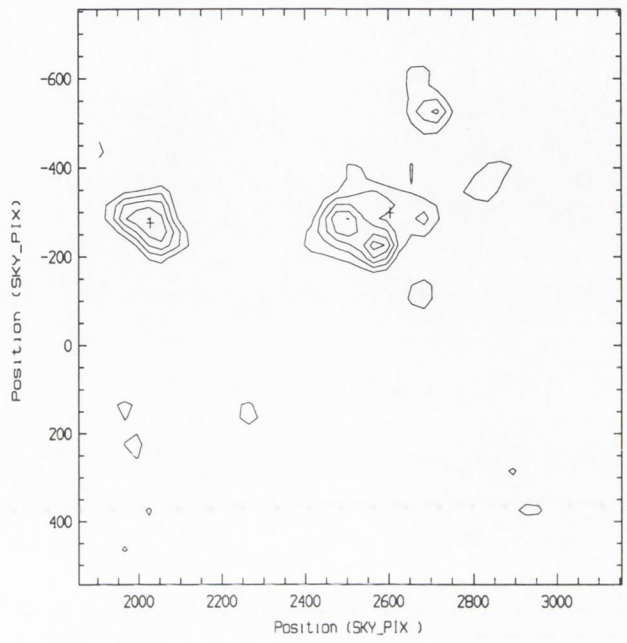


Figure 6.17: Contour plot for the galaxy cluster MS1546.1+1132

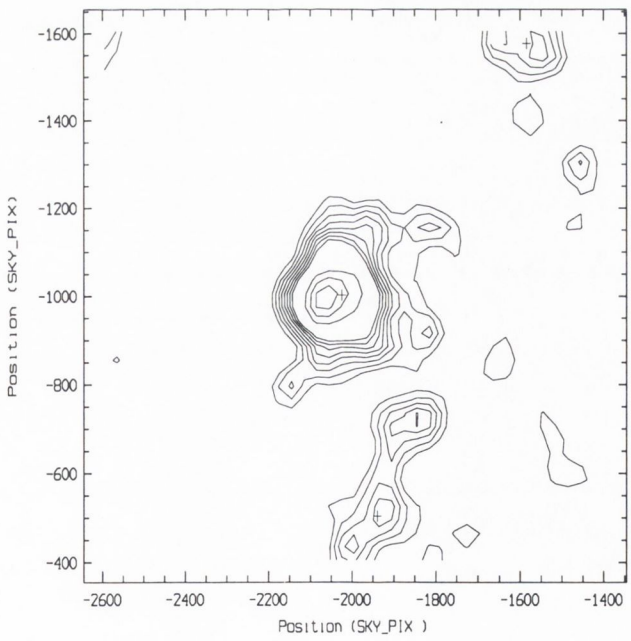


Figure 6.18: Contour plot for the galaxy cluster MS1617.1+3237

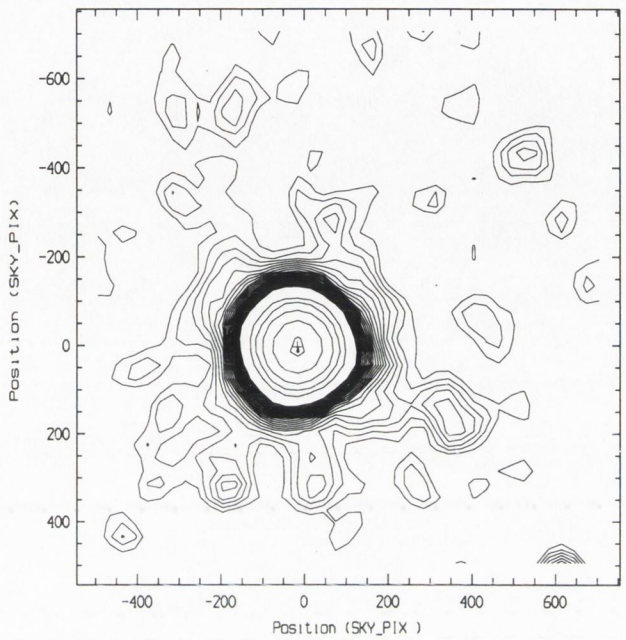


Figure 6.19: Contour plot for the galaxy cluster MS2137.3-2353

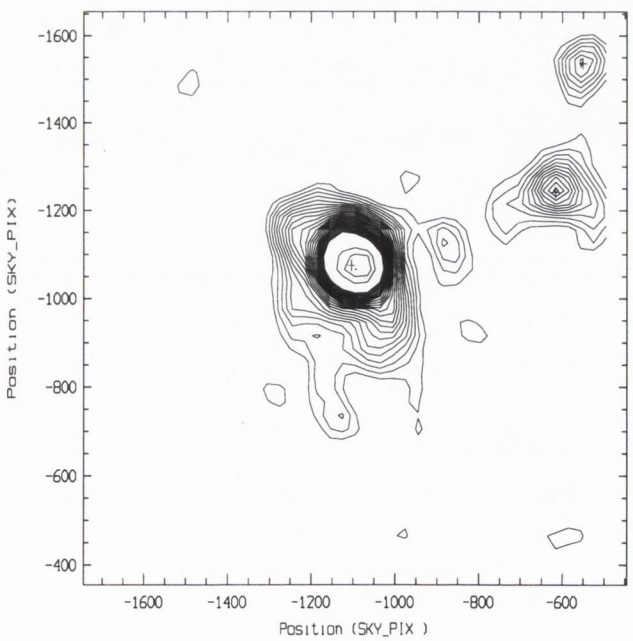


Figure 6.20: Contour plot for the galaxy cluster MS2255.7+2039

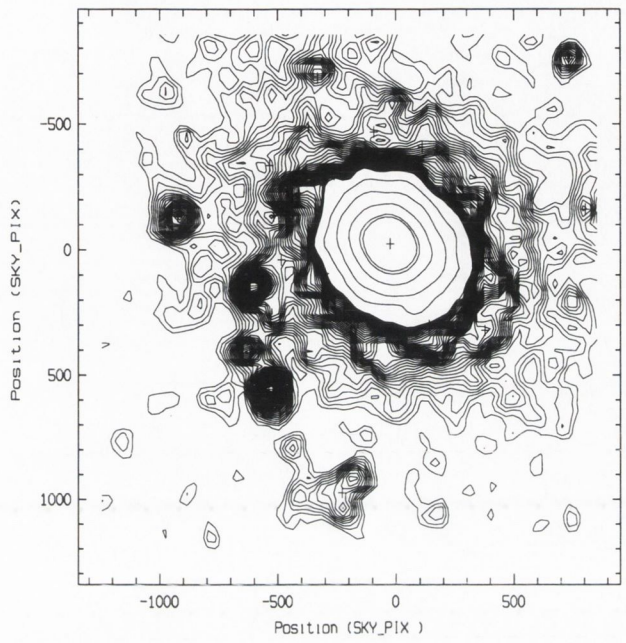


Figure 6.21: Contour plot for the galaxy cluster MS2311.2-4259

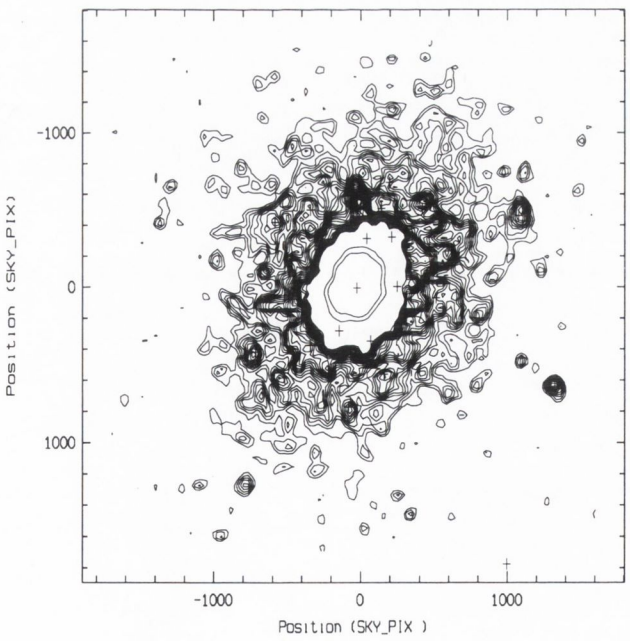


Figure 6.22: Contour plot for the galaxy cluster MS2354.4-3502

Chapter 7

Isothermal β Model Fits

We show the fits of the Isothermal β model fits to the 22 EMSS clusters in our sample.

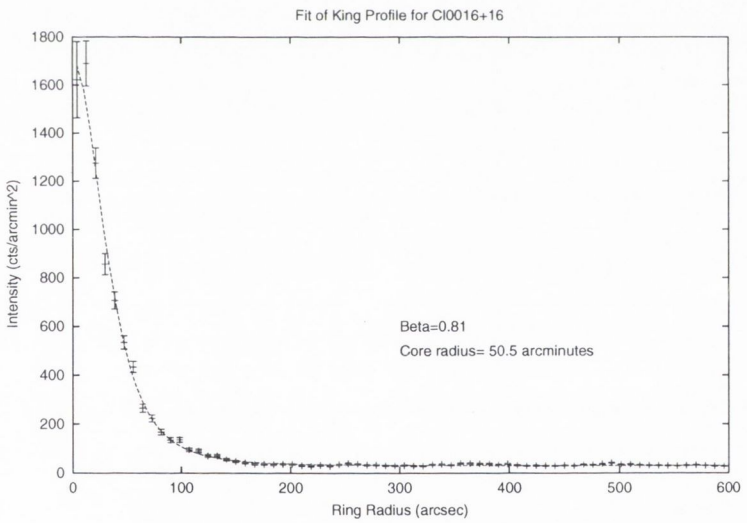


Figure 7.1: Fit of the Isothermal β model to the radial profile of MS0015.9+1609. We measure $\beta = 0.81^{+0.03}_{-0.03}$ and a core radius $=51^{+1}_{-4}$. The Isothermal β model fits the radial profile with a reduced χ^2=2.48.

EMSS Name	β	R_c (")	Net Cts	Red χ^2	r_c (Kpc)	β lit	$R_c$lit	Cut rad	No.
(1)	(2)	(3)	(4)	(5)	(6)	(7)	(8)	(9)	10
MS0015.9+1609	$0.82^{+0.03}_{-0.03}$	52^{+1}_{-4}	3989	1.67	401^{+8}_{-32}	$0.81^{+0.09}_{-0.07}$	372^{+52}_{-62}	0	1
MS0353.6-3642	$0.78^{+0.06}_{-0.15}$	75.8^{+5}_{-25}	173	0.79	352^{+24}_{-116}		225^{+37}_{-31}*	10	2
MS0418.3-3844	$0.56^{+0.02}_{-0.02}$	127^{+48}_{-49}	230	0.77	646^{+244}_{-247}		474^{+92}_{-75}*	0	3
MS0451.5+0250	$0.61^{+0.03}_{-0.01}$	86^{+3}_{-7}	1585	1.3	251^{+9}_{-21}	$0.49^{+0.08}_{-0.08}$	100^{+50}_{-50}	0	4
MS0451.6-0305	$1.04^{+0.03}_{-0.16}$	58^{+2}_{-12}	1586	1.25	450^{+16}_{-94}	$0.92^{+0.11}_{-0.11}$	360^{+80}_{-80}	0	5
MS0735.6+7421	$0.80^{+0.03}_{-0.09}$	57^{+5}_{-16}	2586	0.98	179^{+16}_{-50}		234^{+40}_{-40}	20⋆	6
MS0811.6+6301	$0.67^{+0.05}_{-0.22}$	98^{+10}_{-50}	124	0.61	445^{+45}_{-182}		274^{+92}_{-75}*	0	7
MS1020.7+6820	$0.73^{+0.01}_{-0.27}$	50^{+1}_{-13}	595	1.24	147^{+3}_{-38}			0	8
MS1111.8-3753	$0.67^{+0.01}_{-0.06}$	83^{+5}_{-20}	5771	1.36	156^{+9}_{-38}			0⋆	9

EMSS Name	β	R_c (")	Net Cts	Red χ^2	r_c (Kpc)	β lit	$R_c$lit	Cut rad	No.
(1)	(2)	(3)	(4)	(5)	(6)	(7)	(8)	(9)	10
MS1201.5+2824	$0.51^{+0.02}_{-0.11}$	37^{+1}_{-19}	3875	1.59	89^{+3}_{-46}		14^{+4}_{-4}"	0	10
MS1208.7+3928	$0.66^{+0.02}_{-0.36}$	53^{+1}_{-45}	988	1.11	262^{+5}_{-223}			15	11
MS1308.8+3244	$0.58^{+0.02}_{-0.08}$	32^{+2}_{-10}	440	0.91	114^{+7}_{-36}			0	12
MS1335.2-2928	$0.41^{+0.01}_{-0.1}$	131^{+10}_{-90}	1000	1.41	360^{+27}_{-250}			60	13
MS1358.4+6245	$0.87^{+0.07}_{-0.01}$	42^{+8}_{-1}	2678	1.99	199^{+39}_{-4}	$0.84^{+0.06}_{-0.06}$	133^{+21}_{-20} *	10$\star$	14
MS1426.4+0158	$0.88^{+0.10}_{-0.33}$	129^{+5}_{-69}	235	0.61	600^{+23}_{-320}		302^{+43}_{-38}*	0	15
MS1512.4+3647	$0.55^{+0.04}_{-0.01}$	39^{+2}_{-10}	237	2.58	211^{+11}_{-54}	$0.55^{+0.04}_{-0.04}$	114^{+14}_{-14} *	50$\star$	16
MS1546.1+1132	$0.76^{+0.55}_{-0.05}$	123^{+5}_{-100}	58	0.74	404^{+16}_{-330}			0	17

EMSS Name	β	R_c (")	Net Cts	Red χ^2	r_c (Kpc)	β lit	$R_c$lit	Cut rad	No.
(1)	(2)	(3)	(4)	(5)	(6)	(7)	(8)	(9)	10
MS1617.1+3237	$1.21^{+0.01}_{-0.25}$	84^{+1}_{-29}	196	0.62	334^{+4}_{-115}			0	18
MS2137.3-2353	$0.87^{+0.14}_{-0.01}$	25^{+14}_{-1}	2140	1.42	113^{+64}_{-4}		49^{+2}_{-3}	0	19
MS2255.7+2039	$0.66^{+0.1}_{-0.01}$	39^{+11}_{-1}	409	0.7	163^{+209}_{-4}			0	20
MS2311.2-4259	$0.63^{+0.06}_{-0.01}$	41^{+15}_{-1}	22551	2.21	35^{+12}_{-2}	$0.57^{+0.01}_{-0.01}$	37^{+3}_{-2}	0	21
MS2354.4-3502	$0.6^{+0.05}_{-0.02}$	86^{+2}_{-15}	10394	1.89	57^{+2}_{-10}	$0.58^{+0.02}_{-0.01}$	90^{+9}_{-8}	50	22

Table 7.1: Table of measured β and core radius for all the clusters in our sample.Col (3) the core radius in arcseconds, Col (4) the net number of counts available for each cluster,Col(5) is the reduced χ^2 of the fit to the isothermal β model, Col(6) is the core radius in Kpc, Col(7) is β as measured in the literature and (8) is the Core radius as measured from the literature in Kpc (except MS1201.5+2824 which is given in arcseconds), an $*$ indicates that r_c was calculated assuming β =2/3. References for r_c are given in Appendix B Col(9) is the cut radius in arcseconds to get the best fit (those marked with a $\star$ are known cooling flows c.f Appendix A for the references and Col (10) notes on individual clusters (see Appendix A). .

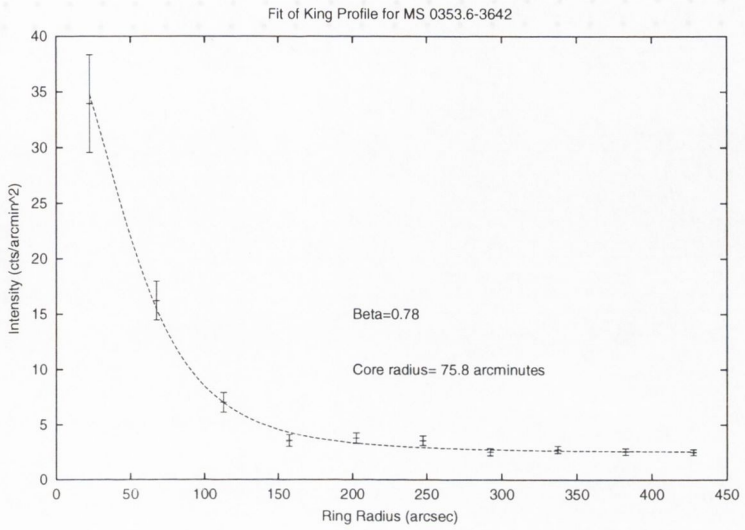


Figure 7.2: Fit of the Isothermal β model to the radial profile of MS0353.6-3642. We measure $\beta = 0.78^{+0.06}_{-0.15}$ and a core radius $=75.8^{+5}_{-25}$. The Isothermal β model fits the radial profile with a reduced χ^2=0.79.

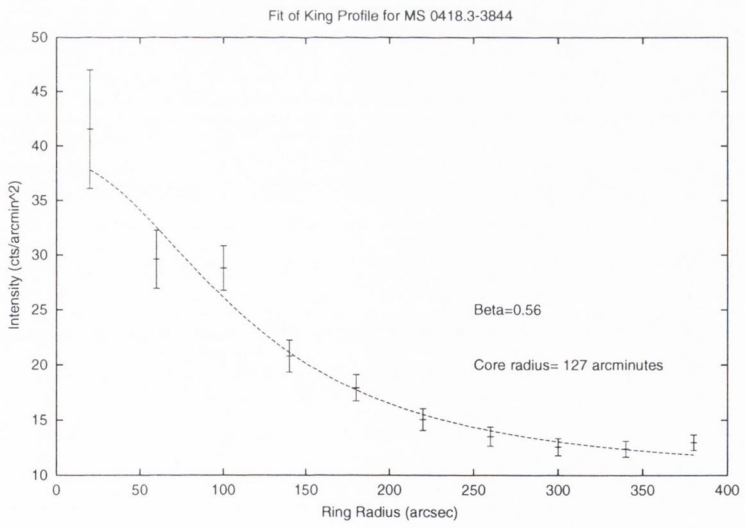


Figure 7.3: Fit of the Isothermal β model to the radial profile of MS0418.3-3844. We measure $\beta = 0.56^{+0.02}_{-0.02}$ and a core radius $=127^{+48}_{-49}$. The Isothermal β model fits the radial profile with a reduced χ^2=0.77.

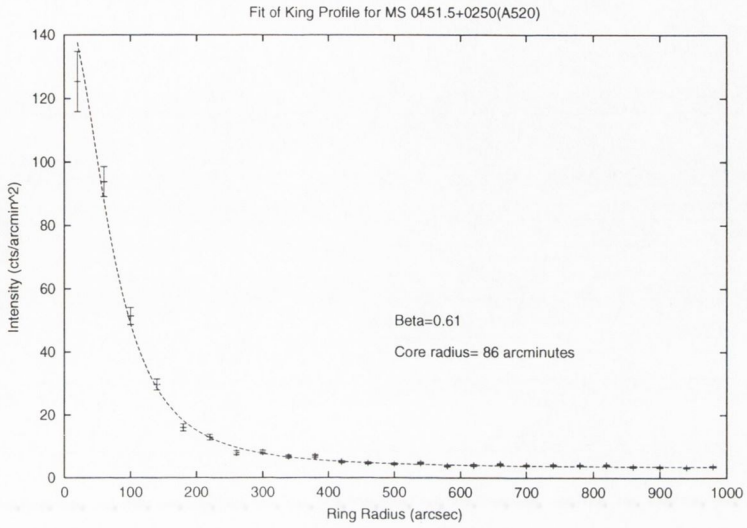


Figure 7.4: Fit of the Isothermal β model to the radial profile of MS0451.5+0250 . We measure $\beta = 0.61^{+0.03}_{-0.01}$ and a core radius $=86^{+3}_{-7}$. The Isothermal β model fits the radial profile with a reduced χ^2=1.3

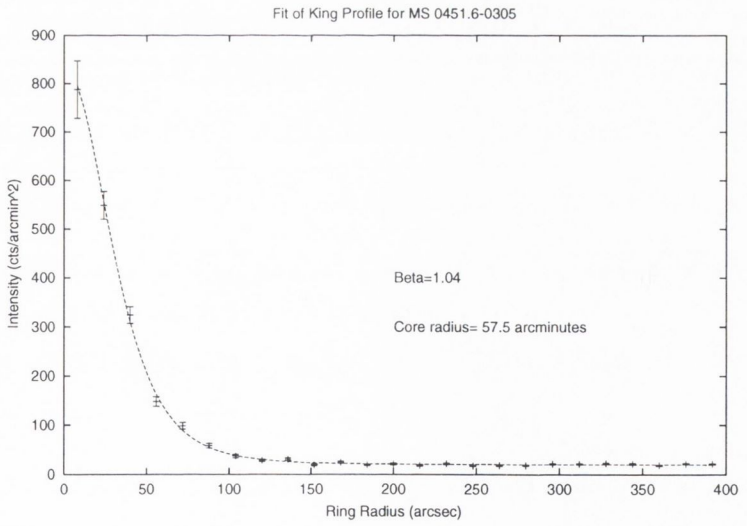


Figure 7.5: Fit of the Isothermal β model to the radial profile of MS0451.6-0305. We measure $\beta = 1.04^{+0.03}_{-0.16}$ and a core radius $=58^{+2}_{-12}$. The Isothermal β model fits the radial profile with a reduced χ^2=1.25

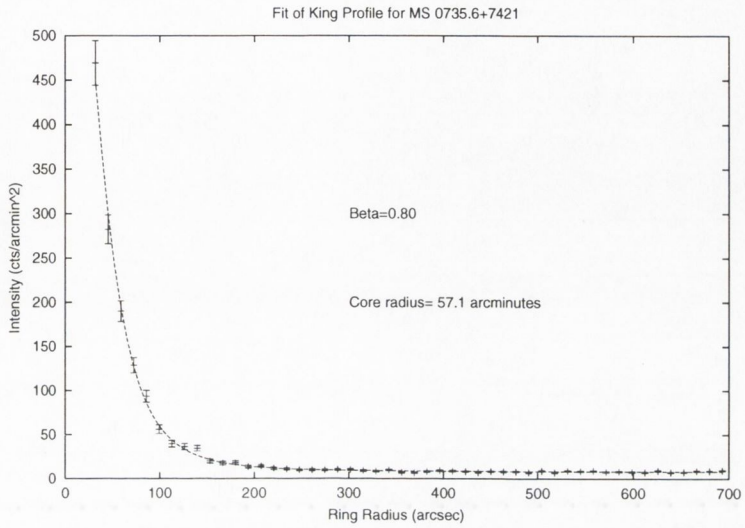


Figure 7.6: Fit of the Isothermal β model to the radial profile of MS0735.6+7421. We measure $\beta = 0.80^{+0.03}_{-0.09}$ and a core radius $=57^{+5}_{-16}$. The Isothermal β model fits the radial profile with a reduced χ^2=0.98

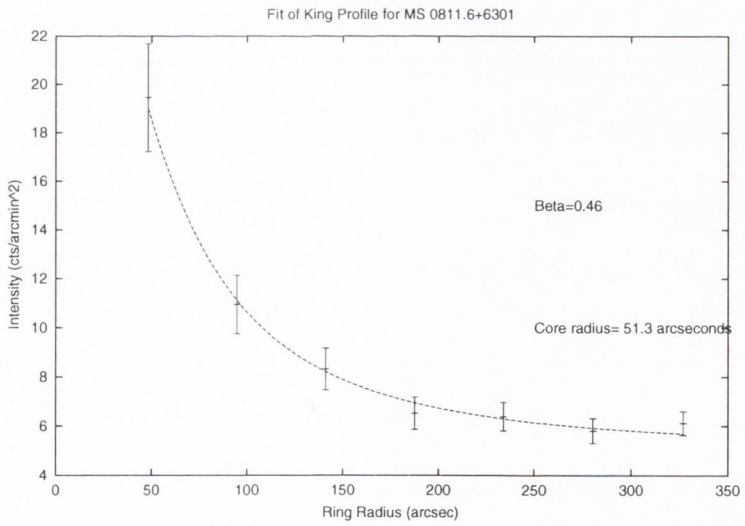


Figure 7.7: Fit of the Isothermal β model to the radial profile of MS0811.6+6301. We measure $\beta = 0.46^{+0.03}_{-0.01}$ and a core radius $=51^{+1}_{-10}$. The Isothermal β model fits the radial profile with a reduced χ^2=080.

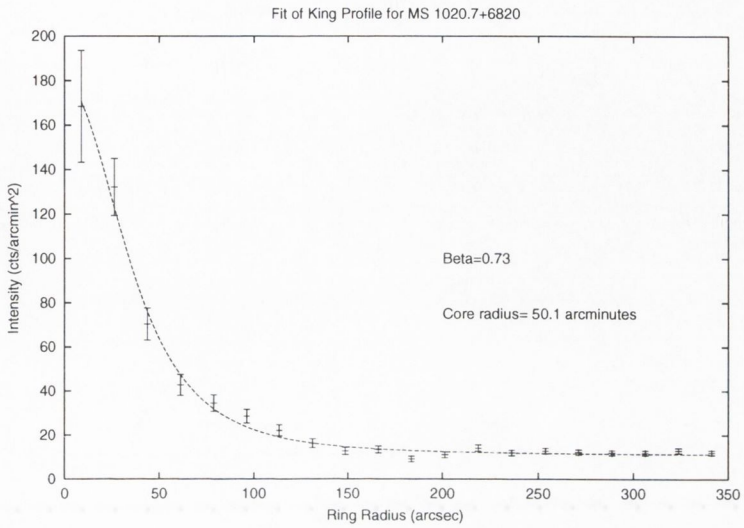


Figure 7.8: Fit of the Isothermal β model to the radial profile of MS1020.7+6820. We measure $\beta = 0.73^{+0.01}_{-0.27}$ and a core radius $=50^{+1}_{-13}$. The Isothermal β model fits the radial profile with a reduced χ^2=1.24

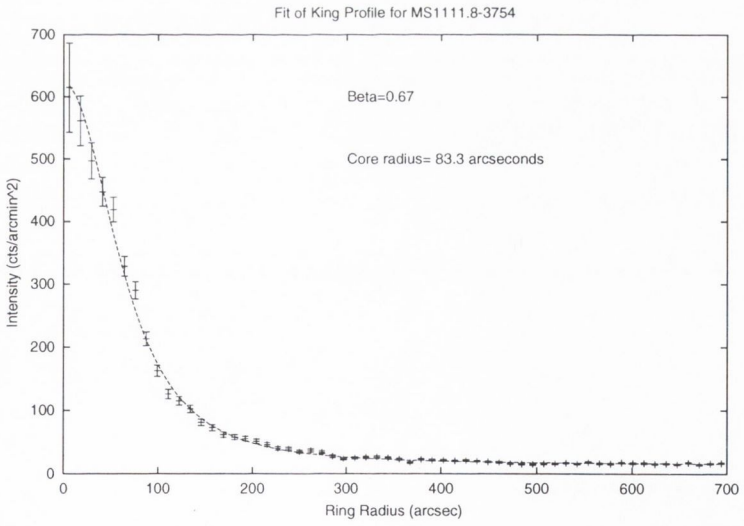


Figure 7.9: Fit of the Isothermal β model to the radial profile of MS1111.8-3754 .We measure $\beta = 0.67^{+0.01}_{-0.06}$ and a core radius $=83^{+5}_{-20}$. The Isothermal β model fits the radial profile with a reduced χ^2=1.36.

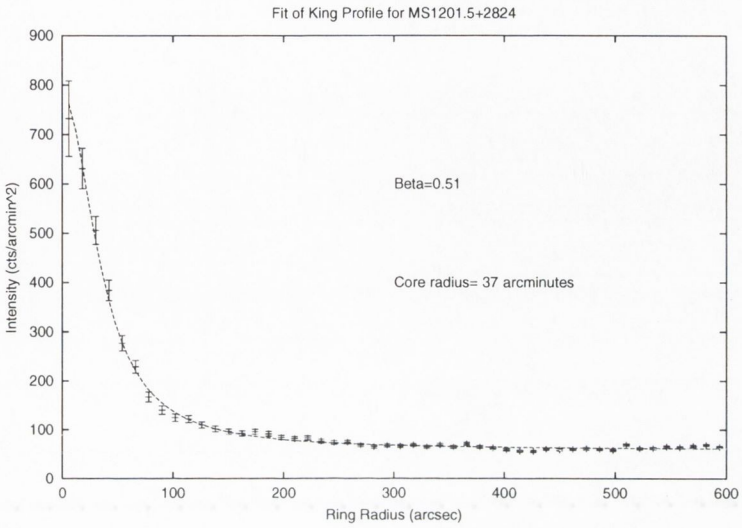


Figure 7.10: Fit of the Isothermal β model to the radial profile of MS1201.5+2824. We measure $\beta = 0.51^{+0.02}_{-0.11}$ and a core radius $=37^{+1}_{-19}$. The Isothermal β model fits the radial profile with a reduced χ^2=1.59

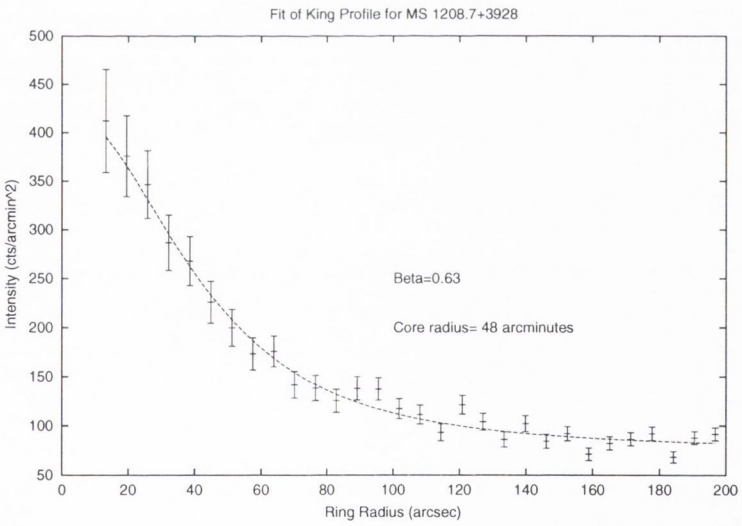


Figure 7.11: Fit of the Isothermal β model to the radial profile of MS1208.7+3928. We measure $\beta = 0.66^{+0.02}_{-0.36}$ and a core radius $=53^{+1}_{-45}$. The Isothermal β model fits the radial profile with a reduced χ^2=1.11.

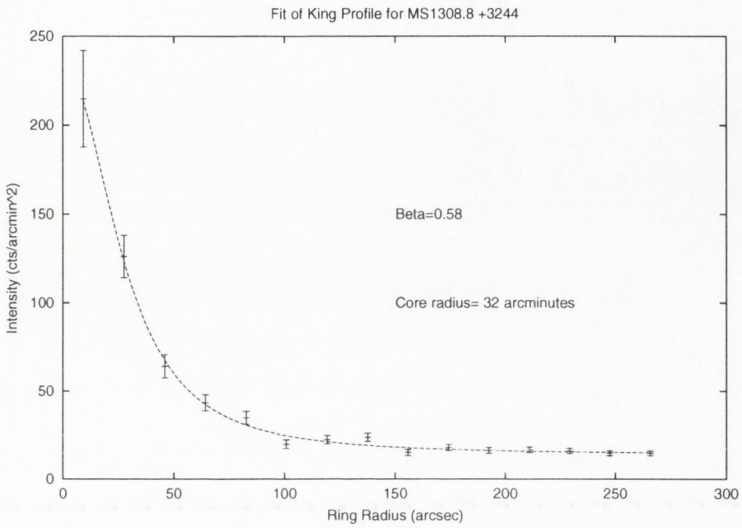


Figure 7.12: Fit of the Isothermal β model to the radial profile of MS1308.8+3244. We measure $\beta = 0.58^{+0.02}_{-0.08}$ and a core radius $=32^{+2}_{-10}$. The Isothermal β model fits the radial profile with a reduced χ^2=0.91.

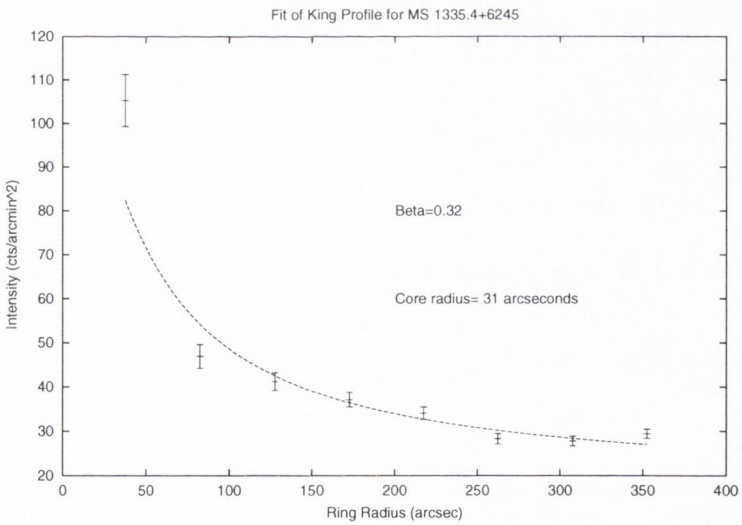


Figure 7.13: Fit of the Isothermal β model to the radial profile of MS1335.2-2928 . We measure $\beta = 0.32^{+0.08}_{-0.01}$ and a core radius $=51^{+67}_{-18}$. The Isothermal β model fits the radial profile with a reduced χ^2=1.51.

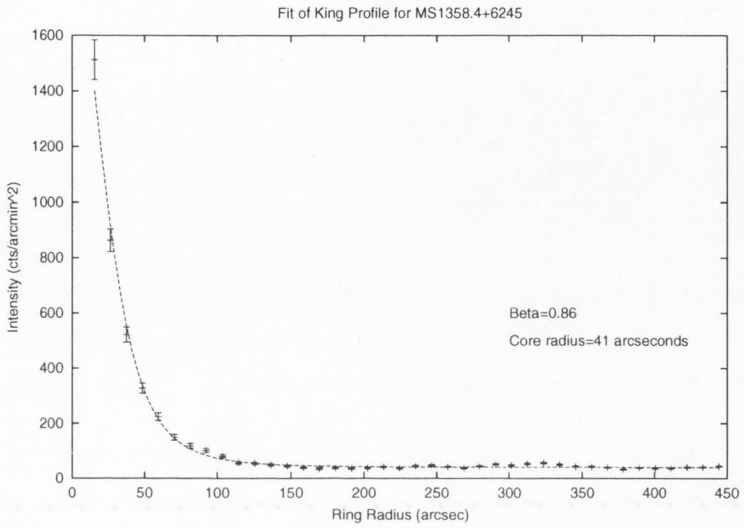


Figure 7.14: Fit of the Isothermal β model to the radial profile of MS1335.2-2928. We measure $\beta = 0.85^{+0.07}_{-0.01}$ and a core radius $=41^{+8}_{-1}$. The Isothermal β model fits the radial profile with a reduced χ^2=2.65.

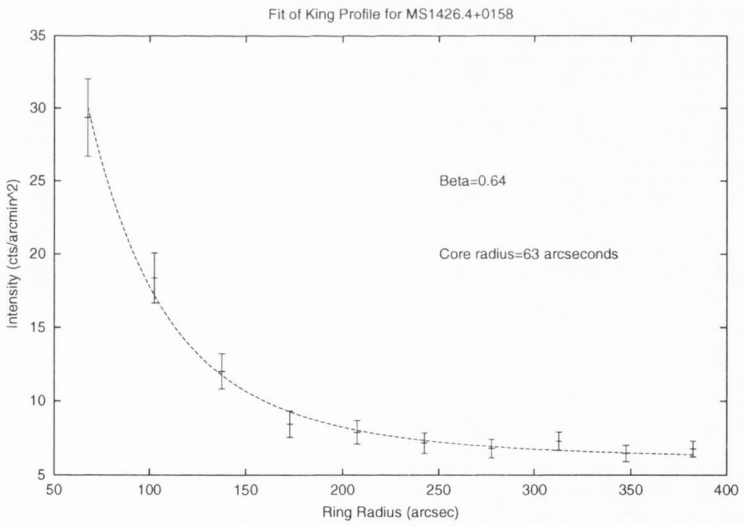


Figure 7.15: Fit of the Isothermal β model to the radial profile of MS1426.4+0158. We measure $\beta = 0.64^{+0.23}_{-0.1}$ and a core radius $=63^{+69}_{-5}$. The Isothermal β model fits the radial profile with a reduced χ^2=0.34.

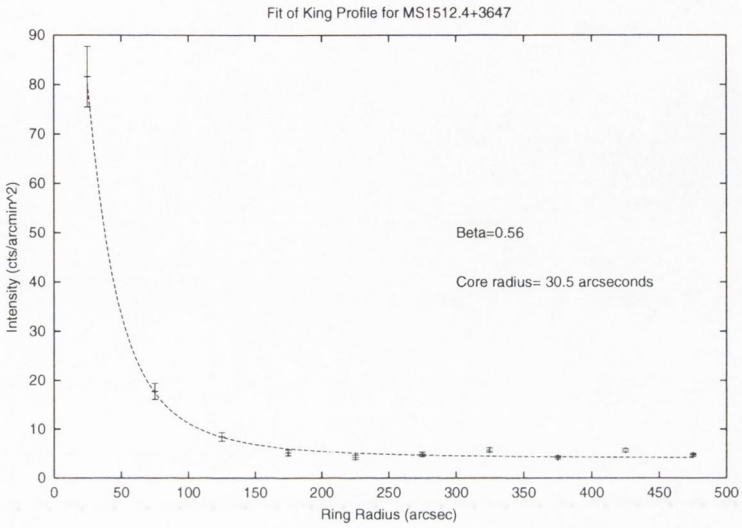


Figure 7.16: Fit of the Isothermal β model to the radial profile of MS1512.4+3647. We measure $\beta = 0.56^{+0.04}_{-0.01}$ and a core radius $=31^{+10}_{-2}$. The Isothermal β model fits the radial profile with a reduced χ^2=3.3.

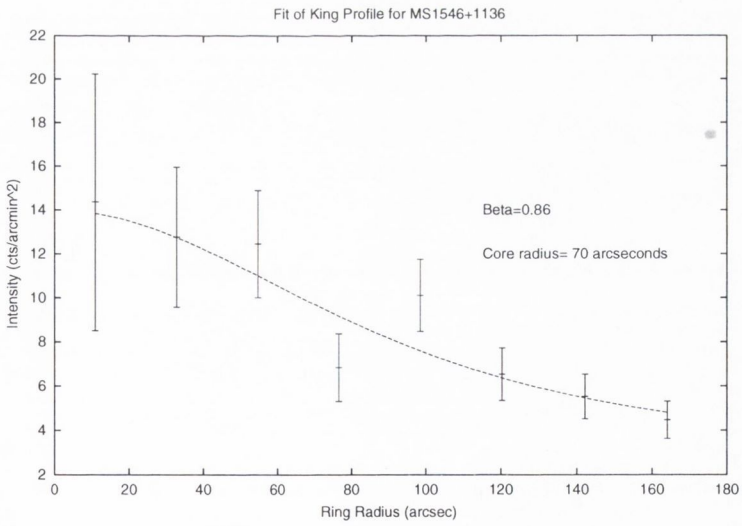


Figure 7.17: Fit of the Isothermal β model to the radial profile of MS1546.1+1132. We measure $\beta = 0.86^{+0.45}_{-0.05}$ and a core radius $=70^{+53}_{-50}$. The Isothermal β model fits the radial profile with a reduced χ^2=0.69.

Chapter 8

Furhter Isothermal β Model Profiles.

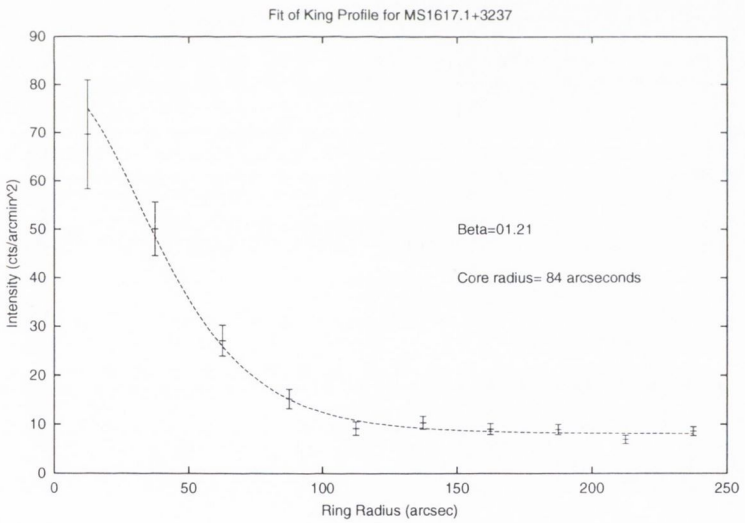


Figure 8.1: Fit of the Isothermal β model to the radial profile of MS1617.1+3237. We measure $\beta = 1.21^{+0.01}_{-0.25}$ and a core radius $=84^{+1}_{-29}$. The Isothermal β model fits the radial profile with a reduced χ^2=0.62.

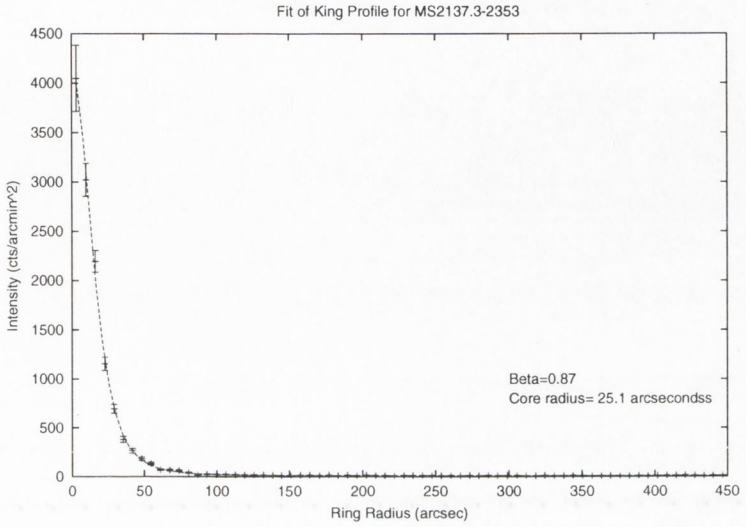


Figure 8.2: Fit of the Isothermal β model to the radial profile of MS2137.3-2353.We measure $\beta = 0.87^{+0.14}_{-0.01}$ and a core radius $=25^{+14}_{-1}$. The Isothermal β model fits the radial profile with a reduced χ^2=1.42.

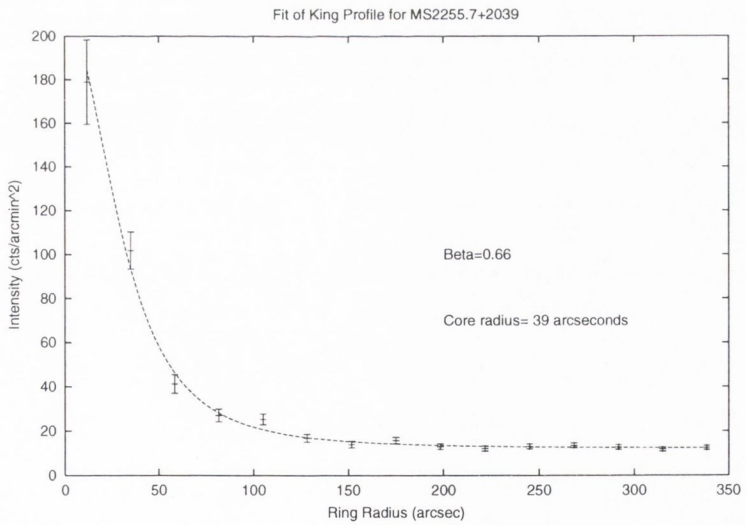


Figure 8.3: Fit of the Isothermal β model to the radial profile of MS2255.7+2039. We measure $\beta = 0.66^{+0.1}_{-0.01}$ and a core radius $=39^{+11}_{-1}$. The Isothermal β model fits the radial profile with a reduced χ^2=0.7.

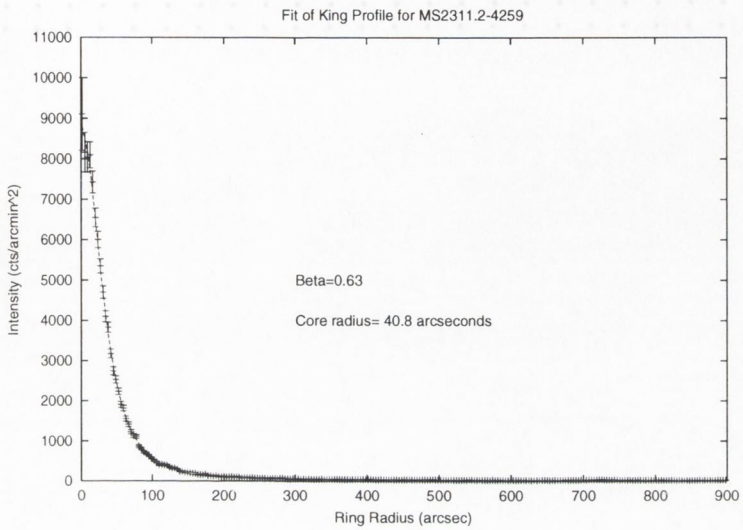


Figure 8.4: Fit of the Isothermal β model to the radial profile of MS2311.2-4259. We measure $\beta = 0.63^{+0.06}_{-0.01}$ and a core radius $=41^{+15}_{-1}$. The Isothermal β model fits the radial profile with a reduced χ^2=2.21.

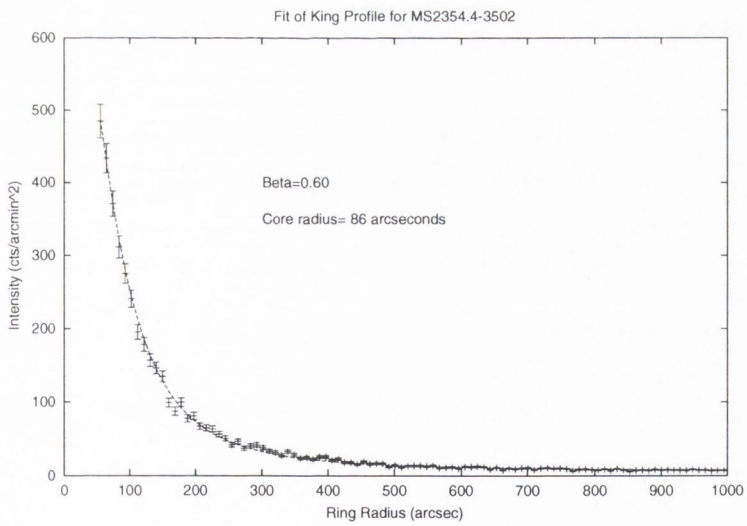


Figure 8.5: Fit of the Isothermal β model to the radial profile of MS2354.4-3502. We measure $\beta = 0.6^{+0.05}_{-0.02}$ and a core radius $=86^{+2}_{-15}$. The Isothermal β model fits the radial profile with a reduced χ^2=1.89.

Chapter 9

ROSAT Hardness Ratio Analysis for Early Type Galaxies

Diffuse X-ray emission from early-type galaxies was discovered by the Einstein observatory launched in 1978. Analysis of Einstein Observatory IPC spectra shows that the emission from luminous elliptical galaxies can be fitted by thermal plasma models with fairly low temperatures, 0.5-2.0 keV (Forman, Jones & Tucker 1985, Davis & White 1996, Trinchieri, Fabbiano & Canizares 1996). These characteristic temperatures are confirmed by observations of individual galaxies by Ginga, ROSAT and ASCA (see Awaki et al. 1991; Forman et al. 1993; Fabbiano, Kim & Trinchieri 1992, Awaki et al. 1994). Davis & White (1996) study an optically magnitude-limited sample consisting of 43 elliptical galaxies. They present X-ray data for 42 of these galaxies from the ROSAT Position Sensitive Proportional Counter (PSPC) (38) and Einstein IPC (Imaging Proportional counter) (4). Of these, 30 have enough X-ray counts (29 ROSAT PSPC, 1 Einstein IPC) to allow temperature determinations by means of spectral modeling. They derive a mean temperature of T = 0.98 keV, applying a single-component isothermal Raymond-Smith model. In this paper, extending the work on temperatures

to a larger sample, we determine temperatures for 86 early type galaxies observed with the ROSAT PSPC. For many of these galaxies (41) there are not a sufficient number of X-ray counts to determine temperatures from spectra, however we determine the gas temperatures by means of a grid of hardness ratios for a range of spectral models, that places limits on N_H and temperature for early type galaxies with poor photon statistics.

Beuing et al.(1999) derived X-ray luminosities from the RASS for a magnitude-limited optical sample ($B_T \leq 13.5$ mag) of early-type galaxies. They publish results for 101 detections and 192 upper limits. Of this sample (293) we select those which have subsequently been observed by the ROSAT PSPC. Extracting hardness ratios from these observations, we use the simulated hardness ratio grid to set limits on the temperatures of these galaxies. In order to evaluate the reliability of our method our temperatures are compared with those derived by spectral fitting by Davis & White (1996) for all of their galaxies with ROSAT PSPC temperatures for which we have a reliable estimate of temperature from our simulations (24).

9.1 Selection of Galaxies and X-ray Data Analysis

The ROSAT data archive was searched (using HEASARC BROWSE) for PSPC observations of the 293 early type galaxies listed as either positive detections or upper limits in Beuing et al. (Beuing et al. 1999) . The data sets were then processed using standard EXSAS (Zimmermann et al. 1992) procedures.

9.1.1 Data Analysis

A source detection is carried out and an offset calculated from the optical position. The source with the minimum offset is then chosen and hardness ratios are calculated. Sources with an offset greater than 2 arc minutes are rejected. In total we have 86 ROSAT PSPC observations of early type galaxies. The image of each galaxy is passed through a Gaussian filter (3-sky

pixels) and contour plots are produced. Some of the galaxies are embedded in galaxy clusters so the galaxy must be separated from the cluster. Using radial profiles and the optical size of the galaxy (from NED) the X-ray size of the galaxy is determined. Photons are extracted from this area and a background is calculated taking an annulus around the source or from a nearby area free of sources. Hardness ratios (ratios that compare the photon counts in selected bands of the spectra) are then derived.

Figures 1-3 show contour plots for three types of early type galaxy sources NGC 221, NGC708, and NGC1316. NGC221 (Figure 9.1) is isolated and doesn't have any nearby sources; we simply take an annulus around the source, as the background. NGC708 (Figure 9.2) is embedded in cluster emission so the extent of the galaxy is estimated from its radial profile (details in Section 6.3) and photons extracted from this area. An annulus around this area is taken for determining the background. NGC1316 (Figure 9.3) is the most complicated of the three cases. The galaxy is situated in a galaxy cluster. The size of the cluster is again estimated from the radial profile and photons extracted. To estimate the background it is not possible to extract an annulus due to the presence of several strong sources nearby. We must therefore use a source-free area as near as possible to the source.

9.2 Determination of the Extent of the Early Type Galaxies

Many of the galaxies in our sample are embedded in galaxy clusters. To extract accurate hardness ratios for these galaxies we must first estimate their extent, so that we include all the emission from the galaxy but restrict the inclusion of photons from the surrounding cluster. To this end we produce a radial profile of the entire cluster. In many cases such as Figure 9.4 the emission from the galaxy clearly stands out above the emission of the cluster (i.e. we have a clear point source above the background). In these cases we remove the galaxy from the cluster. We then fit an isothermal β model (see Chapter 5) and check that the fit with the centre extracted is better than the fit with the centre intact. Confident of the extent of the early type

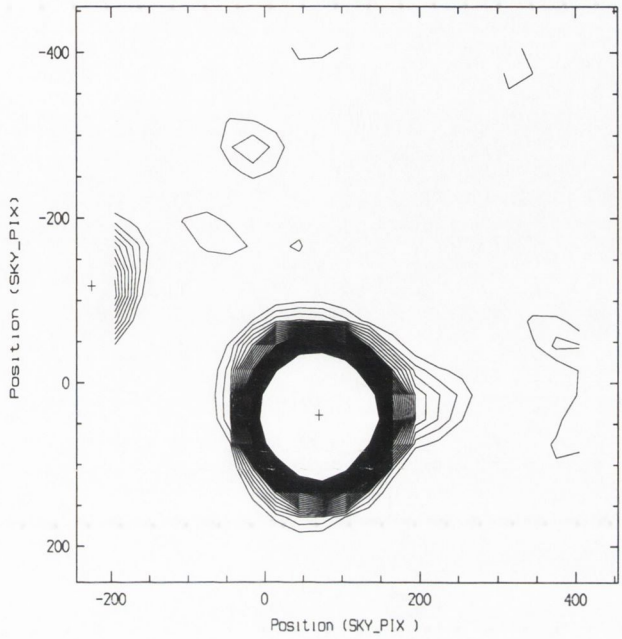


Figure 9.1: Contour plot for the early type galaxy NGC2329. The + signs denote detected X-ray sources. Contour levels begin at 2 σ above the mean background

galaxies we extract photons from this radius and calculate hardness ratios after background subtraction.

Because of x-ray scattering in the ROSAT mirror assembly the minimum suggested extraction radius is 90 arcseconds, which is the 99.5 % encircled energy radius for a 1keV spectrum (Davis & White 1996). In any case where we estimate an extraction radius less than 90 arcseconds we round it up to 90 arcseconds .

In certain cases it is not so clear-cut. In these cases we estimate a size for the galaxy using the radial profile and the optical size. An example is shown in Figure 9.5. Examining the radial profile we find the Isothermal β model (dashed line) begins to deviate from the observed intensity around 80 arcseconds. The photons inside 80 arcseconds are extracted and the remaining photons are fitted to the isothermal β model. This process is repeated for several estimates of the size of the galaxy until we get a best possible fit

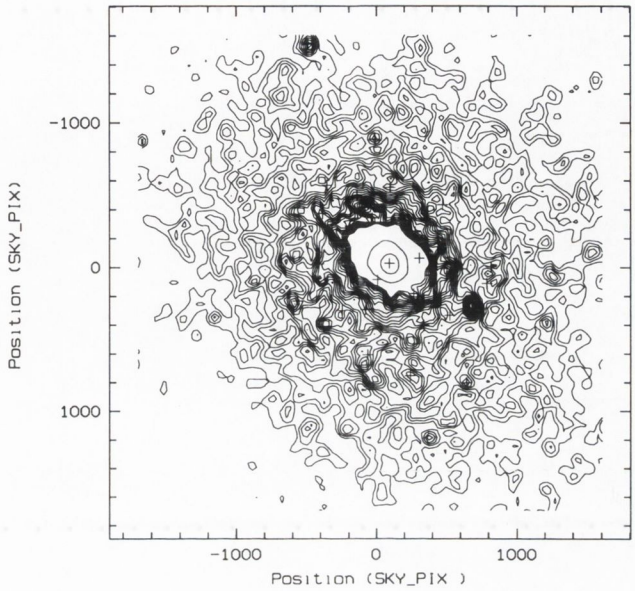


Figure 9.2: Contour plot for the early type galaxy NGC708. The + signs denote detected X-ray sources. Contour levels begin at 2 σ above the mean background.

to the remaining cluster emission. Photons are then extracted out to this radius and used to calculate hardness ratios. In this case as the estimated radius is less than 90 arcseconds we round up to 90 arcseconds.

9.3 Hardness Ratio Spectral Grids

Spectra are modeled for Raymond-Smith models (Raymond & Smith 1977), multiplied by an absorption model, as the X-ray emission of early-type galaxies is known to mostly originate from a hot interstellar gas (Forman, Jones & Tucker 1985), as outlined in Chapter 5. The resulting simulated grid is shown in Figure 9.6 (high temperature) and Figure 9.7 (low temperature).

The resulting grid can be used to convert grid points for T in the range 0.2-15 keV and N_H=0.05–1.25 $\times 10^{21} cm^{-2}$ by means of interpolation.The error bars on HR1 and HR2 (EHR1 and EHR2) are used determine the errors on T and N_H.

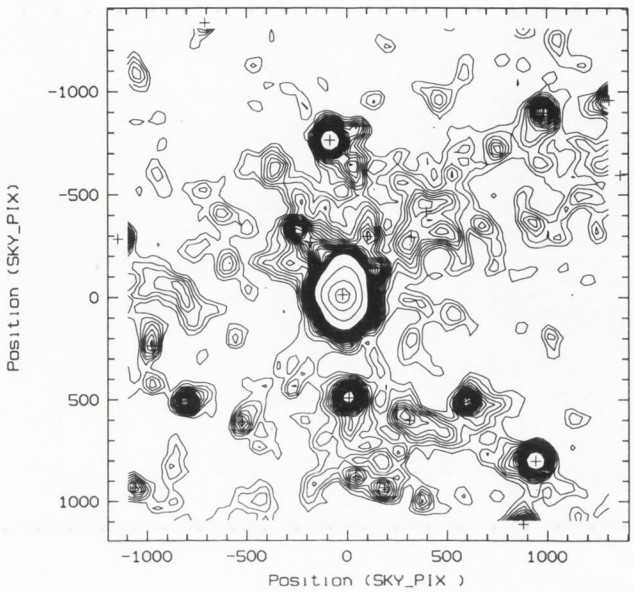


Figure 9.3: Contour plot for the early type galaxy NGC1316. The + signs denote detected X-ray sources.Contour levels begin at 2 σ above the mean background

When estimating the values of N_H we compare with the Galactic values of Dickey & Lockman (1990). If the values derived from the HRs agree within errors with the Galactic value (or are less than) we take the Galactic value. Otherwise we use the derived value (see Table 9.1). In Table 9.1 for each galaxy we give optical position and redshift, the HR's, the temperature determined from our simulated grid, the galactic N_H and the value of N_H determined from our grid.

9.4 Reliability of the Simulated Grid

Davis & White (1996) (hereafter DW) determine the temperatures of 30 elliptical galaxies (29 using PSPC) by means of spectral modeling. Four of these 29 have offsets greater than 2 arc minutes so were rejected from our sample, and the HRs of one lay outside the limits of our grid so the value of T derived is not very reliable. The other 24 may be used to test the reliability

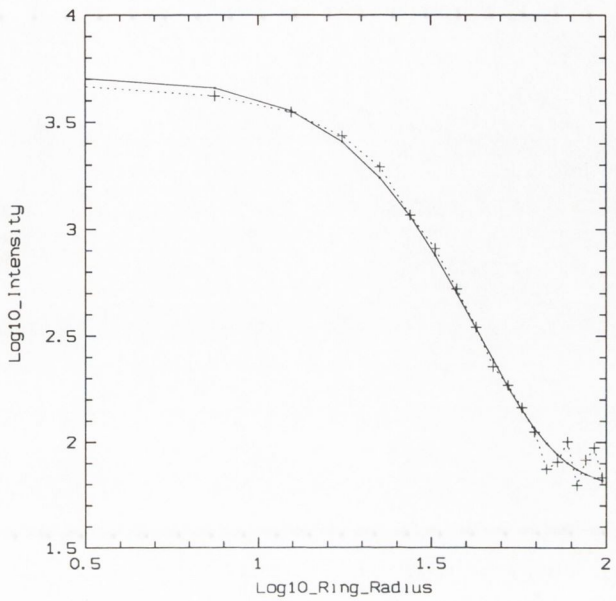


Figure 9.4: Radial profile of the early type galaxy IC 310. The galaxy emission stands out against the cluster emission.

of our grid and we calculate N_H and T from their observed hardness ratios comparing with the T derived by DW from spectral fits. In Figure 9.24 and Figure 9.25 (The two points with highest DW temperatures are excluded to allow us to zoom in. The exclusion of these points is purely for illustrative reasons) we plot the temperatures of DW (derived from spectral fits) against the temperatures derived from HRs using simulated HR grids. In general our grid temperatures are in good agreement with those of DW. Several of our temperatures are lower than those of DW. This may be caused by the number of bins (up to 177 bins) used by DW in their spectral analysis. There are several problems with the methodology of DW:

1. From the Shannon information theorem it can be derived that the optimal data binning for a Gaussian redistribution function is about $\Delta E/3$, for spectra of the order of $10^3 - 10^5$ counts, otherwise information may be lost (Kaastra 1997). At 1 keV (for the ROSAT PSPC) this is about 0.15 keV, which implies an optimal number of bins of 16. When dealing with low counts then even less bins may be used to ensure a high signal to noise .

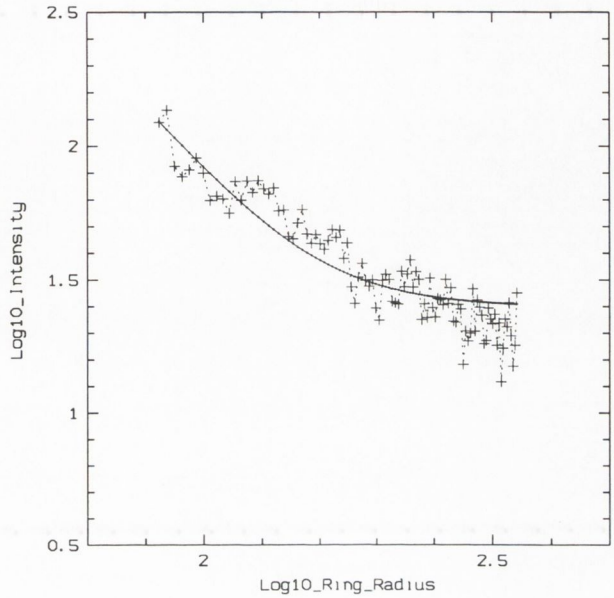


Figure 9.5: Radial profile of the early type galaxy IC 1860. In this case the extraction of the galaxy from the cluster emission is more complicated

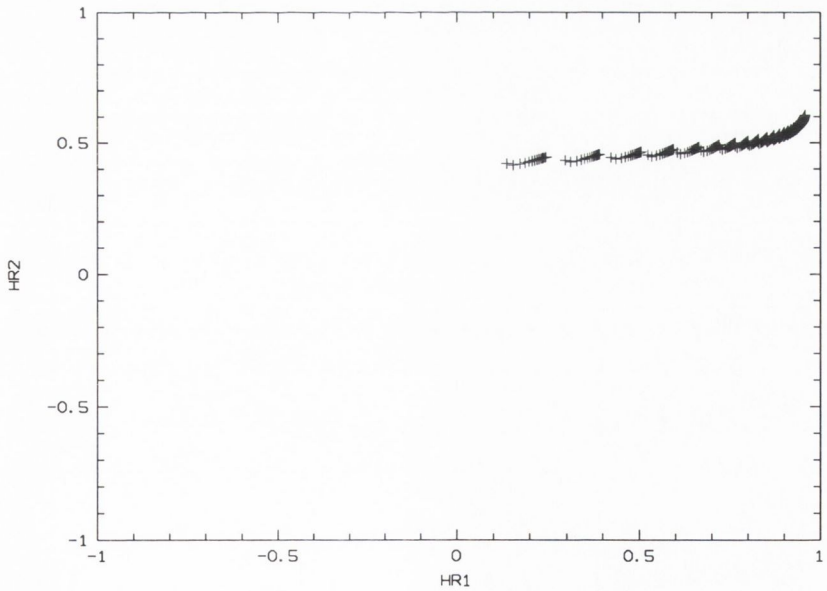


Figure 9.6: Grid at z=0, for T $\geq$ 2 KeV in steps of 1 keV and N_H=0.05-1.25 $\times 10^{21} cm^{-2}$

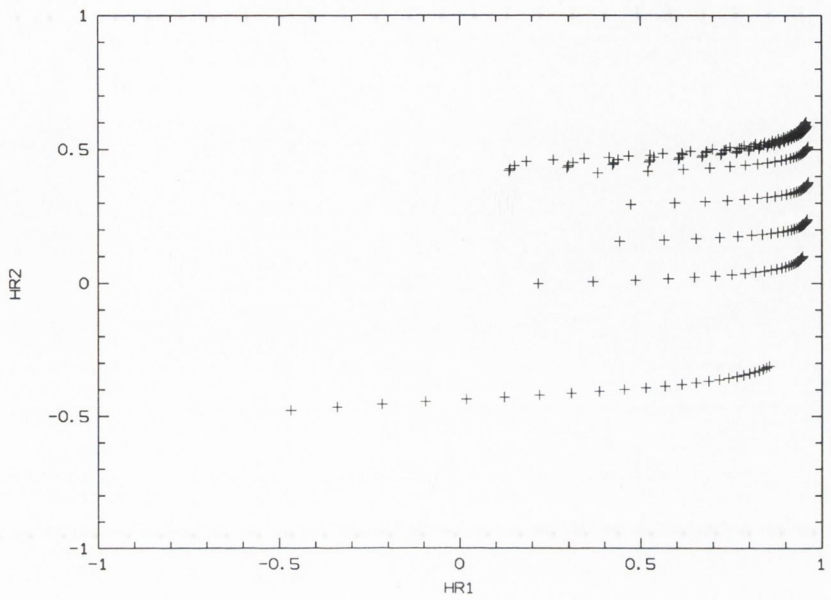


Figure 9.7: Grid at z=0, for T $\leq$ 2 keV in steps of 0.2, N_H=0.05-1.25 $\times 10^{21} cm^{-2}$. T increases from 0.2 KeV to 2 keV on going from bottom to top, and N_H increases on going from left to right.

2. They allow the optical photometry to dictate the spatial size of the X-ray spectral regions, extracting spectra from within $6r_e$, where r_e is the galaxy's optical effective radius.

3. They extract a background from an annulus around each galaxy extending from $6r_e$ out to $12r_e$, excluding all detectable point sources. By over-estimating the radius their background is taken from an annulus further from the source than necessary.

4. Temperature, abundance and N_H are allowed to vary. In some cases they take a value of N_H which is below the galactic value. When there were insufficient counts they fix N_H to the galactic N_H value (Stark et al. 1992) and the abundance to 0.2 solar. In comparison we fix the abundances at 0.3 solar and allow the value of N_H to vary above the galactic N_H of Dickey & Lockmann (1990).

Finally some of their spectral determinations come from observations with as little as 75 counts, from which it is impossible to determine reliable spectral parameters.

To get a handle on what effect this might have on the spectral determinations of DW we analyze the spectra of 4 galaxies namely NGC1399, NGC1404, NGC4472 and NGC5322. In general the temperature determinations of DW agree within errors with our spectral determinations, but there is some evidence that for galaxies with less counts (NGC5322) they do overestimate the temperature. Overall we may conclude that the temperatures derived from our grid are accurate. Seventeen of the galaxies in our sample lie outside the limits of our grid and are thus not well described by a Raymond-Smith model. It may be that these galaxies would be better described by a composite model comprising a Raymond-Smith with a power law component. Unfortunately the use of composite models is probably too complicated for a grid approach. Twelve of the galaxies in our sample have values of N_H above the galactic value, this may have implications for the values of fluxes and luminosities calculated in the literature e.g. (O'Sullivan et al. 2001).

9.4.1 NGC1399

DW determine a temperature of kT= $1.08^{+0.02}_{-0.01}$ keV from spectral analysis. Using our grid we determine a temperature of $0.69^{+0.47}_{-0.07}$ keV both of these values agree within limits but we determine a lower best fit value. Using spectral analysis and 2 and 1 dimensional χ^2 plots (see Figure 9.9 and Figure 9.10 we determine a temperature of 1.06 ± 0.01 keV.

9.4.2 NGC1404

DW determine a temperature of kT= $0.62^{+0.03}_{-0.02}$ keV from spectral analysis. Using our grid we determine a temperature of $0.42^{+0.89}_{-0.02}$ keV both of these values agree within limits but we determine a lower best fit value. Using spectral analysis and 1 and 2 dimensional χ^2 (see Figure 9.13 and Figure 9.12 plots we determine a temperature of 0.65 ± 0.01 keV.

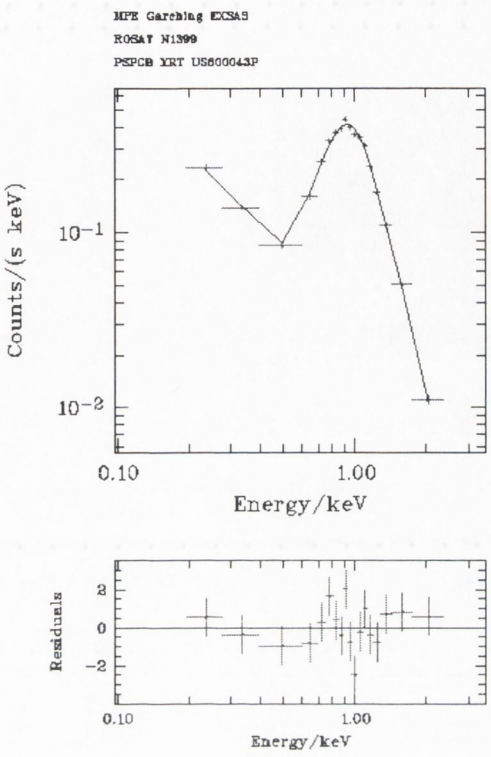


Figure 9.8: Spectrum of NGC1399.

9.4.3 NGC4472

DW determine a temperature of kT= $1.01^{+0.02}_{-0.02}$ keV from spectral analysis. Using our grid we determine a temperature of kT= $0.56^{+0.44}_{-0.04}$ keV both of these values agree within limits. Using spectral analysis and 1 and 2 dimensional χ^2 (see Figure 9.16 and Figure 9.15 plots we determine a temperature of 0.96 ± 0.01 keV.

9.4.4 NGC5322

DW determine a temperature of kT= $0.51^{+0.18}_{-0.14}$ keV from spectral analysis. Using our grid we determine a temperature of $0.37^{+0.47}_{-0.0}$ keV both of these values agree within limits. Using spectral analysis and 1 and 2 dimensional χ^2 (see Figure 9.19 and Figure 9.18) plots we determine a temperature of 0.26 ± 0.02 keV.

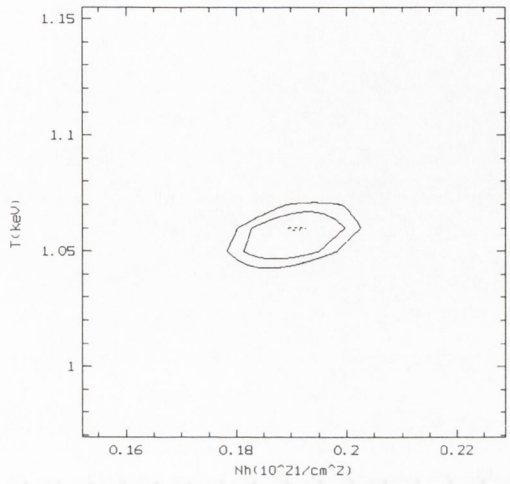


Figure 9.9: 2 dimensional χ^2 plot for the elliptical galaxy NGC1399 as a function of the temperature and the column density for two confidence levels of 68.3% and 94.5 %.

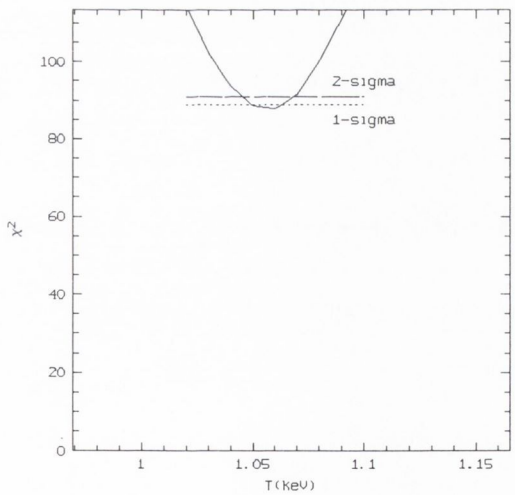


Figure 9.10: 1 dimensional χ^2 plot for the elliptical galaxy NGC1399 as a function of temperature for three confidence levels of 68.3% and 94.5 %.

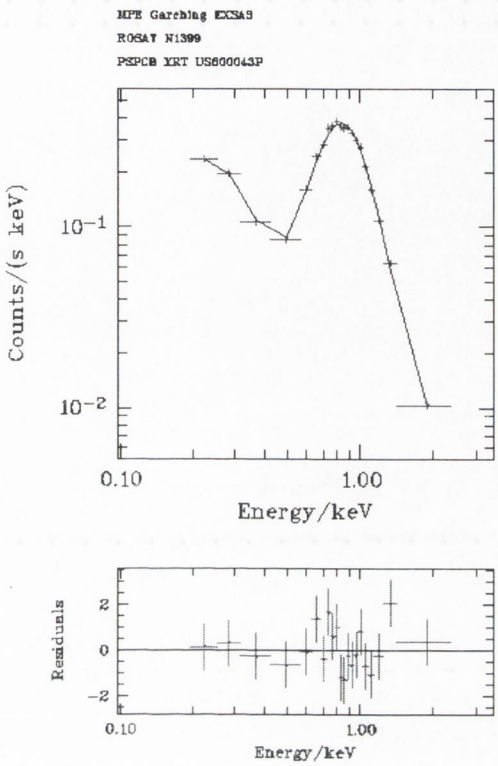


Figure 9.11: Spectrum of NGC1404.

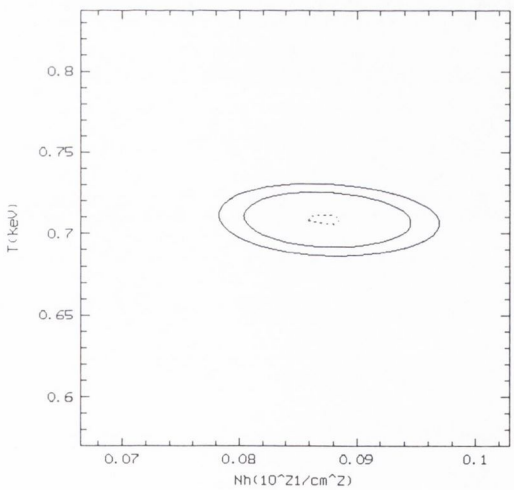


Figure 9.12: 2 dimensional χ^2 plot for the elliptical galaxy NGC1404 as a function of the temperature and the column density for two confidence levels of 68.3% and 94.5 %.

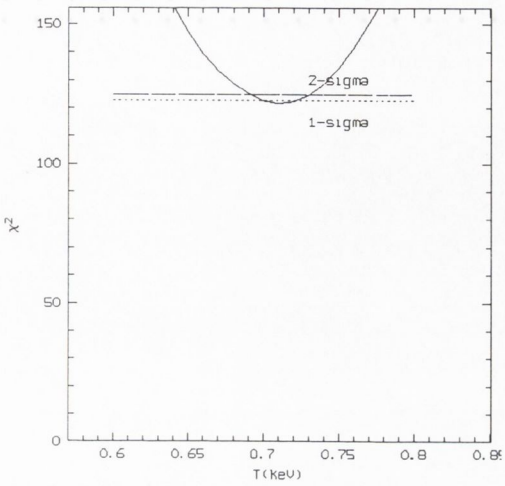


Figure 9.13: 1 dimensional χ^2 plot for the elliptical galaxy NGC1404 as a function of temperature for two confidence levels of 68.3% and 94.5 %.

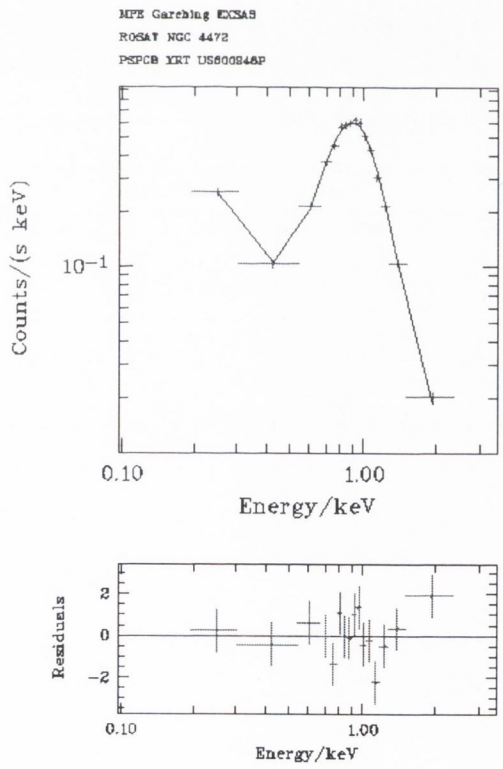


Figure 9.14: Spectrum of NGC4472.

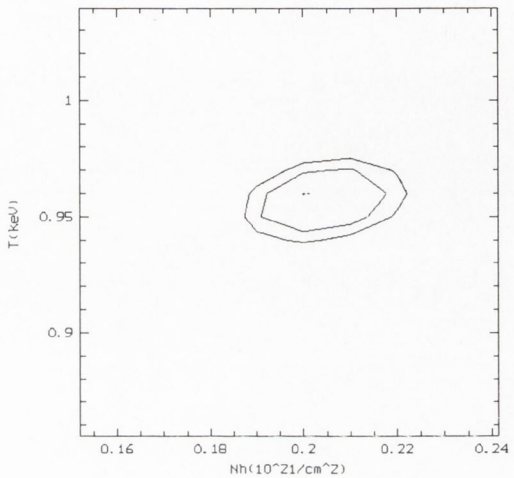


Figure 9.15: 2 dimensional χ^2 plot for the elliptical galaxy NGC4472 as a function of the temperature and the column density for two confidence levels of 68.3% and 94.5 %.

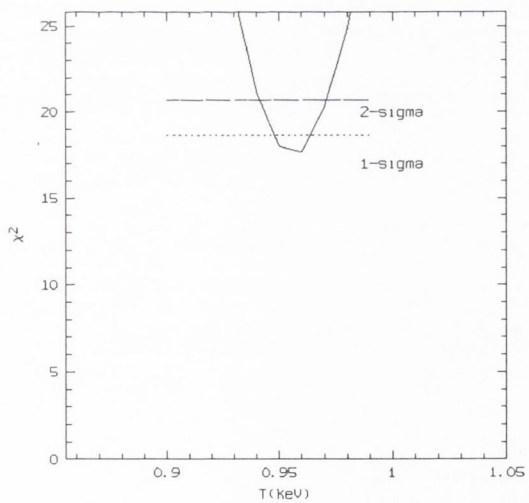


Figure 9.16: 1 dimensional χ^2 plot for the elliptical galaxy NGC4472 as a function of temperature for two confidence levels of 68.3% and 94.5 %.

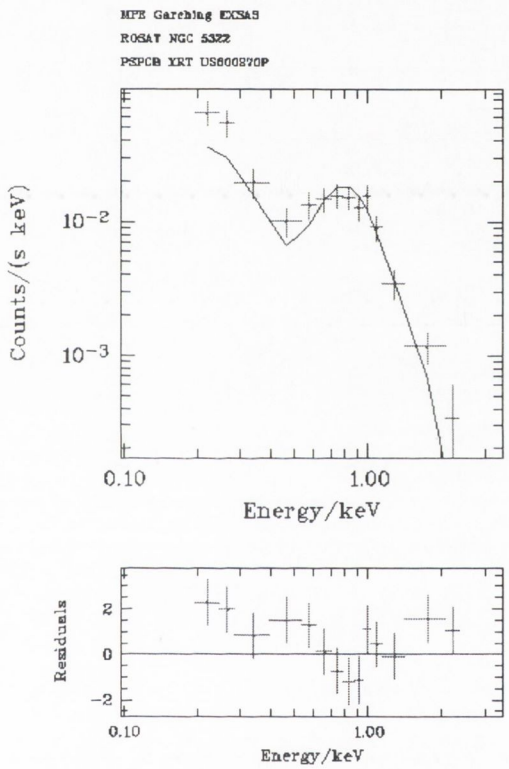


Figure 9.17: Spectrum of NGC5322.

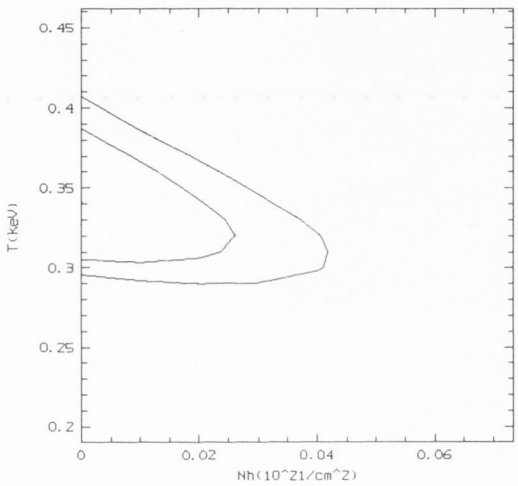


Figure 9.18: 2 dimensional χ^2 plot for the elliptical galaxy NGC5322 as a function of the temperature and the column density for two confidence levels of 68.3% and 94.5 %.

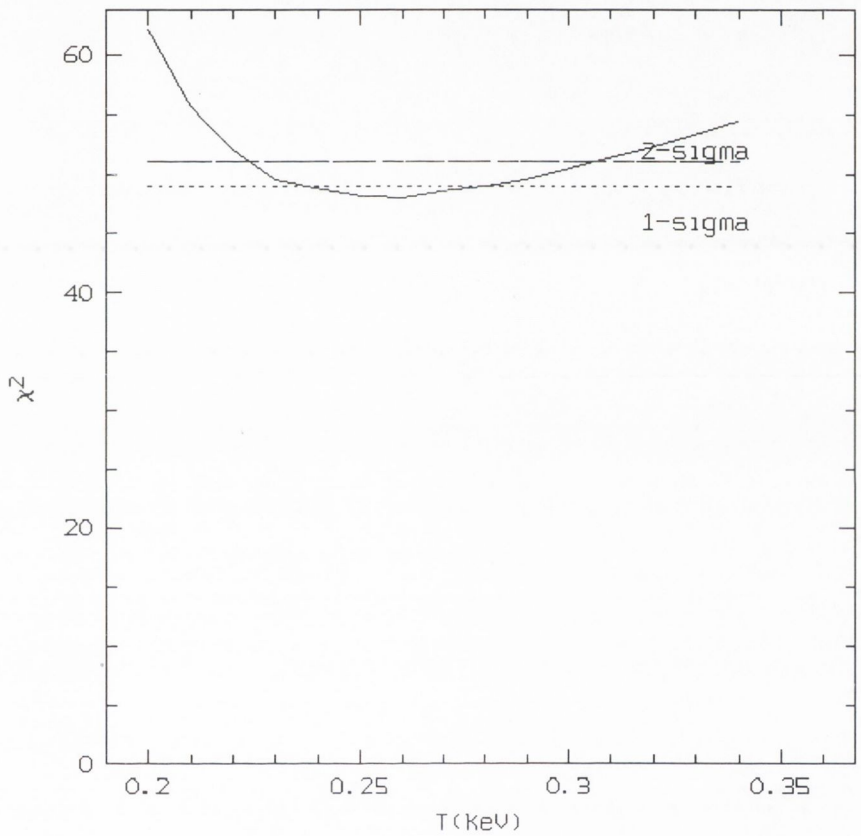


Figure 9.19: 1 dimensional χ^2 plot for the elliptical galaxy NGC5322 as a function of temperature for two confidence levels of 68.3% and 94.5 %.

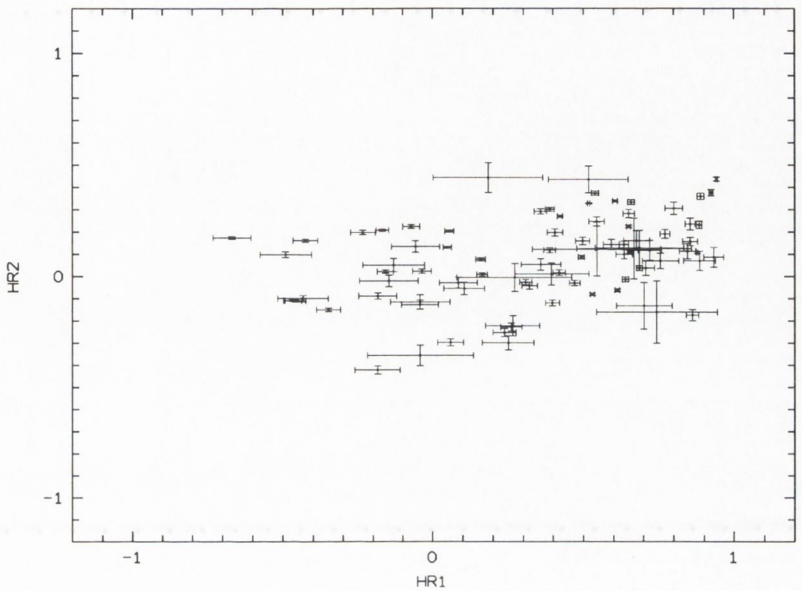


Figure 9.20: Observed values of HR1 and HR2.

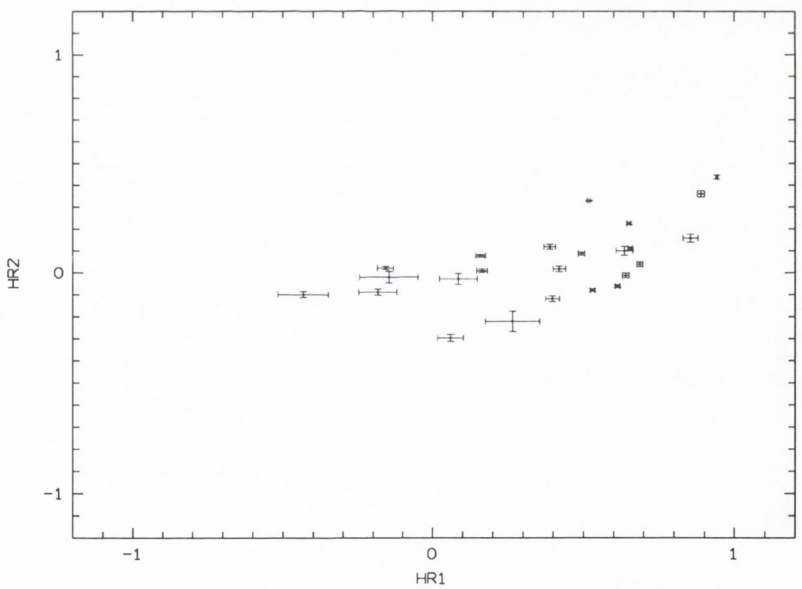


Figure 9.21: Observed values of HR1 and HR2 for the 24 galaxies which have both DW temperatures and reliable temperature estimates from our simulated grid. They are distributed similarly to the entire sample shown above.

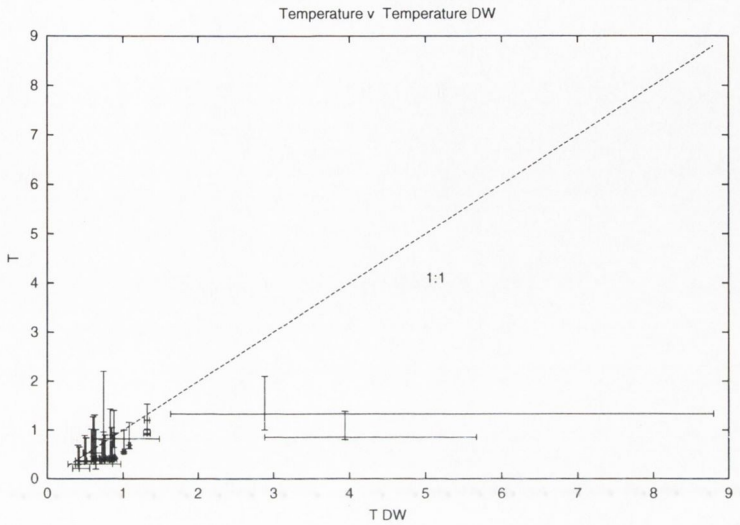


Figure 9.22: Comparison of Temperatures with those of DW, for the 24 galaxies in our sample for which we have reliable temperatures.

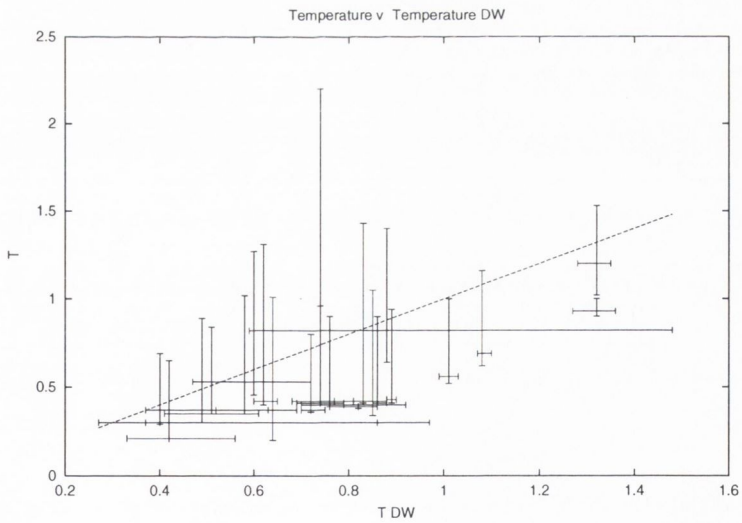


Figure 9.23: Comparison of Temperatures with those of DW, this time we exclude the two galaxies with the highest Davis & White derived temperature.

Name	ROSAT ID	Right Asc	Dec	z	HR1	EHR1	HR2	EHR2	T	Cts	N_H Grid	Ext Rad
(1)	(2)	(3)	(4)	(5)	(6)	(7)	(8)	(9)	(10)	(11)	(12)	(13)
IC310	800032	49.1788	41.3249	5660	0.88	0.01	0.23	0.02	$0.72^{+0.48}_{-0.07}$	3051	1.30	180
IC1459 $\star$	600266	344.294	-36.4622	1691	0.39	0.02	0.12	0.01	$0.53^{+0.74}_{-0.07}$	2745	0.12	90
IC1860	600590	42.3905	-31.1891	6886	0.65	0.02	0.28	0.02	$0.82^{+0.44}_{-0.03}$	1529	0.21	90
NGC315*$\star$	700424	14.4537	30.3525	4942	0.93	0.04	0.09	0.05	$0.49^{+0.68}_{-0.09}$	474	0.59	90
NGC221	600068	10.6744	40.8644	145	0.89	0.01	0.36	0.02	$0.85^{+0.43}_{-0.05}$	4592	0.63	150
NGC499	600254	20.7979	33.4606	4399	0.69	0.20	0.12	0.14	$0.58^{+0.60}_{-0.18}$	46	0.52	90
NGC507	600254	20.9167	33.2556	4934	0.85	0.02	0.24	0.03	$1.02^{+0.14}_{-0.03}$	1073	0.52	90
NGC533	600541	21.381	1.759	5549	0.77	0.02	0.19	0.02	$0.64^{+0.51}_{-0.01}$	1645	0.31	90
NGC708 $\star$	800254	28.192	36.152	4855	0.92	0.01	0.38	0.02	$0.94^{+0.52}_{-0.04}$	3346	0.54	90
NGC720	600005	28.252	-13.738	1745	0.40	0.03	-0.12	0.02	$0.37^{+0.65}_{-0.02}$	2081	$0.20^{+0.01}_{-0.02}$	130
NGC741	800507	29.088	5.629	5561	0.85	0.03	0.11	0.04	$0.54^{+0.48}_{-0.09}$	682	0.44	90

Name	ROSAT ID	Right Asc	Dec	z	HR1	EHR1	HR2	EHR2	T	cts Grid	N_H	Ext rad
(1)	(2)	(3)	(4)	(5)	(6)	(7)	(8)	(9)	(10)	(11)	(12)	(13)
NGC1316⋆	700437	50.673	-37.209	1760	0.47	0.02	-0.03	0.01	$0.40^{+101}_{-0.03}$	3125	0.19	90
NGC1395	600133	54.623	-23.027	1717	0.16	0.02	0.01	0.01	$0.39^{+0.01}_{-0.01}$	3288	$0.91^{+0.12}_{-0.15}$	250
NGC1399	600043	54.622	-35.452	1425	0.65	0.01	0.22	0.01	$0.69^{+0.57}_{-.07}$	15820	$0.69^{+0.06}_{-0.07}$	90
NGC1404	600043	54.717	-35.593	1947	0.53	0.01	-0.01	0.01	$0.42^{+0.89}_{-0.02}$	13789	$0.21^{+0.02}_{-0.04}$	90
NGC1553⋆	600623	64.043	-55.781	1080	-0.04	0.04	0.02	0.01	$0.39^{+0.88}_{-0.01}$	1598	0.15	200
NGC2329	800575	107.283	48.615	2329	0.72	0.04	0.12	0.05	$0.55^{+0.52}_{-0.13}$	318	0.74	90
NGC2563	600542	125.149	21.068	2563	0.59	0.03	0.14	0.02	$0.60^{+0.47}_{-0.02}$	950	0.42	90
NGC2832	600547	139.945	33.750	6948	0.50	0.02	0.16	0.02	$0.64^{+0.82}_{-0.03}$	1439	0.16	90
NGC2300	900161	113.081	85.709	1938	0.32	0.03	-0.04	0.02	$0.40^{+1.56}_{-0.01}$	1340	0.53	350
NGC3226⋆	700996	155.863	19.898	1151	0.66	0.01	0.33	0.01	$0.86^{+0.63}_{-0.03}$	4031	0.21	125
NGC3862	800153	176.271	19.6063	6511	0.49	0.01	0.13	0.01	$0.62^{+0.71}_{-0.01}$	5600	0.23	100

Name	ROSAT ID	Right Asc	Dec	z	HR1	EHR1	HR2	EHR2	T	cts Grid	N_H	Ext rad
(1)	(2)	(3)	(4)	(5)	(6)	(7)	(8)	(9)	(10)	(11)	(12)	(13)
NGC4073	800127	181.112	1.897	5952	0.54	0.01	0.38	0.01	$2.41^{+1.19}_{-1.39}$	4600	0.19	160
NGC4125⋆	600253	182.023	65.175	1356	0.06	0.04	-0.30	0.02	$0.21^{+0.44}_{0}$	555	0.18	150
NGC4203*⋆	600130	183.771	33.197	1086	0.06	0.02	0.20	0.01	$0.70^{+0.70}_{-0.50}$	4681	0.12	90
NGC4261⋆	700425	184.847	5.82522	2238	0.42	0.02	0.02	0.02	$0.42^{+1.01}_{-0.01}$	2081	0.16	90
NGC4278⋆	701413	185.028	29.2808	649	0.09	0.06	-0.03	0.03	$0.30^{+0.71}_{-0.10}$	255	0.18	150
NGC4291	700434	185.074	75.3708	1757	0.26	0.04	-0.23	0.02	$0.30^{+0.42}_{-0.01}$	762	0.30	125
NGC4365	600009	186.117	7.31750	1243	-0.16	0.03	0.02	0.01	$.82^{+0.58}_{-0.18}$	1311	0.16	175
NGC4374⋆	701404	186.265	12.8870	1060	0.64	0.03	0.01	0.02	$0.41^{+0.55}_{-0.01}$	1793	0.26	175
NGC4406	600105	186.549	12.9462	-244	0.69	0.01	0.04	0.01	$0.43^{+0.51}_{-0.02}$	5207	0.26	90
NGC4472	600248	187.445	8.00042	997	0.65	0.01	0.11	0.01	$0.56^{+0.44}_{-0.04}$	10577	$0.20^{+0.02}_{-0.01}$	180
NGC4486	800365	187.706	12.3911	1307	0.52	0.01	0.33	0.01	$1.2^{+0.33}_{-0.18}$	50854	0.25	115

Name	ROSAT ID	Right Asc	Dec	z	HR1	EHR1	HR2	EHR2	T	cts Grid	N_H	Ext rad
(1)	(2)	(3)	(4)	(5)	(6)	(7)	(8)	(9)	(10)	(11)	(12)	(13)
NGC4552⋆	600586	188.916	12.5562	340	0.16	0.02	0.08	0.01	$0.42^{+1.78}_{-0.01}$	3961	0.26	250
NGC4627	600129	190.499	32.5736	765	0.25	0.09	-0.30	0.03	$0.21^{+0.52}_{-0.01}$	301	0.13	90
NGC4636⋆	600016	190.708	2.68806	938	0.62	0.01	-0.06	0.01	$0.37^{+0.43}_{-0.01}$	10872	$0.32^{+0.01}_{-0.04}$	190
NGC4649	600017	190.915	11.5526	1117	0.49	0.01	0.01	0.01	$0.41^{+0.49}_{-0.01}$	7193	0.22	225
NGC4696	800192	192.205	-41.311	2958	0.94	0.01	0.44	0.01	$0.93^{+0.07}_{-0.03}$	10176	0.81	90
NGC4697	600262	192.149	-5.80081	1244	-0.15	0.10	-0.02	0.03	$0.35^{+0.54}_{-0.05}$	205	0.21	250
NGC5044	800020	198.850	-16.3851	2704	0.88	0.01	0.11	0.01	$0.50^{+0.48}_{-0.08}$	26676	$0.56^{+0.01}_{-0.02}$	93
NGC5129	800489	201.042	13.9766	6908	0.76	0.06	0.07	0.04	$0.46^{+0.54}_{-0.01}$	692	$0.74^{+0.05}_{-0.52}$	175
NGC5216	800476	203.029	62.7006	2955	0.40	0.12	0.01	0.05	$0.42^{+1.58}_{-0.02}$	175	0.19	100
NGC5419	800274	210.910	-33.9804	4172	0.68	0.04	0.16	0.05	$0.63^{+0.63}_{-0.08}$	293	0.55	90
NGC5846⋆	600257	226.622	1.60570	1714	0.64	0.01	-0.01	0.01	$0.40^{+0.50}_{-0.02}$	4448	0.43	250

Name	ROSAT ID	Right Asc	Dec	z	HR1	EHR1	HR2	EHR2	T	cts Grid	N_H rad	Ext
(1)	(2)	(3)	(4)	(5)	(6)	(7)	(8)	(9)	(10)	(11)	(12)	(13)
NGC6160*	800363	246.922	40.9267	9523	-0.01	0.03	0.22	0.01	$1.1^{+0.9}_{-0.9}$	1584	0.09	200
NGC6166	800644	247.160	39.5516	9100	0.42	0.01	0.27	0.01	$0.62^{+0.92}_{-0.20}$	13695	$0.3^{+0.01}_{-0.01}$	90
NGC6173*	8.00363	247.437	40.8116	8784	-0.17	0.02	0.21	0.10	$1.1^{+0.9}_{-0.9}$	2825	0.10	300
NGC6269	600583	254.492	27.8543	10433	0.80	0.03	0.31	0.03	$0.86^{+0.45}_{-0.04}$	921	0.48	150
NGC6868	700488	302.475	-48.3798	2854	0.31	0.02	-0.03	0.01	$0.48^{+1.77}_{-0.08}$	2627	0.49	300
NGC7619	600134	350.060	8.20611	3762	0.71	0.03	0.04	0.03	$0.43^{+0.53}_{-0.01}$	571	0.50	90
NGC7626	600134	350.176	8.21736	7626	0.89	0.05	0.07	0.04	$0.49^{+0.57}_{-0.09}$	563	$0.81^{+0.40}_{-0.21}$	150
IC4765	800256	281.825	-63.3300	4507	0.63	0.02	0.14	0.02	$0.62^{+0.45}_{-0.02}$	2333	0.71	250
ESO3060	300023	85.0258	-40.8360	10734	0.54	0.03	0.25	0.02	$0.80^{+0.41}_{-0.05}$	1606	0.32	90
IC1633	800276	17.4784	-45.9326	7270	0.36	0.02	0.30	0.02	$0.80^{+0.80}_{-0.18}$	1997	0.20	100
IC5358	800354	356.938	-28.1407	8646	0.39	0.02	0.30	0.01	$1.32^{+0.41}_{-1.02}$	3611	0.16	115

Name	ROSAT ID	Right Asc	Dec	z	HR1	EHR1	HR2	EHR2	T	cts Grid	N_H rad	Ext
(1)	(2)	(3)	(4)	(5)	(6)	(7)	(8)	(9)	(10)	(11)	(12)	(13)
NGC1052⋆	600520	40.2889	-8.119	1470	-0.43	0.08	-0.10	0.01	$1.33^{+0.77}_{-0.33}$	118	0.31	100
NGC1199*	800566	45.9107	-15.6140	2570	-0.13	0.10	0.05	0.03	$1.1^{+0.9}_{-0.9}$	93	0.43	90
NGC1379	600043	54.0165	-35.4413	1324	0.60	0.01	0.34	0.05	$0.86^{+0.70}_{-0.06}$	21558	1.31	275
NGC1380	600043	54.1139	-34.9760	1877	0.36	0.07	0.05	0.03	$0.48^{+1.68}_{-0.05}$	1689	1.31	225
NGC1407	600163	55.0493	-18.5801	1779	0.85	0.02	0.16	0.02	$0.40^{+0.46}_{-0.06}$	2926	0.54	
NGC1411*	150082	54.6866	-44.1004	983	-0.43	0.04	0.16	0.01	$1.1^{+0.9}_{-0.9}$	763	0.17	125
NGC1427*	800300	55.5810	-35.3926	0	-0.05	0.08	-0.13	0.03	$0.30^{+0.10}_{-0.10}$	68	0.12	90
NGC1705	600436	73.5570	-53.3613	628	-0.04	0.18	-0.36	0.05	$0.24^{+0.78}_{-0.04}$	255	0.42	250
NGC2577	700831	125.681	22.5531	2057	0.74	0.20	-0.16	0.14	$0.31^{+0.10}_{-0.09}$	39	$0.52^{+0.58}_{-0.33}$	90
NGC2887	500130	140.851	-63.8125	2907	0.70	0.09	-0.13	0.10	$0.34^{+0.53}_{-0.07}$	78	$0.44^{+0.27}_{-0.15}$	90
NGC3073*	700319	150.218	55.6182	1217	-0.47	0.03	-0.11	0.01	$0.20^{+1.04}_{-0.0}$	98	0.08	90

Name	ROSAT ID	Right Asc	Dec	z	HR1	EHR1	HR2	EHR2	T	Cts	N_H Grid	Ext rad
(1)	(2)	(3)	(4)	(5)	(6)	(7)	(8)	(9)	(10)	(11)	(12)	(13)
NGC3115	600120	151.308	-7.71856	720	0.69	0.15	0.13	0.08	$0.55^{+0.58}_{-0.13}$	135	0.43	150
NGC3193*	800125	154.604	21.8940	1399	-0.04	0.10	-0.12	0.03	$0.33^{+0.46}_{-0.13}$	103	0.21	100
NGC3585	600524	168.321	-26.7551	1399	0.26	0.09	-0.22	0.05	$0.30^{+0.39}_{-0.01}$	113	0.56	125
NGC3599*	300169	168.863	18.1103	835	-0.69	0.06	0.17	0.01	$1.1^{+0.9}_{-0.9}$	192	0.14	125
NGC3610	600250	169.605	58.786	1696	-0.49	0.09	0.09	0.01	$2.36^{+0.04}_{-0.04}$	107	0.74	100
NGC3923*	600533	177.757	-28.806	1788	0.86	0.02	-0.17	0.03	$0.6^{+0.4}_{-0.4}$	1287	0.62	90
NGC4621*	600017	190.510	11.6467	410	0.18	0.18	0.44	0.07	$5.7^{+10}_{-4.16}$	159	0.22	125
NGC4638	600017	190.697	11.4425	1164	0.27	0.19	-0.01	0.06	$0.39^{+0.07}_{-0.03}$	172	0.22	125
NGC4660	600017	191.133	11.1903	1083	-0.35	0.04	-0.15	0.01	$1.87^{+0.05}_{-1.67}$	68	0.21	150
NGC5061	600528	199.520	-26.8363	2661	0.54	0.21	0.12	0.12	$0.59^{-0.13}_{-0.24}$	49	0.62	90
NGC5102	600526	200.490	-36.6302	467	-0.18	0.01	-0.42	0.02	$0.20^{+0.01}_{-0.01}$	170	0.43	100

Name	ROSAT ID	Right Asc	Dec	z	HR1	EHR1	HR2	EHR2	T	Cts	N_H Grid	Ext rad
(1)	(2)	(3)	(4)	(5)	(6)	(7)	(8)	(9)	(10)	(11)	(12)	(13)
NGC5173	600158	202.105	46.5915	2419	-0.46	0.03	-0.11	0.01	$0.23^{+0.02}_{-0.01}$	1083	0.17	150
NGC5253*	600534	204.983	-31.64	404	0.24	0.04	-0.25	0.02	$0.20^{+0.48}_{-0.0}$	660	0.39	100
NGC5322⋆	600270	207.313	60.191	1781	-0.18	0.06	-0.09	-0.01	$0.37^{+0.47}_{-0.0}$	709	0.18	150
NGC5838*⋆	600257	226.359	2.099	1363	-0.04	0.06	-0.13	0.02	$0.30^{+0.40}_{-0.10}$	369	0.42	125
NGC6861	701057	301.830	-48.370	2819	0.41	0.03	0.20	0.02	$0.73^{0.44}_{-0.05}$	1832	0.48	250
NGC7144*	600512	328.179	-48.254	1932	0.52	0.13	0.44	0.06	$1.47^{+0.53}_{-0.47}$	193	0.28	100

Name	ROSAT ID	Right Asc	Dec	z	HR1	EHR1	HR2	EHR2	T	Cts	N_H Grid	Ext rad
(1)	(2)	(3)	(4)	(5)	(6)	(7)	(8)	(9)	(10)	(11)	(12)	(13)
NGC7145*	600512	328.335	-47.882	1891	-0.23	0.04	0.20	0.01	$1.1^{+0.9}_{-0.9}$	674	0.27	150
NGC7176*	800419	330.535	-31.992	2511	0.11	0.07	-0.05	0.03	$0.30^{+0.10}_{-0.1}$	219	0.16	125
NGC7097*	701180	325.054	-42.5370	2539	-0.26	0.12	-0.002	0.03	2.2^{+1}_{-1}	67	0.25	150

Table 9.1: Column (1)the galaxy name,(an $*$ marks galaxies whose values of HR1 and HR2 lie outside the limits of our grid .i.e they are not well described by a Raymond-Smith model. We estimate a rough value of T and N_H, using nearby points (an error is given as well but the temperatures could be anywhere from T=0 to T= 16 keV.) (a $\star$ marks an active galaxy.(2) the sequence number allocated of the observation in the ROSAT data archive,(3)the Right Ascension in degrees, (4) the Declination in degrees, (5)the redshift, (6) HR 1, (7) the error in HR 1, (8) HR 2, (9) the error in HR 2, (10) The best fit temperature as estimated from our grid with errors, (12) N_H as estimated for the grid, if $\geq N_H$ galactic. Where the galactic value is taken no errors are given. Col (13) The extraction radius in arcseconds.

9.5 kT-σ Correlation

Davis & White plot kT (in keV) against σ, the central line -of-sight stellar velocity dispersions within the galaxies (using values of σ taken from Faber et al. (1989) and Dressler, Faber & Burstein (1991). Neglecting three galaxies with high temperatures (NGC 221, NGC 1052 and NGC 2768), they find the best fit yields $kT \propto \sigma^{1.45\pm0.20}$ for the 27 galaxies plotted. They conclude that this correlation is shallower than what would be obtained if the gas and the stars had the same kinetic temperature, indicating that warm diffuse gas is being detected down to low luminosities and velocity dispersions. David, Forman & Jones (David et al. 1999) and Ciotti et al. (Ciotti et al. 1991) expected such gas to be swept away by winds. They also conclude that the global gas temperatures are hotter than the kinetic temperatures of luminous stars in the galaxies, since $kT < \mu m_p \sigma^2$. We extend this analysis to our sample. Sixty nine of our galaxies have reliable temperature determinations (see Table 6.1) and of these we were able to find velocity dispersions for 52 (using the same sources of velocity dispersions as DW). We have 24 of these which overlap with the temperature determinations of DW. So we plot 2 samples, sample A (those which overlap with DW), and sample B (all 52 galaxies). We give the equations for the fit of DW (EQ. 2/ 9.1) and the fit if the gas and stars have the same kinetic energy (EQ. 1/ 9.2).

$$kT = \mu m_p \sigma^2 \tag{9.1}$$

where T is the temperature, σ is the velocity dispersion and μm_p is the reduced mass of the particles (in this case the stars).

$$kT \propto \sigma^{1.45} \tag{9.2}$$

In Figure 9.24 we see that the fit of DW agrees with about half the galaxies in the sample with several galaxies above this line (but their line fits all but three if the DW temperatures are used.). For the remaining galaxies the line EQ 3 is a much better fit implying that the gas and the stars have the same kinetic temperature for these galaxies. Extending this work to the full sample of 52 (Figure 9.25) we find that whilst the fit of DW does describe some galaxies ($\sim$ 10) many galaxies are represented by EQ.1, and there are

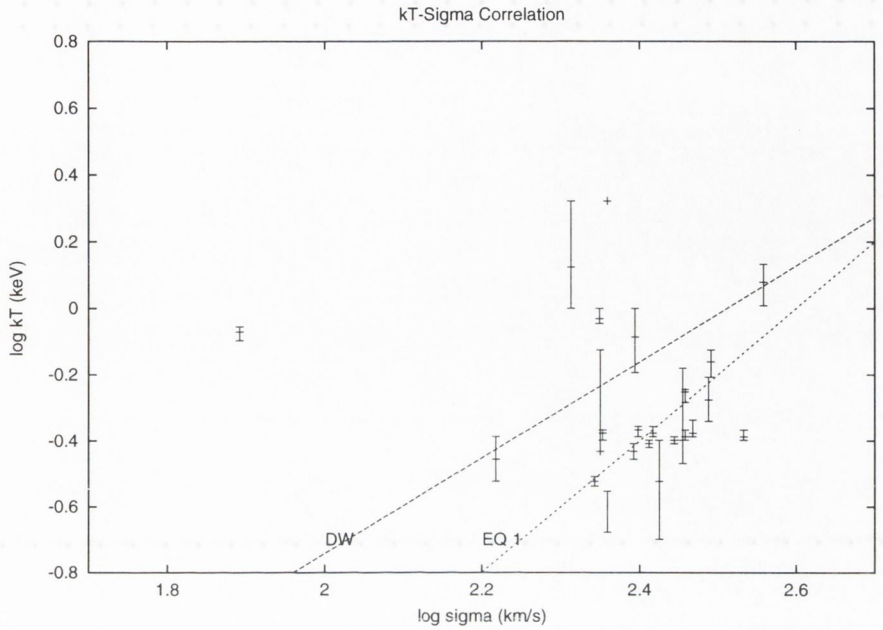


Figure 9.24: The log of kT versus the log of the velocity dispersion, for the sample used in DW, using the temperatures derived from HRs. The line DW represents $kT \propto \sigma^{1.45}$ and EQ. 3 represents $kT = \mu m_p \sigma^2$ i.e the fit if the gas and stars have the same kinetic energy.

galaxies (about seven) which lie above the fit of DW. These may contain a lot of warm diffuse gas (1-2 keV). We conclude that we can see two distinct populations i.e. galaxies whihc conatin a lot of warm diffuse gas and galaxies in which the gas and the stars have the same kinetic energy.

9.6 The L_x:T_x relation

In their 2003 paper O'Sullivan et al.(2003), using a sample of 34 galaxies observed with the ROSAT PSPC, produce a plot of the L_x:T_x relation (X-ray luminosity versus X-ray temperature). They find a tight relation between L_x and T_x with only a small number of outlying points and that their data follow a relation of similar slope to that for galaxy groups (Heldson & Ponman 2000) but offset to a lower luminosity or higher temperature(about a factor of 3 less luminous for a given temperature). We extend this work to a sample

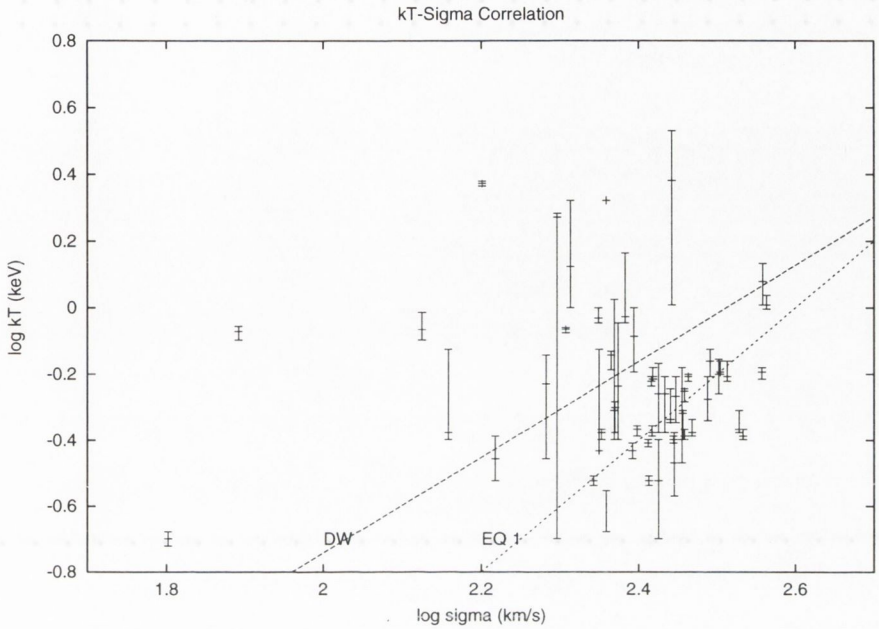


Figure 9.25: The log of kT versus the log of the velocity dispersion, for the sample B (all 52 galaxies with σ and reliable grid temperatures), using the temperatures derived from HRs. The line DW represents $kT \propto \sigma^{1.45}$ and EQ. 3 represents $kT = \mu m_p \sigma^2$ .i.e the fit if the gas and stars have the same kinetic energy.

of 54 galaxies. In Figure 9.26 below our data are consistent with the fit of O'Sullivan with only a handful of outlying points at low luminosities. The steep slope is usually explained as a product of preheating- the additional heating of the gas raises the temperature slightly and moves gas to a higher radii, lowering the central density and thus L_x. If we assume that the steep slope is caused by the same processes that cause it in groups, then this relation is a strong piece of evidence for the effects of preheating in galaxies (O'Sullivan et al. 2003).

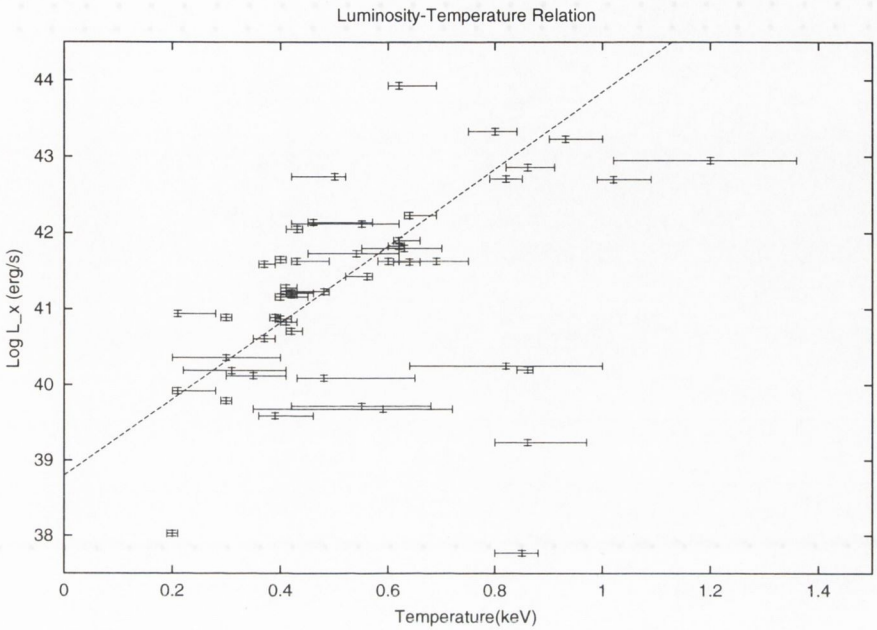


Figure 9.26: Log L_x plotted against temperature for the 54 galaxies in our sample which have an error of less than 0.2 keV in their temperature determinations. The solid line shown is the fit of O'Sullivan et al.(2003) for a sample of 34 galaxies observed with the ROSAT PSPC. All luminosities are taken from O'Sullivan et al. (2001)

9.7 Using Grids to search for activity

From 86 galaxies, we where able to determine accurate temperature estimates for 69, of the 17 that remain 14 lie outside the limits of our Raymond-Smith grid. In Figure 9.27 we plot these outlying points against a Raymond-Smith grid and in Figure 9.28 we plot these outlying points against a Power law grid. From these plots we conclude that the outlying galaxies are better described by a Power-law model and thus may be active galaxies. On checking the archives we find that most of these galaxies show signs of activity. This provides us with the means to check for signs of activity in galaxies just from looking at their hardness ratios.

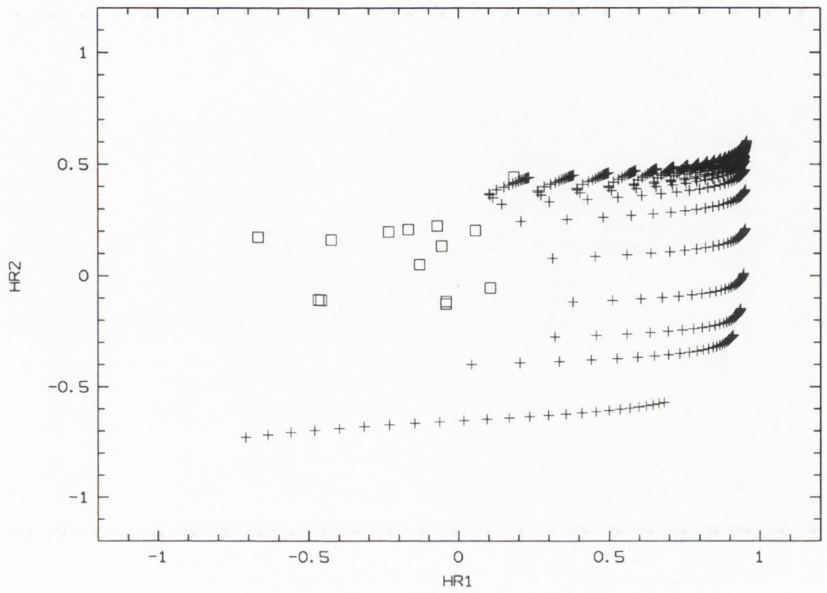


Figure 9.27: Outlying galaxies plotted against the Power Law grid. The boxes indicate observed hardness ratios for outlying galaxies, crosses indicate simulated grid points using the Raymond-Smith model.

9.8 Results

A histogram of determined temperatures is shown in Figure 9.29. We find only 3 of the 69 galaxies have values above 1.5 keV (namely NGC3610, NGC4660 and NGC4073 with no evidence in the literature that any of these three are unusual or contain AGNs), with a peak between 0.4-0.7 keV. In Figure 9.30 a plot is shown of HR1 against recessional velocity for all 86 elliptical galaxies in our sample. We see a trend of lower values of HR1 below a velocity of 3,000 km/s. In Figure 9.31 we observe lower values of HR2 below a velocity of 3,000 km/s. The histogram of counts for the 86 galaxies in our sample (Figure 9.32) shows that 41 galaxies in our sample have less than 1,000 counts and are thus unsuitable for spectral analysis. We plot luminosity against HR1,HR2 in Figure 9.33 and Figure 9.34. Active galaxies are marked by a □. We see no correlation between between activity and luminosity.

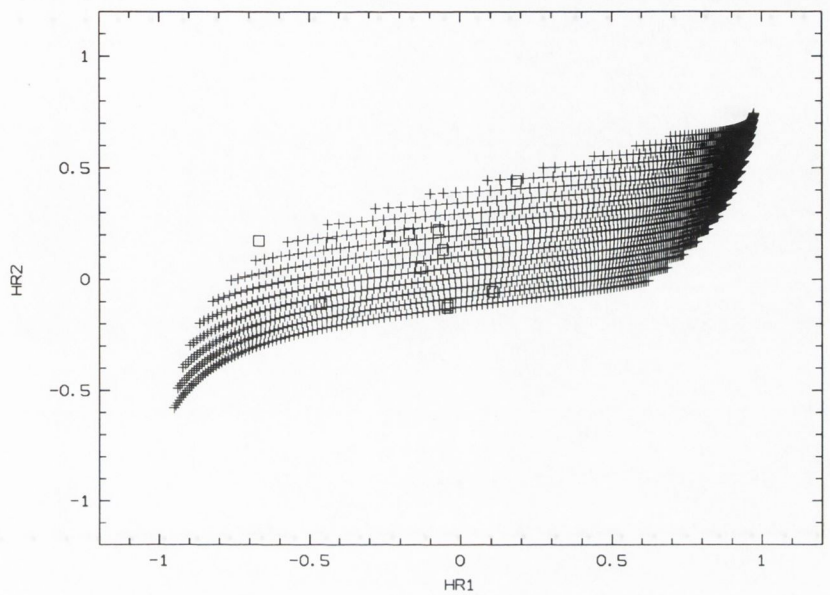


Figure 9.28: Outlying galaxies plotted against the Power Law grid. The boxes indicate observed hardness ratios for outlying galaxies, crosses indicate simulated grid points using the Power-law model.

9.9 Conclusion

We have analyzed 86 elliptical galaxies using data from the ROSAT PSPC, determining reliable temperatures for 69 of these. These temperatures are compared with, and found to be in good agreement with, values in the literature (Davis & White 1996) and with our own spectral analysis. Forty five of these ROSAT PSPC temperatures are new. We also have determined that twelve of our sample contain values of N_H above the galactic value. These values of N_H and temperature may be used to calculate more accurate fluxes and luminosities than those determined in the literature e.g. O'Sullivan et al. 2001. The temperatures have been used used to produce a plot of L_x-T_x using the luminosities of O'Sullivan et al.(2003), extending the sample to 54 galaxies in comparison with similar work of O'Sullivan using 39 galaxies.We find that the slope of the L_x-T_x plot is consistent with the slope found by O'Sullivan. This relation is strong evidence for the presence of pre-heating in galaxies. Seventeen of our sample lie outside the limits of our simulated

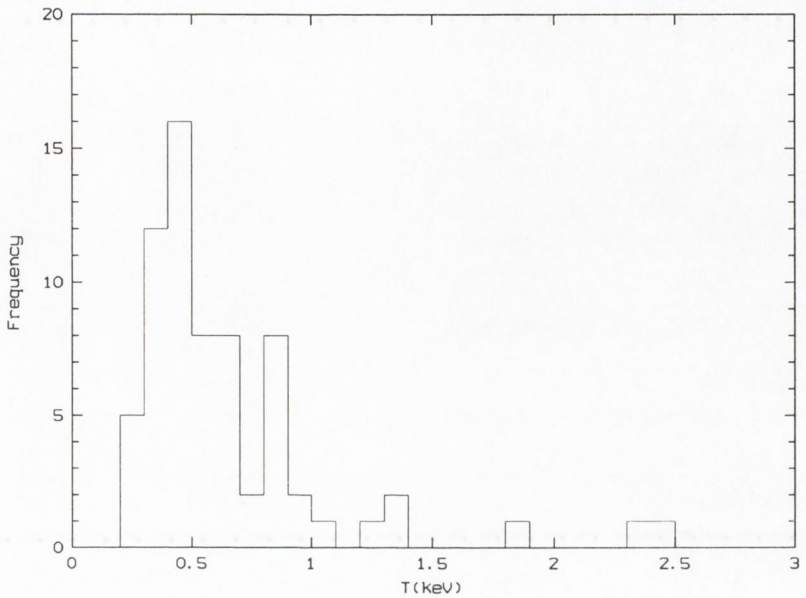


Figure 9.29: Histogram of temperatures, for the 69 galaxies in our sample with a reliable temperature determination.

grid, so we conclude that these galaxies are not well described by a Raymond-Smith model but are well described by a Power-law model i.e. there hardness ratios are consistent with values produced using a Power-law grid. This provides us with a method of selecting active galaxies just by looking at their hardness ratios. For NGC4486 and IC1459 DW fit a composite model using a Raymond-Smith model with a power law component, but we determine values consistent with theirs from our simulated grid.

9.10 Notes

9.10.1 NGC221

A temperatures of $3.94^{+1.73}_{-1.06}$ is observed by DW, which is much greater than those of other galaxies with similar velocity dispersions (Davis & White 1996). We observe a temperature of $0.85^{+0.03}_{-0.05}$ consistent with galaxies with similar velocity dispersions

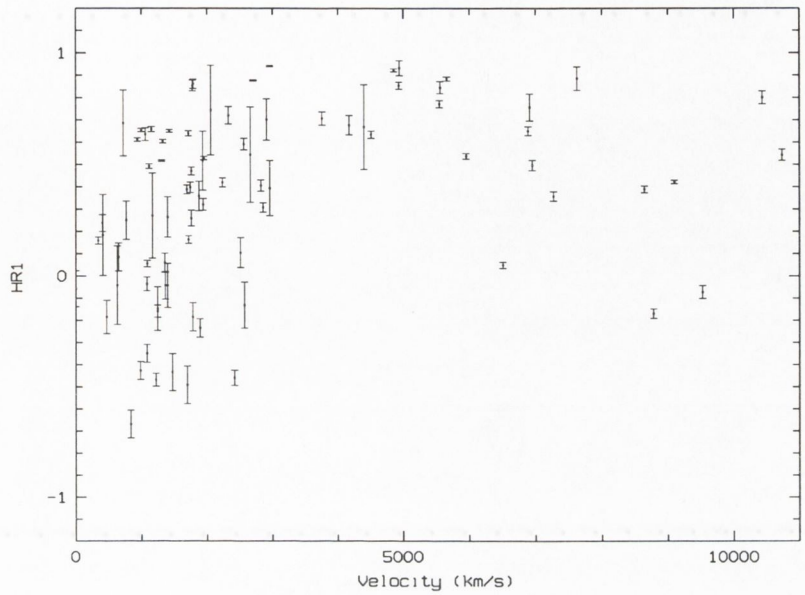


Figure 9.30: Plots of Hardness Ratio 1 against recessional velocity for 86 elliptical galaxies. As can be seen there is some correlation between HR1 and recessional velocity with lower values of HR1 below a velocity of 3,000 km/s.

9.10.2 NGC1052

A temperatures of $2.88^{+5.92}_{-1.25}$ is observed by DW, which is much greater than those of other galaxies with similar velocity dispersions (Davis & White 1996). We observe a temperature of $1.33^{+0.77}_{-0.33}$.

9.10.3 NGC 4486

Contains an AGN, need to fit composite models consisting of Raymond-Smith plus a power law spectral component (Davis & White 1996).We do determine a temperature of $1.2^{+0.33}_{-0.18}$ using our grid, which is consistent with the value of DW using a composite model $1.32^{+0.03}_{-0.04}$. HR1, HR2 doesn't deviate in HR1 v HR2 plots.

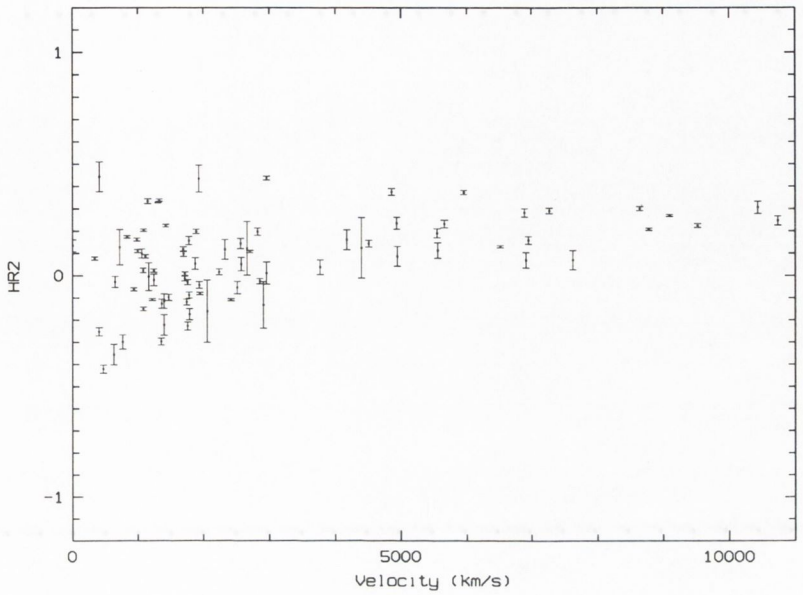


Figure 9.31: Plots of Hardness Ratio 2 against recessional velocity for 86 elliptical galaxies. Some evidence of a correlation between HR2 and recessional velocity is observed with lower values of HR2 below a velocity of 3,000 km/s

.

9.10.4 IC 1459

Contains an AGN, need to fit composite models consisting of Raymond-Smith plus a power law spectral component (Davis & White 1996). We do determine a temperature of $0.53^{+0.74}_{-0.07}$ using our grid, which is consistent with the value of DW using a composite model $0.60^{+0.12}_{-0.13}$. HR1, HR2 doesn't deviate in HR1 v HR2 plots.

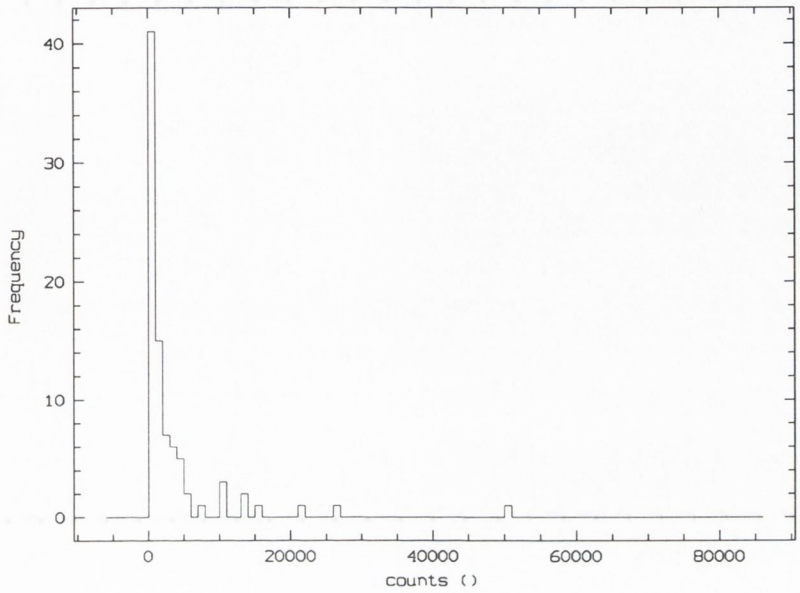


Figure 9.32: Histogram of counts, for the 86 galaxies in our sample. The first peak represent the 41 galaxies in our sample with less than 1000 counts.

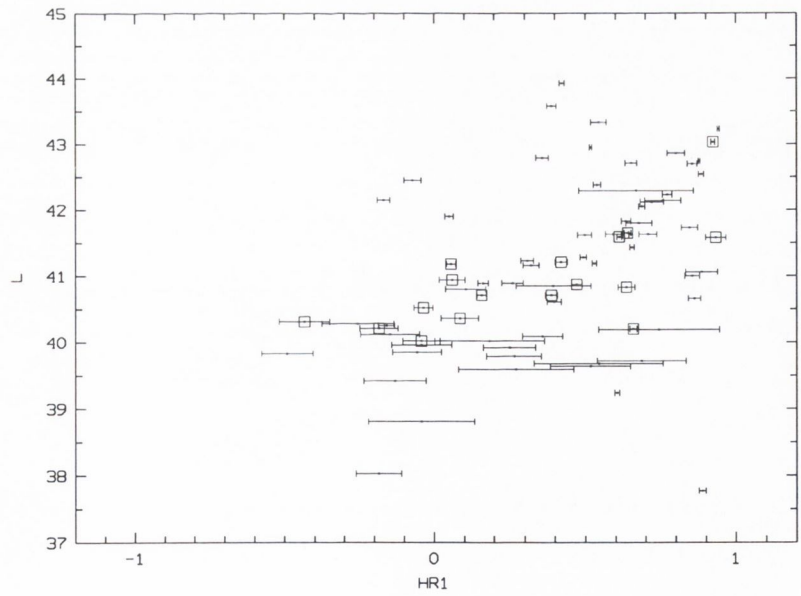


Figure 9.33: HR1 against luminosity from the literature O' Sullivan et al. 2001. Active galaxies are marked by a □.

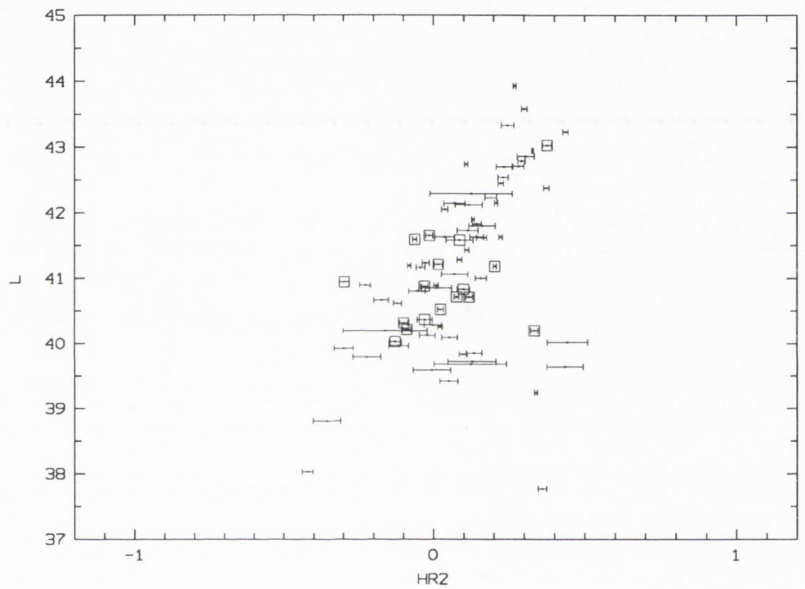


Figure 9.34: HR1 against luminosity from the literature O' Sullivan et al. 2001. Active galaxies are marked by a □.

Chapter 10

Conclusions and Future Work

10.1 Conclusions

We have introduced the concept of modeling spectra using a Power-Law model/Raymond-Smith model to produce grids of Hardness Ratios. These grids are then used to relate HR's (of observations with less than 1000 counts) to spectral properties (temperatures and N_H in the case of the Raymond-Smith model). The validity of this approach was confirmed by comparing spectral information retrieved from observations with more than 1000 counts, with information extracted using the hardness ratio grids. Satisfied with the validity of this approach we then used the Power-law grid to search for the presence of processed gas in three voids. We find evidence for the presence of processed gas in two of the Voids. Further work(see below) is required to get a better handle of the quantities involved, but this gas does have implications for the dark matter problem and for large scale structure formation models. In the second part of this thesis temperatures are determined for 22 EMSS clusters using the Raymond-Smith grid. The grid is validated using the galaxy clusters with more than 1000 observed photons. The temperatures are then used to calculate more accurate values of flux and luminosities for these galaxies. In the final part of the thesis the Raymond-Smith grid is used to extract temperatures for 69 elliptical galaxies observed with the ROSAT PSPC. These temperatures are the used to plot L_x:T_x for 53 galax-

ies confirming the slope found by O'Sullivan et al. (2003) for 39 galaxies providing strong evidence for the presence of pre-heating in galaxies.

10.2 Future Work

What direction might future work take to enhance the findings of this thesis, and make use of the HR grids developed here.

1. Voids: It would be useful to extend this work to other nearby voids, both using data from the ROSAT PSPC and other instruments with greater spectral resolution, both to confirm our findings of the presence of processed gas in voids, and to get more accurate measurements of the quantities involved.

2. Clusters: It is possible using the Raymond-Smith HR grid developed in this thesis to set limits on the temperatures of all clusters with less than 1000 counts present in the ROSAT data archive. Using these temperature more accurate flux and luminosity determinations are possible.

3. Elliptical galaxies: The temperatures derived for a sample of 69 elliptical galaxies may be used to investigate relations such as L_x:L_B (the X-ray luminosity versus the bolometric luminosity), σ:T_x (the velocity dispersion versus the X-ray temperature).

4. Grids: The Raymond-Smith grids modeled here may be used to obtain data from observations of other objects e.g. stars. Having shown the validity of modeling HR grids is would be possible to model similar grids for other models e.g Thermal Bremsstrahlung, or modeling Raymond-Smith and Power-law models for observation with other instruments e.g. ASCA, XMM.

Bibliography

Allen S.& Fabian A.1998. MNRAS, 297, L57-63.

Arons, J. 1972 ApJ, 172, 553.

Awaki, H.; Koyama, K.; Kunieda, H.; Takano, S.; Tawara, Y.; Ohashi, T. 1991. ApJ,366,88

Awaki, Hisamitsu; Mushotzky, Richard; Tsuru, Takeshi; Fabian, Andrew C.; Fukazawa, Yasushi; Loewenstein, Michael; Makishima, Kazuo; Matsumoto, Hironori;Matsushita, Kyoko; Mihara, Tatehiro 1994. PASJ, 46, L65

Bahcall, J.H. & Spitzer, L.,Jr. 1969 ApJ. 156, L63.

Ballanvd, C., Silk, J., & Schaeffer, R, 1998 ApJ, 497, 541

Baum, W. 1992 "A & A Encyclopaedia",(CUP), p76.

Bautz M.W., et al., 2002 Astro-ph/02022338

Böhringer H., et al., 2000. ApJS, 129, 435.

Beuing, J.; Dobereiner, S.; Bohringer, H.; Bender, R. 1999. MNRAS, 302, 209-221.

Bingelli, B. 1989 "Large-Scale Structure and Motions in the Universe", ed M. Mezetti, (Dordrecht: Kluwer),p47

Boller, T.H; Meurs, E.J.A & Adorf, H.-M. 1992 A & A , 259, 101B.

Bothun, Gregory D.; Schombert, James M.; Impey, Christopher D.; Sprayberry, David; McGaugh, Stacy S. 1993 AJ, 106, 530

Carlberg, R. G.; Yee, H. K. C.; Ellingson, E.; Abraham, R.; Gravel, P.; Morris, S.; Pritchet, C. J. 1996. ApJ, 462 ,32.

Carr M.J.,& Meurs E.J.A,. In press.2003

Carr M.J.,& Meurs E.J.A,. In prep. 2003

Coles P.,& Lucchin F.1995. "Cosmology" (Wiley) p67.

Colless, Matthew; Dalton, Gavin; Maddox, Steve; Sutherland, Will; Norberg, Peder; Cole, Shaun; Bland-Hawthorn, Joss; Bridges, Terry; Cannon, Russell; Collins, Chris; 2001 MNRAS, 328, 1039

Chincarini, G.; Thompson, L. A.; Rood, H. J. 1981 ApJ, 249, l47

Ciotti, Luca; Pellegrini, Silvia; Renzini, Alvio; D'Ercole, Annibale 1991 ApJ, 376, 121

Collinge et al. 2001 ApJ, 557:2-17.

da Costa, L. Nicolaci; Willmer, C. N. A.; Pellegrini, P. S.; Chaves, O. L.; Rit, C.; Maia, M. A. G.; Geller, M. J.; Latham, D. W.; Kurtz, M. J.; Huchra, J. P.;1998 AJ,116,1D

da Costa, L. Nicolaci; Geller, M. J.; Pellegrini, P. S.; Latham, D. W.; Fairall, A. P.; Marzke, R. O.; Willmer, C. N. A.; Huchra, J. P.; Calderon, J. H.; Ramella, M.; et al.1994 ApJ, 424, L1.

David L.P., Forman W., Jones C.1999. ApJ, 519, 533.

Davis D.S, & White R.E.I.,1996. ApJ, 470, l35

Dav, Romeel; Hernquist, Lars; Katz, Neal; Weinberg, David H. 1999 ApJ., 511, 521D.

Dekel, A. & Silk, J. 1986. ApJ. 303, 39

de Lapparent V., Geller M.J. & Huchra J.P. ApJ 302, L1

de Lapparant V., Geller M.J. & Huchra J.P 1988 "Large Scale Structures of the Universe:" Proc 130th symp IAU. p519

Dickey J.M., & Lockman F.J. 1990 ARA&A, 28, 215.

Donahue, M.1996. ApJ, 468, 79.

Donahue M., & Stocke J.T 1995. ApJ. 449, 554.

Donahue M.,Stocke J.T, Gioia I.M.,1992. ApJ, 385, 49

Dressler,A., Faber,S.M. & Burstein, D.,1991 ApJ, 368, 54

Ebeling H.,& Wiedenmann G.,1993. Phys. Rev. 47, 704.

Ebeling H.,Ebeling, H.; Edge, A. C.; Allen, S. W.; Crawford, C. S.; Fabian, A. C.; Huchra, J. P.,2000 MNRAS, 318, 333-340.

Ellis S.C., Jones L.R.,2001. MNRAS, 330, 631

Evrard A., et al, 1996. ApJ 469, 494.

Fairley, B. W.; Jones, L. R.; Scharf, C.; Ebeling, H.; Perlman, E.; Horner, D.; Wegner, G.; Malkan, M. 2000. MNRAS 315, 669.

Fabian, A. 1994 Ann.Rev A&A 32:277.

Fabbiano,G., Kim, D, & Trincieri, G. 1992 ApJS, 80, 531.

Faber, S.M. et al.1989 ApJS, 69, 763.

Forman,W., et al., 1993. MNRAS, 221, 1049.

Forman,W., Jones, C.,& Tucker, W.1985. ApJ, 293, 102

Gioia I.M.,Maccacaro T.,Schild R.E., et al,1990. ApJS, 72, 567

Giovanelli , R.& Haynes, M. 1991 ARA& A, 29, 499.

Gott, et al. 1986. ApJ, 306, 341.

Gregory, S.A. & Thompson, L.A. 1978 ApJ, 222, 784

Grogin, N.A, & Geller, M.J. 2000, AJ, 119, 32

Henning, P.A. & Kerr, F.J. 1989, ApJ, 347, L1.

Henry, J.P..1997 ApJ, 489, L1-L5

Hoffman, Y. Silk, J., & Wyse, R.F.G, 1992 ApJ. 388, L13.

Hubble, E. 1929 Proc NAS, 15, 168

Icke, V. 1984 MNRAS, 206, 1p.

Icke, V. & Van de Weygaert., 1989 A&A , 213, 1

Ikebe, Y. et al 2002 A&A, 383, 7731

Ingalls, J. C.; Bania, T. M.; Chamberlin, R. A.; Jackson, J. M.; Lane, A. P.; Rumitz, M.; Stark, A. A. 1998..AFA..2001.

Johnstone, R.M & Fabian, A.C, MNRAS, 237, 27.

Jones, C., & Forman W. ApJ, 276, 38

Jones, L. R.; Scharf, C.; Ebeling, H.; Perlman, E.; Wegner, G.; Malkan, M.; Horner, D.1998. ApJ, 495, 100-114.

Kaastra J.S. 1992 A&A, 264, 654

Kaastra, J.S., Ferrigno, C., Tamura, T., et al, 2001 A&A, 365, L99

Kaastra,J. 1997 "X-ray spectroscopy in Astrophysics", EADN Astrophysics School X, Amsterdam, The Netherlands, (Springer) p134.

Komossa,S., & Fink, H.,1997 A&A 322 719.

Komossa,S., & Fink, H.,1997 A&A 327, 555.

Kolb E.W & Turner M.S. 1989. "The Early Universe" (Addison-Wesley) p5.

Koopmans L.V.E 2001 PASA. 18 179.

Kirshner, Robert P.; Oemler, Augustus, Jr.; Schechter, Paul L.; Shectman, Stephen A.. 1987 ApJ, 314, 493.

Kuhn, B., Hopp, U., & Elsasser, H. 1997 A& A, 318,405.

Lacey, C., Guiderdoni, B., et al. 1993 ApJ, 402, 15

Lewis, Aaron D.; Ellingson, E.; Morris, Simon L.; Carlberg, R. G. 1999. ApJ, 517, 587-608.

Lynden-Bell D.1964 ApJ, 139 1195.

Maddox, Steve; 2DF Galaxy Redshift Survey Team; Bland-Hawthorn, Joss; Cannon, Russell; Cole, Shaun; Colless, Matthew; Collins, Chris; Couch, Warrick; Dalton, Gavin; Driver, Simon; and 12 coauthors 1998 "Large Scale Structure: Tracks and Traces. Proceedings of the 12th Potsdam Cosmology Workshop" Eds. V. Mueller, S. Gottloeber, J.P. Muecket, J. Wambsganss World Scientific 1998, p. 91-96.

Manning, C.V., 2002 AJ, 574, 599

Markevitch M.& Vikhlinin A., 1997. ApJ, 482, L13

Markevitch, Maxim; Forman, William R.; 1998 ApJ, 503, 77.

Mason, K. O.; Carrera, F. J.; Hasinger, G.; Andernach, H.; Aragon-Salamanca, A.; Barcons, X.; Bower, R.; Brandt, W. N.; Branduardi-Raymont, G.; Burgos-Martn, J.; and 18 coauthors 2000 MNRAS 311, 456-484.

Matsushita, K.; Makishima, K.; Awaki, H.; Canizares, C. R.; Fabian, A. C.; Fukazawa, Y.; Loewenstein, M.; Matsumoto, H.; Mihara, T.; Mushotzky, R. F.; 1994, ApJ, 436, L41

McLin, Kevin M.; Stocke, John T.; Weymann, R. J.; Penton, Steven V.; Shull, J. Michael 2002 AJ. 574, L115.

Mecke, K. R.; Buchert, T.; Wagner, H. 1994 A&A, 288, 697

Mewe, R.; Lemen, J. R.; van den Oord, G. H. J. 1986 A & AS, 65, 511

Mewe, R. 1997 "X-ray spectroscopy in Astrophysics", EADN Astrophysics School X, Amsterdam. The Netherlands, (Springer) p230.

Mohr J.J., & Evrard A.E. 1997 ApJ, 491 ,38.

Molendi, S. Maccacaro, T. & Schaeidt, S. 1993 A& A, 271, 18.

Molendi, S. & Maccacaro, T. 1994 A& A, 291, 420-424

Miralda-Escude, Jordi; Cen, Renyue; Ostriker, Jeremiah P.; Rauch, Micha 1996 ApJ, 471, 582.

Morrison R., & McCammon,D. 1983 ApJ, 270, 119.

Murphy, Edward M.; Lockman, Felix J.; Laor, Ari; Elvis, Martin. 1996 ApJS, 105, 369.

Mushotzky R.F.,& Scharf C.A.1997 ApJ, 482, L13.

Navarro, J.F.,Frenk, C.S & White, S.D.M 1995 MNRAS, 275, 720.

Nichol, R. C.; Holden, B. P.; Romer, A. K.; Ulmer, M. P.; Burke, D. J.; Collins, C. A. 1997, ApJ, 481, 644.

Neumann D. & Arnaud M. 1999. A&A, 348, 711.

Neumann D.& Boehringer H.1997. MNRAS, 289, 123N.

Osterbrock,D.1989. "Astrophysics of Gaseous Nebulae and Active Galactic Nuclei". Eds. University Science Books.

Page, M. J.; Mason, K. O.; Carrera, F. J.; Clavel, J.; Kaastra, J. S.; Puchnarewicz, E. M.; Santos-Lleo, M.; Brunner, H.; Ferrigno, C.; George, I. M.;, 2001 A & A., 365L,152.

O'Sullivan, Ewan; Forbes, Duncan A.; Ponman, Trevor J. 2001. MNRAS, 328,461.

O'Sullivan, Ewan; Ponman, Trevor; & Collins, Ross. 2003 astro-ph 0301153

Phillips K.J.H et al. 1999. A & AS., 138., 381P

Pierre, M. 1996 Les Houches, Session LX Cosmology & LSS p78.

Perlmuter, S. et al. 1997 ApJ., 483., 565.

Popescu, C.C.,Hopp, U., & Elsasser, H, 1997 A&A, 325, 88.1

Pustilnik, S.A., 2002 A&A, 389, 405.

Raymond J.C.,& Smith B.W.1977 ApJS, 35, 419.

Rector T.A., Stocke J.T.,Perlman E.S., 1998 ApJS, 516, 145

Rector, Travis A.; Stocke, John T.; Perlman, Eric S.; Morris, Simon L.; Gioia, Isabella M. 2000 AJ, 120, 1626

Rush, B. et al., 1996 ApJ, 471, 190

Shectmann S.A.,& Landy S.D.. 1996 ApJ, 470, 172

Smoot, G. F.; Bennett, C. L.; Kogut, A.; Wright, E. L.; Aymon, J.; Boggess, N. W.; Cheng, E. S.; de Amici, G.; Gulkis, S.; Hauser, M. G.; 1992 ApJ, 396, L1

Sparke, L.S. & Gallagher, J.S. 2000 "Galaxies in the Universe", (Cambridge University Press) p94.

Stark, Antony A.; Gammie, Charles F.; Wilson, Robert W.; Bally, John; Linke, Richard A.; Heiles, Carl; Hurwitz, Mark.1992. ApJS, 79, 77.

Stocke, John T.; Morris, Simon L.; Gioia, I. M.; Maccacaro, T.; Schild, R.; Wolter, A.; Fleming, Thomas A.; Henry, J. Patrick. 1991. ApJS, 76, 813.

Stocke, John T.; Perlman, Eric S.; Gioia, Isabella M.; Harvanek, Michael, 1999 AJ, 117, 1999

Szomoru, Arpad; van Gorkom, J. H.; Gregg, Michael D.; Strauss, Michael A. 1996 AJ, 111, 2150

Tanvir, N. R.; Shanks, T.; Ferguson, H. C.; Robinson, D. R. T. 1995 Nature, 327,27.

Trinchieri,G., Fabbiano, G., & Canizares, C.R. 1986. ApJ, 310, 637

Van den Bergh, S.,1992 Science, 258, 421.

Voges, W.; Aschenbach, B.; Boller, Th.; Bruninger, H.; Briel, U.; Burkert, W.; Dennerl, K.; Englhauser, J.; Gruber, R.; Haberl, F,1999 A&A, 349, 389.

Vikhlinin, A.; McNamara, B. R.; Forman, W.; Jones, C.; Quintana, H.; Hornstrup, A. 1998. ApJ, 502, 558.

Wang, Q.& Stocke, J.T. 1993 ApJ. 408, 71

Warwick,R.S.,Done,C.,Smith,D.A. 1995 MNRAS,275,1003.

Weinberg, David H.; Szomoru, Arpad; Guhathakurta, P.; van Gorkom, J. H. 1991 ApJ, 372, L13.

White, N.E.,Giommi,P. & Angelini.1994 AAS, 185,4111

Willick, J. & Butra, P. 2001 ApJ, 548, 564.

Wise, M. W.; McNamara, B. R.; Houck, J. C.; Davis, D. S.; Canizares, C. R.; Nulsen, P. E. J.; David, L. P. AAS, 32, 1703

Xu Haiguang; Jin Guangxue; Wu Xiang-Ping. 2001 ApJ, 553, 78

Yang, Y.; Wilson, A. S.; Ferruit, P. 2001 ApJ, 563, 124.

Zimmermann, H. U.; Belloni, T.; Boese, G.; Izzo, C.; Kahabka, P.; Schwentker, O. 1992 In Proc. European ISY meeting. Symposium Space Sciences.

NED http://nedwww.ipac.caltech.edu/

ROSAT data archive ftp.xray.mpe.mpg.de/rosat/archive/

Simbad http://simbad.u-strasbg.fr/sim-fid.pl

W3Browse http://heasarc.gsfc.nasa.gov/Tools/w3pimms.html

Appendix A

Spectral fits for the EMSS clusters

In this chapter we show the spectral fits for all 22 EMSS galaxy clusters from Chapter 5. The results from the spectral fits are outlined below in Table ??

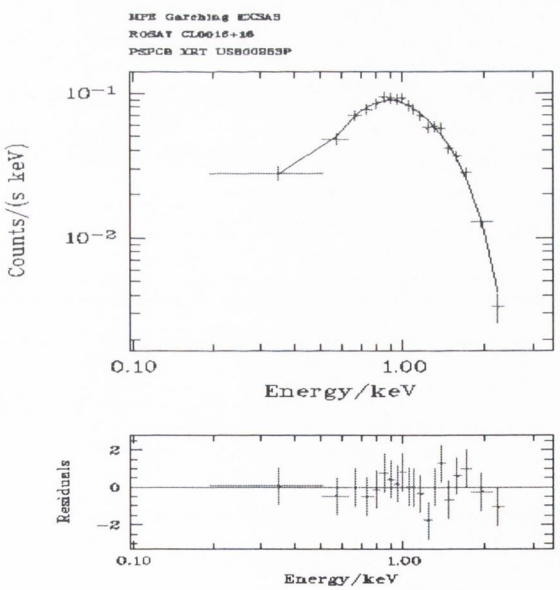


Figure A.1: Spectral fit of the Raymond-Smith model to the galaxy cluster MS0015.9+1609 with a reduced χ^2=1.01.

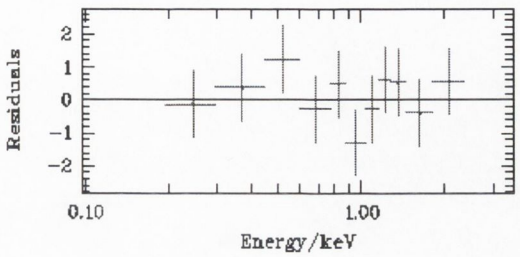


Figure A.2: Spectral fit of the Raymond-Smith model to the galaxy cluster MS0353.6-3642 with a reduced χ^2= 0.98.

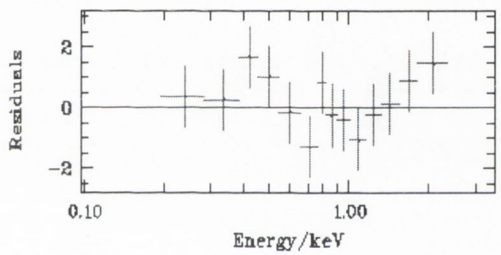


Figure A.3: Spectral fit of the Raymond-Smith model to the galaxy cluster MS0418.3-3844with a reduced χ^2=1.57.

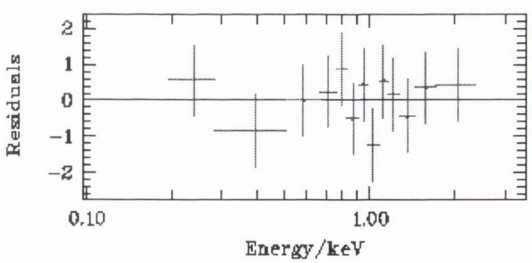


Figure A.4: Spectral fit of the Raymond-Smith model to the galaxy cluster MS0451.5+0250with a reduced χ^2=0.84.

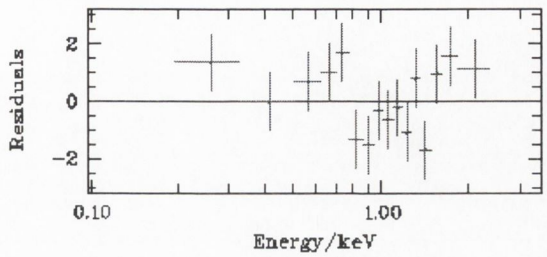


Figure A.5: Spectral fit of the Raymond-Smith model to the galaxy cluster MS0451.6-0305 with a reduced χ^2=1.55.

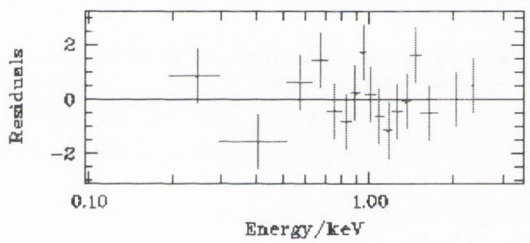


Figure A.6: Spectral fit of the Raymond-Smith model to the galaxy cluster MS0735.6+7421 with a reduced χ^2=0.70.

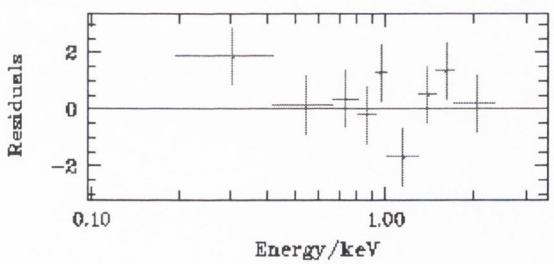


Figure A.7: Spectral fit of the Raymond-Smith model to the galaxy cluster MS0811.6+6301 with a reduced χ^2=1.40.

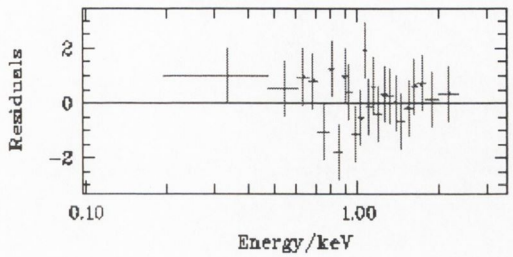


Figure A.8: Spectral fit of the Raymond-Smith model to the galaxy cluster MS1020.7+6820 with a reduced χ^2=1.26.

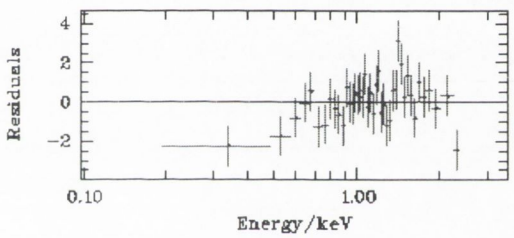


Figure A.9: Spectral fit of the Raymond-Smith model to the galaxy cluster MS1111.8-3754 with a reduced χ^2=1.32.

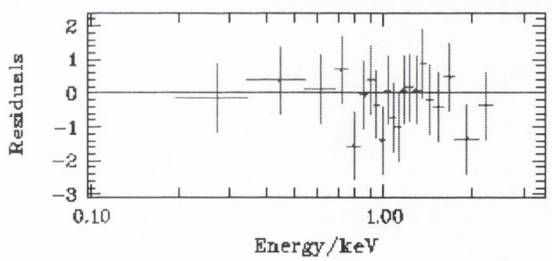


Figure A.10: Spectral fit of the Raymond-Smith model to the galaxy cluster MS1201.5+2824 with a reduced χ^2=0.64.

Appendix B

Further Spectral Fits of EMSS Clusters

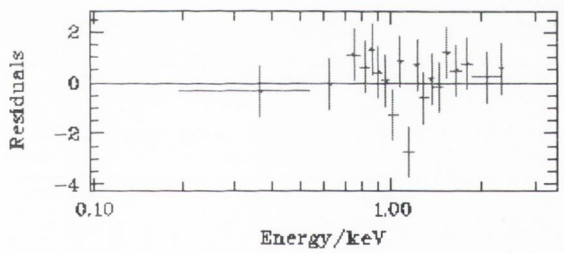


Figure B.1: Spectral fit of the Raymond-Smith model to the galaxy cluster MS1208.7+3928 with a reduced χ^2=1.22.

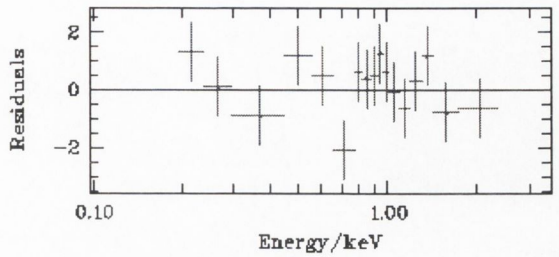


Figure B.2: Spectral fit of the Raymond-Smith model to the galaxy cluster MS1308.8+3244 with a reduced χ^2=1.16 .

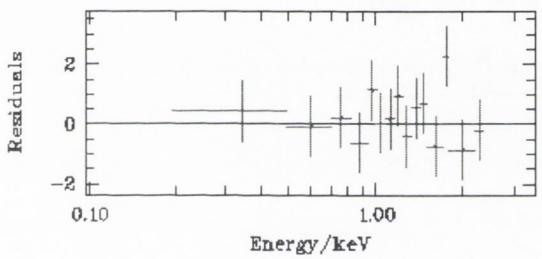


Figure B.3: Spectral fit of the Raymond-Smith model to the galaxy cluster MS1335.2-2928 with a reduced χ^2=1.60.

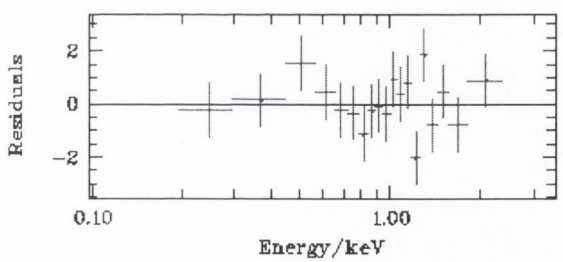


Figure B.4: Spectral fit of the Raymond-Smith model to the galaxy cluster MS1335.2-2928 with a reduced χ^2=0.77.

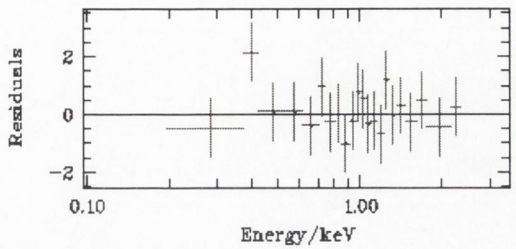


Figure B.5: Spectral fit of the Raymond-Smith model to the galaxy cluster MS1426.4+0158 with a reduced χ^2=0.58.

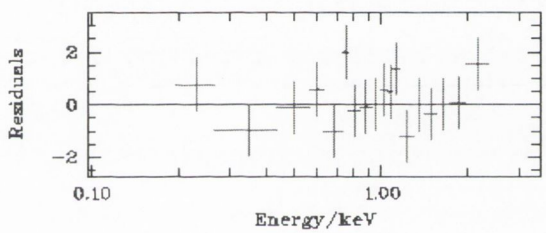


Figure B.6: Spectral fit of the Raymond-Smith model to the galaxy cluster MS1512.4+3647 with a reduced χ^2=0.59.

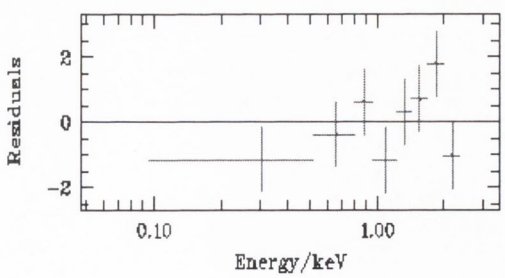


Figure B.7: Spectral fit of the Raymond-Smith model to the galaxy cluster MS1546.1+1132 with a reduced χ^2=1.35.

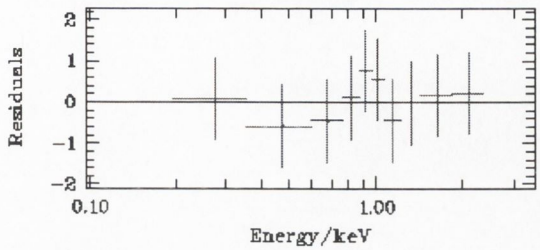


Figure B.8: Spectral fit of the Raymond-Smith model to the galaxy cluster MS1617.1+3237 with a reduced χ^2=0.20.

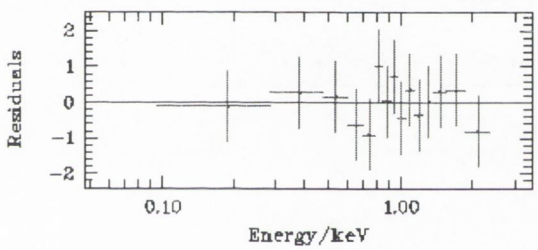


Figure B.9: Spectral fit of the Raymond-Smith model to the galaxy cluster MS2137.3-2353 with a reduced χ^2=0.07.

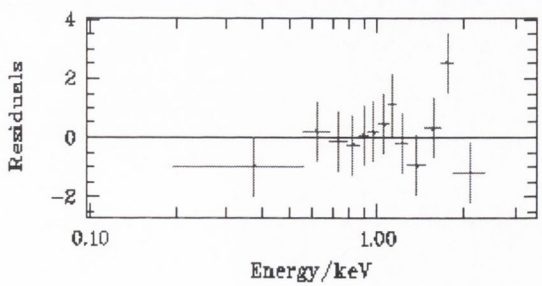


Figure B.10: Spectral fit of the Raymond-Smith model to the galaxy cluster MS2255.7+2039 with a reduced χ^2=0.64.

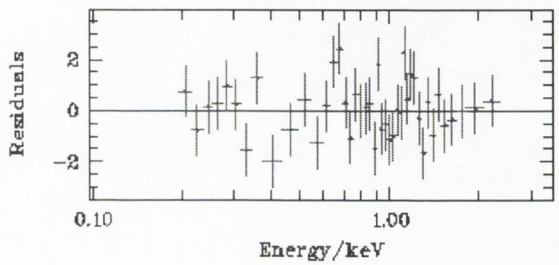


Figure B.11: Spectral fit of the Raymond-Smith model to the galaxy cluster MS2311.2-4259 with a reduced χ^2=1.22.

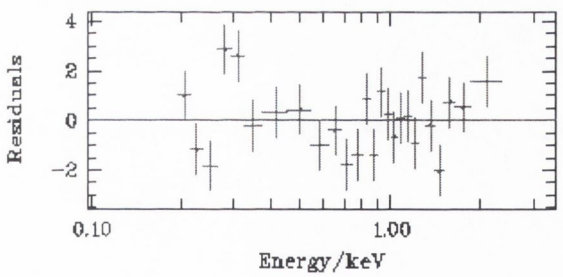


Figure B.12: Spectral fit of the Raymond-Smith model to the galaxy cluster MS2354.4-3502 with a reduced χ^2=1.96.

Appendix C

2 Dimensional χ^2 for the EMSS Galaxy Clusters

We present 2 dimensional χ^2 plots of N_H against temperature for two confidence levels of 68.3 % and 95.5 % for the 22 EMSS Galaxy clusters discussed in chapter 5. Some plots show a third contour (either a dot or a dashed line) this is the minimum in the chi-squared value.

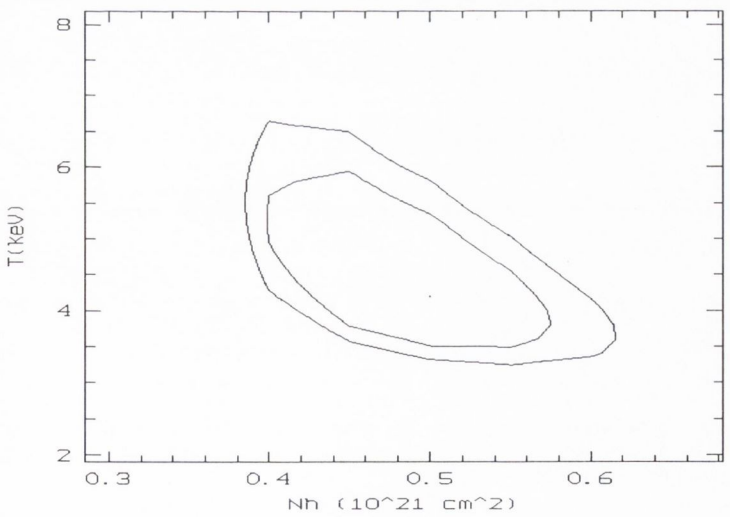


Figure C.1: 2 dimensional χ^2 plot for the galaxy cluster MS0015.9+1609.

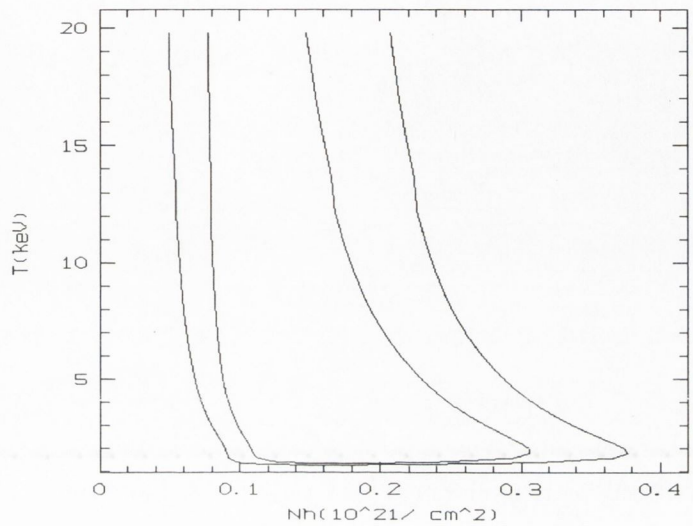


Figure C.2: 2 dimensional χ^2 plot for the galaxy cluster MS0353.6-3642 .

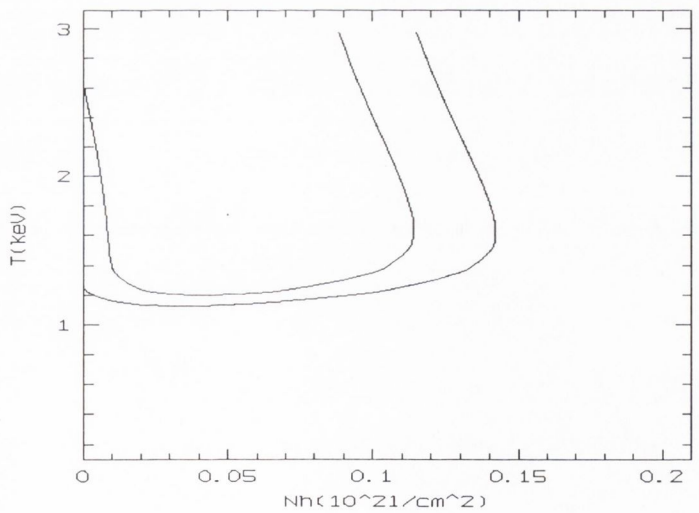


Figure C.3: 2 dimensional χ^2 plot for the galaxy cluster MS0418.3-3844 .

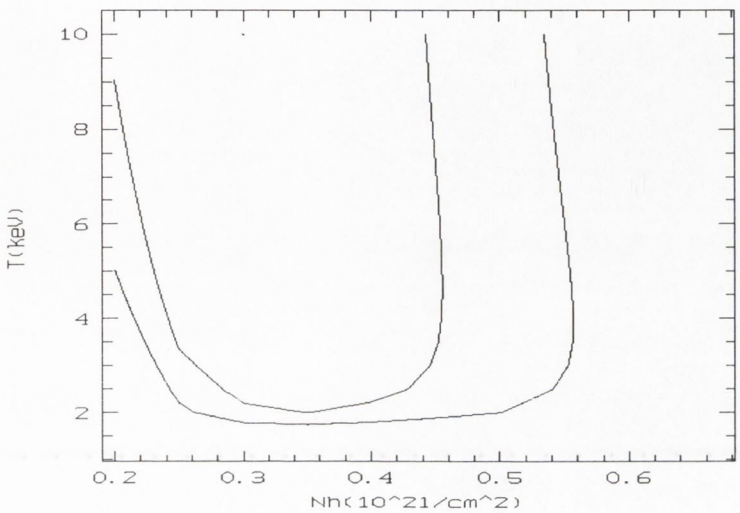


Figure C.4: 2 dimensional χ^2 plot for the galaxy cluster MS0451.5+0250.

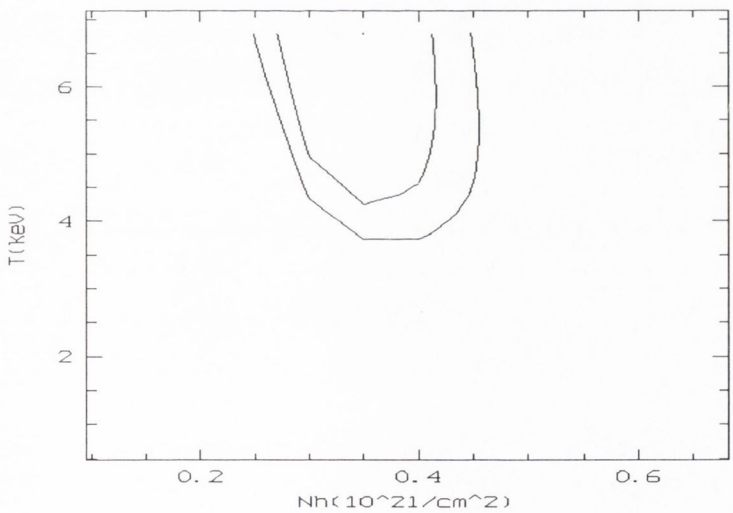


Figure C.5: 2 dimensional χ^2 plot for the galaxy cluster MS0451.6-0305.

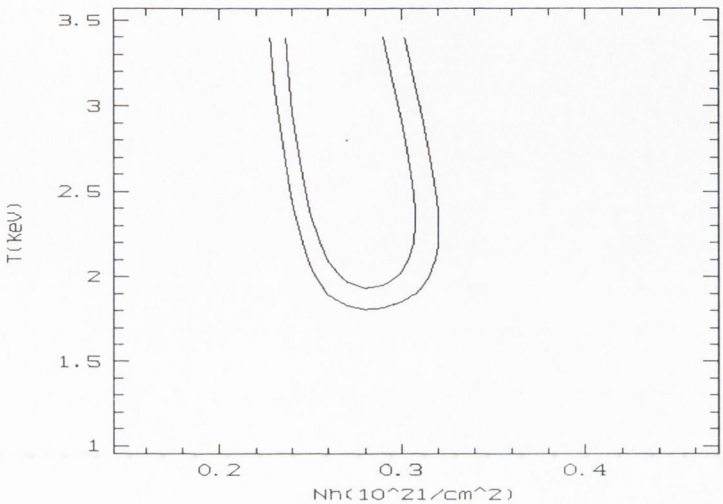


Figure C.6: 2 dimensional χ^2 plot for the galaxy cluster MS0735.6+7421.

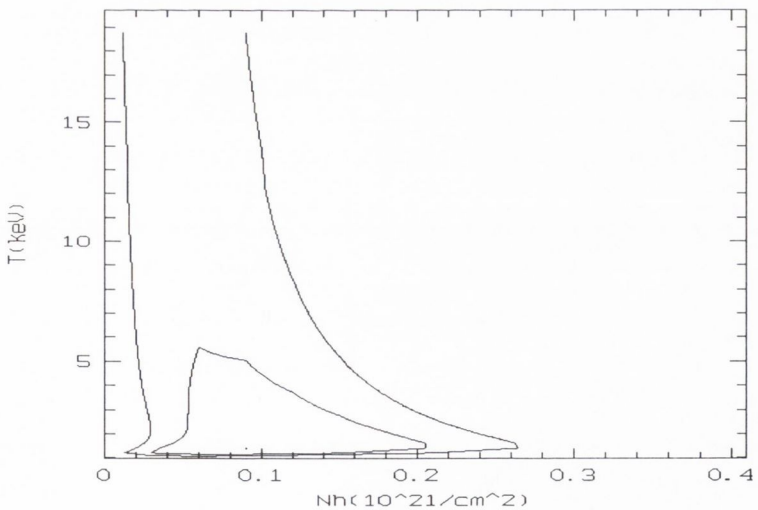


Figure C.7: 2 dimensional χ^2 plot for the galaxy cluster MS0811.6+6301.

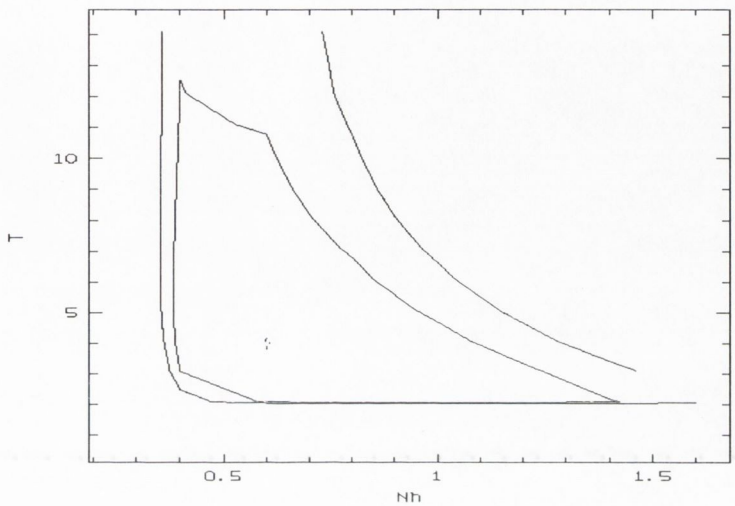


Figure C.8: 2 dimensional χ^2 plot for the galaxy cluster MS1020.7+6820.

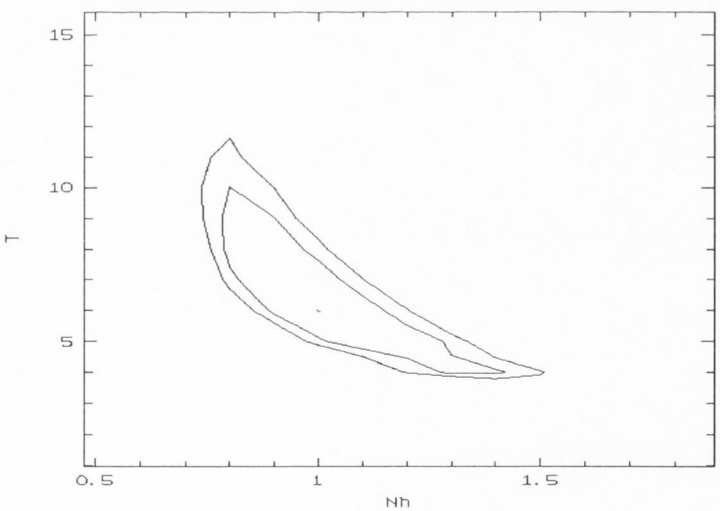


Figure C.9: 2 dimensional χ^2 plot for the galaxy cluster MS1111.8-3754 .

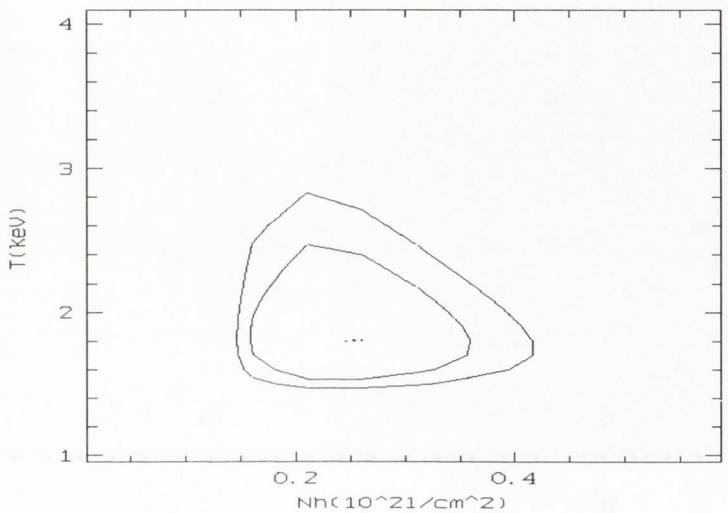


Figure C.10: 2 dimensional χ^2 plot for the galaxy cluster MS1201.5+2824.

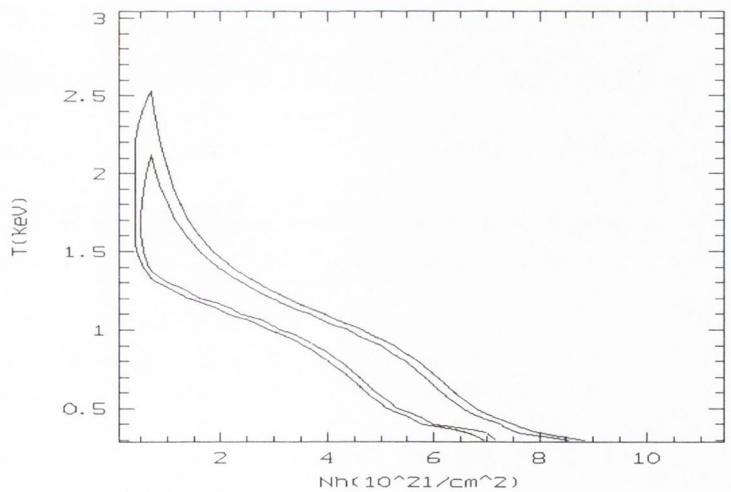


Figure C.11: 2 dimensional χ^2 plot for the galaxy cluster MS1208.7+3928.

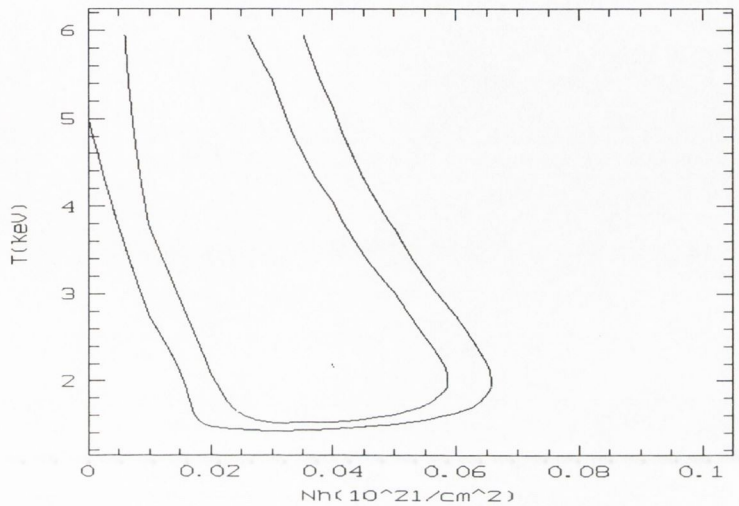


Figure C.12: 2 dimensional χ^2 plot for the galaxy cluster MS1308.8+3244.

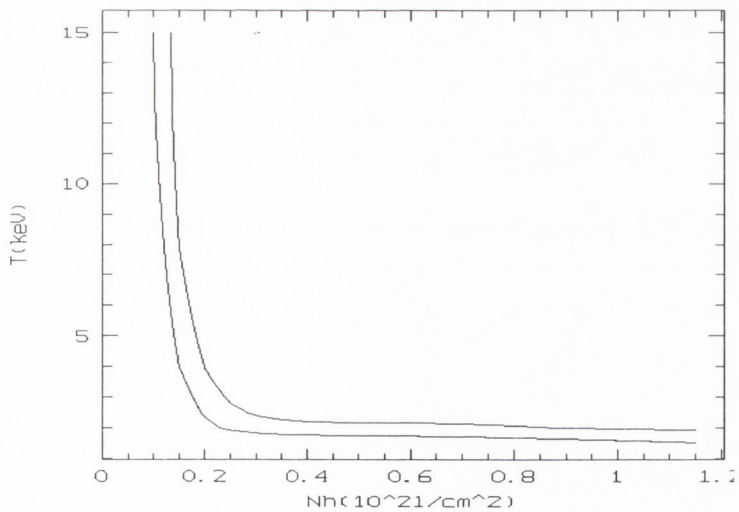


Figure C.13: 2 dimensional χ^2 plot for the galaxy cluster MS1335.2-2928 .

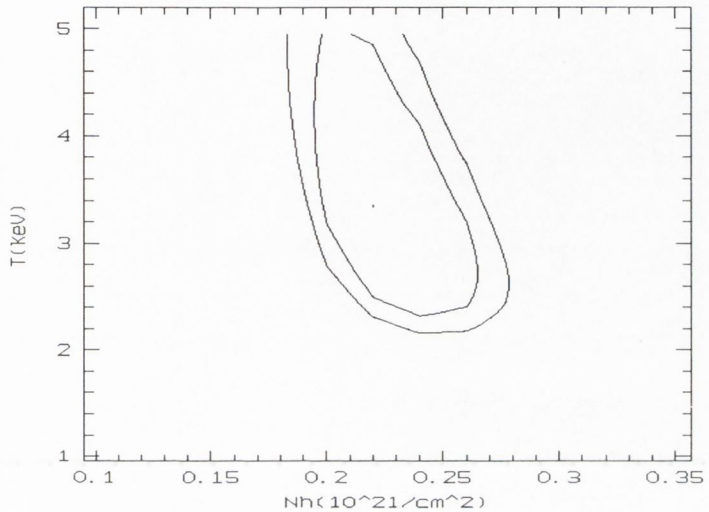


Figure C.14: 2 dimensional χ^2 plot for the galaxy cluster MS1358.4+6245.

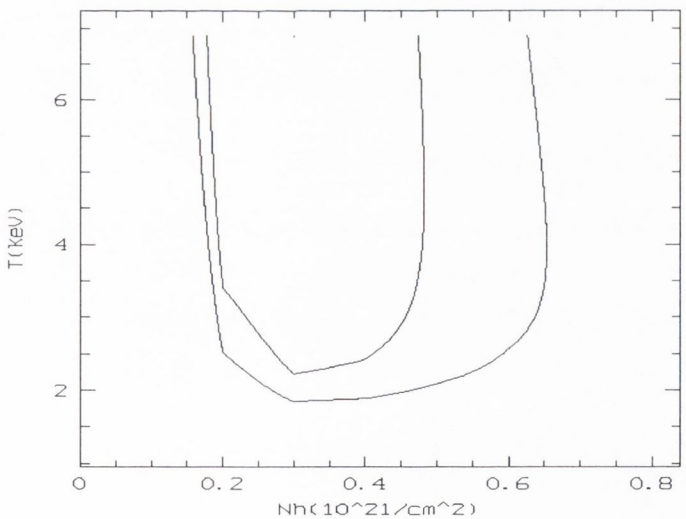


Figure C.15: 2 dimensional χ^2 plot for the galaxy cluster MS1426.4+0158.

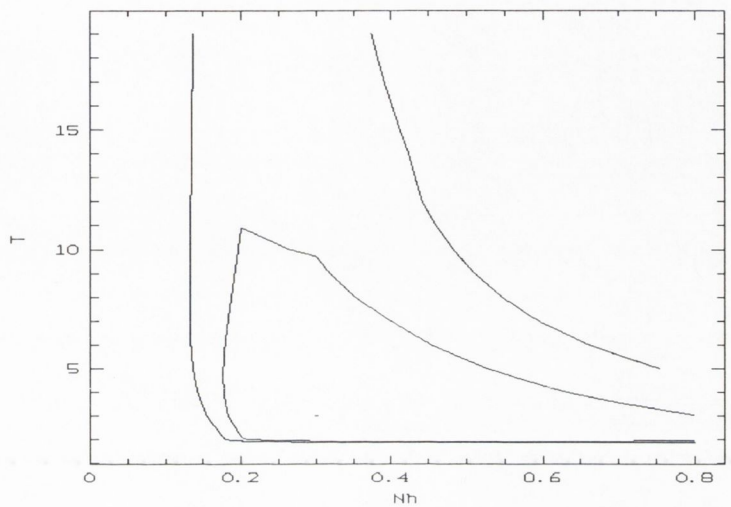


Figure C.16: 2 dimensional χ^2 plot for the galaxy cluster MS1512.4+3647.

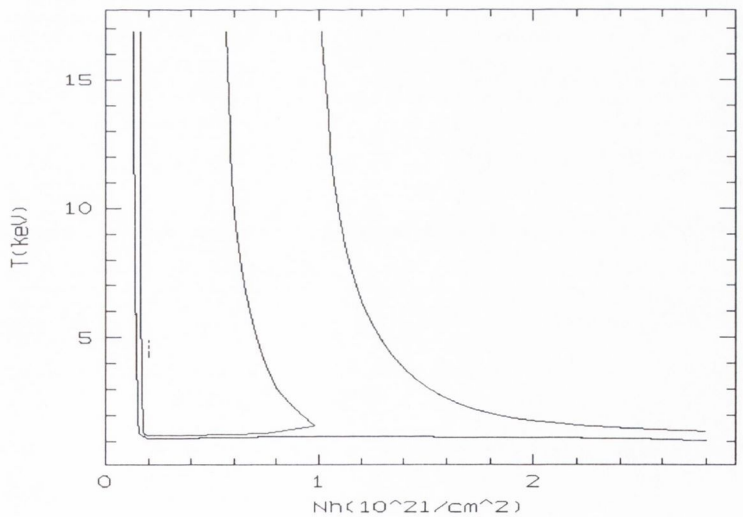


Figure C.17: 2 dimensional χ^2 plot for the galaxy cluster MS1546.1+1132.

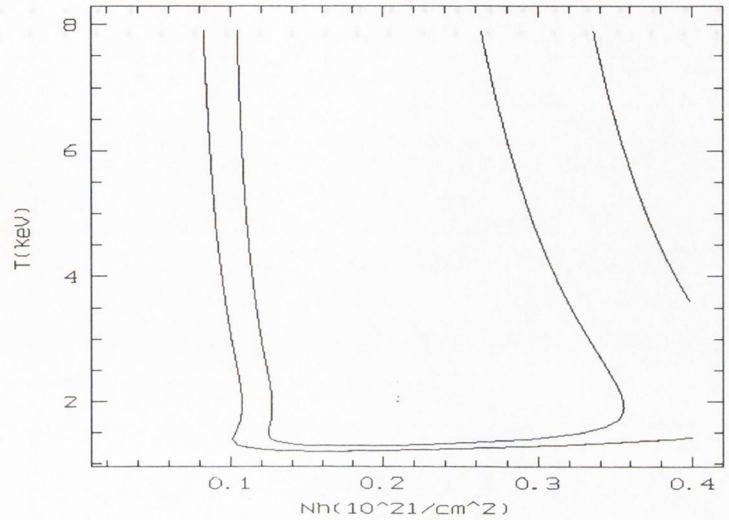


Figure C.18: 2 dimensional χ^2 plot for the galaxy cluster MS1617.1+3237.

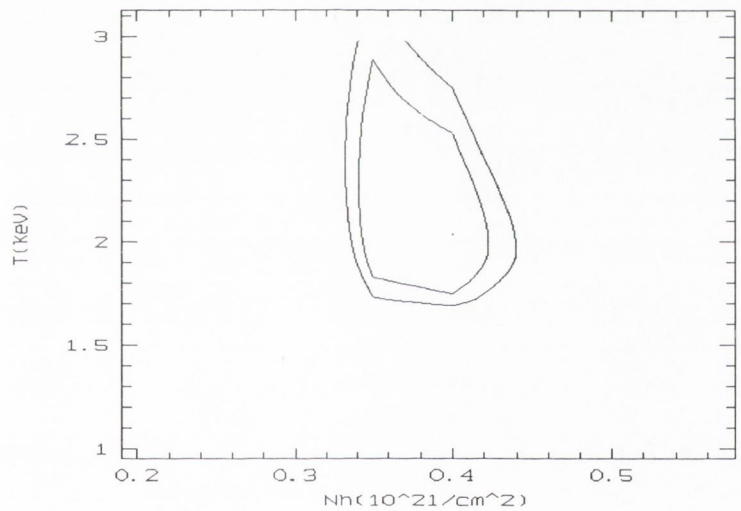


Figure C.19: 2 dimensional χ^2 plot for the galaxy cluster MS2137.3-2353.

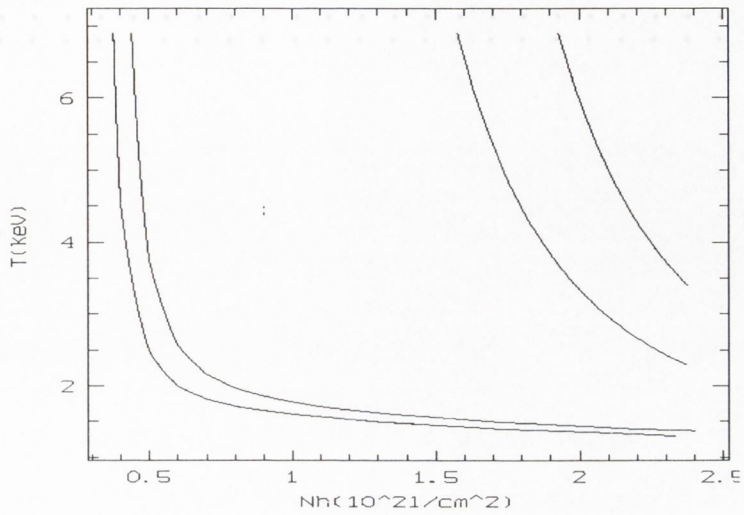


Figure C.20: 2 dimensional χ^2 plot for the galaxy cluster MS2255.7+2039.

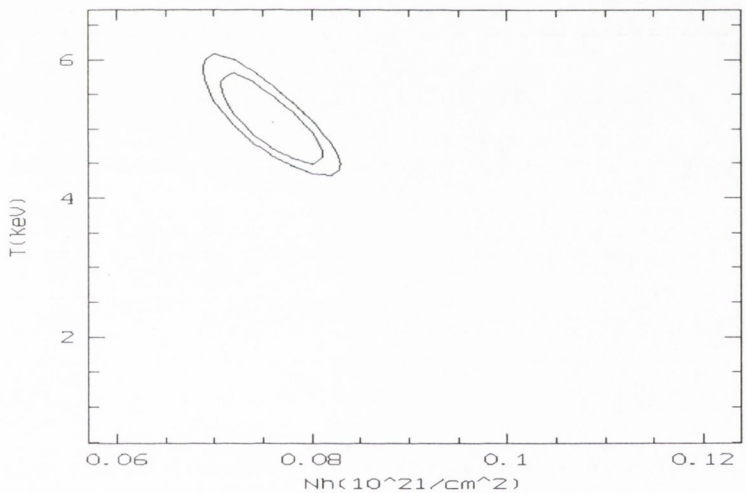


Figure C.21: 2 dimensional χ^2 plot for the galaxy cluster MS2311.2-4259.

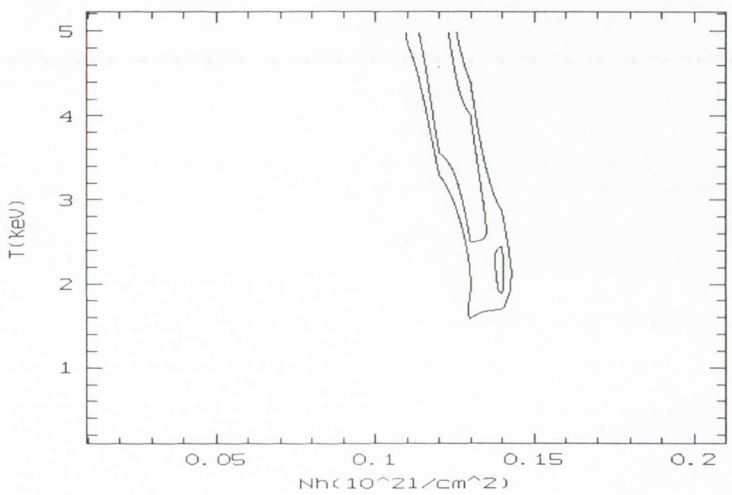


Figure C.22: 2 dimensional χ^2 plot for the galaxy cluster MS2354.4-3502.

Appendix D

1 dimensional χ^2 for the EMSS Galaxy Clusters

We present 1 dimensional χ^2 plots of temperature for two confidence levels of 68.3 % and 95.5 % for the 22 EMSS Galaxy clusters in chapter 5. The best fit value of N_H has been fixed at the value derived from the 2 dimensional χ^2 plot.

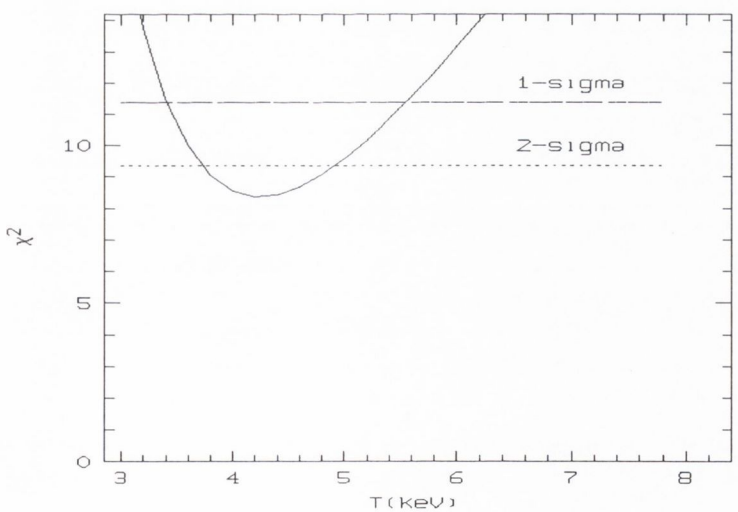


Figure D.1: 1 dimensional χ^2 plot for the galaxy cluster MS0015.9+1609, for N_H fixed at 0.6 $\times 10^{21} cm^{-2}$.

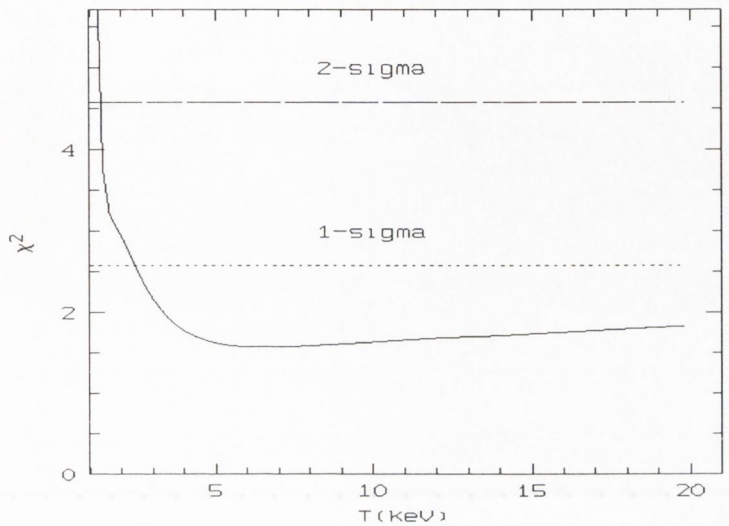


Figure D.2: 1 dimensional χ^2 plot for the galaxy cluster MS0353.6-3642 , for N_H fixed at 0.1 $\times 10^{21} cm^{-2}$.

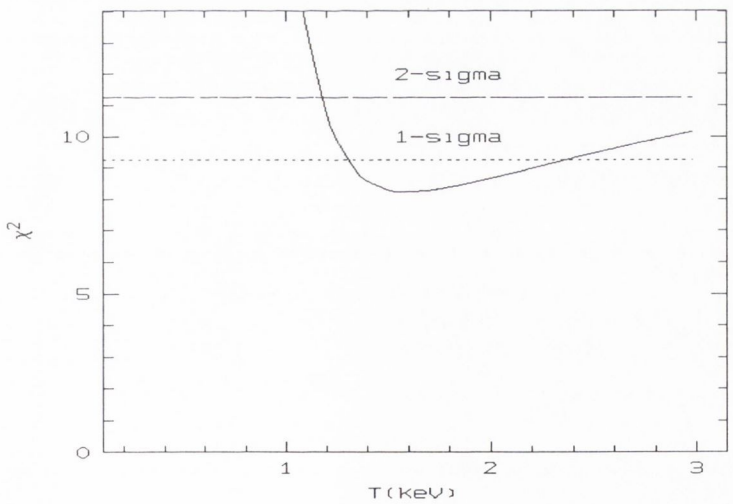


Figure D.3: 1 dimensional χ^2 plot for the galaxy cluster MS0418.3-3844, for N_H fixed at 0.207 $\times 10^{21} cm^{-2}$.

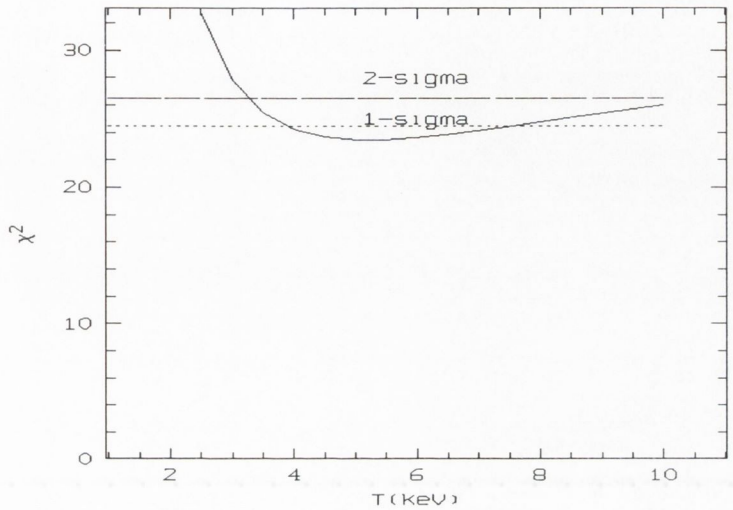


Figure D.4: 1 dimensional χ^2 plot for the galaxy cluster MS0451.5+0250, for N_H fixed at 0.78 $\times 10^{21} cm^{-2}$.

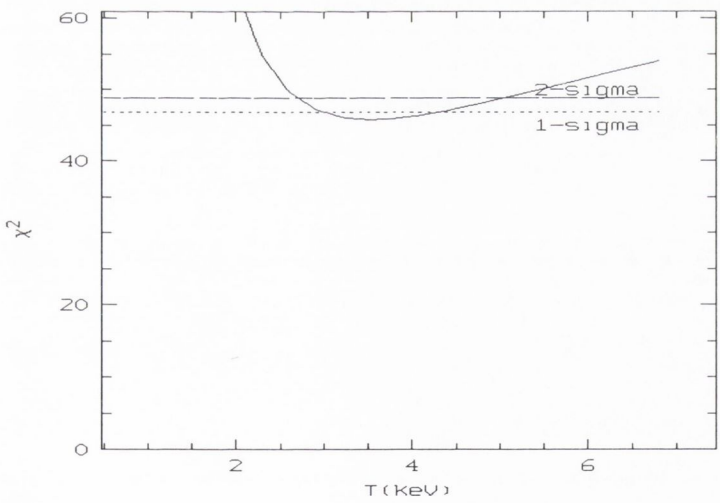


Figure D.5: 1 dimensional χ^2 plot for the galaxy cluster MS0451.6-0305,for N_H fixed at galactic value, 0.437 $\times 10^{21} cm^{-2}$.

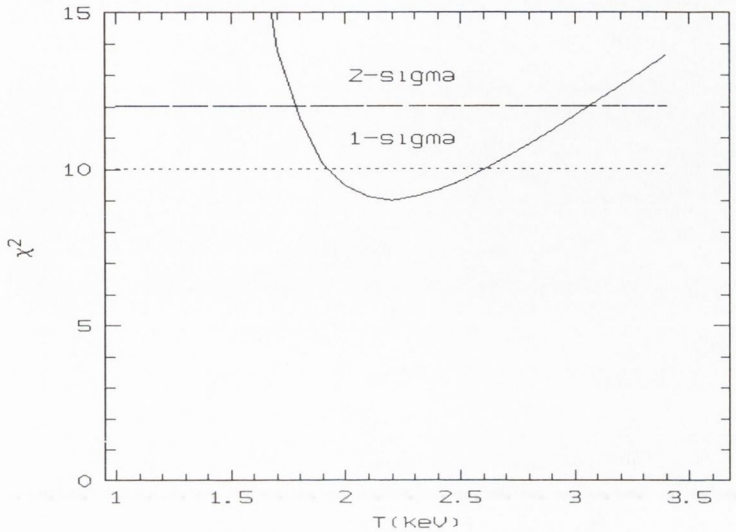


Figure D.6: 1 dimensional χ^2 plot for the galaxy cluster MS0735.6+7421,for N_H fixed at galactic value ,0.348 $\times 10^{21} cm^{-2}$.

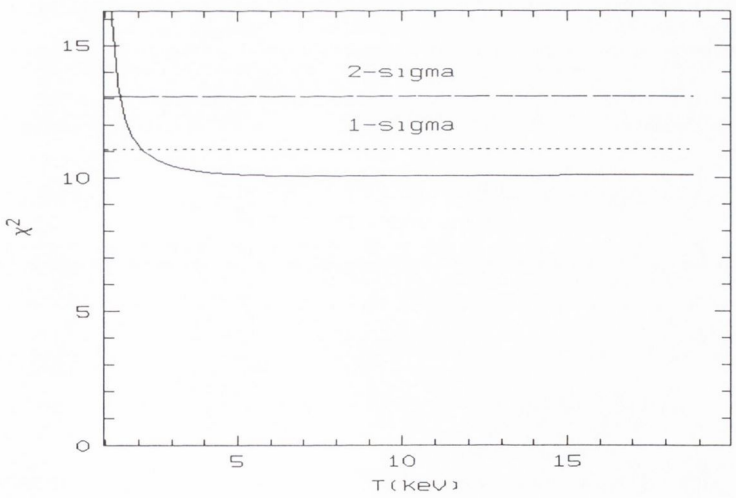


Figure D.7: 1 dimensional χ^2 plot for the galaxy cluster MS0811.6+6301,for N_H fixed at galactic value, 0.428 $\times 10^{21} cm^{-2}$.

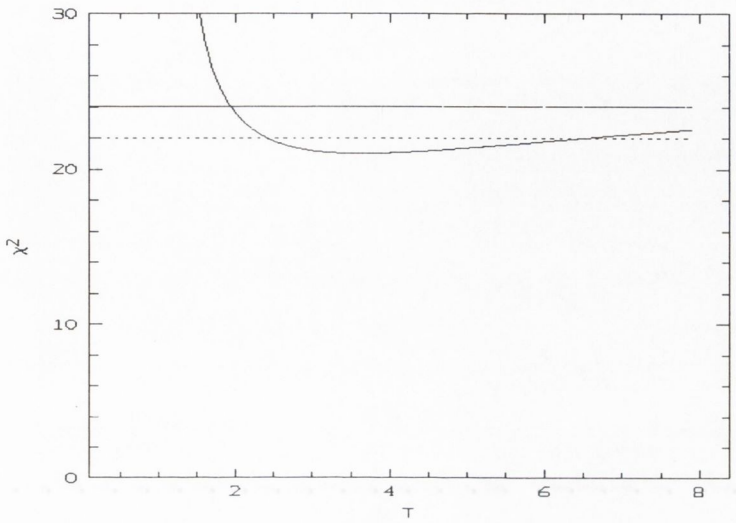


Figure D.8: 1 dimensional χ^2 plot for the galaxy cluster MS1020.7+6820, for N_H fixed at 0.6 $\times 10^{21} cm^{-2}$.

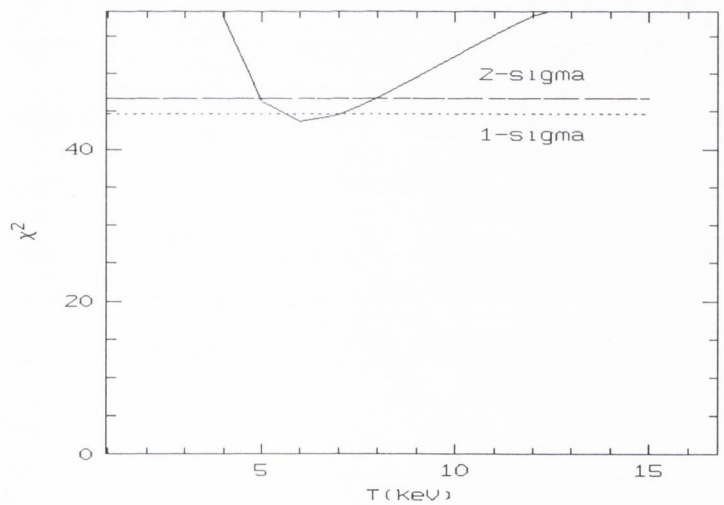


Figure D.9: 1 dimensional χ^2 plot for the galaxy cluster MS1111.8-3754,for N_H fixed at 1 $\times 10^{21} cm^{-2}$.

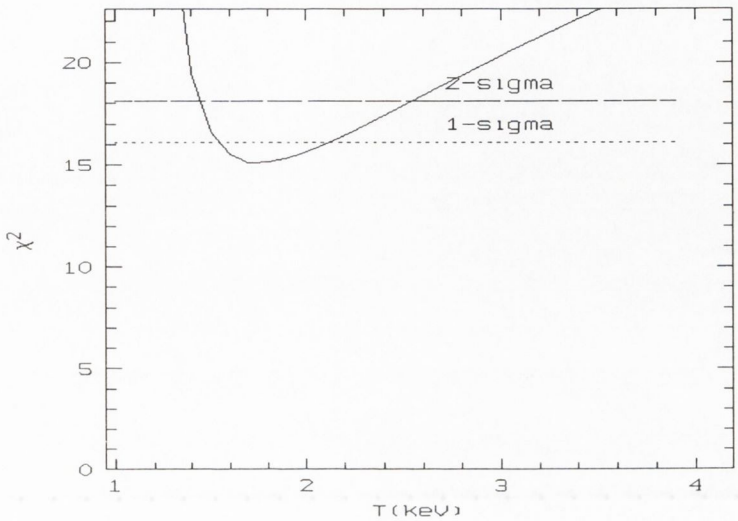


Figure D.10: 1 dimensional χ^2 plot for the galaxy cluster MS1201.5+2824,for N_H fixed at galactic value, 0.244 $\times 10^{21} cm^{-2}$.

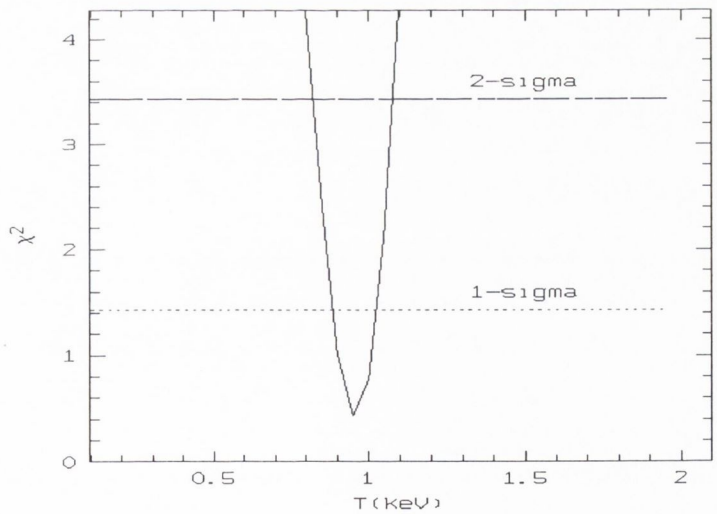


Figure D.11: 1 dimensional χ^2 plot for the galaxy cluster MS1208.7+3928, for N_H fixed at $10^{21} cm^{-2}$.

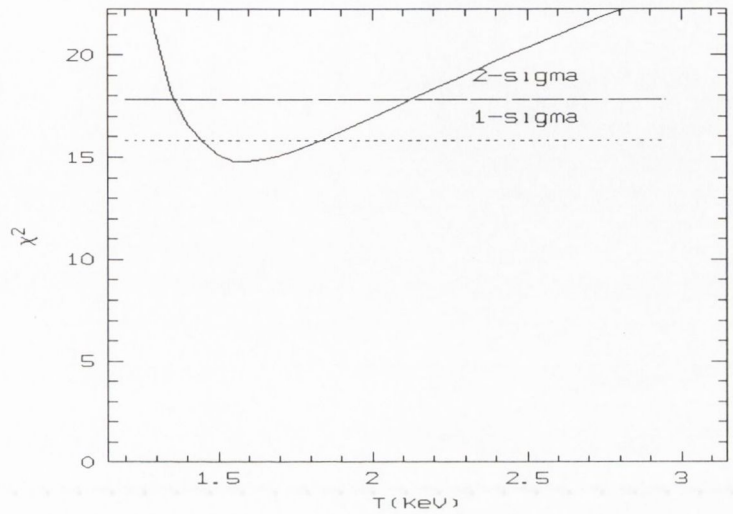


Figure D.12: 1 dimensional χ^2 plot for the galaxy cluster MS1308.8+3244, for N_H fixed at galactic value, 0.296 $\times 10^{21} cm^{-2}$.

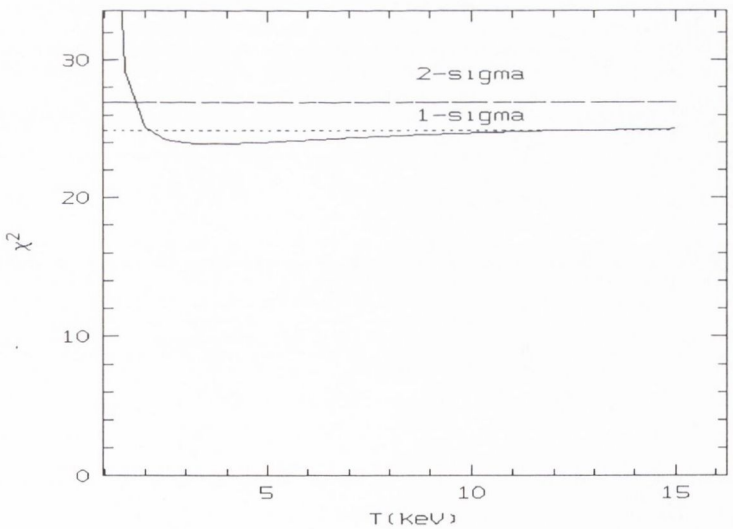


Figure D.13: 1 dimensional χ^2 plot for the galaxy cluster MS1335.2-2928, for N_H fixed at galactic value, 0.373 $\times 10^{21} cm^{-2}$.

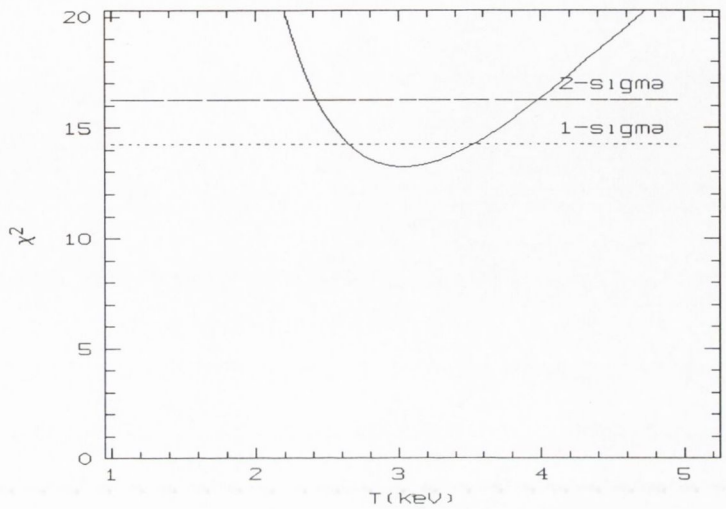


Figure D.14: 1 dimensional χ^2 plot for the galaxy cluster MS1358.4+6245,for N_H fixed at 0.244 $\times 10^{21} cm^{-2}$.

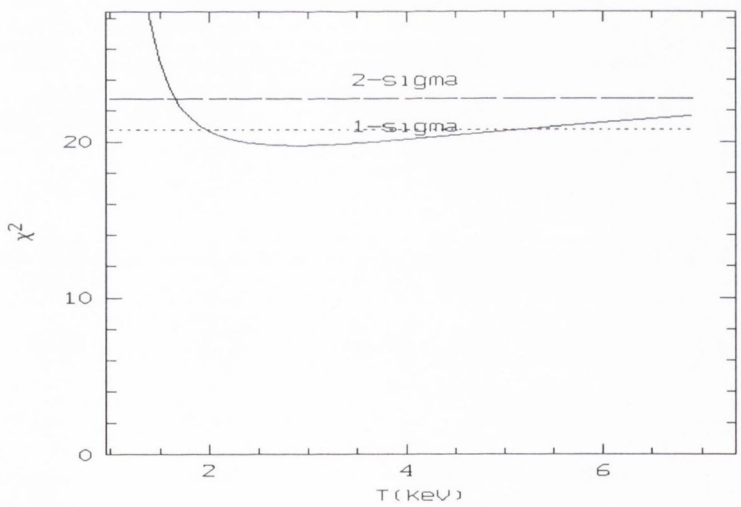


Figure D.15: 1 dimensional χ^2 plot for the galaxy cluster MS1426.4+0158,for N_H fixed at 0.3 $\times 10^{21} cm^{-2}$.

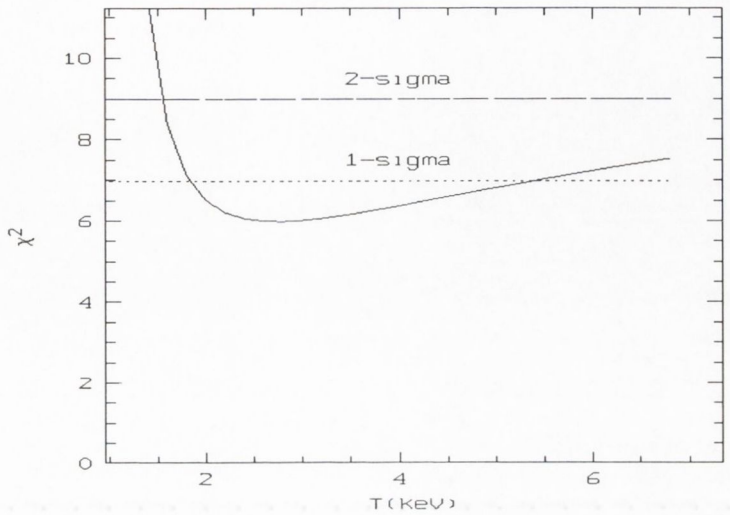


Figure D.16: 1 dimensional χ^2 plot for the galaxy cluster MS1512.4+3647, for N_H fixed at 0.3 $\times 10^{21} cm^{-2}$.

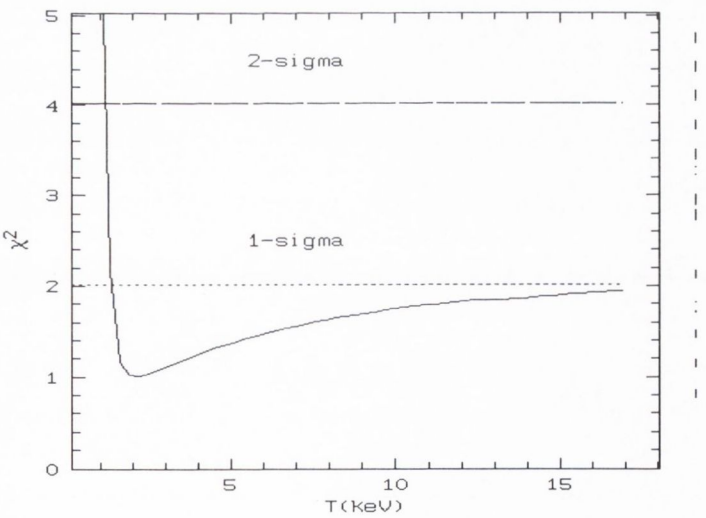


Figure D.17: 1 dimensional χ^2 plot for the galaxy cluster MS1546.1+1132, for N_H fixed at galactic value, 0.361 $\times 10^{21} cm^{-2}$.

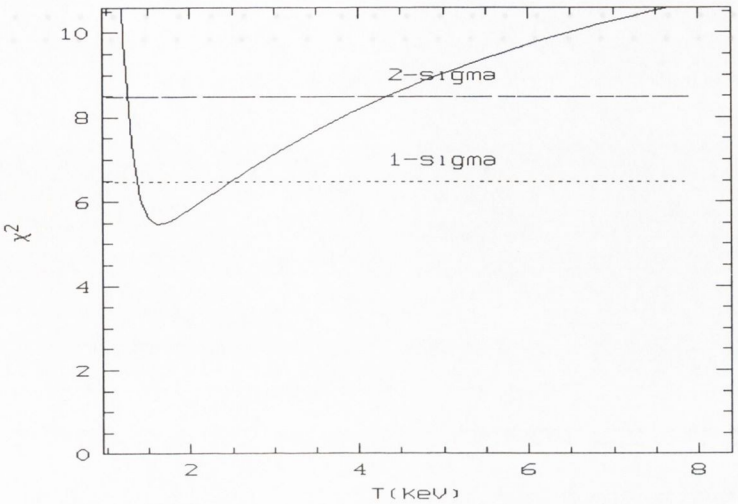


Figure D.18: 1 dimensional χ^2 plot for the galaxy cluster MS1617.1+3237,for N_H fixed at 0.2 $\times 10^{21} cm^{-2}$.

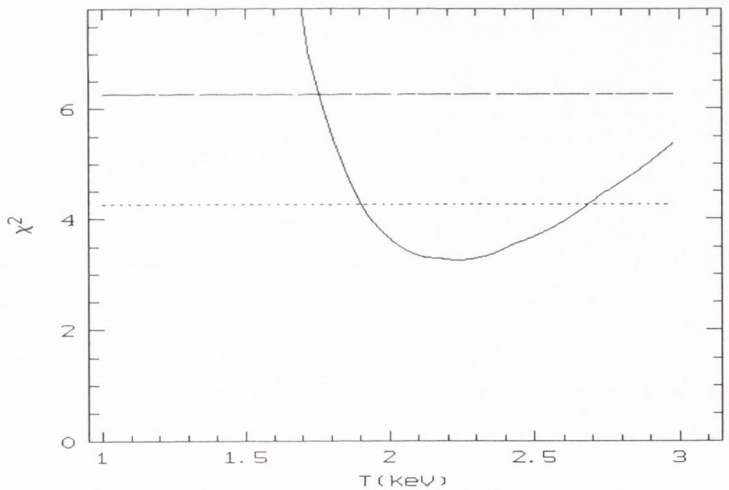


Figure D.19: 1 dimensional χ^2 plot for the galaxy cluster MS2137.3-2353,for N_H fixed at 0.4 $\times 10^{21} cm^{-2}$.

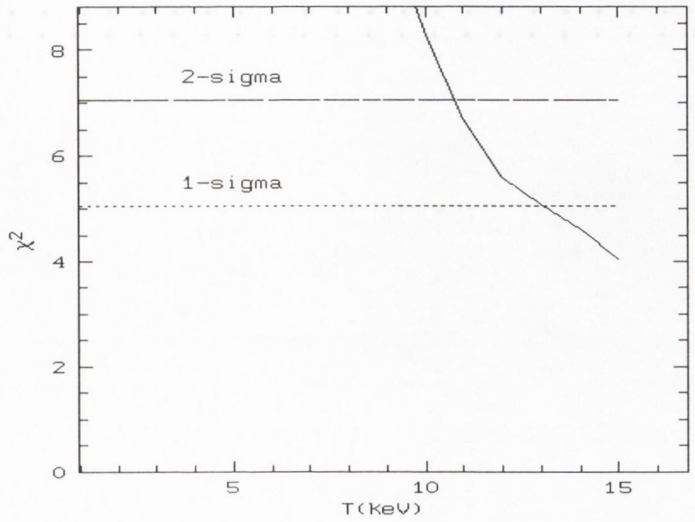


Figure D.20: 1 dimensional χ^2 plot for the galaxy cluster MS2255.7+2039, for N_H fixed at 1.1 $\times 10^{21} cm^{-2}$.

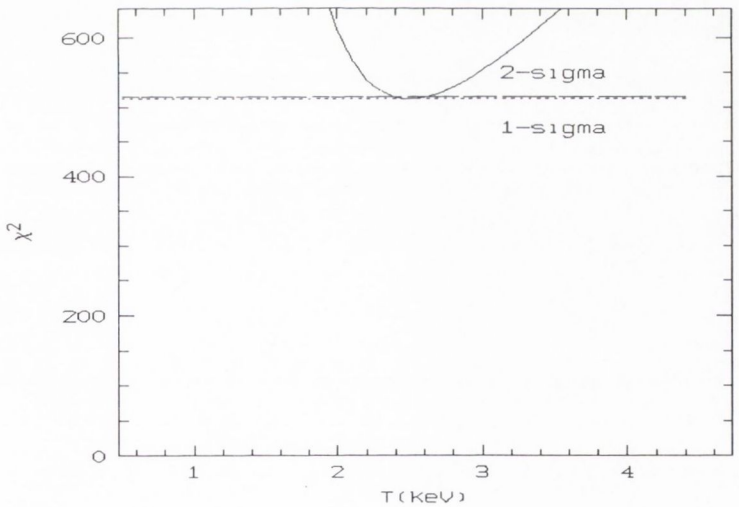


Figure D.21: 1 dimensional χ^2 plot for the galaxy cluster MS2311.2-4259, for N_H fixed at galactic value 0.176 $\times 10^{21} cm^{-2}$.

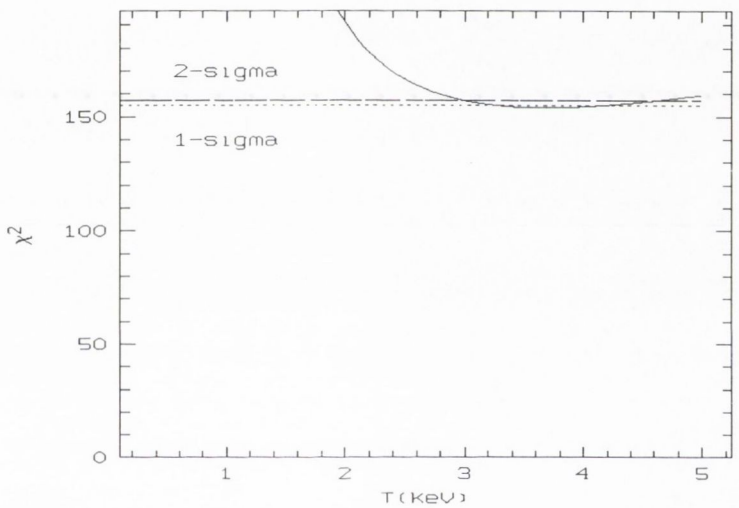


Figure D.22: 1 dimensional χ^2 plot for the galaxy cluster MS2354.4-3502,for N_H fixed at 0.12 $\times 10^{21} cm^{-2}$.

D.1 Notes on Individual Clusters discussed in chapter 5

D.1.1 MS 0015.9 +1609 (Cl0016+16)

MS 0015.9+1609 is a well studied cluster with HRI, PSPC, ASCA and lensing data. At z=0.547 it is the most distant cluster in our sample. The central cooling time for a gas of temperature 8.4 keV and for the density profile obtained from the isothermal β model fit is less than 10^{10} years. Therefore the cluster cannot yet have formed a steady cooling flow (Neumann & Boehringer 1997). They record a temperature in the range 6–10 keV. Lewis et al. (Lewis et al. 1999) claim to see evidence of a cooling flow. Analysed as part of WARPS (Jones et al. 1998).

D.1.2 MS 0353.6-3542 (S400)

Temperature measured by ASCA $6.2^{+1.0}_{-0.8}$ keV (Henry et al. 1997). Only 173 photons with the ROSAT PSPC resulting in a temperature = ($1.6^{+1.4}_{-0.2}$ keV). No evidence of substructure from our contour plot.

D.1.3 MS 0418.3-3844

Only 230 photons with the ROSAT PSPC; no evidence of substructure in our contour plot.

D.1.4 MS 0451.5+0250(A520)

Contains two dominant galaxies and two peaks in its galaxy velocity distribution (Carlberg et al. 1996). Strong candidate for a core merger, is a non-cooling flow cluster based on the non detection of Hα by Donahue (Donahue et al. 1992) and the lack of a bright peak in the X-ray surface brightness profile (Lewis et al. 1999).

David, Forman and Jones (David et al. 1999) calculate a count rate of 0.255 cts/s and $L_{0.5-2.0keV} = 6.17 \times 10^{44}$ ergs^{-1}. Analysed as part of

WARPS (Jones et al. 1998). Definitely not a cooling flow cluster (Lewis et al. 1999). Böhringer et al.(2000) used RASS (ROSAT ALL SKY SURVEY) data to determine count rate = 0.36 cts/s, $f_x = 8.33 \times 10^{-13} \mathrm{ergs}^{-1} cm^{-2}$ and $L_{0.5-2.0keV} = 14.52 \times 10^{44} \mathrm{ergs}^{-1}$. Ebeling et al.(2000) measure a count rate =0.40 $\pm$0.09 cts/s,$f_x(0.1 - 2.4keV) = 8.4 \times 10^{-13}$ $\mathrm{ergs}^{-1} cm^{-2}$ and $L_{0.1-2.4keV} = 14.44 \times 10^{44}$ ergs^{-1}.

D.1.5 MS 0451.6-0305

The most luminous cluster in the EMSS and one of the most luminous clusters known. Donahue & Stocke(1995) detect 1400 cts for the cluster and fit a column density of $N_H = 3.2^{+0.5}_{-0.5} \times 10^{20} cm^{-2}$ which is significantly lower than the galactic value of $4.37 \times 10^{20} cm^{-2}$. They measure $T \geq 3.5$ keV (using 2-D χ^2 plot)and a luminosity (within 100″) = $15.6 \times 10^{44} h_{50}^{-2}$ ergs^{-1}. In contrast we fix N_H to the galactic value and measure T = $4^{+0.5}_{-0.1}$ keV (using a 1-D χ^2 plot). Lewis et al.(Lewis et al. 1999) find no evidence of a cooling flow. Analysed as part of WARPS (Jones et al. 1998).

D.1.6 MS 0735.6 +7421(z1370)

Donahue & Stocke (1995) measure T = $2.4^{+2.2}_{-0.8}$ assuming 30% metallicity and a Raymond-Smith model with $N_H = 3.4^{+0.5}_{-0.5} \times 10^{20} cm^{-2}$ consistent with our temperature ($4.1^{+0.7}_{-0.5}$ keV) and galactic N_H, and designate it a cooling flow cluster. Böhringer et al. (2000) using RASS data determine a count rate = 0.19 $ctss^{-1}$, $f_x = 4.06 \times 10^{-13}$ erg $s^{-1} cm^{-2}$ and $L_{0.5-2.0keV} = 7.94 \times 10^{44}$ ergss^{-1}. Ebeling et al. (2000) measure a count rate =0.23 $\pm$ 0.06, f_x(0.1-2.4 keV)=40×10^{-13} $\mathrm{ergss}^{-1} cm^{-2}$ and $L_{0.1-2.4keV} = 7.9 \times 10^{44}$ ergs s^{-1}. Analysed as part of WARPS (Jones et al. 1998).

D.1.7 MS0811.6+6301

ASCA Temperature = $4.6^{+0.9}_{-0.6}$ (Henry et al. 1997).

D.1.8 MS 1020.7+6820(A981)

D.1.9 MS1111.8-3754

A cooling flow cluster (Johnstone & Fabian 1989).

D.1.10 MS1201.5 +2824(A1455)

$f_x = 26.6 \pm 3.8 \times 10^{-14}$ ergs $s^{-1}cm^{-2}$ (Vikhlinin et al. 1998). David, Forman and Jones (David et al. 1999) observe a count rate of $\leq$ 0.0109 (cts/s) and $L_{0.5-2.0keV} \leq 1.44 \times 10^{43}$ ergs s^{-1}. Böhringer et al.(2000) determine a count rate = 0.07 ctss^{-1}, $f_x(0.1 - 2.4keV) = 1.42 \times 10^{-13}$ erg $s^{-1}cm^{-2}$ and $L_{0.5-2.0keV} = 1.63 \times 10^{44}$ ergs s^{-1} using RASS data. Analysed as part of WARPS (Jones et al. 1998).

D.1.11 MS 1208.7+3928

$f_x(0.1-2.4keV) = 102.6 \pm 11.4 \times 10^{-14}$ ergs $s^{-1}cm^{-2}$ (Vikhlinin et al. 1998)). $r_c = 32 \pm 3$". Analysed as part of WARPS (Jones et al. 1998).

D.1.12 MS 1308.8+3244

$f_x(0.1 - 2.4keV) = 46.7 \pm 5.8 \times 10^{-14}$ ergs $s^{-1}cm^{-2}$ and $r_c = 22 + / - 3$ arcseconds (Vikhlinin et al. 1998). Analysed as part of WARPS (Jones et al. 1998).

D.1.13 MS 1335.2-2928

Analysed as part of WARPS (Jones et al. 1998).

D.1.14 MS 1358.4+6245(ZW6429)

Definite cooling flow cluster (Lewis et al. 1999). Boehringer et al.(Böhringer et al. 2000) determine a count rate = 0.1 ctss^{-1}, a flux $F_x = 1.97 \times 10^{-13}$ ergs $s^{-1}cm^{-2}$ and a luminosity of $L_{0.5-2.0keV} = 8.83 \times 10^{44}$ ergs s^{-1} using

RASS (ROSAT ALL SKY SURVEY) data. Mason et al. (Mason et al. 2000) measures a count rate =0.018 $\pm$ 0.001 and a flux of f_x (0.1-2.4 keV)= 2.8 $\times$ 10^{-13} ergs$^{-1}cm^{-2}$. Observed by Chandra (Bautz et al. 2002) they measure $r_c = 12^{+30}_{-12}$ kpc. Analysed as part of WARPS (Jones et al. 1998).

D.1.15 MS1426.4+0158

ASCA temperature = $5.5^{+1.1}_{-0.7}$ (Henry et al. 1997).

D.1.16 MS1512.4+3647

Lewis et al.(Lewis et al. 1999) determine (from combined ROSAT HRI and PSPC data) $\beta = 0.55^{+0.04}_{-0.04}$ and $r_c = 29^{+7}_{-7}$kpc. Also find HRI image is somewhat elliptical, uniform and with a slight peak. There is evidence for a small cooling flow. Analysed as part of WARPS (Jones et al. 1998).

D.1.17 MS 1546.1+1132

Only detect 78 photons using the ROSAT PSPC and measure a lower limit of 2 keV.

D.1.18 MS1617.1+3237

Only detect 196 photons using the ROSAT PSPC nevertheless we get good errors for our temperature estimate, $1.6^{+0.9}_{-0.3}$.

D.1.19 MS2137.3-2353

Analysed as part of WARPS (Jones et al. 1998).

D.1.20 MS2255.7+2039(A2092)

Analysed as part of WARPS (Jones et al. 1998).

D.1.21 MS2311.2-4259 (Abell S1101)

Temperature = $2.6^{+0.50}_{-0.50}$ measured by XMM EPIC (Kaastra et al. 2001) in good agreement with our ROSAT PSPC temperature of $2.5^{+0.1}_{-0.1}$. Ikebe et al.(2002) measure a flux of $244 \pm 4 \times 10^{-13}$ ergs s^{-1}cm^{-2} whereas we measure a flux of $260^{+4}_{-3} \times 10^{-13}$ ergs $s^{-1}cm^{-2}$.

D.1.22 MS2354.4-3502 (Abell 4059)

ASCA temperaure = $3.94^{+0.15}_{-0.15}$ (Ikebe et al. 2002). Our ROSAT PSPC temperature = $2.9^{+0.1}_{-0.1}$. Ikebe et al. also measure a flux of $310 \pm 7 \times 10^{-13}$ergs$s^{-1}cm^{-2}$ whereas we measure a flux of $265^{+4}_{-4} \times 10^{-13}$ergs$s^{-1}cm^{-2}$.

D.2 Comparison of β values obtained with published values with other work

In this section we compare β and r_c with other work especially Lewis et al.(1999) and Ellis & Jones(2001).

1. MS0015.9 +1609: r_c= 50.5 " $\beta = 0.80^{+0.09}_{-0.07}$ (Neumann & Boehringer 1997). $\beta = 0.81^{+0.02}_{-0.08}$ and $r_c = 196^{+5}_{-23}$(kpc) using combined HRI and PSPC data (Lewis et al. 1999). Both in good agreement with our results.

2. MS 0353.6-3642: r_c=225^{+37}_{-31}(kpc) assuming β=2/3 (Ellis & Jones 2001).

3. MS0418.3-3844: r_c=474^{+92}_{-75}(kpc) assuming β=2/3 (Ellis & Jones 2001).

4. MS0451.5+0250 : Using both ROSAT PSPC and HRI $\beta = 0.49^{+0.08}_{-0.08}$ r_c = 100^{+50}_{-50} (Lewis et al. 1999).

5. MS0451.6-0305: Using both ROSAT PSPC and HRI $\beta = 0.84^{+0.06}_{-0.06}$ and $r_c = 175^{+14}_{-15}$ (Lewis et al. 1999). Only using PSPC data $\beta = 0.92 \pm$ 0.11 consistent with our measurement. $r_c = 175^{+14}_{-15}$(kpc) assuming β=2/3(Ellis & Jones 2001). $\beta = 1.00^{+0.4}_{-0.3}$ and $r_c = 360^{+80}_{-36}$ (Donahue & Stocke 1995).

6. MS0735.6+7421(z1370) r_c = 234 ± 40 Kpc and β of 0.80±0.25 on fitting a King model with a gaussian central source (Donahue & Stocke 1995).

7. MS0811.6+6301: r_c=474^{+92}_{-75}(Kpc) assuming β=2/3 (Ellis & Jones 2001).

8. MS1201.5+2824(A1455) $r_c = 14 \pm 4$" (Vikhlinin et al. 1998).

9. MS1208.7+3928 $r_c = 32 \pm 3$" (Vikhlinin et al. 1998).

10. MS1358.4+6245: Using both ROSAT PSPC and HRI $\beta = 0.84^{+0.06}_{-0.06}$ and $r_c = 133^{+21}_{-20}$ in accordance with our measurements (Lewis et al. 1999). r_c=133^{+21}_{-20}(Kpc) assuming β=2/3 (Ellis & Jones 2001). Chandra measures $r_c = 12^{+30}_{-12} h_{50}^{-1}$ kpc (Bautz et al. 2002).

11. MS1426.4+0158: $r_c = 302^{+43}_{-38}$(Kpc) assuming $\beta = 2/3$ (Ellis & Jones 2001).

12. MS1512.4+3647: $\beta = 0.55^{+0.04}_{-0.04}$ and $r_c = 29^{+7}_{-7}$ combining ROSAT PSPC and HRI (Lewis et al. 1999). r_c=114^{+14}_{-14}(Kpc) assuming $\beta = 2/3$(Ellis & Jones 2001).

13. MS2137.3-2353: r_c=49^{+2}_{-3}(Kpc) assuming $\beta = 2/3$ (Ellis & Jones 2001).

As can be seen from Table 7 and the discussion above our measured values for β and r_c are in good agreement with values obtained from the literature, lending weight to our determinations of β (15) and core radius(10) for galaxy clusters which perviously had no published values.